CAVITATION INCEPTION SCALE EFFECTS

I. Nuclei Distributions in Natural Waters

II. Cavitation Inception in a Turbulent Shear Flow

Thesis by

Timothy John O'Hern

In Partial Fulfillment of the Requirements

for the Degree of

Doctor of Philosophy

California Institute of Technology

Pasadena, California

1987

(Submitted May 4, 1987)

ACKNOWLEDGEMENTS

Special thanks to my thesis advisor, Professor A.J. Acosta, whose insight and direction were irreplaceable in the course of this work. I especially appreciate the opportunities I have had to attend a number of technical meetings to present various aspects of this work. Thanks also to Professors R.F. Sabersky, C.E. Brennen and A. Roshko for their continuing interest in my research and welfare.

Professor J. Katz of Purdue University, my immediate predecessor on these projects, was a valuable colleague and motivating force during the early stages of this research. Special thanks also to Luca d'Agostino, a current colleague, who has provided much valuable insight in the course of our work together.

The friendship and assistance of Elton Daly, Joe Fontana, Rich Eastvedt and Leonard Montenegro of the W.M. Keck Laboratory of Hydraulics and Water Resources were of particular importance in construction and trouble-shooting of the experimental apparatus. I feel indebted to Cecilia Lin for her long hours of drawing and figure preparation needed for this manuscript. Several students have been involved in the data collection and reduction aspects of these experiments, and I would especially like to acknowledge Theresa Rueen-Fang Wang, Sheldon Green, Richard Arrieta and Cindy Morss for their assistance in the holographic testing and analysis. Judy Goldish and Matt Compton were also of great assistance for their support during some of the water tunnel experiments.

I very much appreciate the financial support provided by the Earle C. Anthony Fellowship for my first year of graduate study. I would also like to give special acknowledgement of the financial support of myself and this research provided by the Office of Naval Research and by the Naval Sea Systems Command General Hydromechanics Research Program administered by the David W. Taylor Naval Ship Research and Development Center. This support is deeply appreciated. Special thanks to Dr. T.T. Huang of DTNSRDC for his personal involvement and interest in this work.

Finally, deepest thanks go to my family for their understanding and support over the years of my formal education. I dedicate this thesis with love to my wife, Charlotte Jesse Welty, whose encouragement and tolerance were often needed and always appreciated.

ABSTRACT

Cavitation scale effects can be grouped into two major categories: susceptibility of the water to cavitation, i.e., the amount, size, and type of microbubbles or microparticulates in the water acting as inception nuclei, and flow field effects due to such factors as velocity and pressure distributions, body size and shape, viscous effects, and turbulent phenomena. Experimental investigations into these two aspects of scale effects were performed in the present study.

Field investigations of marine nuclei populations were made using underwater holography to observe microbubbles and particulates, including microplankton in oceanic waters of Los Angeles Harbor, San Pedro Channel and near Santa Catalina Island. Holographic detection was shown to be a reliable method of measuring the nuclei number concentration density distributions. Overall, very high concentrations of the various types of potential cavitation nuclei were observed at all of the test sites and depths examined, although the statistical significance of these results is strong only in the smaller size ranges (less than 50 μm), where a significant number of counts were made. Relatively high bubble concentrations during calm sea conditions, and their population inversion below the thermocline where organism activity was high, indicate a possible biological source of bubble production rather than the usual surface mechanisms of breaking waves and whitecaps. The measured population of particulates is somewhat higher than comparable data in the ocean or in cavitation test facilities, and the number density distribution of particulates decreases approximately as the fourth power of the particle size, as often reported in the literature. An increase in particle concentration near the bottom of the thermocline in clear coastal waters is observed. The total concentration of particles and bubbles in a liquid provides an upper bound on the number of potentially active cavitation nuclei. The measured bubble sizes can be used to indicate that the average tensile strength of the ocean waters examined in this study should be on the order of

a few thousand Pascals, with a minimum expected value of about one hundred Pascals. The present results support the recommendation of Billet (1985), that a concentration of at least 3 bubbles per cm^3 in the 5 to 20 μm radius range is needed in test facility water in order to model marine conditions.

Experimental studies were also made on the inception processes in a large turbulent free shear layer generated by a sharp edged plate in a water tunnel at Reynolds numbers up to 2×10^6. Two distinct types of vortex motion were evident in the shear layer, the primary spanwise and the secondary longitudinal vortices. Cavitation inception occurs consistently in the secondary shear layer vortices and more fully developed cavitation is visible in both structures, with the streamwise cavities primarily confined to the braid regions between adjacent spanwise vortices. A Rankine vortex model indicates that the secondary vortex strength is always less than 10% of that of the primary structure. Measurements of fluctuating pressures in the turbulent shear layer are made by holographically monitoring the size of air bubbles injected into the non-cavitating flow, showing that pressure fluctuations were much stronger than previously reported, with positive and negative pressure peaks as high as 3 times the freestream dynamic pressure, sufficient to explain the occurrence of cavitation inception at high values of the inception index. Cavitation inception indices display a strong dependence on the dissolved air content and thus on the availability of freestream bubble cavitation nuclei. The present inception data do not display a clear dependence on freestream velocity (or Reynolds number) but do fall into the overall range of data of previous bluff body investigations. The occurrence of inception in the secondary vortices of the shear layer, and previous reports of velocity dependence of these cores (Bernal 1981) may provide the key to explaining the commonly observed Reynolds number scaling of the inception index in shear flows.

TABLE OF CONTENTS

NOMENCLATURE

A	projected frontal area
C_{pb}	base pressure coefficient $(= (p_B - p_\infty)/(\frac{1}{2}\rho {U_\infty}^2))$
C_D	drag coefficient $(= F_D/(\frac{1}{2}\rho {U_\infty}^2 A))$
C_p	pressure coefficient $(= (p - p_\infty)/(\frac{1}{2}\rho U_\infty^2))$
C_{pmin}	minimum pressure coefficient
d	disk diameter
D	diameter of hologram
D_m	mass diffusivity
f	vortex shedding or passage frequency
F_D	drag force
g	gravitational acceleration constant
h	distance from stagnation to separation points on face of sharp edged plate
l	average vortex spacing
n	refractive index
$n(R)$	nuclei number density distribution function
$N(R)$	concentration of nuclei with radius smaller than R
N_g	number of nuclei counts in each radius group
N_{tot}	total particle concentration in the measured radius range
ΔN	nuclei concentration in the radius range ΔR
p_b	pressure at the bubble wall
p_B	base pressure
p_c	pressure at the core of a vortex
p_g	gas partial pressure in a bubble
p_{local}	pressure in the vicinity of air bubble pressure sensor
p_L	"Local" pressure above the shear layer
p_{mean}	mean static pressure
p_{min}	minimum pressure in the flow

p_o	bubble equilibrium external pressure
p_{ref}	freestream dynamic pressure
p_v	water vapor pressure
p'	instantaneous pressure fluctuation ($=p_{local} - p_{mean}$)
p_∞	reference pressure or freestream pressure
$(p - p_v)_{crit}$	bubble critical tension
r	velocity ratio ($= U_2/U_1$)
r_c	vortex core radius
R	bubble or particle radius
R_{crit}	bubble critical radius
R_{eq}	bubble equilibrium radius
R_o	initial bubble radius
R_x	bubble radius at downstream distance x
$\dot{R}, \ddot{R}$	first and second time derivatives of bubble radius
$\overline{R}$	nominal radius of each data group
ΔR	nuclei radius range about R
Re_L	"Local" Reynolds number ($= 2hU_L/\nu$)
S	surface tension
St	Strouhal number ($= 2hf/U_L$)
t	time
T	liquid temperature
T_b	characteristic bubble response time
U	velocity
U_c	convection velocity
U_L	"Local" velocity above the shear layer
U_T	bubble terminal velocity
$U_{x,y,z}$	velocity components
U_1	velocity of high speed stream in plane mixing layer
U_2	velocity of low speed stream in plane mixing layer
U_∞	undisturbed freestream velocity

U_θ	tangential velocity around vortex core
ΔU	velocity difference across shear layer
V_s	liquid sample volume
x	downstream distance from the sharp edge
x_o	shear layer virtual origin
y	distance normal to the sharp edge
z	spanwise distance
z	object to film plane distance
α	dissolved air content
α	velocity parameter $(=(U_1 - U_2)/(U_1 + U_2) = (1-r)/(1+r))$
β	Henry's Law constant
δ	shear layer thickness
γ	polytropic gas constant
Γ_p	circulation of primary (spanwise) vortex
Γ_s	circulation of secondary (streamwise) vortex
λ	laser wavelength
λ_s	vortex wavelength or spanwise spacing of longitudinal vortices
ν	kinematic viscosity of water
μ	absolute viscosity of water
ρ	density of water
σ	cavitation number $(= (p_\infty - p_v)/(\frac{1}{2}\rho U_\infty^2))$
σ_i	cavitation inception index
σ_L	"Local" cavitation number $(= (p_L - p_v)/(\frac{1}{2}\rho U_L^2))$
σ_o	steady-state cavitation index
τ	bubble dissolution time
ω_n	bubble natural frequency

LIST OF FIGURE CAPTIONS

Figure I.2.7. Photograph of the reconstruction monitor screen displaying the focused image of a transparent plastic ruler. Magnification is 16X on the monitor and the smallest visible division on the ruler is 1/32 inch. This reconstruction is from the off-axis hologram shown in Figure I.2.6.

Figure I.2.8. Schematic diagram of the in-line reconstruction of the hologram of a single point object.

Figure I.2.9. Reconstruction systems
(a) Line diagram of in-line reconstruction system
(b) Line diagram of off-axis reconstruction system

Figure I.2.10. Photograph of the reconstruction monitor screen displaying the focused image of a marine organism from one of the open ocean in-line holograms. Organism body length $\simeq$ 600 μm.

Figure I.3.1. Photograph of the holographic submersible tank on board the *R/V Seawatch* during transport.

Figure I.3.2. Map of the Los Angeles coastal area indicating the holographic test sites. Details of the location and test conditions for stations 3, 4 and 5 are given in Table I.3.1.

Figure I.3.3. Schematic of the reflection and refraction of light incident on an air bubble in water.

Figure I.3.4. Effect of group size N_g on the number density distribution function $n(R)$. Circles denote data points calculated with N_g=2, yielding an expected r.m.s. error in computation of $n(R)$ of 70%. Triangles indicate N_g=10, for a standard error of 32%.

Figure I.3.5. Comparison of two techniques for determination of the number density distribution function $n(R)$. Triangles indicate $n(R)$ determined using fixed size interval "bins," circles indicate grouping of adjacent counts with group size N_g=4.

Figure I.4.11. Reconstructed "particle" images from various stations and depths.
(a) Station 2, 3 m. Generic particle.
(b) Station 3, 30 m. *Chaetoceros* diatom.
(c) Station 4, 32 m. Copepod.
(d) Station 5, 6 m. Nauplius (immature stage) of copepod.
(e) Station 5, 12 m. Radiolarian. "Spines" up to 400 μm long.
(f) Station 5, 3 m. Dinoflagellate *Ceratium*.

Figure I.4.12. Number density distribution function $n(R)$ as a function of equivalent radius R for total particles observed at Stations 1 and 2. Bubble data from Figure I.4.2 are also included. Diamonds indicate objects with radii less than 10 μm for which no distinction as to type was attempted.

Figure I.4.13. Total particle number density distribution function $n(R)$ vs. equivalent radius R for Station 3. (a) through (f) show the six depths examined, as indicated on the legend of each plot. Circles give the particle data, open and closed indicating a change in volume examined. Bubble data from Figure I.4.4 are also included as solid squares in order to show their relative abundance. Triangles indicate objects with radii less than 10 μm for which no distinction as to type was attempted.

Figure I.4.14. Total particle number density distribution function $n(R)$ vs. equivalent radius R for Station 4. (a) and (b) show the two depths examined, as indicated on the legend of each plot. Circles give the particle data, open and closed indicating a change in volume examined. Bubble data from Figure I.4.6 are also included as solid squares in order to show their relative abundance. Triangles indicate objects with radii less than 10 μm for which no distinction as to type was attempted.

Figure I.4.15. Total concentration of objects with radii less than 10 μm and of particles in the 10 to 50 μm equivalent radius range at Stations 3 and 4 as a function of depth.

Figure II.4.1. Sketch indicating overall mean shape of the separated flow.

Figure II.4.2. 1/4 *sec* exposure photograph showing time-averaged growth rate of the turbulent shear layer. $U_L = 7.81\ m/s$, $Re_L = 1.52 \times 10^6$, $\sigma_L = 0.16$.

Figure II.4.3. Side view photographs showing change in cavitation behavior with decreasing cavitation index σ. A different lighting scheme was used for (b).

Figure II.4.4. Simultaneous top and side photographs of free shear layer cavitation inception. $U_L = 7.81\ m/s$, $\sigma_L = \sigma_i = 1.52$, $Re_L = 1.42 \times 10^6$, $\alpha = 9.9\ ppm$.

Figure II.4.5. Simultaneous top and side photographs of early stage of cavitation in the free shear layer. $U_L = 11.38\ m/s$, σ_L=0.65, $Re_L = 2.06 \times 10^6$, $\alpha = 9.9\ ppm$.

Figure II.4.6. Simultaneous top and side photographs of early stage of cavitation in the free shear layer. $U_L = 11.38\ m/s$, σ_L=0.65, $Re_L = 2.06 \times 10^6$, $\alpha = 9.9\ ppm$.

Figure II.4.7. Simultaneous top and side photographs of early stage of cavitation in the free shear layer. $U_L = 11.75\ m/s$, σ_L=0.62, $Re_L = 2.13 \times 10^6$, $\alpha = 4.2\ ppm$.

Figure II.4.8. Simultaneous top and side photographs of early stage of cavitation in the free shear layer. $U_L = 11.75\ m/s$, σ_L=0.62, and Re_L=2.13×10^6, $\alpha = 4.2\ ppm$.

Figure II.4.9. Simultaneous top and side photographs of well-developed cavitation in the free shear layer. $U_L = 10.14\ m/s$, σ_L=0.39, $Re_L = 1.84 \times 10^6$, $\alpha = 10.1\ ppm$.

Figure II.4.10. Simultaneous top and side photographs of well-developed cavitation in the free shear layer. $U_L = 10.14\ m/s$, σ_L=0.39, $Re_L = 1.84 \times 10^6$, $\alpha = 10.1\ ppm$.

Figure II.4.11. High speed movie sequence showing top view of inception, growth and collapse of an axial cavity. Sequence runs from right to left as numbered. Flow direction is right to left. The steady streamwise line covering full length of each frame is a scratch on the lucite viewing window. Elapsed time between frames is 2 ms, exposure time is approximately 200 μs. $U_L = 9.5\ m/s$, $\sigma_L = 0.88$, Re_L=1.84×10^6, α= 4.70 ppm.

Figure II.4.12. High speed movie sequence showing top view of fairly heavy cavitation in the shear layer. Sequence runs from right to left as numbered. Flow direction is right to left. The steady streamwise line covering full length of each frame is a scratch on the lucite viewing window. Elapsed time between frames is 4.2 ms, exposure time is approximately 170 μs. $U_L = 11.60\ m/s$, $\sigma_L = 0.63$, Re_L=2.26×10^6, α= 2.72 ppm.

Figure II.4.13. Shear layer growth rate. "Visual" thickness of layer measured from high-speed motion pictures at fixed downstream stations.

Figure II.4.14. Shear layer total pressure profiles.
(a) U_L= 3 m/s, Re_L=5.28×10^5
(b) U_L= 7 m/s, Re_L=1.23×10^6

Figure II.4.15. Trajectory of spanwise vortices in shear layer behind sharp edged plate. $U_L = 10.76\ m/s$, $\sigma_L = 0.37$, $Re_L = 1.95 \times 10^6$.

Figure II.4.16. Average convection velocity of spanwise vortices as a function of freestream velocity above the shear layer (from 8 motion picture sequences).

Figure II.4.17. Convection velocity frequency distribution. Spread of convection velocity values measured during tracking of a single spanwise core. Average $U_c = 0.33\ U_L$ for this case.

Figure II.4.18. Measured downstream distances to first pairing event for three freestream velocities.

Figure II.4.19. Strouhal number as a function of downstream distance. Dashed line indicates the measured results of Kermeen & Parkin (1957) for the wake of a sharp edged disk assuming $D = 2h$.

Figure II.4.20. Distribution of vortex passage frequencies measured at fixed downstream stations.
(a) x/h= 1.0, U_L=10.76 m/s, $\overline{St} = 2.57$.
(b) x/h= 2.0, U_L=10.76 m/s, $\overline{St} = 1.43$.

Figure II.4.21. Spacing l of spanwise vortices as a function of downstream distance. Error bars indicate $\pm$ one standard deviation from the mean.

Figure II.4.22. Distribution of spanwise vortex wavelengths measured at fixed downstream station x/h=2.0. Mean value $\bar{l} = 10.2$ cm.

Figure II.4.23. Average spanwise spacing of longitudinal vortices as a function of downstream distance.

Figure II.4.24. Determination of three-dimensional velocity components from double-pulsed holographic images. Center photograph is of hologram (including tip of sharp edged plate); upper shows reconstructed image demonstrating translation of 1.7 mm long streamwise vortex core, and lower shows translation of 100 μm diameter bubble. Separation period between laser pulses is 200 μs. U_L=7 m/s, $\sigma_L = 0.50$, α=3.3 ppm.

Figure II.4.25. Normalized pressure fluctuation distribution. Polytropic constant $\gamma = 4/3$.

Figure II.4.26. Normalized pressure fluctuation distribution. Polytropic constant $\gamma = 1.0$.

Figure II.4.27. Cavitation inception indices in the free shear layer. Note sharp dependence of inception index on dissolved air content.

Figure II.4.28. Comparison of the data of Figure II.4.27 with inception measurements on sharp edged disks by Kermeen & Parkin (1957) and Arndt (1978), and on blunt circular cylinders by Katz (1981).

Figure II.4.29. Bubble number density distribution function $n(R)$ in LTWT under steady and instantaneous conditions (from Katz & O'Hern 1983).

Figure II.4.30. Bubble number density distribution function $n(R)$ in LTWT in flow regions above and below the shear layer behind the sharp edged plate. Particulate concentration measured with HIAC optical counter also included.

LIST OF TABLE CAPTIONS

Table I.4.5. Measured concentrations of total particles in discrete equivalent radius intervals examined for Stations 1 and 2. Heavy lines indicate change in size of volume examined. Volumes examined in each size interval are given in Table I.4.1 (b).

Table I.4.6. Measured concentrations of total particles in discrete equivalent radius intervals examined for Station 3. Heavy lines indicate change in size of volume examined. Volumes examined in each size interval are given in Table I.4.2 (b).

Table I.4.7. Measured concentrations of total particles in discrete equivalent radius intervals examined for Station 4. Heavy lines indicate change in size of volume examined. Volumes examined in each size interval are given in Table I.4.3 (b).

Table I.4.8. Measured concentrations of total particles in discrete equivalent radius intervals examined for Station 5. Heavy lines indicate change in size of volume examined. Volumes examined in each size interval are given in Table I.4.4 (b).

Table II.4.1. Relative strength of streamwise and spanwise vortices in the shear layer. The streamwise vortex strength was determined using the Rankine vortex model and measurements from photographs recorded near inception.

Table II.4.2. Measured velocity components near one of the streamwise cores. The freestream speed is nominally 7 m/s. U_x is the measured velocity in the mean flow direction, U_y is normal (up) and U_z is in the spanwise direction. The cavitation index $\sigma_L = 0.5$.

PREFACE

Cavitation is the formation of vapor or gas filled cavities in a liquid by the explosive growth of small bubbles or nuclei that are brought to instability by a low instantaneous local pressure. Cavitation is differentiated from boiling by the usual neglect of thermal effects in cavitating flows (Plesset & Prosperetti 1977); that is, boiling is the temperature dominated cavity formation mechanism, while cavitation is pressure-controlled. The term hydrodynamic cavitation is sometimes used to stress the dominant role of dynamic pressure in the cavitation process, and to allow differentiation from such phenomena as acoustic cavitation, which is controlled by acoustic pressure pulses. Cavitation is likely to occur in those liquid flows in which the local velocity is high, or local pressure low, at some point in the flow. This is a common situation in many liquid flows of engineering interest, in particular, in turbulent flows where large instantaneous velocity and pressure fluctuations are often observed.

The field of cavitation encompasses a wide range of phenomena from inception, the first appearance of cavitation in an otherwise single phase flow, through supercavitation, in which a large cavity becomes attached to the test body or cavitating surface. Cavitation inception is generally a very transient event, requiring the coincidence of a suitably low pressure with an unstable cavitation nucleus. A newly formed cavity usually collapses when it is convected into a region of higher pressure. This random and transient nature of cavitation inception greatly complicates detection and measurement procedures.

From an engineering viewpoint, cavitation is generally undesirable because of the associated problems of noise and vibration caused by cavity collapse, and material damage by cavitation erosion. The practical applications behind the

study of cavitation are in control and prediction of the extent of these cavitation-related problems and their accompanying performance degradations. Efficiency losses include such commonly observed problems as the lowered thrust of ship propellers, lowered head supplied by pumps, and lowered lift and increased drag on hydrofoils. The extent of the two-phase flow created by cavitation is also an important consideration in the prediction of such factors as pressure coefficients on test bodies, as well as flow rates and heat transfer coefficients, a possible example of which is the speculated significance of cavitation of the main cooling water pumps in the 1986 Chernobyl nuclear reactor explosion, leading to the official U.S.S.R. decision to outfit all of its reactor pumps with "cavitation detectors" (Levi 1986; Plesset 1986).

Clearly, understanding and prediction of cavitation and its associated effects are vital in the design of fluid machinery in which efficiency, life expectancy, material requirements and cost are all key considerations. However, the study of cavitation is a complex one because it involves such diverse factors as fluid dynamics and water chemistry, and because of its transient nature. Cavitation has been an important topic of naval hydrodynamics research since the late 19th century, when the first high-speed propellers were introduced. During sea trials of the *H.M.S. Daring* in 1895, lowered propeller efficiencies at higher rotation speeds were observed and attributed to void formation on the suction side of the blades, a phenomenon termed "cavitation" by R.E. Froude (Wislicenus 1969; Trevena 1984). Early studies were primarily concerned with avoidance of cavitation and its harmful effects, particularly erosion, on propeller and turbine blades (see, for example, the work of Parsons reviewed in Burrill 1951). Since that time, the prediction of cavitation inception has remained an area of considerable research interest in fluids engineering and naval hydrodynamics. Understanding of the basic cavitation characteristics in simple flows is needed to allow prediction of cavitation in prototype situations, or in common engineering applications such as boiler feed pumps, hydraulic turbines and ship propellers. The complex

flows through or around most engineering fluid devices require the use of model tests to predict prototype behavior, since analytical and numerical techniques generally cannot be solved exactly for flows with complicated geometry or in turbulent flows. Model results are extended to full-scale conditions through the use of similarity parameters and scaling laws. Model testing is particularly important in those cases in which the physical scale of the device of interest may be very large (airplane wings, dam spillways, or ship propellers, for example) or the flow complicated, so that testing can be performed only on a dynamically similar small scale or simplified model of the prototype. For example, ship hull drag is often measured on small-scale models of the ship while being carefully towed in a controlled laboratory environment.

The presence of cavitation complicates most flows to the extent that their characteristics cannot be analytically predicted and model testing becomes necessary. The fundamental parameter in cavitation testing is the the cavitation index σ, defined as

$$\sigma = \frac{p_\infty - p_v(T_\infty)}{\frac{1}{2}\rho U_\infty^2}$$

where p_∞ is the reference pressure, $p_v(T_\infty)$ the vapor pressure evaluated at the reference temperature T_∞, ρ the liquid density and U_∞ the reference velocity. Measurement of these parameters just at the moment that cavitation begins allows formulation of the cavitation inception index σ_i, defined as

$$\sigma_i = \frac{p_{\infty_i} - p_v(T_\infty)}{\frac{1}{2}\rho U_{\infty_i}^2}$$

where the subscript i indicates evaluation at inception. The classical theory of cavitation similarity states that similar flows will have identical cavitation behavior if their cavitation indices are equal (Holl & Wislicenus 1961). This theory is based on several assumptions: that all pressure differences are proportional to the velocity squared so that only inertial forces are important (i.e., frictionless,

incompressible fluid without action of body forces); that the critical pressure for inception is exactly equal to the vapor pressure, with the vapor pressure assumed constant throughout the flow field; and that cavitation occurs instantaneously when the vapor pressure p_v is reached, so that there is zero response time and no tension effects. In addition, the surface tension S is generally assumed constant and is based on the liquid bulk temperature, neglecting local temperature changes as well as the effect of contaminants.

The assumptions contained in the classical theory of cavitation similarity clearly are not valid in many cases, so "it is actually surprising that the classical similarity relation based on these assumptions has served so well" (Holl & Wislicenus 1961). Scale effects are defined as deviations from classical inception index scaling, that is, cavitation behavior dependence upon additional parameters besides the cavitation index. If σ were the only significant parameter, the prediction of prototype cavitation characteristics from model results would be a straightforward matter. However, scale effects have been observed in many experimental investigations. For example, Kermeen & Parkin (1957) reported a strong Reynolds number dependence of the inception index in the free shear flow behind a sharp edged disk. Further early experimental observations demonstrating the dependence of the inception index on such parameters as Reynolds number, body size, and velocity for streamlined bodies, hydrofoils, and zero-caliber ogives are reported in Holl & Wislicenus (1961). The most notable example of scale effects is the round-robin test conducted by the International Towing Tank Committee (ITTC) on a standard axisymmetric hemispherical headform, as reported by Johnsson (1969) and discussed by Acosta & Parkin (1974). The results of these tests showed inception indices ranging from 0.4 to 1.1 for the same test body in nominally the same flow at 14 different test facilities. The physical appearance of cavitation was observed to vary significantly as well, depending on such factors as the nuclei availability in the test facility, and on the boundary layer characteristics that controlled whether a travelling bubble

or band type cavitation occurred in the flow around the headform (indicative of boundary layer turbulent transition and laminar separation, respectively). These investigations demonstrate that the cavitation inception index for a similar flow can vary widely between test facilities, or even between different tests in a single facility. In such cases, laboratory results cannot be relied upon to provide a reasonable estimate of full-scale behavior, and the scaling laws required to relate model results to prototype conditions cannot be defined. In a few cases, such as flows around axisymmetric hemispherical headforms (Arakeri & Acosta 1973; Huang 1981; Katz 1984), significant progress has been made toward understanding the cavitation scaling laws. However, these results cannot be readily applied to new flow conditions, so some *a priori* knowledge of the flow type becomes necessary in order to predict its cavitation behavior. The study of scale effects has become a major topic of cavitation research, and discussions are included in Holl & Wislicenus (1961); Huang & Peterson (1976); and Arndt (1981), to name just a few.

Scale effects can be divided into two major categories, the susceptibility effects and the flow field effects. While both effects are important in most cases, it is useful to draw some distinction between the two in order to facilitate their study.

The first category of cavitation scale effects involves the susceptibility of water to cavitation, that is, the size, type and concentration of cavitation nuclei. The tap water commonly used as the working fluid in experimental facilities is neither pure nor homogeneous, but may contain dissolved gases, microbubbles, particulate matter and biological organisms. At least some of these objects act as cavitation nuclei, or preferential sites for cavitation inception. The presence of nuclei is supported by the results of investigations into the tensile strength of water, defined here as the critical tension that must be applied in order to create a void in the water. According to the "kinetic theory of liquids" (Frenkel 1946; Plesset 1969), pure homogeneous water should be able to withstand tensions on

the order of several thousand atmospheres before macroscopic voids are created. However, careful laboratory tests using Bertholet tubes, bellows, and centrifugal devices demonstrate maximum tensile strengths of less than 300 atmospheres, and commonly find tensile strengths on the order of 1 atmosphere, as reported in Knapp et al. (1970) and Trevena (1984). In engineering applications, cavitation is observed to occur under either very small applied tensions or under slight positive pressures. Various types of nuclei have been proposed and studied, including "clean" gas bubbles, gas bubbles stabilized by semi-permeable organic skins (Fox & Herzfeld 1954; Johnson & Cooke 1981) and particles with attached gas pockets in the "Harvey model" (Harvey et al. 1947).

Flow field effects include those caused by deviations from the ideal flow assumed in development of the classical cavitation scaling law because of such mechanisms as viscous effects, that is, the details of the velocity and pressure distributions, as well as such factors as body shape and size, and turbulent phenomena. Arakeri & Acosta (1973, 1979) demonstrated the important role of boundary layer separation, transition, and reattachment on cavitation inception in the flow around various axisymmetric bodies, and were able to classify the bodies according to their viscous flow and inception scaling trends. Huang & Peterson (1976) studied the effect of boundary layer development and characteristics on cavitation scaling, and concluded that pressure fluctuations in the boundary layer transition and separation regions controlled inception. Billet & Holl (1979) studied the effect of changing size and velocity for a variety of hydrofoil sections, and found significant dependence of the inception index on these additional parameters.

The two aspects of scale effects have no doubt played important roles in the experiments leading to much of the available cavitation inception data, so that the data for nominally similar experiments actually represent very different "hydrodynamic and nucleation environments" (Acosta & Parkin 1975). Both aspects of cavitation scale effects, the susceptibility of the water and the fluid

mechanical effects, will be examined in this thesis. Part I describes studies of the cavitation nuclei population distributions in ocean waters and Part II describes an investigation into cavitation inception in a turbulent shear flow.

PART I
NUCLEI DISTRIBUTIONS IN NATURAL WATERS

CHAPTER I.1
INTRODUCTION

I.1.1 Cavitation Nuclei

Calculations of the tension required to rupture an instantaneously occurring molecular level void in otherwise pure water yield expected critical tensions in the range of 1200 to 10000 *atm* (Frenkel 1946; Plesset 1969; Knapp et al. 1970). However, numerous experimental investigations of the critical tension of "pure" water have found maximum required tensions of less than 300 atmospheres (Knapp et al. 1970; Trevena 1984). The maximum tensile stress of liquids is considerably reduced by the presence of impurities, generically called nuclei, which act as preferential sites for the occurrence of liquid rupture. Waters typically found in laboratory facilities or engineering applications are neither pure nor homogeneous, but contain relatively high concentrations of cavitation nuclei, and the critical tensile strength of these waters is typically at least an order of magnitude less than those calculated or measured for pure water (Holl 1970).

It is now fairly well established that bubbles, some kinds of solid particles and gas pockets inside crevices and cracks on the surface of particulates suspended in the liquid can act as cavitation nuclei. When these nuclei are exposed to a low enough pressure, an unstable cavity will form on or grow from them, which may then grow explosively to become a visible cavitation event. The effect of these freestream nuclei generally dominates that of the nuclei located at the liquid boundaries, as has been demonstrated by Godefroy et al. (1981) and Billet (1985). The present examination is concerned only with freestream nuclei as opposed to wall or test body nucleation sites.

The liquid characteristics that affect the occurrence of cavitation through

their influence on the nuclei population are collectively termed liquid quality. For the purpose of cavitation research, the concentration of nuclei in the liquid and their dynamic behavior when exposed to a change of pressure are required for predictions of cavitation inception and to deduce scaling laws capable of correlating the results from model tests to full-scale operation. Not all nuclei respond in the same way to a change of the surrounding pressure. The dynamic properties of gas bubbles in mechanical equilibrium can be directly related to their size, so the liquid quality can be adequately described by the nuclei number concentration distribution as a function of bubble size. The nuclei number concentration distribution is also generally used to characterize the liquid quality even when the main nuclei source is particles, whose dynamic behavior cannot be directly related to their geometry. In this case the size measurements of particulates contained in liquids still provide an upper limit for the concentration of potentially active cavitation nuclei.

Theoretical investigations of nuclei characteristics, and establishment of their nature in the laboratory environment have been topics of considerable research effort. Plesset (1949) used the Rayleigh equation of cavity dynamics to model quite accurately the experimental observations of Knapp & Hollander (1948) of the bubble motion in the flow past a 2 inch diameter 0.5 caliber ogive. Billet & Gates (1979) measured the nuclei distributions in two Caltech water tunnels and related them to inception observations, Gowing & Ling (1980) measured distributions in the 12 inch water tunnel at the David W. Taylor Naval Ship Research and Development Center (DTNSRDC), and both Katz (1981) and Ooi (1981) made extensive nuclei measurements in relation to their inception studies. These are just a few of the numerous examinations of nuclei effects in test facilities, some of which will be discussed in Chapter II.5. For the marine waters of interest in naval hydrodynamics, however, the nature and typical concentration of nuclei have yet to be determined because of the inherent experimental difficulties involved in making these measurements. Detailed

knowledge of the sea water liquid quality is essential for the simulation of marine conditions in the laboratory and for the scaling of model test results to ocean prototype operation. For example, the concept of flow seeding to simulate marine conditions in laboratory facilities requires detailed data on marine nuclei populations under various conditions in order to establish useful nuclei standards. The various types of objects potentially acting as nuclei in the ocean are of interdisciplinary interest in such fields as marine biology, meteorology, oceanography and ocean acoustics, leading previous researchers to separately explore bubbles (see for example Medwin 1970, 1977; Johnson & Cooke 1979); particles (Peterson 1974; Carder et al. 1982) and organisms (Stewart et al. 1973; Pieper & Holliday 1984). Recently, quantitative results of studies of marine nuclei from a cavitation viewpoint have started to become available. For example, Shen et al. (1986) have determined the critical tensile strength of ocean water to vary from 0.3 to 1.7 *atm* in the test sites examined in their study.

At least three distinct types of objects may act as cavitation nuclei in the sea; these are gas bubbles, solid particles and microorganisms. A brief discussion of these three potential types of nuclei is included here.

I.1.1.1 Bubbles as Nuclei

Gas bubbles are the "standard" cavitation nuclei, and it has been demonstrated numerous times that an increase of bubble concentration in a test facility leads to an increased inception index; that is, the water will be more susceptible to cavitation. Most theoretical approaches to predicting inception assume bubbles as the active nuclei, and generally also assume that single bubble dynamics control the response of the flow to a change in cavitation index, neglecting bubble interaction effects.

A brief review of some of the key findings of bubble dynamics (from Strasberg 1957; Knapp et al. 1970) will used to examine the criteria for bubble instability. Consider an isolated small spherical bubble of radius R surrounded by an

infinite fluid, subject to the time-dependent fluid pressure $p_\infty(t)$. The bubble may contain vapor at pressure $p_v(T)$, where T is the bubble wall temperature, and may also contain non-condensable gas at partial pressure p_g. The governing equation for such a case is the Rayleigh-Plesset equation:

$$R\ddot{R} + \frac{3}{2}\dot{R}^2 = \frac{1}{\rho}\left[p_v + p_g - p_\infty(t) - \frac{2S}{R} - \frac{4\mu\dot{R}}{R}\right] \tag{I.1.1}$$

where S is the surface tension, ρ the liquid density, μ the liquid viscosity and $\dot{R}$ and $\ddot{R}$ the first and second time derivatives of R, respectively. At equilibrium the bubble radius is fixed at $R = R_{eq}$ and Equation I.1.1 reduces to:

$$0 = p_v + p_g - p_\infty(t) - \frac{2S}{R_{eq}} \tag{I.1.2}$$

or, for perfect gas behavior of the gas component of the bubble

$$0 = p_v + \frac{KT}{{R_{eq}}^3} - p_\infty(t) - \frac{2S}{R_{eq}} \tag{I.1.3}$$

where K is a constant. The stability of this equilibrium can be analyzed by applying $R = R_{eq}[1 + \epsilon(t)]$ in Equation I.1.1 and linearizing for small $\epsilon(t)$. This leads to an expression for the bubble natural frequency as:

$${\omega_n}^2 = \frac{3}{\rho {R_{eq}}^2}\left[\gamma(p_\infty - p_v) + \frac{4S}{3R_{eq}}\right] \tag{I.1.4}$$

where γ is the ratio of specific heats for the gas and an adiabatic bubble pressure-volume relation has been assumed (Plesset & Prosperetti 1977).

When viscosity effects are neglegible, the stability analysis also leads to the critical pressure for bubble instability, given by:

$$(p - p_v)_{crit} = -\frac{4S}{3R_{crit}} \tag{I.1.5}$$

In general, the equilibrium radius R_{eq} is not equal to the critical radius R_{crit}. The conditions for stability of the bubble static equilibrium require that:

$$R_{crit} = \sqrt{3KT/2S} \tag{I.1.6}$$

for constant K and T. Thus, R_{crit} can be expressed in terms of R_{eq} by solving Equation I.1.3 for KT in terms of R_{eq} and using this in Equation I.1.6. Application of this result to Equation I.1.5 yields:

$$(p - p_v)_{crit} = -\frac{4S}{3R_{eq}} \left[3 \left(1 + \frac{p_\infty - p_v}{2S/R_{eq}} \right) \right]^{-1/2} \tag{I.1.7}$$

For fixed T (i.e., fixed S and p_v) a bubble will become unstable whenever the surrounding liquid pressure is low enough to satisfy Equation I.1.7, and lower pressures will lead to rapid bubble growth. Equation I.1.7 can be used to define the range of bubble radii of interest as cavitation nuclei by determining the pressure required to cause bubble instability. Examples of bubble critical pressure and natural frequency values are given in Table I.1.1 for several bubble equilibrium radius values within the size range of interest for typical microbubble nuclei. Assuming single bubble nuclei, Equation I.1.7 also can be used to estimate the tensile strength of water, if the critical tension is taken to be equal to the critical pressure of the most unstable bubble nucleus.

An important area of concern in the field of bubble nuclei is the mechanism of persistence or stabilization of equilibrium bubbles. Vapor bubbles are expected to dissolve when the liquid pressure is greater than the vapor pressure, and are in a state of unstable equilibrium when the liquid pressure is less than vapor pressure. One would expect a small gas bubble to dissolve because of its surface tension, even in a saturated solution (Epstein & Plesset 1950), while a large gas bubble would rise by its buoyancy at a reasonable velocity, to leave the liquid at the surface or collect at a boundary. Holl (1970) uses the results

of Epstein & Plesset (1950) to derive a characteristic time for complete solution of a bubble of initial radius R_o

$$\tau = \frac{{R_o}^2 \beta}{3 D_m B_s T} \left[\frac{R_o (p_b - p_v)}{2S} + 1 \right] \tag{I.1.8}$$

where β is the Henry's law constant, D_m the mass diffusivity, T the absolute temperature, B_s the specific gas constant, p_b the liquid pressure at the bubble wall, p_v the vapor pressure, and S the surface tension. For example, Equation I.1.8 leads to a dissolution time of 6.63 *sec* for an air bubble of 10 μm radius in a saturated water solution. Liebermann (1957) experimentally verified that "small" air bubbles in water (either 50% or 100% saturated) will completely dissolve in a matter of minutes. Additional examples of the time required for complete disappearance of air bubbles in a saturated water solution are included in Table I.1.1.

Bubble terminal rise velocities can be easily calculated for the Stokes flow regime (applicable for bubble radii less than 200 μm, Liebermann 1957) as:

$$V_t = \frac{2}{9} \frac{g R^2}{\nu} \tag{I.1.9}$$

The terminal rise velocity of several air bubbles in the radius range of interest are included in Table I.1.1., indicating that fairly large bubbles rise at moderate terminal velocities.

Bubble persistence mechanisms may not be too significant in most engineering applications and large experimental test facilities, since new bubbles are constantly generated. However, the question of bubble persistence becomes quite important in the study of marine bubble nuclei, since processes for continuous generation have not been proven, although they may in fact be quite important (Medwin 1977; Mulhearn 1981). Expected mechanisms for bubbles to enter the ocean include the action of waves and surface spray, rain droplets carrying air down below the surface, cosmic radiation, dust (Turner 1961), and possibly the

action of microorganisms and decay of organic matter. Garretson (1973) concludes that surface bubble generation sources must be supplemented by volume and bottom sources in order to explain measured bubble concentrations at sea.

Bubble nuclei have been shown to have unexpected long lifetimes by numerous experimental measurements in both test facilities and in the ocean (Mulhearn 1981), and several mechanisms have been proposed to explain this persistence. For example, Cha (1981) employed a thermodynamic theory for dilute solutions to show that a bubble composed of gas and vapor can remain in stable equilibrium in a liquid.

Fox & Herzfeld (1954) proposed a mechanism in which bubble stability is provided by an immiscible organic skin or membrane on the bubble surface that acts as a barrier to gas diffusion, maintaining a constant gas mass inside the bubble until a pressure low enough to burst the membrane is achieved in the cavitation inception process. The skin also enables the bubble to support a tangential force as if it were a rigid spherical shell. The organic matter forming the skin may be produced through such mechanisms as decaying plant matter in the sea. Yount et al. (1984) proposed a similar mechanism, and provided some experimental evidence to support it, in their work on skins of varying permeability formed by surface-active molecules on sub-micron bubbles. In this model, the bubble is essentially gas-permeable, and becomes impermeable only under the action of a large compression on the order of 8 $atm.$ Microscopic observations of distilled water and liquid gelatins by Yount et al. showed that small bubble nuclei existed in Brownian motion, and remained visible for several minutes, at least two orders of magnitude longer than would be expected for a pure gas bubble.

Mulhearn (1981) reviews ocean bubble measurements and finds some experimental evidence supporting the concept of a diffusion barrier, based primarily on the results of Medwin (1977). Mulhearn agrees with Medwin that large bubbles (radii above about 60 μm) may be continuously generated by decaying

organic matter at the sea floor, but that smaller bubbles are formed at the surface and, once formed, persist indefinitely by means of surfactant coatings and attachment to particles. Johnson & Cooke (1981) also performed experiments that seem to verify the stabilization of bubbles in seawater, possibly through the action of an organic skin. Their experiments involved injection of bubbles into natural seawater, then monitoring the bubble sizes through use of a photomicroscope. They found that some of the bubbles quickly dissolved while others stabilized with diameters of from less than 1 μm up to 13.5 μm. Observations of a group of such stabilized bubbles at atmospheric pressure over a 22 hour period indicated little reduction in the total number, and only a small decrease in the bubble diameters. The capability of several seawater samples collected at different times of the year to sustain stable microbubbles varied significantly, possibly indicating a relation between stable microbubble formation and the seasonal occurrence of natural organic particles. However, they also report that application of a slight overpressure (0.13 atm) was sufficient to cause the collapse of all stabilized microbubbles, casting some doubt as to their persistence outside the laboratory.

The concept of skin-stabilized bubbles has not been proven, and several investigators have raised concerns about its usefulness. Experimental examinations by Liebermann (1957) showed that the diffusion rate of air out of bubbles remained essentially unchanged whether they were suspended in pure water, sea water, or aqueous environments contaminated with various acids, oils and detergents. In addition, the organic skin theory cannot explain the stable existence of nuclei in organic liquids, such as benzene (Messino et al. 1967), or in the presence of chemical reagents that strongly affect organic materials. Plesset (1969) notes that the addition of such chemicals in moderate amounts does not affect the tensile strength of liquids.

Turner (1961) used ultrasonic attenuation to experimentally verify the existence of stable microbubbles up to 30 μm radius in test water samples, and

proposed a slightly different stabilization mechanism in which the bubble "intercepts" numerous small particles that cling to its surface until a continuous surface of particles is formed, in the "compressed wall stabilization hypothesis."

I.1.1.2 Solid Particles

A large number of solid particles are always present in test facilities, even with filtering (see Peterson 1972; Katz 1981; or Part II of this thesis) and are also present in widely varying but generally large amounts in sea water. The action of solid particles as stable cavitation nuclei is therefore a very important consideration, one that has been examined by several investigators.

Harvey et al. (1947) first proposed a stabilization mechanism in which undissolved gas is trapped in the crevices of a hydrophobic (non-wetted) particle, a situation now commonly referred to as the "Harvey model." The gas pressure in the crevice is lower than the surrounding water pressure because of surface tension at the gas-liquid interface, so the gas is stabilized in the crevice and will not dissolve into the liquid. The concave interface toward the gas is established by the hydrophobic nature of the particle, and results in surface tension acting to oppose the liquid pressure. The amount of trapped gas depends on crevice geometry, dissolved gas content and local pressure. The gas pocket will remain in permanent stable equilibrium in the crevice so long as the external liquid pressure remains high enough, but will expand to "seed" the flow when the liquid pressure drops below the gas internal pressure. The Harvey model can be used to explain observations of increased tensile strength with increases in previously applied pressure, since this high pressure would tend to force the gas deeper into crevices and further stabilize it there.

No direct observations of the Harvey mechanism have been made, but several investigations have provided indirect support. Liebermann (1957) has shown experimentally that air bubbles less than 1 μm "lodged on hydrophobic particles are not soluble and can exist indefinitely." In this investigation, bubbles were

allowed to dissolve in water containing chalk dust. After bubble disappearance, an insoluble residue remained. When the pressure was lowered to 1/4 *atm* a visible bubble grew out of the residual nucleus. Turner (1961) showed that leaving a test container open to atmospheric dust particle deposition led to an increase in nuclei as detected by ultrasonic attenuation, although he speculated that these were actually microbubble nuclei rather than Harvey-type particles. Messino et al. (1967) provide additional experimental support of the Harvey model in examinations of the nuclei content of water doped with various impurities, including hydrophobic Teflon particles, finding that the addition of non-wettable particles to a pure water sample increases the number of ultrasonically detected nuclei. Seawater experiments performed by Riley (1963) and Sutcliffe et al. (1963) summarized in Peterson (1972) indicate that aeration of filtered seawater leads to the formation of small insoluble particulates, which eventually coalesce to form fairly large aggregate particles.

There is some question as to the means of persistence of the suspension of solid particle nuclei in the Harvey model, as discussed in Peterson (1972). Maintenance of the particles in suspension in quiescent waters would require a very small particle size to allow suspension by Brownian motion, or for larger particles either a very high gas concentration or very low particle density to provide suspension by neutral buoyancy. Most waters of interest, including those of the oceans, are not quiescent, so the particles could well maintain their state of suspension through continuous regeneration or by the action of turbulent diffusion.

The "compressed wall stabilization hypothesis" proposed by Turner (1961) and discussed above also requires the presence of numerous small particles to form the continuous particle surface on the stabilized bubble. Whether solid particles act as Harvey nuclei, as a means for formation of a particle coating on bubbles, or as a site for attachment of skin-stabilized microbubbles (Mulhearn 1981), some measure of their spectra and typical concentrations will be required

in order to estimate the potential number of such nuclei in ocean waters.

I.1.1.3 Microorganisms

Ocean waters contain an additional potential source of nuclei besides bubbles and solid particles; these are the numerous microorganisms always present in the sea. The two major categories of marine microorganisms are the phytoplankton, usually unicellular algae, that form the base of the marine food chain and cover the size range from submicron up to several hundred microns; and the zooplankton, generally larger and less abundant marine animals that typically feed on the phytoplankton. Total phytoplankton concentrations can reach up to the order of 100 or more per cm^3, while the larger zooplankton typically are found in concentrations of 10 or fewer per cm^3 (Stewart et al. 1973). Some marine organisms are known to contain gas inclusions, such as the gas-filled pneumataphore of the physonectid siphonophores (e.g., *Nanomia bijuga*), and the gas-filled swim bladder of fishes (Holliday & Pieper 1980). Many species of blue-green algae occupying the upper 5 m of the ocean contain tiny gas vacuoles in their cells which act to control their buoyancy (Walsby 1977). Along with the fact that gas inclusions or metabolic gases may cause organisms to act directly as nuclei under appropriate applied pressures (never directly observed), marine organisms may also be important in terms of their bubble production capabilities. Mulhearn (1981) and Alldredge (1986, private communication) have pointed out the possibility of O_2 bubble production during the phytoplankton photosynthetic process.

I.1.2 Techniques for Measurement of Nuclei

The field of particle size measurement is currently a very dynamic one, driven to a large extent by advances in powder technology, and a significant number of commercial particle measuring devices are now available (Bunville

1984). However, many of these devices are not suitable for the measurement of cavitation nuclei, which are often transient, present in high speed liquid flows, and are best studied *in situ*. In addition, cavitation nuclei are usually larger than the atmospheric aerosols for which most commercial devices have been optimized. Significant efforts have been made to develop suitable methods of nuclei detection in liquids, based on various physical principles.

A brief discussion of several of the more common existing measurement devices and their usage will be given here. Additional reviews of nuclei measuring techniques can be found in such references as Morgan (1972), who listed the criteria for an ideal nuclei detector, Shen & Peterson (1983) and Billet (1985). A few of the key requirements listed by Morgan are that the instrument first have the capability to examine both the particle size range (roughly 10 to 250 μm diameter) and typical velocities (up to 25 m/s) commonly seen in cavitating flows; that it measure size and concentration with sufficient accuracy, and preferably distinguish the nucleus type; that it not disturb the sample volume; and that it operate continuously with essentially real time results. Preliminary results of venturi measurements of active cavitation nuclei (presented below), reported by LeGoff & Lecoffre (1983) and Billet (1985), indicate that the lower limit of bubble nuclei diameter should possibly be extended down to 2 μm. An additional requirement that the instrument be field operable may also be useful. *In situ* investigation of nuclei distributions is desirable since the sampling process introduces several potential error sources, in particular changes in the bubble size distribution if the sea water is subjected to a change in pressure.

The detection and measurement of cavitation nuclei constitute a persistent outstanding problem in the study of cavitation inception and scale effects. This was discussed by Kuiper (1985), who pointed out that evaluation of nuclei detection instrumentation was a primary recommendation of both the 12th and 17th International Towing Tank Conferences (1966 and 1984, respectively). Figure I.1.1 shows nuclei distribution measurements made by several investigators

at different sites and test conditions, using a variety of detection techniques. Results are plotted in terms of the nuclei number density distribution function $n(R)$. The number density distribution function is a standard measure that indicates the concentration of nuclei in a particular radius range divided by the span of that range. This parameter will be more fully examined in Chapter I.1.3. Amplitude variations between the distribution curves are as high as two orders of magnitude, although the slopes are roughly equal, indicating a fairly consistent distribution following a general formula like $n(R) \simeq R^{-n}$, where the exponent n ranges from about 3 to 4. Note that the nuclei of interest range over several decades in both radius and number density distribution function.

Examples of the use of several of these techniques in cavitation studies, in particular for the measurement of nuclei in the ocean, will be given following introductory descriptions of some of the more commonly used devices.

A simple and fairly standard indication of bubble nuclei availability is the total gas content of the liquid, often measured with a van Slyke blood gas analyzer (van Slyke & Neill 1924). A clear correlation between total gas content and bubble concentration has been demonstrated by several investigators (see for example Peterson 1972; Katz 1981; Shen et al. 1986; and Part II of this thesis); however, the total gas content is insufficient for determination of tensile strength since the bubble radii must be known, as per Equation I.1.7. In addition, the van Slyke device operates only on discrete samples taken from the test waters.

One of the standard particle counting devices is the Coulter Counter, which has been extensively applied both to cavitation nuclei investigations (Oba et al. 1981) and to ocean particle and organism measurements (e.g., Carder et al. 1971; Sheldon et al. 1972; Peterson 1974). The Coulter Counter measures the change in resistance of a test fluid due to the presence of a non-conducting particle or bubble. This technique has the advantages of high number counting accuracy, the ability to sample fairly concentrated solutions, applicability

in cases in which optical access is unavailable or optical examination impossible (such as in liquid metals), and has had extensive use in the field. However, there is some question as to its particle sizing accuracy, due primarily to difficulties in calibration (see Appendix II); in general, it cannot distinguish bubbles from particles (see, however, Oba et al. 1981 for a possible solution to this), and it inevitably interferes with the flow by requiring the examination of discrete samples. The pressure in the throat of the Coulter Counter orifice will, in general, differ from that seen by bubbles in the original sample location, and their measured sizes would be expected to change accordingly.

The light scattering technique has been applied in various configurations since the pioneering work of Keller (1972), and is probably the most common means of nuclei detection today. Light scattering devices typically illuminate a sample volume with a high intensity laser or incoherent light beam and record the intensity of light scattered by nuclei in the volume at one or more fixed recording angles over a time period long enough to allow a statistically significant number of scatterers to be detected. The light scattered by individual particles or bubbles is usually collected by a lens and transferred to a photodetector tube. The scattered light intensity is a function of the nucleus size, shape, and index of refraction, as well as of the optical characteristics of the illuminating beam. Small nuclei are very efficient scatterers of incident light, with Rayleigh scattering dominant for particle diameters less than about 0.1 μm (small relative to the incident wavelength), and Mie scattering theory used for larger particles (such as typical cavitation nuclei). The desire to examine single particle scattering restricts the size of sample volume and increases the recording time accordingly. System calibration is required, and is usually done by measuring the scattering from a latex sphere or an electrolytically produced bubble whose size is calculated from its measured terminal rise velocity. The quality of the results of this technique are strongly dependent on the calibration, as well as on the uniformity of the illuminating beam. Billet (1984) has performed an analysis

showing that a matrix inversion technique may be needed to correct light scattering measurements for illumination beam non-uniformity. The light scattering technique has the advantages of continuous operation, immediate results, and (indirect) determination of particle type.

Acoustic detection of bubbles relies on the fact that the acoustic scattering cross section of a bubble is many times the actual bubble dimension, so that bubbles very effectively scatter acoustic waves near their natural resonant frequency (Medwin 1977). Acoustic techniques can measure either the acoustic energy scattered by bubbles in a sample or the attenuation of an acoustic beam due to scattering and absorption by the bubbles. Calculation of bubble size from acoustic signals requires that the bubble natural frequencies be known, meaning that the physical characteristics of each bubble must be known or assumed. The bubbles are usually assumed to contain pure air, but ocean waters are likely to contain bubbles of oxygen, carbon dioxide, carbon monoxide, hydrogen sulfide and methane, although the ratio of specific heats for each of these gases are quite close to that of air and would lead to only minor corrections in the natural frequency calculation of Equation I.1.4 (Medwin 1970). The calculation also requires that an organic skin, if present, has no effect on the bubble natural frequency. A bubble size distribution is developed by using a range of excitation frequencies in order to detect the resonant response of bubbles of different size. The acoustic techniques have the advantages of allowing close to real time data analysis, and capability of *in situ* operation, with extensive use in the ocean already (Medwin 1970, 1977). Disadvantages (besides the above mentioned uncertainty in computing bubble natural frequency) include the fact that the acoustic techniques measure only attenuation or scattering due to resonant bubbles and thus are not suited to measurement of solid particulate nuclei (although they have been applied to zooplankton studies, Pieper & Holliday 1984) and restrictions to fairly dilute concentrations as indicated by the results of Schiebe & Killen reported in Oldenziel (1979), which show that acoustic tone

burst attenuation is valid only in the 0.3 to 1.0 *ppm* bubble concentration range. In addition, practical limitations restrict the smallest detectable bubble radius to about 15 μm, due to structural and reflected noise interference (Medwin 1970, 1977; Shen & Peterson 1983).

Photographic investigations are attractive since the photographic process is well established and high resolution is possible. Photography of small cavitation nuclei places special restrictions on the process, requiring very short exposure times to avoid blurring of moving nuclei and high resolution to detect nuclei in the size range of interest. Diffraction limited resolution is given by

$$\delta = \frac{1.22\lambda l}{D}$$

where λ is illumination wavelength, l is the object to film distance, and D is the limiting aperture of the system. The achievable resolution δ of photographic systems is generally sufficient for the relatively large nuclei of interest for cavitation inception; however, the depth of focus Δf is given by

$$\Delta f = \frac{2\delta^2}{\lambda}$$

so high resolution (small δ) leads to short depth of field, making it difficult to define the boundaries of the sampled volume, that is, to determine whether an observed particle lies inside or outside the sample volume.

The holographic technique will be described in detail in the next chapter, so only a brief description will be included here. Holography provides a three-dimensional image of the original sample volume, which can be analyzed in detail for its nuclei content. The three-dimensional aspect allows simultaneous matching of the requirements for high resolution and good depth of field, unlike the photographic process. Holography has been applied to various aerosol particle studies, such as Thompson & Ward (1966), and combustion studies such as Trolinger (1975) and Trolinger & Heap (1979). Holography instantaneously records information from a fairly large volume for later reconstruction

and analysis under high magnification, and allows visual classification of nuclei as bubbles, solid particles or microorganisms. The holographic technique has been specifically applied to the study of cavitation nuclei by Feldberg & Shlemenson (1973); Peterson (1972); Gates (1977) and Katz (1981), to name but a few. Some of the advantages of holography are formation of a permanent record, the capability of direct visual sizing and determination of object type, and the instantaneous recording of all objects in a large sample volume. In addition, the holographic technique does not require calibration (after initial system set-up). However, holographic reconstruction and detailed data acquisition are very time-consuming, requiring on the order of several "man-days" for examination of the several hundred particle images needed for statistical significance in a simple holographic analysis.

A relatively new device in determination of liquid quality is the venturi cavitation susceptibility meter, in which a liquid sample is forced through a venturi tube with a known throat pressure, and the number of cavitation events detected either optically (Oldenziel 1979, 1982; d'Agostino & Acosta 1983) or acoustically (Lecoffre & Bonnin 1979; Shen et al. 1986). This device is different from the others discussed above in that it determines the susceptibility of the water to cavitate at a known pressure, and thus measures the concentration only of unstable or "active" nuclei at that pressure. The major usefulness of the venturi meter is this capability to provide a concentration of active rather than potential nuclei. For example, early work reported by Lecoffre & Bonnin (1979) indicated that often less than one particle per million acts as an active nucleation site. Also, according to LeGoff & Lecoffre (1983) and Billet (1985), active nuclei measured in the venturi have equivalent bubble diameters of as low as 2 μm. If this is the case, the venturi device, with no lower measurable size limit, has an inherent advantage over other techniques that may be unable to detect the smallest nuclei. Additional advantages of the venturi device are near real time data analysis and proven applicability in the field (Shen et al. 1986). However,

a restriction must be made on the nuclei concentration to about 10 per cm^3 in order to avoid coincidence of events at the throat; the machining of the venturi throat is critical to achieve a known, clean flow; and extremely accurate throat pressure measurements must be made.

A number of comparisons between several of the nuclei measuring devices listed above have been made over the past 20 years. In general, the results of these comparative studies show moderate qualitative agreement between the various devices, but considerable quantitative differences are often observed. The statistical significance of most of these comparisons is limited by the high sampling error due to a sparse number of data counts. Peterson et al. (1975) compared light scattering and holographic techniques and found very good agreement between the two devices. Billet & Gates (1979) compared a laser light scattering device with a holographic device in two Caltech water tunnels. The light scattering results consistently indicated fewer nuclei, leading to further work on the interpretation of light scattering data with respect to sample size, calibration and illumination beam uniformity (Billet 1984). Godefroy et al. (1981) compared laser light scattering, holography, an ultrasonic Doppler scatterometer and two venturi systems in tests performed in a test rig at the Delft Hydraulics Laboratory. They claim good agreement between the holographic and light scattering bubble concentration determinations, although their data indicate fairly large discrepancies. The ultrasonic scattering device showed up to a factor of two fewer bubbles than holography. The two venturi devices showed good agreement, and the bubble concentrations inferred from these data were in general a factor of 2 to 3 higher than those determined holographically. Katz et al. (1983) made simultaneous measurements of the bubble concentration of the Caltech Low Turbulence Water Tunnel (see Chapter II. 2) with a ruby laser holographic system and an incoherent light scattering device developed by Gowing & Ling (1980) at DTNSRDC. The comparison was limited to bubbles with radii above 10 μm. The holographic device generally measured higher bubble concentrations by up

to a factor of two, although the limited number of total counts restricted the statistical significance of this result to the 20 to 50 μm bubble radius range. The source of this discrepancy seems to be in measurement of the illuminating beam intensity and initial calibration of the light scattering system.

As mentioned at the beginning of this chapter, a great deal of data is presently available concerning nuclei distributions in various laboratory test facilities. A discussion of the results of several of these investigations will be given in Chapter II.5 in relation to the water tunnel nuclei measurements of the present research. Overall, the results indicate large variations in nuclei content at different facilities and under different test conditions within a single facility.

I.1.3 Field Nuclei Measurements

The determination of the number, type and size of bubbles and particulates in the ocean is a problem of great interdisciplinary interest, and the scientific literature contains scattered results on particle, bubble and organism populations measured separately and from vastly different viewpoints. Some of the nuclei distribution curves shown in Figure I.1.1 represent data recorded in the ocean. The importance of the study of ocean nuclei to the naval hydrodynamics community has been mentioned above and is supported by the observation by Shen et al. (1986) that propeller cavitation data from the same class of ships in the ocean display a wide range of inception values.

Some of the field techniques used and the goals of these investigations will be presented here, with the specific results to be discussed in Chapter I. 5 in relation to the present results. Use of an *in situ* nuclei detection system allows the natural undisturbed population to be measured, whereas any sampling involves risk of alteration. The problem of population alteration is especially a problem for bubble measurement, since any change in ambient pressure will immediately affect the bubble radius. Light scattering, acoustic, photographic, holographic and venturi techniques have been applied *in situ*, whereas to date the Coulter

Counter technique has been applied only to discrete collected samples. A review of some of the work on nuclei detection in lake and ocean waters pertaining to cavitation is included in Billet (1985).

The Coulter Counter has had fairly extensive use in the ocean environment, including studies of the particulate content of surface and deep waters at several sites in the Atlantic and Pacific oceans by Sheldon et al. (1972) and the study of particulate concentration and its relation to light propagation in the ocean, in particular near sewage outfalls, by Peterson (1974).

Keller & Weitendorf (1979) performed laser light scattering measurements near the propeller of the container ship *Sydney Express* and found a large number of cavitation nuclei always present, and suggested that some of the nuclei may be small solid particles with diameters less than 20 μm. Shen et al. (1984, 1986) used an incoherent white light scattering device to examine the bubble concentration and spectra in ocean and lake water samples retrieved from depth and brought aboard at the local pressure of the collection depth. Their primary result was that the existence of gas bubbles to depths of 200 m was strongly indicated in the ocean waters near the Bahamas and Florida. The ocean bubble concentrations were seen to correlate well with biological activity and dissolved oxygen level. Higher nuclei concentrations were observed in the waters of Lake Pend Oreille, Idaho, than in the ocean.

Medwin (1970, 1977) used an acoustic attenuation technique to make detailed ocean bubble measurements under a variety of test conditions, and found bubbles with radii 15 to 200 μm present to depths of 40 m both day and night, even in the absence of breaking waves. Thorpe (1982) measured the acoustic scattering caused by bubble clouds in the fresh surface waters of Loch Ness, and in the sea near Oban, Scotland, and found a strong dependence of bubble concentration on wind speed. Pieper & Holliday (1984) have successfully applied a high-frequency (0.5 to 3 MHz) acoustic scattering technique to examine zooplankton concentrations in coastal waters off southern California.

Medwin (1970) examined bubbles at the surface and at 3 m submergence in calm, clear waters of Monterey Marina, using a photographic technique with illumination that allowed detection of bubbles by their specular reflections of the light sources. He found high bubble densities in the surface waters, and determined that the high count was due to the effect of marine organisms at that site, and that the count may have included some non-bubbles. Medwin concluded that an acoustic detection technique would be more useful in counting a statistically significant number of bubbles. Johnson & Cooke (1979) used a similar photographic technique to study the concentration of bubbles with radii greater than 17 μm in ocean surface waters under a variety of wind conditions, and found high bubble concentrations and strong dependence of the concentration on the wind speed, with higher wind speeds yielding much higher bubble concentrations.

The venturi cavitation susceptibility meter has been employed to make *in situ* measurements of the tensile strength of lake and seawater by Shen et al. (1984, 1986). Overall, they concur with Keller & Weitendorf, that ocean water is full of active nuclei, and they found the critical tensile strength of both lake and ocean waters examined to vary from 0.3 to 1.7 atm, comparable to typical tensile strength measurements in laboratory test facilities.

Knox (1966) used a pulsed ruby laser holographic system for a laboratory study of ocean water samples for their zooplankton content. He achieved high quality images of diatoms, copepods and fish eggs and larva, and suggested that a field operable version of such a system would be ideal for *in situ* organism analysis. However, the application of holography to field measurements has probably been hampered by the difficulty in packaging the laser and optical components to insure stable operation in a rough environment, and only a few ocean holographic imaging experiments are reported in the literature. Stewart et al. (1973) developed and deployed a prototypical xenon laser holographic system with the capability of recording large sample volumes up to 100 l. The

system was developed for an examination of marine plankton as part of a larger study of the marine food chain and was used in the ocean, but no results were reported. Carder et al. (1982) developed a free-floating sediment trap equipped with a shutter-equipped in line He-Ne holographic camera. This device was successfully deployed at 30 m depth in an examination of the *in situ* settling rates of naturally occurring marine particulate matter near the Bahamas.

I.1.4 Scope of the Present Work

Although the ocean is a very important environment for cavitation research, little is known about its cavitation nuclei characteristics. Typical values for marine bubble concentrations are simply not known because of difficulties in their measurement. Data are available on particulate and organism distributions in the ocean, but not in the cavitation context and not in relation to the bubble concentrations at the same site.

The primary goal of the present investigation is to demonstrate the feasibility of using a pulsed ruby laser holographic device for very short exposure *in situ* hologram recording. Analysis of the holograms recorded at various depths, locations and sea conditions will provide a great deal of data on what types of bubble, particle and organism population distributions may be found in the ocean, as possible input for determination of standards for flow seeding. Bubble measurements will be used to directly determine an expected tensile strength for the various test waters.

A comparison of the present results with those of previous ocean investigators found in the scientific literature will be made in order to relate the various measuring devices and their results in terms applicable to cavitation research. To a limited extent, the present work extends the preliminary holographic investigations of zooplankton made in the laboratory by Knox (1966) and in the field by Stewart et al. (1973), although detailed examination of the ocean holograms from a marine biology viewpoint is not intended.

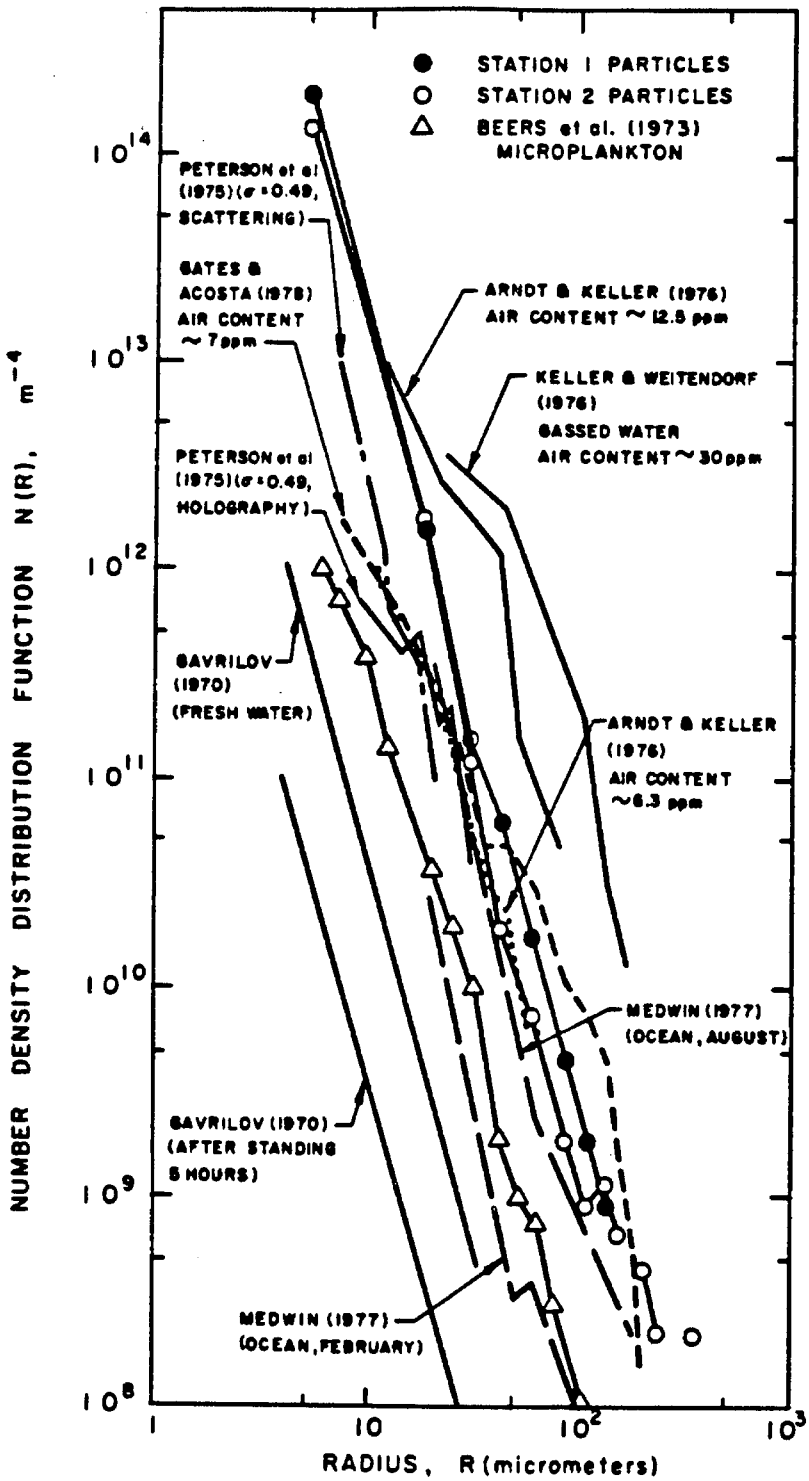

Figure I.1.1. Total nuclei density distributions from several investigators showing the several orders of magnitude difference commonly seen in various laboratory and ocean investigations. Present data added to that presented in Katz (1981).

	Equilibrium Bubble Radius (μm)			
	1	10	50	100
Critical Pressure $(p - p_v)_{crit}$ (Pa) : (psi) :	-4.3×10^4 -6.26	-2.0×10^3 -0.29	-1.9×10^2 -0.02	-6.7×10^1 -0.01
Natural Frequency f_n $(= \omega_n/2\pi)$ (kHz)	4290	336	64	32
Time to Dissolve τ (sec)	0.014	6.60	744	5.8×10^3
Terminal Velocity V_t (cm/s)	2.2×10^{-4}	2.2×10^{-2}	0.54	2.2

Table I.1.1. Characteristics of air bubbles in water over the radius range of interest as cavitation nuclei, from Equations I.1.4, I.1.7, I.1.8 and I.1.9. The value $(p_\infty - p_v)$ in Eqs. I.1.4 and I.1.7 is taken to be 10^5 Pa, $T = 20°C$, and water is saturated with air.

CHAPTER I.2
EXPERIMENTAL APPARATUS

A holographic system has been developed and used in various cavitation experiments at Caltech for several years (Gates 1977; Katz 1981). This system has been modified to allow submersible operation in the course of the present examination. This chapter describes the holographic technique and details of the present system.

I.2.1 Particle Field Holography

A hologram is an interference pattern formed by mixing of two coherent wave components, a subject wave reflected or scattered from the object or volume of interest, and a reference wave. Traditional off-axis holography involves the use of separate subject and reference beams, usually derived from the same coherent light source. Holographic reconstruction creates three-dimensional real and virtual images of the original test object, which can then be examined in detail. A complete examination of the holographic process can be found in such texts as Collier et al. (1971).

Holographic images of particle fields contain information on the size, shape and spatial position of each individual particle comprising the field. Detailed examination of such images in a flow field can be used as a means of studying either the particles themselves, their spatial distribution, or the flow field as visualized by the particles as tracers. Holography has become a fairly common technique for the study of particles with diameters larger than about 5 μm. Examinations are typically performed by visual observation of the reconstructed images, although automated analysis techniques are a topic of current interest

(e.g., Haussmann & Lauterborn 1980). The holographic technique has been applied to a variety of particle field examinations, including aerosols (Thompson & Ward 1966); coal combustion (Trolinger & Heap 1979); bubble chamber studies (Thompson & Ward 1966; Harigel et al. 1986) and cavitation nuclei in test facilities (see, for example, Peterson 1972; Feldberg & Shlemenson 1973; Gates 1977; Katz 1981; Ooi 1981). Excellent reviews of the use of holography for particle field measurements are given in such articles as Thompson (1974) and Trolinger (1975).

As briefly mentioned in Section I.1.2, holography has several unique advantages over some of the other standard particle measuring devices. In particular, a hologram contains both phase and intensity information about a scene, allowing exact wavefront reconstruction and therefore determination of the exact location of particles in a fluid, for example. Holography allows detailed visual examination of all objects in a particle field and thus is especially useful in a study like the present one in which the population distribution, or even the major component of the population, cannot be estimated *a priori*. Determination of the nature of the marine particulates may be vital, for example, for verification of whether bubbles are the only active cavitation nuclei in sea water, as most theoretical cavitation inception models assume. Trolinger (1980) demonstrates that the great depth of field of a hologram gives it several orders of magnitude greater capacity than a photograph for storing volumetric information. The requirements of high resolution and a large sample volume often needed in particle studies are in opposition in the photographic process but can be simultaneously satisfied using holography.

The Fraunhofer holographic technique, also referred to as in-line or far-field holography, is an approach in which a single laser beam is used as both reference and subject beam in the holographic recording. This is accomplished by illuminating the sample volume with a collimated coherent light beam (see Figure I.2.1). Part of the beam is scattered by objects in the liquid sample volume,

while the remainder passes through the volume undiffracted, acting as a collinear reference beam. The hologram is formed by recording the interference of these two beam components on a high resolution film. The detailed mathematical development of Fraunhofer diffraction and the in-line holographic technique can be found in such references as Parrent & Thompson (1964); DeVelis et al. (1966) or Tyler & Thompson (1976). Illumination of a single point particle with a collimated coherent light beam will, in general, produce a Fresnel diffraction pattern. However, when the far-field condition is satisfied, i.e., $z >> d^2/\lambda$, where z is the object to observation plane distance, d is the object diameter, and λ the wavelength of the illuminating beam, the Fraunhofer diffraction pattern will be seen at the observation plane. The hologram recorded on a film plane in the far-field of a point object is the interference pattern between the spherical wave diffracted by the object and the plane collinear reference wave.

The in-line holographic technique is simpler and requires considerably fewer optical components than the off-axis or double-beam method; minimizes path length variations between the subject and reference beams, thus lowering light source temporal coherence requirements; minimizes recording material resolution requirements; and minimizes sensitivity of the system to vibration. However, in-line holographic real images generally contain a high background noise component, caused by the background presence of the virtual image and out-of-focus objects (Thompson 1974; Dunn & Walls 1979a). The virtual image contribution is fairly small since it produces a uniform intensity background and is far removed from the focused image when the far-field condition is satisfied; however, any contribution is larger than that in off-axis holography where the two images are not collinear, so the virtual image does not disturb the real image. By definition, the far-field condition must be met in Fraunhofer holography; however, Vikram & Billet (1984) have shown that images of objects recorded at just a few far field distances are of fairly high quality, with a well-defined edge and suffering only from lower background contrast than those

recorded at farther far-field distances. The Fraunhofer holographic technique is limited to cases in which the sample is composed of a dilute concentration of small particles in order to maintain a sufficiently strong undiffracted collinear reference beam. Witherow (1979) recorded holograms of various concentration solutions of glass spheres with a mean diameter of 25 μm suspended in silicon oil, and showed that high quality images could be obtained with a concentration of $10^3/cm^3$, fair images with $10^4/cm^3$ and poor quality images with $10^5/cm^3$. The critical concentration is expected to vary, depending on the recording beam energy, exposure time and mechanical stability of the recording system.

Some advantages of the off-axis holographic technique are that it allows the use of diffuse illumination of the sample volume; permits the use of a perfectly filtered and well-controlled reference beam; is not subject to the far-field restrictions on object size and distance from the film plane; and is not limited to dilute particle concentrations but can actually be used for non-transmissive volumes in a reflective mode. The use of separate subject and reference beams does, however, place additional coherence requirements on the light source. The off-axis holographic process also has several inherent advantages over the in-line technique in regard to the differences in reconstruction. In the off-axis reconstruction configuration, the axis of the holographic images does not coincide with the reconstruction laser beam, so the viewing system is not continuously exposed to direct illumination by the reconstruction beam and the noise due to the reconstruction light source can be eliminated. Also, the in-line hologram of a sample volume with a large object (such as a submerged test body) contains a transparent section. This leads to part of the reconstruction He-Ne beam passing undisturbed through the hologram directly into the viewing system, creating large intensity gradients in the neighborhood of this large object and making detection of small particles nearby very difficult. This problem does not exist when the off-axis technique is applied, since the angle of observation prevents direct illumination of the viewing system.

The in-line technique has some advantages in analysis of semi-transparent droplets or particles, such as better particle-to-background contrast (Prikryl & Vest 1982). In addition, reconstruction is generally performed on a negative hologram, which is simply the developed holographic film. In this case, the reconstructed image of an in-line hologram will be a negative of the original field, so that the image of a field of particles will appear as bright objects against a dark background, whereas off-axis holograms always produce positive images. The detection of bright objects against a dark background is generally a more efficient approach. When a hologram is recorded on a photographic emulsion, the absorption pattern formed by the silver crystals on the film corresponds to the spatial intensity of the incident light. If the hologram is bleached to convert the silver to a transparent silver salt compound, a nearly transparent phase hologram is formed. This hologram will act to modulate the spatial phase of the reconstruction beam in order to form an image corresponding to the intensity pattern incident on the film at the time of recording (Collier et al. 1971). Absorption holograms provide higher contrast images than phase holograms, and are thus more suitable to particle concentration analysis, although phase holograms have higher diffraction efficiency and provide greater edge resolution for shape analysis (Dunn & Walls 1979b). Both in-line and off-axis holograms have been used in the course of the present experiments, as will be detailed below, and all holograms analyzed were of the absorption variety.

Several factors must be considered in the design of an accurate holographic recording system. Spatial and temporal coherence of the light source are vital to assure efficient interference of the beams at the film plane, and thus require use of a laser that can produce polarized, monochromatic and single-mode beams of sufficient energy to properly expose the recording film. The finite coherence length of existing lasers necessitates careful optical design in order to achieve satisfactory interference. Sufficient mechanical stability is required to maintain all optical components stationary to within $\lambda/10$ during exposure, where λ is

the wavelength of the illuminating beam. Holographic examination of moving objects imposes a restriction on the exposure time, with the general rule of thumb for image clarity being that the object moves less than 1/10 of its diameter during the exposure, so, for example, the exposure time for a 10 μm diameter object moving at 10 m/s should be less than 100 ns. High resolution generally requires that the sample volume be located close to the film plane, often requiring the use of a lens system to relay the volume image onto the film plane. The recording medium, usually film, must have sufficient resolution to be able to record accurately the fringe pattern formed by beam interference. The required resolution of the recording medium can be determined by calculating the interference fringe spacing on the film plane and assuming some criterion for satisfactory recording of the diffraction pattern of a particle, say that the central maximum and three side lobes of the diffraction pattern must be recorded, as suggested by Thompson (1974), whose analysis leads to the requirement that for satisfactory recording of the diffraction pattern of a 10 μm particle, a recording resolution of about 2500 lines/mm is needed. Spatial filtering by a pinhole aperture is generally required to eliminate beam impurities due to diffraction caused by dust particles, impurities of optical components or inherent optical noise of the laser beam. The pinhole is located at the focal point of a microscope objective lens that focuses the laser beam to a waist. The pinhole blocks all but the lowest order diffraction, acting as a low pass spatial frequency filter to smooth out small scale beam intensity variations.

I.2.2 Holographic Nuclei Detector

The criteria discussed in the previous section were taken into consideration in the design and construction of the present submersible holographic system. A pulsed ruby laser is used as the coherent light source for hologram recording because its short (20 to 50 nanosecond) pulses are needed to freeze images of small objects streaming through the test volume. A Pockels Cell electro-optical

Q-switch is used as a high speed intracavity shutter. The laser cavity is normally blocked to light oscillation by an air-spaced Glan polarizer crossed with the ruby. When laser output is desired, a half-wave voltage pulse (about 4 kV) is applied to the Pockels Cell KD^*P crystal. This voltage acts on the crystal to produce a 90° rotation of the laser beam polarization, allowing it to pass through the Glan polarizer. The laser cavity is thus open to allow a single laser pulse of about 15 mJ to be emitted at the ruby wavelength of 0.6943 μm. The short pulse durations assure that sufficient freedom from vibration will be maintained during the exposure period. An 11 μm pinhole is used to spatially filter the laser beam at its waist when focused by an 11 mm focal length microscope objective lens. The laser beam is collimated to produce a plane wave with divergence less than 1 $m$rad as it passes through the sample volume. The recording medium, Agfa-Gevaert 10E75 roll film, was selected to meet fringe resolution requirements with its resolution of about 2800 lines/mm, and requires an exposure energy flux of approximately 1 to 3 $\mu J/cm^2$ for optimum exposure, well within the laser capabilities. A 100 foot roll of film, sufficient for recording about 300 holograms, is held under fairly high tension in a film drive mechanism to maintain a flat recording surface.

Figures I.2.2 (a) and (b) are schematic diagrams of the holographic system in the in-line and off-axis configurations, respectively. Figure I.2.3 is a photograph of the laser cavity and some of the optical components, corresponding directly to the diagram of Figure I.2.2 (b), with the optical components identified according to the key given in the diagram. Most of the optical components are mounted on a 1/2 inch thick aluminum plate that is connected to the submersible tank structure through a drawer mechanism mounted on four rubber shock absorbers. This creates a fairly stable optical base that can be easily pulled out of the tank for optical alignment or cleaning. The ruby laser resonant cavity is 40 cm long, enclosed by a 100% reflecting dielectric back mirror and a sapphire etalon (about 60% reflectivity) needed for longitudinal mode control

of the laser output. The active medium is a 75 *mm* long, 6 *mm* diameter ruby rod with anti-reflection coated faces. The rod is mounted in the center of the laser pump source, a helical xenon flashlamp. Both the ruby and the flashlamp are surrounded by a polished aluminum reflector. Ruby lasers are fairly inefficient, with the excess pump energy remaining in the rod as heat, which must be removed in order to avoid a drop in the laser gain (an important consideration in 3-level laser systems such as ruby, see Koechner 1976) and to avoid thermal lensing of the rod itself. This cooling is achieved by enclosing the ruby rod, flashlamp and reflectors in a sealed water-filled housing, with continuous injection of filtered, deionized water into the region between the flashlamp and the ruby rod. The water is typically recirculated at the rate of about 1 *gpm*. The ruby faces are isolated from the cooling water through O-rings, and the ruby mount allows the rod to be rotated upon its axis for proper polarization without opening the sealed housing or moving the flashlamp. As mentioned above, a Pockels cell and glan calcite polarizers are used to Q-switch the laser, allowing selection of either one or two carefully timed laser pulses. When double pulsing is used, the time delay between the two pulses can be accurately controlled from about 20 μs up to 500 μs. The final components of the laser cavity are two iris apertures, used to limit the output beam diameter to about 1 to 2 *mm* in order to assure generation of the TEM_{00} (Gaussian) transverse mode. The laser output beam is sampled by a PIN diode, split by a beam splitter in the off-axis configuration, spatially filtered and collimated before illuminating the sample volume and film. A neutral density filter is used to attenuate the output beam to the proper energy for optimum film exposure. An autocollimater and a 1/2 *mW* He-Ne laser are also mounted on the optical base and used for alignment of all optical components.

Primary controls and power supplies for the holographic system are contained in a shipboard control rack, which is connected to the submersible by about 35 *m* of waterproof cable. The operator controls the laser flashlamp en-

ergy and the timing and number of laser pulses (1 or 2). Circuits inside the submersible expose the film through an automatic shutter (minimum opening time of 40 ms) and advance the film drive corresponding to each laser firing. A PIN diode signal relayed to an oscilloscope at the control rack allows monitoring of the laser pulse timing and intensity. The length of the electrical cables controlling and monitoring the laser and associated equipment limit the maximum submersion depth to 34 m. Appendix I contains schematic electrical diagrams detailing the electronic circuitry of the ruby laser holographic camera system.

The ruby laser and optical base are mounted inside a submersible hull with windows through which the expanded laser beam passes to illuminate an external water sample. The submersible tank is constructed of a 3 foot long section of 24 inch diameter schedule 20 steel pipe with each end fitted with an elliptical end bell. Stainless steel mating surfaces are welded to the pipe ends and end bells, so that the tank can be well sealed, using O-rings and clamping the end bells with Marmom clamps. The tank structure is held by a steel framework and the entire assembly is mounted on wheels for transport. The assembled submersible tank with all components in place weighs about 1000 pounds. Figure I.2.4 is a photograph showing the submersible tank with its back end bell removed to show some of the optical components inside. Also visible are the electronic control rack and the waterproof cable connecting the controls to the tank. The optical path for illuminating the external sample volume can be seen in Figure I.2.5. The path is constructed of 4 inch schedule 40 PVC pipe and fittings, and contains two flat mirrors to direct the output laser beam into the sample volume. The sample volume is bounded by two high quality precision optical flat windows in order to avoid beam distortion. The windows are flat to within $\lambda/20$ on one side and $\lambda/10$ on the other, and are left uncoated since they are exposed to sea water and therefore must be frequently cleaned. The sample volume is 25 cm long, and is illuminated by a 6.4 cm diameter beam, producing a cylindrical sample volume of about 800 cm^3. The film plane lies 15 cm inside

the near window. The windows and PVC pipe fittings are held in place with O-ring seals to prevent leaks. A leak detection circuit is used to indicate any sea water intrusion or cooling water leak sufficient to close a small contact in the circuit.

The holographic system is constructed in such a manner that it can be fairly easily converted from an off-axis to an in-line mode and has been used in both configurations for portions of the present experiments. As can be seen in Figures I.2.2 (a) and (b), the transformation simply requires removing the beam splitter from the off-axis system, placing the spatial filter on the single beam and rotating as well as shifting the film drive position to face the sample volume.

Preliminary system testing of the underwater device was performed in the Caltech swimming pool in July, 1983 and at the Long Beach Shipyard in March, 1984. Off-axis holography was used in these experiments, with the reference beam about ten times stronger than the subject beam, the path length difference between the two beams kept to less than 1.5 *mm*, and the film facing the bisector of the 30° angle between the beams. This configuration had been successfully operated in preliminary laboratory tests, producing dozens of high quality holograms of relatively large objects positioned throughout the sample volume. The system was less reliable in the field, with the result that only about 10 good holograms were recorded while submerged in the swimming pool, and none of the 30 holograms recorded while submerged in the sea water at the shipyard produced useful images. The experimental difficulties encountered in these trials were primarily due more to electronic than to optical problems, leading to slight electronic modifications prior to the open ocean tests. Figure I.2.6 is a print of one of the off-axis holograms recorded in the Caltech swimming pool, and Figure I.2.7, a photograph of one plane of the reconstructed image from this hologram, showing one of several transparent plastic rulers that were placed in the sample volume.

Experience from the preliminary trials led to several system modifications. An external heat exchanger for ruby rod temperature control was added; a dessicant bank, small recirculating fan, and dry nitrogen purge system for humidity control in the submersible were installed; thorough leak-testing procedures were implemented; and an interference filter was added to allow hologram recording during daylight hours. The interference filter was a 3-cavity near infrared bandpass type with a 12.1 $\pm$ 1.5 *nm* bandwidth centered at the ruby wavelength. A pair of remotely controllable stepper motors were added to the spatial filter assembly in order to allow pinhole alignment without opening the submersible tank. A beam expander was also added to the spatial filter assembly in order to lower the incident energy flux at any point on the focusing lens (microscope objective), to prevent localized burning of this component. Finally, a sealed enclosure was built around the laser cavity with a continuously operating fan supplying filtered air to maintain a slight positive pressure inside, thus preventing dust intrusion or deposition on any of the cavity optical components.

In addition, the decision was made to use the in-line technique for the open ocean holographic tests. This decision was made based on the considerable experience with the in-line technique gained in water tunnel testing (see Part II) and because the in-line technique requires fewer components than an off-axis system, thus minimizing alignment difficulties that could be most difficult while at sea. In addition, the best off-axis holograms recorded (both in the lab trials and in the swimming pool) produced fairly weak real images that became difficult to examine at magnifications above about 100X. As discussed above, the Fraunhofer technique is very well suited to examination of the types of samples expected in the sea, that is, fairly dilute concentrations of small objects. The particle fields of interest in the present study generally satisfy both the far-field condition and the low concentration requirement.

I.2.3 Holographic Reconstruction System

After recording, the holographic film is removed from the film drive and developed so that the "negative" hologram can be mounted for reconstruction. A spatially filtered, expanded and collimated 5 mW He-Ne laser beam illuminates the hologram, which acts as a diffraction grating to form three-dimensional real and virtual images of the original sample volume, as indicated in the diagram of Figure I.2.8 for the in-line configuration. The in-line and off-axis reconstruction systems are shown diagrammatically in Figures I.2.9 (a) and (b), respectively. The reconstruction system is set up on an 84 $\times$ 24 $\times$ 1 inch aluminum plate for stability. The hologram is mounted on a three-dimensional translating carriage, allowing examination of the real image volume in all three dimensions at magnifications up to 220X, using a microscope objective lens and a lensless closed circuit vidicon (RCA TC 1005/H01) and monitor (RCA TC1110). The system resolution is about 5 μm, approaching but unable to achieve diffraction-limited performance because of optical noise in the recording and reconstruction systems. Calibration of the reconstruction system was performed by analyzing images from holograms recorded of polystyrene spheres of known, uniform size (Katz 1979) and microscope eyepiece reticles. Discrimination of bubbles from solid particulates is made by visually examining the focused image for edge roundness and sharpness, image brightness, and the presence of a dark central spot due to the focusing effect of the bubble geometry. No attempt is made to establish the nature of nuclei with radii smaller than 10 μm, but is made for all larger sizes.

The off-axis reconstruction system is shown diagrammatically in Figure I.2.9 (b). In reconstruction of off-axis holograms, the illuminating beam is the conjugate of the original reference beam; that is, it passes through the film from the opposite side and is directed opposite to the original reference beam. This illumination projects a real pseudoscopic (depth inverted) image field along the

axis of the original subject beam. A magnifying microscope objective, placed on this axis inside the real image field, is used to focus any desired cross section onto the vidicon tube, so the image of that area can be inspected on the monitor. A reconstructed image of a ruler is shown in Figure I.2.7, from the hologram shown in Figure I.2.6, which was recorded as part of the preliminary system tests in the Caltech swimming pool.

The in-line reconstruction system shown in Figure I.2.9 (a) follows the same principles as the double-beam system, but allows a much simpler geometry. The conjugate illuminating beam strikes the hologram on a normal, projecting the real and virtual images along the same axis. Observations are again made in the real image field. Figure I.2.10 shows one cross section from the reconstructed image of a sea water sample, showing the image of a marine organism magnified 220X on the monitor screen.

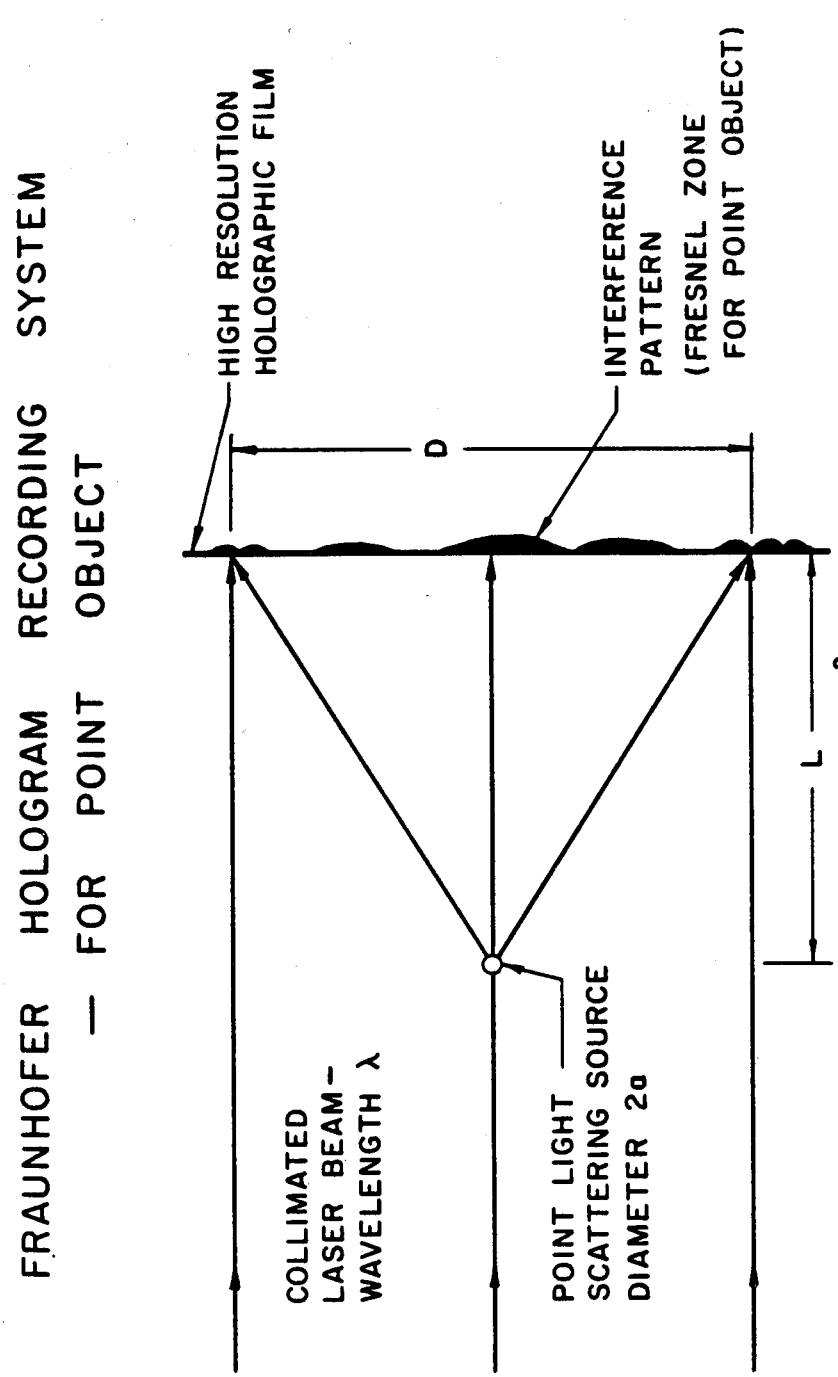

Figure I.2.1. Schematic diagram of the Fraunhofer (in-line) holographic process for a single small particle.

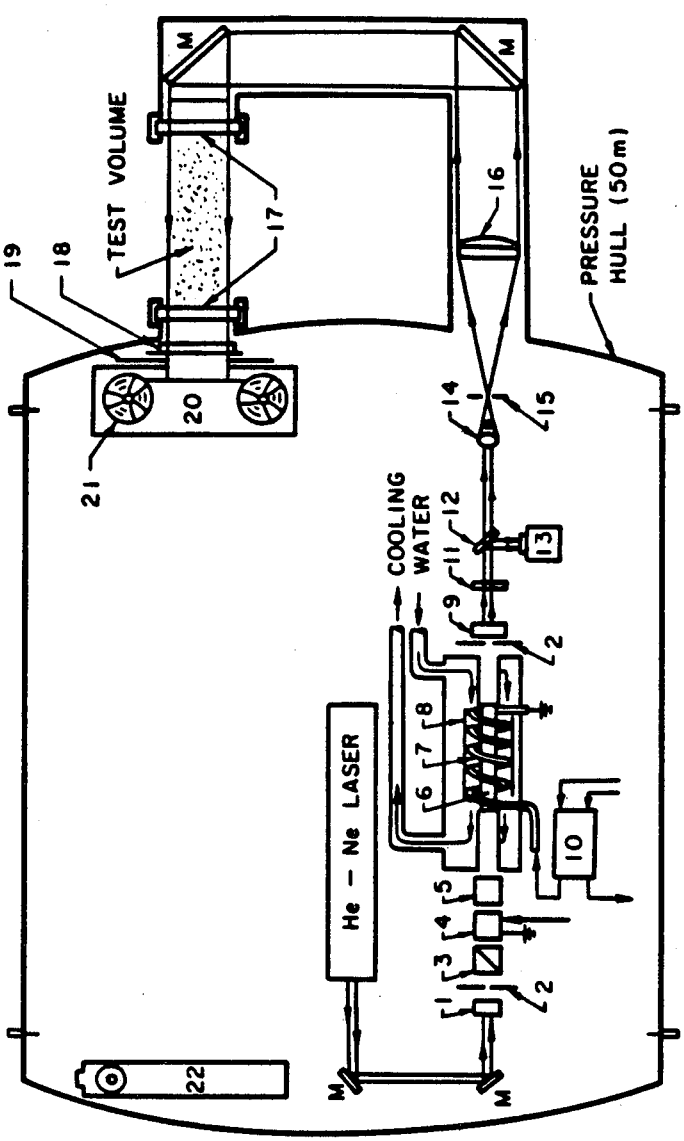

1. BACK MIRROR
2. IRIS APERTURE
3. POLARIZER
4. POCKELS CELL
5. POLARIZER (OPTIONAL)
6. RUBY ROD
7. XENON FLASH LAMP
8. REFLECTOR
9. FRONT MIRROR-SAPPHIRE ETALON
10. TRIGGER TRANSFORMER
11. NEUTRAL DENSITY FILTER
12. BEAM SPLITTER (4% REFLECTIVITY)
13. PIN DIODE
14. MICROSCOPE OBJECTIVE
15. SPATIAL FILTER-10μ PINHOLE
16. COLLIMATING LENS
17. GLASS WINDOWS
18. INTERFERENCE FILTER
19. SHUTTER
20. AUTOMATIC FILM DRIVE
21. HOLOGRAPHIC FILM SPOOLS
22. AUTO COLLIMATOR
M. MIRROR

Figure I.2.2. Line drawing of the holographic camera system mounted inside submersible hull. The surrounding tank structure, return optical path and optical components are shown but not to scale. The legend identifies the major components. (a) In-line configuration (b) Off-axis configuration.

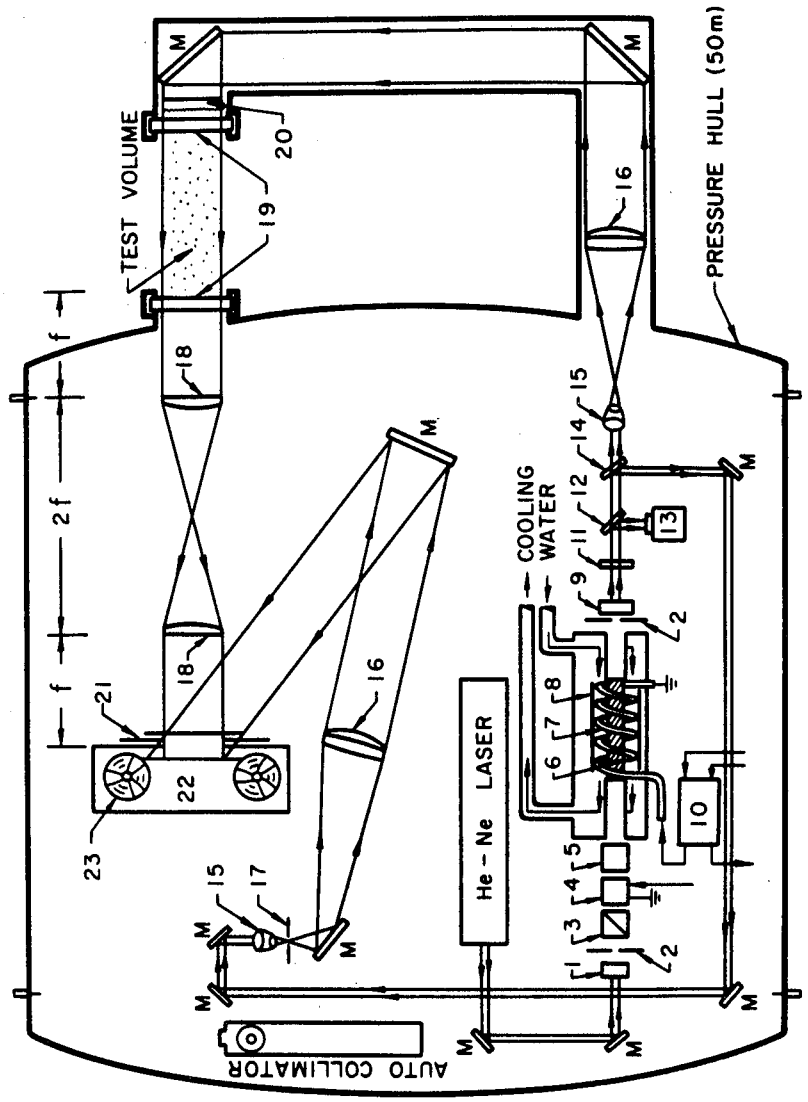

1. BACK MIRROR
2. IRIS APERTURE
3. POLARIZER
4. POCKELS CELL
5. POLARIZER
6. RUBY ROD
7. XENON FLASH LAMP
8. REFLECTOR
9. FRONT MIRROR-SAPPHIRE ETALON
10. TRIGGER TRANSFORMER
11. NEUTRAL DENSITY FILTER
12. BEAM SPLITTER (4% REFLECTIVITY)
13. PIN DIODE
14. BEAM SPLITTER (50% REFLECTIVITY)
15. MICROSCOPE OBJECTIVE
16. COLLIMATING LENS
17. SPATIAL FILTER-10μ PIN HOLE
18. RELAY LENSES
19. GLASS WINDOWS
20. DIFFUSER
21. SHUTTER
22. AUTOMATIC FILM DRIVE
23. HOLOGRAPHIC FILM
M. MIRROR

Figure I.2.2 (b). See caption on p. 47.

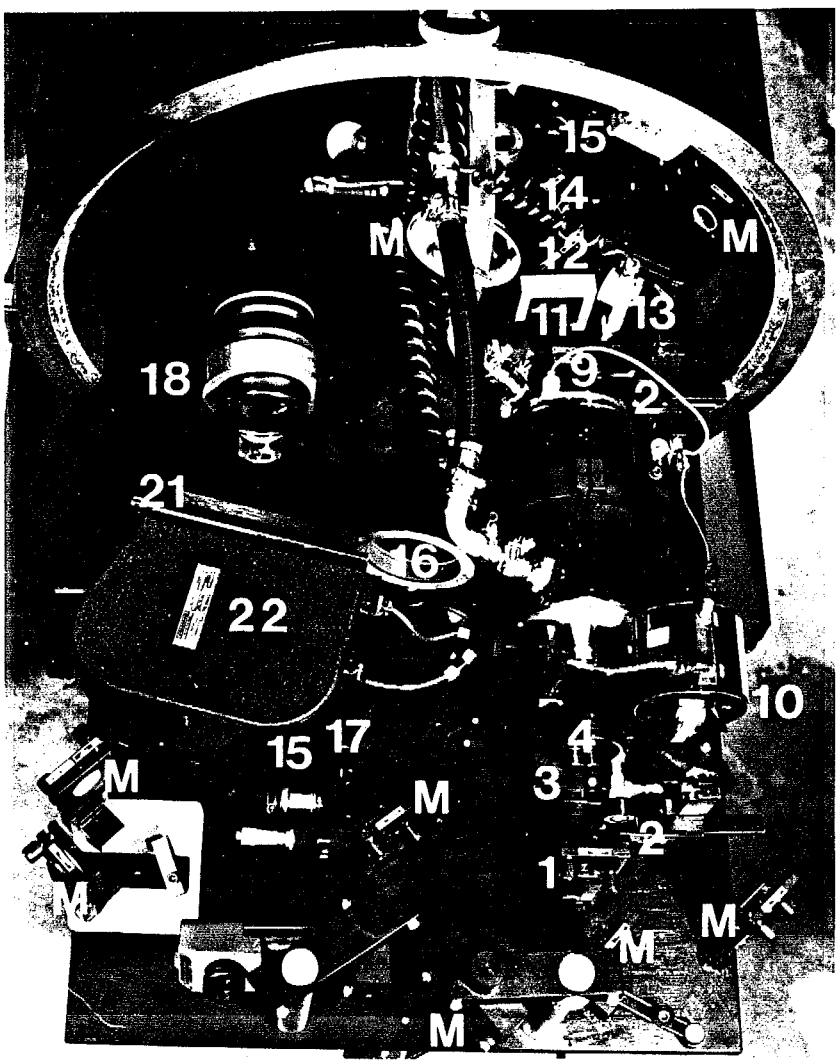

Figure I.2.3. Plan view photograph of optical components of the ruby laser and off-axis holographic system identified according to the legend of Figure I.2.2. The Pockels cell has been removed from its mount in this photograph.

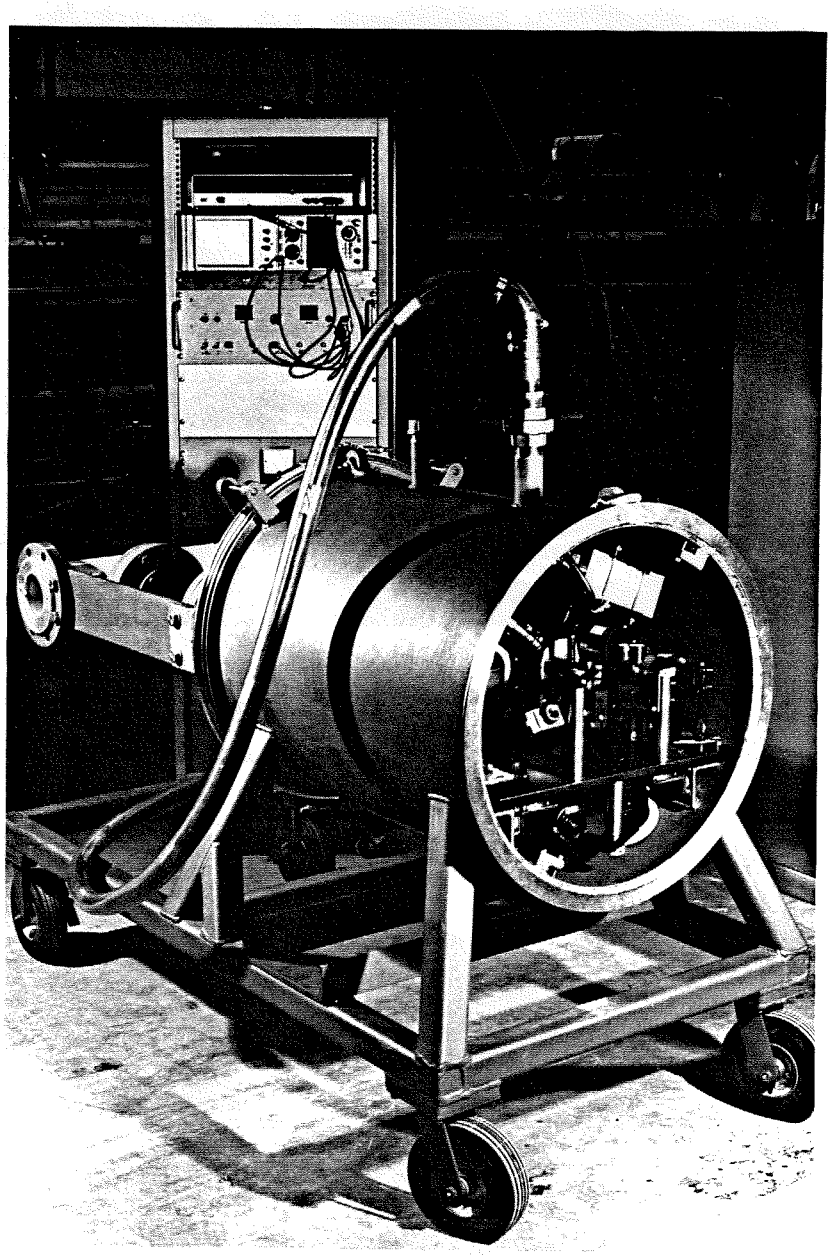

Figure I.2.4. Photograph of the underwater holographic camera system showing the submersible tank structure, waterproof tubing enclosing electrical cables and the electronic main power and control rack. The back end bell is removed to show the optical components interior to the tank.

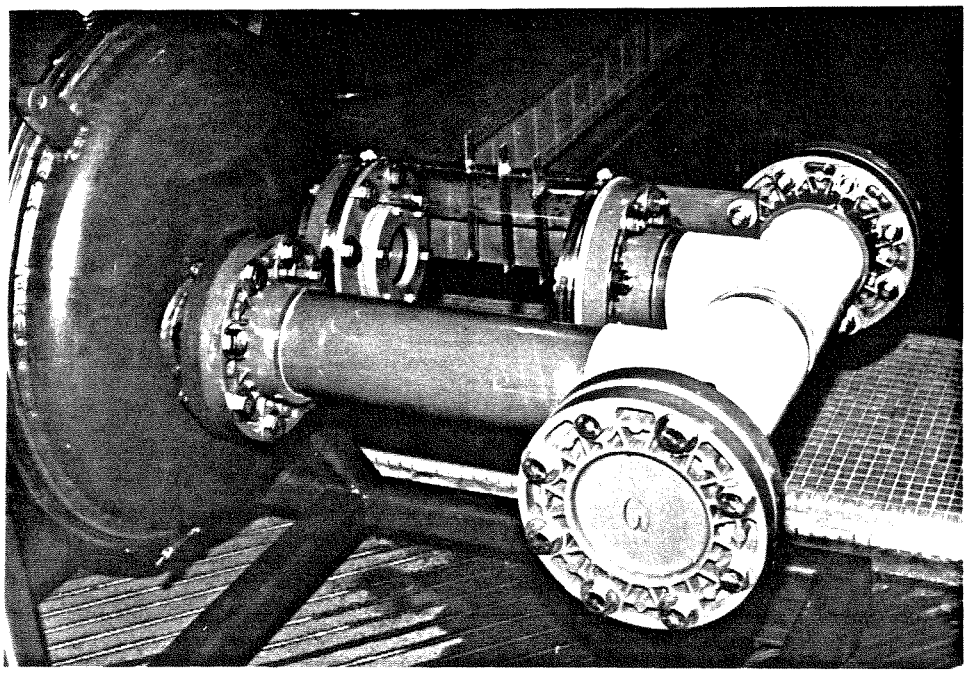

Figure I.2.5. Photograph of the underwater holographic camera system optical return path and sample volume. Transparent plastic rulers are visible in the sample volume.

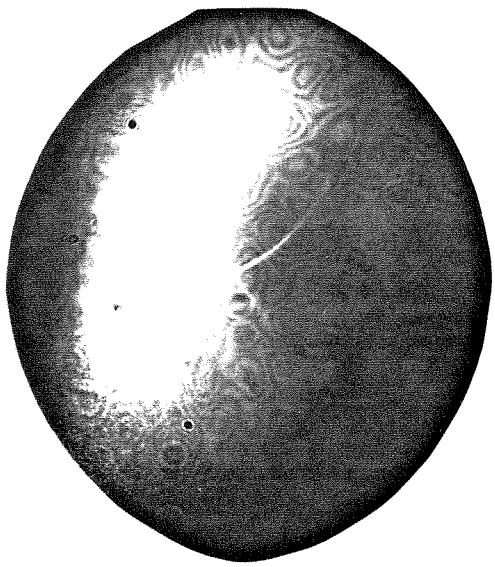

Figure I.2.6. Sample print of an off-axis hologram recorded during preliminary system tests while submerged in the Caltech swimming pool. The recording medium is Agfa-Gevaert 10E75 roll film.

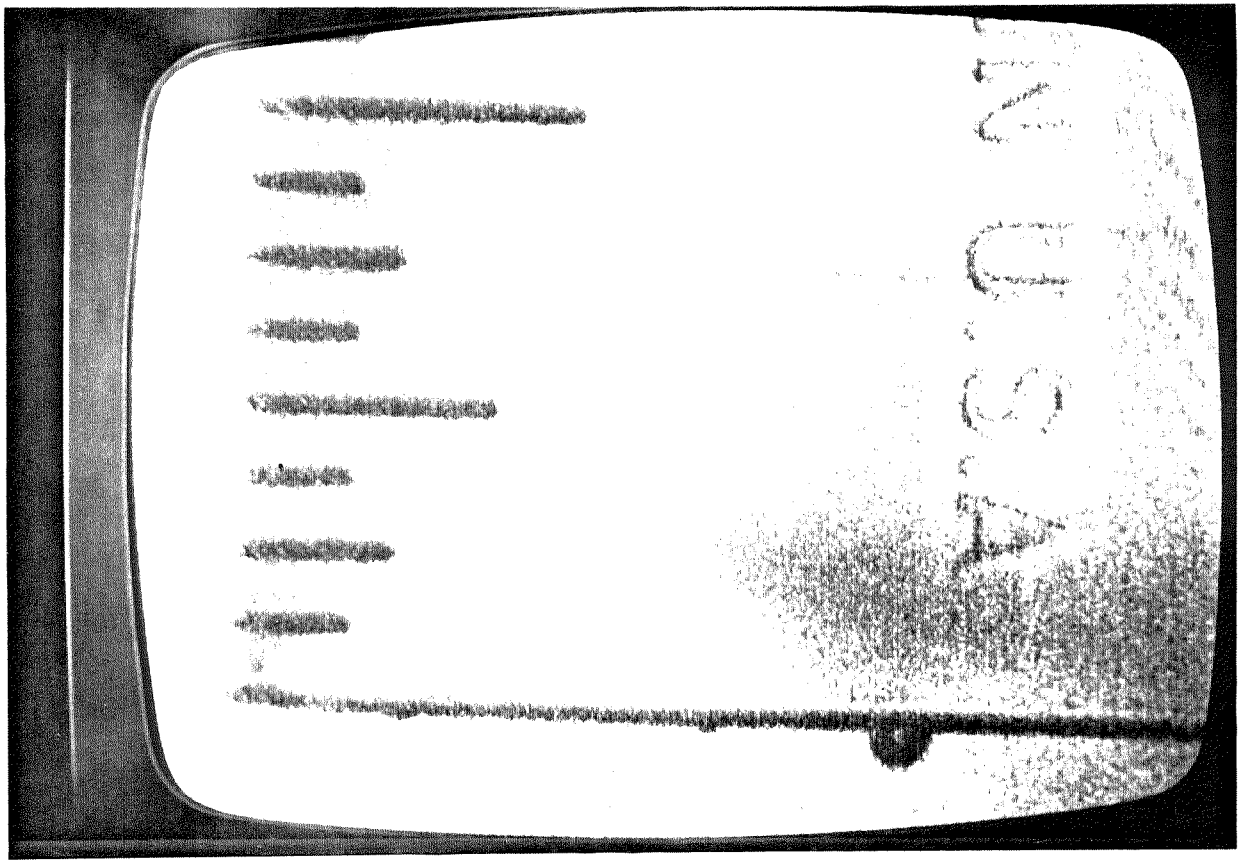

Figure I.2.7. Photograph of the reconstruction monitor screen displaying the focused image of a transparent plastic ruler. Magnification is 16X on the monitor and the smallest visible division on the ruler is 1/32 inch. This reconstruction is from the off-axis hologram shown in Figure I.2.6.

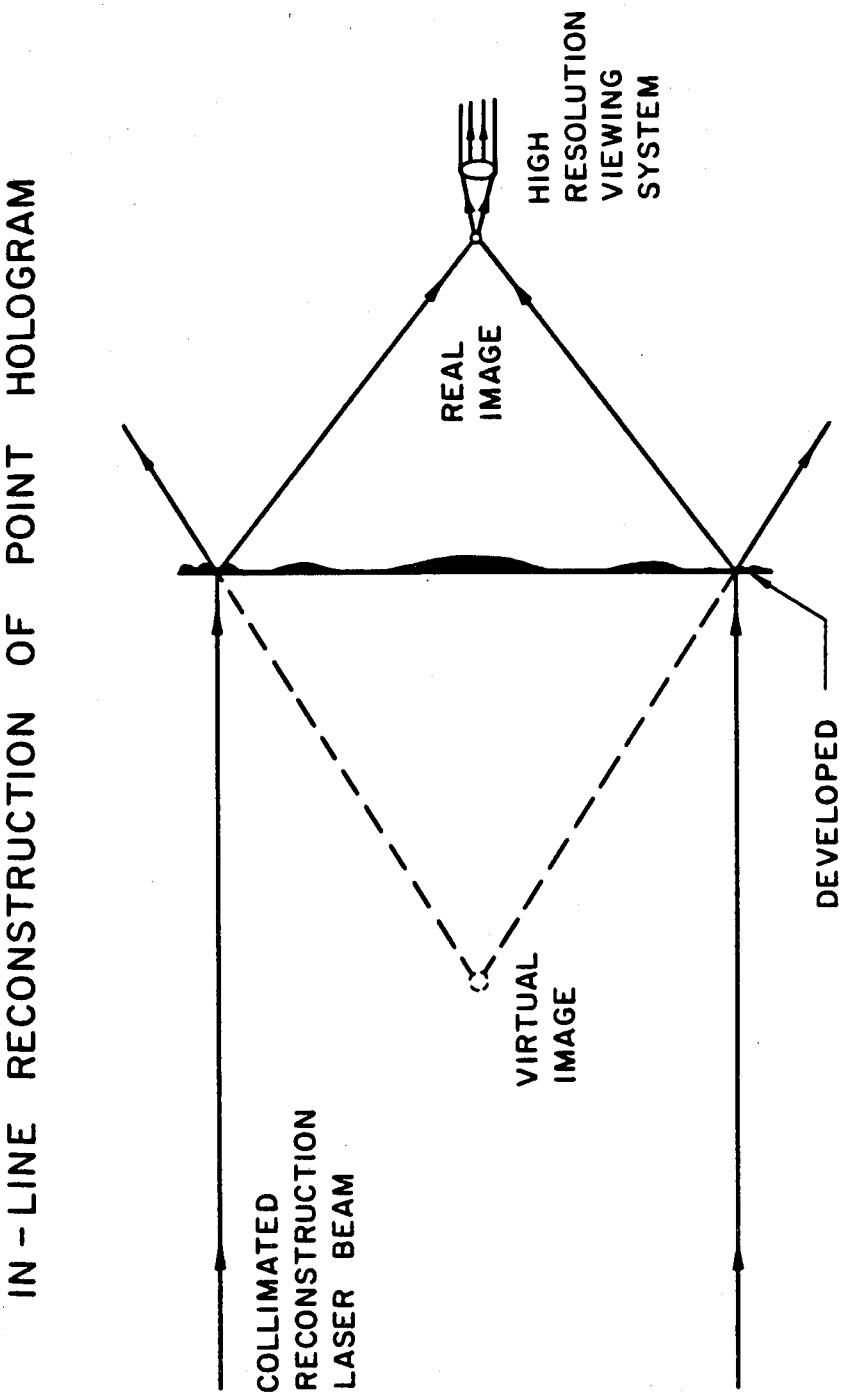

Figure I.2.8. Schematic diagram of the in-line reconstruction of the hologram of a single point object.

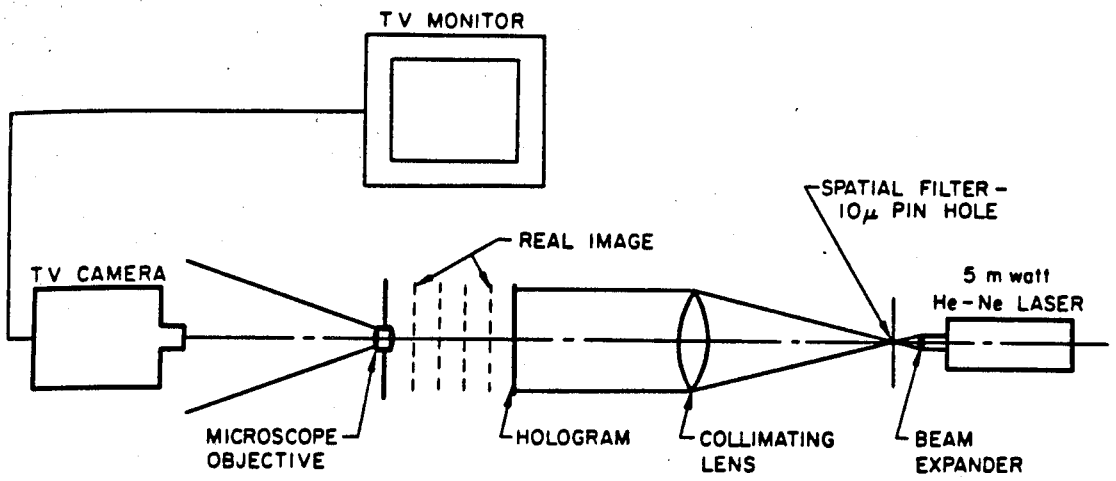

(a)

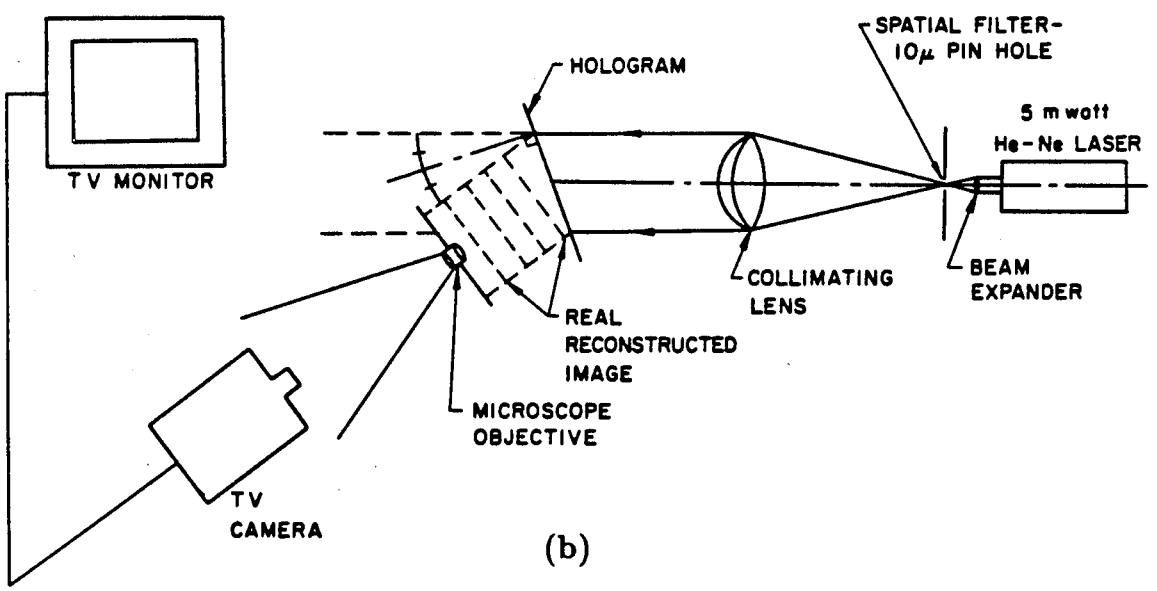

(b)

Figure I.2.9. Reconstruction systems
(a) Line diagram of in-line reconstruction system
(b) Line diagram of off-axis reconstruction system

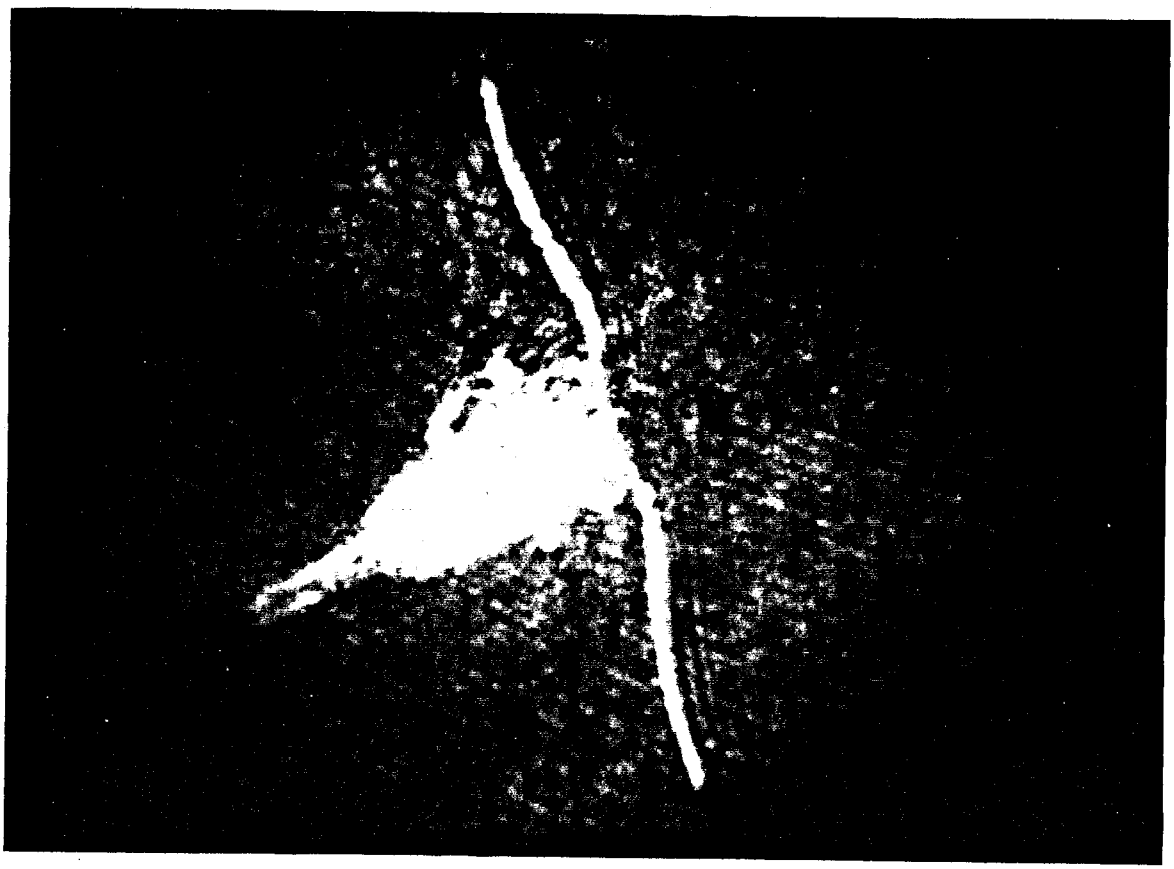

Figure I.2.10. Photograph of the reconstruction monitor screen displaying the focused image of a marine organism from one of the open ocean in-line holograms. Organism body length $\simeq$ 600 μm.

CHAPTER I.3
EXPERIMENTAL TECHNIQUES

I.3.1 Ocean Testing

Upon completion of the preliminary system trials mentioned in the previous chapter, the actual data-gathering ocean tests were scheduled. The vessel used was the 65 foot *R/V Seawatch*, operated by the University of Southern California Institute for Marine and Coastal Studies Marine Support Facility at Terminal Island, California. This vessel was equipped with a motorized winch and stern A-frame, which were used for loading and deployment of the submersible. Figure I.3.1 shows the holographic submersible prepared for transport on the deck of the *R/V Seawatch*. All test locations were within a one-day cruise of the Terminal Island base.

After reaching the location of interest, the test procedure was to fire the laser several times while on board, monitoring to check that all components worked properly and that the laser output was strong. The submersible was then carefully lifted, using the motorized winch and A-frame, lowered into the water just off the stern and allowed to sink to the depth of interest. Holographic data were collected only while the boat was anchored or drifting, to avoid recording artifact propeller-generated bubbles. The first depth examined was usually at maximum submergence (about 33 m). Submergence depth was determined using a calibrated cable payout on the winch, and allowances for plumb angle (modifications in submersion depth due to a cross current) were not made. About five holograms were recorded at each depth, after which a new depth was selected and another group of holograms recorded. The submersible was not pulled out of the water until all test depths had been examined. The laser

power output (output of the PIN diode) was monitored on an oscilloscope at the time of each laser firing to assure that the laser pulse was sufficient to properly illuminate the film. The submersible tank was brought aboard after each set, or whenever the laser performance deteriorated, and the ruby laser cavity components and spatial filter alignment examined and adjusted if necessary.

In support of the holographic measurements, several standard oceanographic measurements were concurrently performed in order to characterize the sea conditions at the time of testing. Bottom depth was determined using a Ross fathometer. Sea water transmissivity was measured using a Beckman Model EV–4 transmissometer, consisting of a light source and detector array used to determine the attenuation of a collimated white light beam over a one-meter path length. Salinity and temperature profiles were obtained as a function of depth at each holographic test site using a Plessey Model 9060 STD probe. Visibility was measured by recording the disappearance depth of a standard 30 cm diameter white Secchi disk. Nansen bottle sampling was performed at several of the holographic test sites so that the collected samples could be stored in bottles and returned to the lab within 24 hours for Coulter Counter examination (see Appendix II). Collection of oceanographic data was done during the time that the holocamera was submerged and operating, and at a distance of no more than 5 m (on deck) in order to assure that the oceanographic data recorded were applicable to the holographic samples.

The first open ocean experiments were performed in December 1984 without oceanographic data support. The first series of holograms was recorded in fairly turbid 13.4 m water, about 100 m inside the breakwater of Los Angeles Harbor, approximately 33°43'12" N, 118°13'12" W (see Figure I.3.2 for a map of all the test stations). Holograms were recorded at several depths from 2 to 5 m submergence while anchored at this site, halfway between the Long Beach and Los Angeles gaps in the breakwall. The water visibility at this station was roughly 1.2 to 2.4 m, with the water surface color somewhat green, indicative

of fairly high particle concentration and high beam attenuance (Peterson 1974). Submersion time at this location was 1 hour. However, electrical problems associated with the Pockels cell Q-switch hampered laser performance to the extent that only one good reconstructable hologram was recorded, this at 5 m depth. A second series of holograms was recorded in the open ocean waters of San Pedro Channel at 33°36'28" N, 118°23'25" W. The bottom depth at this station was about 1000 m, and holograms were recorded at several depths from 3 to 30 m over a period of 4 hours while slowly drifting with the current. Visibility in the water at this location ranged from about 9 to 12 m during the testing period. Difficulties with the Pockels cell led to the recording of only two good reconstructable holograms, both at 3 m submergence.

The second series of field tests was performed in late August 1985 at two locations near Santa Catalina Island, southwest of Los Angeles, and at one location above the sewage outfall pipe of the Los Angeles County Sewage Treatment Plant at Whites Point (see Figure I.3.2). Table I.3.1 lists the conditions and hologram depths at each station examined during these tests. The bottom depth was too great to allow anchoring at any of these test sites, so holograms were recorded while the boat drifted. These particular test sites were chosen to correspond closely to those examined for particle density and light scattering properties by Peterson (1974), using a Coulter Counter and those examined for zooplankton by Pieper & Holliday (1984), using an acoustic scattering technique. The first test location was off Long Point, Santa Catalina Island. The boat drifted in waters ranging from 132 to 228 m depth during the two hours of holographic testing. Thirty holograms were recorded, sampling the water column from the surface to 32 m. The second test location was off the eastern point of Santa Catalina Island. Fourteen holograms were recorded at this station, all at either 27 or 32 m. The third test location was above the sewage outfall of the Los Angeles County Sanitation District's advanced primary treatment plant at Whites Point. This plant discharges on the order of 350×10^6 gallons per

day, containing approximately 500 tons of total suspended solids, through large (90 and 120 inch internal diameter) pipes for sea floor deposition (about 55 m submergence 2 miles from shore). The outfall design relies on the ocean's thermal stratification to restrict the vertical transport of the sewage plume to below the thermocline (Peterson 1974). Holograms were recorded directly above one of the outfall pipe diffuser sections, from the surface to 34 m, well within the concentrated plume of sludge particles.

At the end of each day of testing, the sealed film drive was taken to a darkroom and opened for development of the holograms. Due partly to inherent instability of the ruby laser and partly to unanticipated movement of the Pockels Cell, the laser performance during testing was intermittent to the extent that good holograms were not recorded at every depth examined at each test station. In addition, when multiple good holograms were recorded at the same depth and location, time constraints allowed detailed examination of only the single best one. For these reasons, the "hologram depths" listed in Table I.3.1 are actually those depths at which a single high quality hologram was successfully recorded and examined.

I.3.2 Holographic Reconstruction and Data Analysis

As discussed in Chapter I.2, holographic reconstruction is accomplished by illuminating the developed hologram with a collimated continuous wave He-Ne laser beam. The hologram acts as a diffraction grating to produce three-dimensional real and virtual images of the original volume. Measurements are made by using a closed circuit vidicon system to examine a highly magnified portion of the real image.

Size determinations are made by focusing a highly magnified image of each nucleus on the reconstruction system monitor. At the focused plane, a major and minor diameter can be directly measured for non-circular objects. The volume

is then computed by assuming an ellipsoidal shape with the length of the third axis taken as the geometric mean of the two measured values, or, in cases of long thin objects, by assuming a cylindrical shape. The radius of a sphere of equal volume is then calculated. The resolution is approximately 5 μm.

Discrimination of bubbles from solid particulates is made by visual examination of the magnified image. A sharply defined circular outline and overall uniform high image intensity suggest that an object may be a bubble, but these criteria are insufficient to ensure that spherical particles will not be counted as bubbles. Positive bubble identification requires a careful examination of the scattered light field caused by the object. An air bubble in water has an index of refraction less than that of the surrounding medium, thus acting as a diverging lens to spread plane incident rays in the forward direction, as demonstrated in Figure I.3.3, which also displays one of the internally reflected rays in the bubble. Some of the incident light is reflected at the bubble surface, but a considerable portion is refracted at the surface and projects through the bubble, the bubble in effect acting as a highly aberrated lens (van de Hulst 1981; Prikryl & Vest 1982). Peterson (1972) shows analytically that the holographic image of a bubble can be distinguished from an opaque spherical particle by the presence of a "hot spot" or bright central spot in the slightly unfocused bubble image; due to the virtual light source which comes into focus when the bubble image is just out of focus. The refractive properties of a bubble also cause an internal interference pattern within the bubble outline. Godefroy et al. (1981) include several photographs of reconstructed bubble images clearly showing both the virtual source image and the internal interference pattern for bubbles of various radii. When the in-line holographic technique is used, the image of the virtual source appears dark since, as discussed in Chapter I.2, the holographic image is a "negative." Langley (1984) developed a physical optics approach to model bubble light scattering, and found that the primary forward scattering mechanism was pure scattering, with a secondary component due to the "glory"

rays refracted so as to project out of the bubble parallel to the optic axis. This model also correctly predicts the shape of the interference ring pattern, and several photographs are shown to verify this. The features of a central bright spot and internal interference pattern are not present in images of opaque spherical particles and thus can be used to determine object type. As a practical matter, it becomes difficult to identify these features in small bubbles (less than about 25 μm radius), and cannot be done for the smallest visible objects, so no attempt could be made to establish the nature of nuclei with radii smaller than 10 μm. In this size range bubbles, particles and organisms had to be generically classified together.

Reconstruction was generally done by a team of two operators, one carefully controlling the hologram and camera position in order to define a precise sample volume, and the other making the actual measurements and counts from the images on the closed circuit monitor. These two tasks were frequently swapped in order to avoid fatigue. When any question arose as to the acceptability of a nucleus image, or when the two operators could not agree on its admissibility, it was not counted, so the present results must be considered as minimum values. Repeated examinations of the same hologram by different operators have shown no significant variation in nuclei measurements due to operator judgment.

The statistical error in a counting process is a function of the total number counted, so a high number count is desirable in order to minimize this error. However, the desire for large number counts had to be balanced by the considerable time involved in the process of measuring and counting reconstructed images. Typical volumes examined for nuclei depended on concentration and on the size range of interest, with the intent that several hundred particles (although significantly fewer bubbles) would be counted in each size range. The total recorded volume of each hologram was about 800 cm^3. For objects with radii less than 10 μm about 0.2 cm^3 were typically examined, about 1.5 cm^3 for objects in the 10 to 25 μm radius range, and about 120 cm^3 for objects with

radii larger than 25 μm. The exact volumes examined and the particle count statistics for each hologram will be given in Chapter I.4.

Nuclei populations are commonly expressed in terms of the nuclei number concentration density distribution function:

$$n(R) = \frac{dN}{dR} \simeq \frac{\Delta N}{\Delta R} \tag{I.3.1}$$

where $N(R)$ is the concentration of nuclei with radius smaller than R, and ΔN is the observed concentration of particles with radius in the range ΔR containing the nominal radius R. From this definition it follows that the total concentration of particles in the liquid is:

$$N_{tot} = \int_0^{+\infty} n(R)\, dR \tag{I.3.2}$$

The typical method of determination of $n(R)$ from a list of measured nuclei radius values is to divide the total radius range spanned into a series of radius class intervals or "bins," thus assigning each measured value to a particular bin, and to assign a nominal radius $\overline{R}$ to each bin. The nominal value $\overline{R}$ is usually taken as the arithmetic or geometric mean of the bin end points, or can be determined using a weighting factor based on the distribution shape to find a more representative value. The number density distribution function $n(\overline{R})$ is then given by:

$$n(\overline{R}) = \frac{\text{Total number of objects counted in the radius range } R_1 \text{ to } R_2}{R_2 - R_1}$$

where R_1 and R_2 are, respectively, the small and large radius endpoints of the classification range. The data are usually then presented as $n(\overline{R})$ as a function of R, where the computed values of $n(R)$ are plotted at the point corresponding to $\overline{R}$ on the abscissa, as if each measured value that fell into that radius classification actually had a measured radius of $\overline{R}$. As a practical matter, the class intervals are typically unequal in radius span, since a typical

nuclei distribution is composed of a large number of small objects and very few large ones. This makes selection of the value of $\overline{R}$ very important in the larger radius classifications, whereas for a small radius range (say 5 μm), the selection of a representative $\overline{R}$ for the bin has essentially no effect on the shape of the distribution. However, in both of these cases (few counts in a large radius bin because of the sparsity of nuclei, or few counts in a small radius bin due to cutoff), the relative error can be quite high. This classification technique was used to produce Figure I.1.1, and will be used for some of the present data analysis to be presented in Chapter I.4.

In many of the present examinations the nuclei number density distribution $n(\overline{R})$ is determined in a slightly different manner (as suggested by L. d'Agostino, 1986, private communication) by grouping together adjacent radii counts until a predetermined number of counts N_g is reached. This value is then divided by the corresponding radius range and sampled volume, V_s. Thus, if the nuclei radii are ordered by decreasing size and R_j is the maximum radius of the group:

$$n(\overline{R}) \simeq \frac{N_g}{V_s(R_j - R_{j+N_g})} \tag{I.3.3}$$

The statistical error associated with this procedure is uniform and depends only on the size of the groups, N_g. Assuming that the occurrence of nuclei in the liquid sample volume is a Poisson process, as it should be if the nuclei are spatially uncorrelated, the best estimate of the relative r.m.s. error in the computation of the number concentration density distribution is equal to the reciprocal of the square root of the group size, $[N_g]^{-1/2}$ (see, for example, Herdan 1960). The nominal radius $\overline{R}$ of each group is defined as the geometric mean of the minimum and maximum values of the radii of the group. Figure I.3.4 gives an example of the effect of group size on the distribution, that is, the change of the distribution as the expected statistical error is varied. Two values of the group size are chosen for this comparison, $N_g = 2$ (expected statistical error of about 70%) and $N_g = 10$ (expected statistical error of about 32%). The smaller

grouping size obviously gives an increased number of data points, and for the data plotted (from one of the ocean particle measurements) the shape of the distribution is not significantly affected by choice of N_g, except in the higher radius range where data are sparse. These results are representative of a large number of similar comparisons. The grouping procedure differs slightly from the more common way of computing the number concentration distribution density based on the number of counts observed in each prefixed size interval subdividing the size range. First, it assures that the statistical error due to the finite number of counts of the sampled population is uniform for all the computed data points. Furthermore, by adjusting the size interval to the occurrence of the observed data, it avoids the upward bias that occurs when sparse data are assigned to fixed size intervals and zero counts are neglected, instead of being averaged with the neighboring ones over a wider size range. Finally, it preserves the information on the relative density of the distribution of the available data as a function of size, which would otherwise be lost. Figure I.3.5 shows the same set of data reduced according to these two techniques, providing a direct comparison between them for a set of "real" data. It is clear that the difference between the two techniques is significant only for the large radius values.

The "grouping" rather than the "size classification" technique was used in those cases where a considerable number of data were available. This technique was not used for the bubble data, since few counts were obtained and the grouping size N_g therefore became a significant factor. The expected error in the $n(R)$ determinations will be included in Chapter I.4.

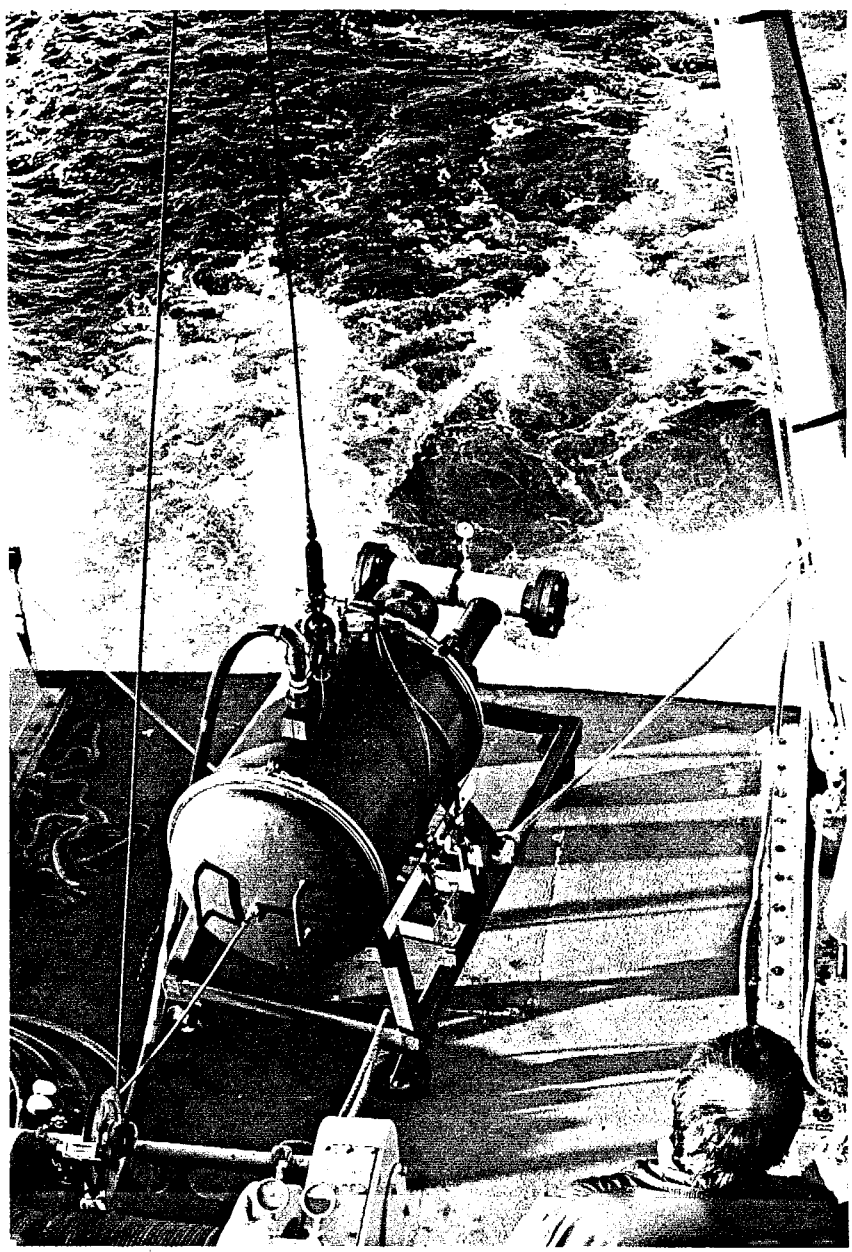

Figure I.3.1. Photograph of the holographic submersible tank on board the *R/V Seawatch* during transport.

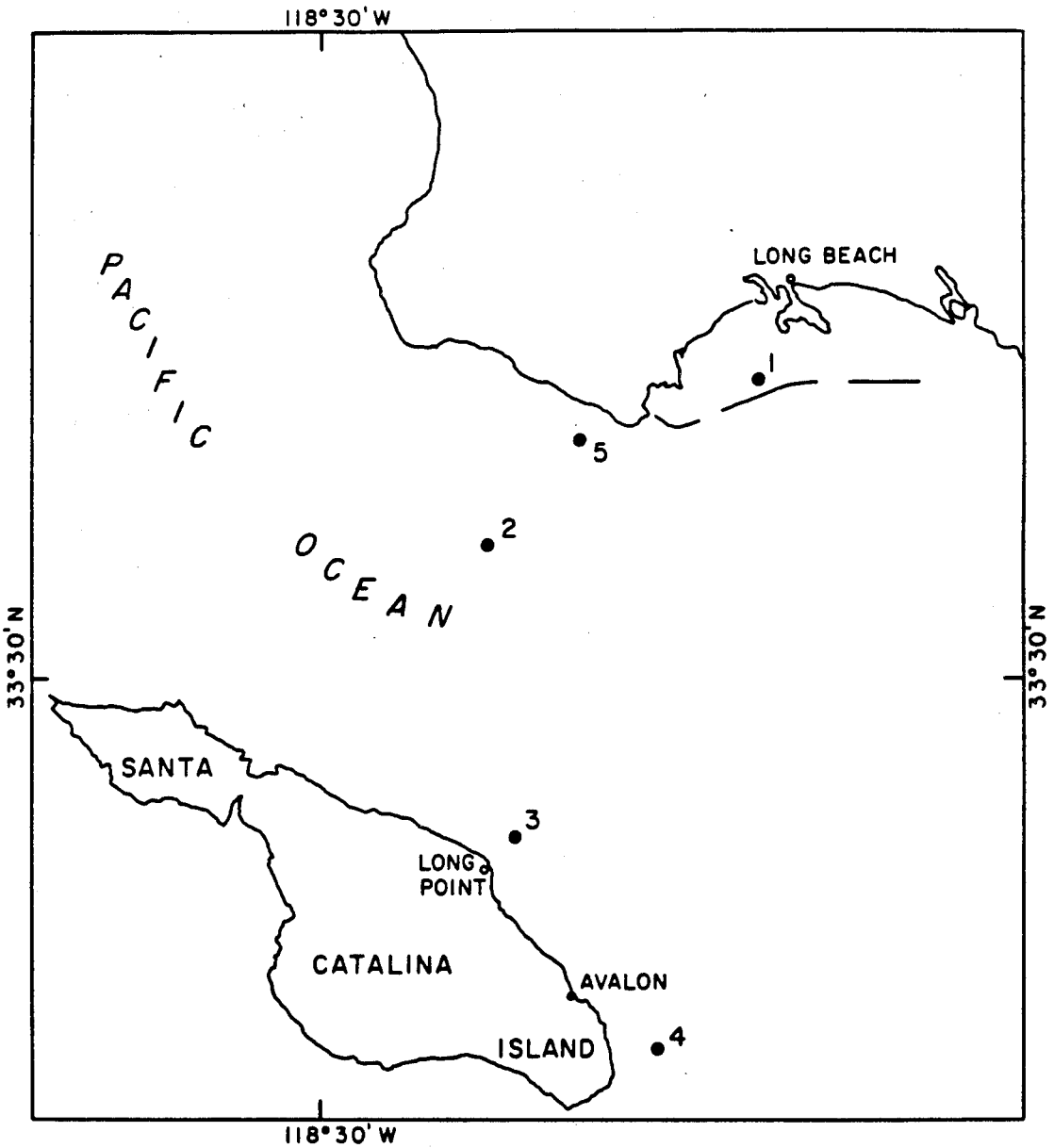

Figure I.3.2. Map of the Los Angeles coastal area indicating the holographic test sites. Details of the location and test conditions for stations 3, 4 and 5 are given in Table I.3.1.

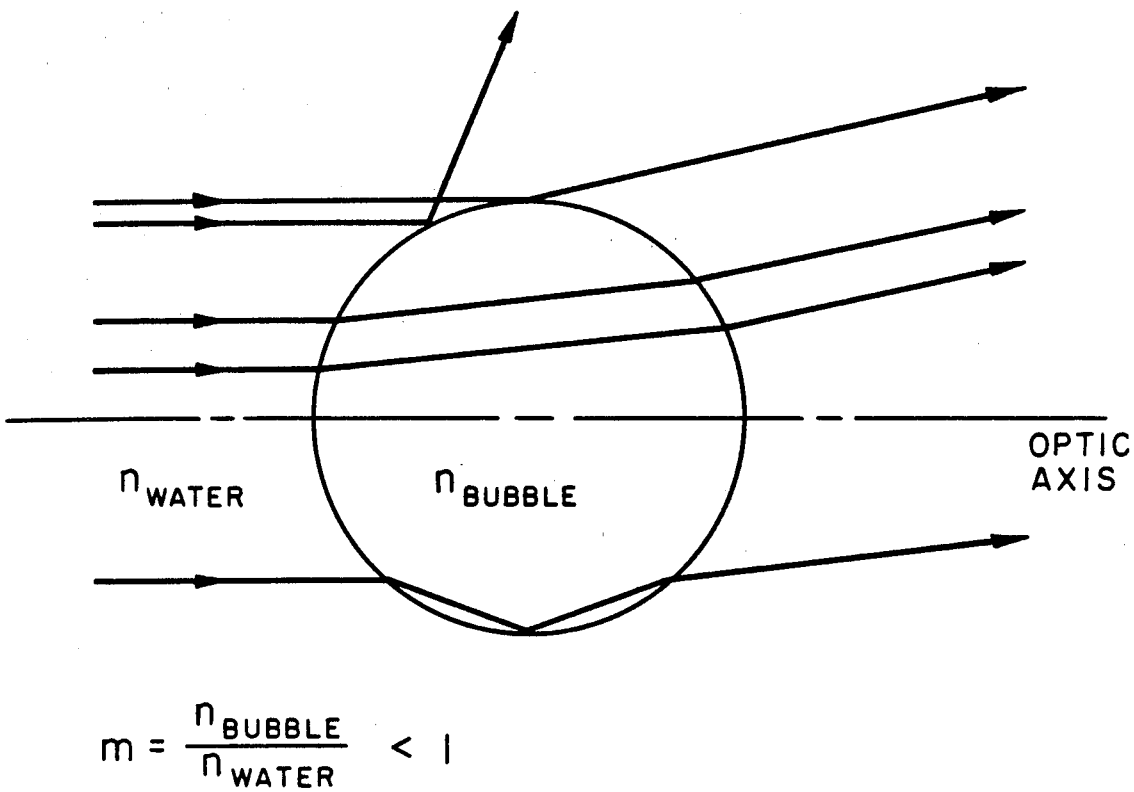

Figure I.3.3. Schematic of the reflection and refraction of light incident on an air bubble in water.

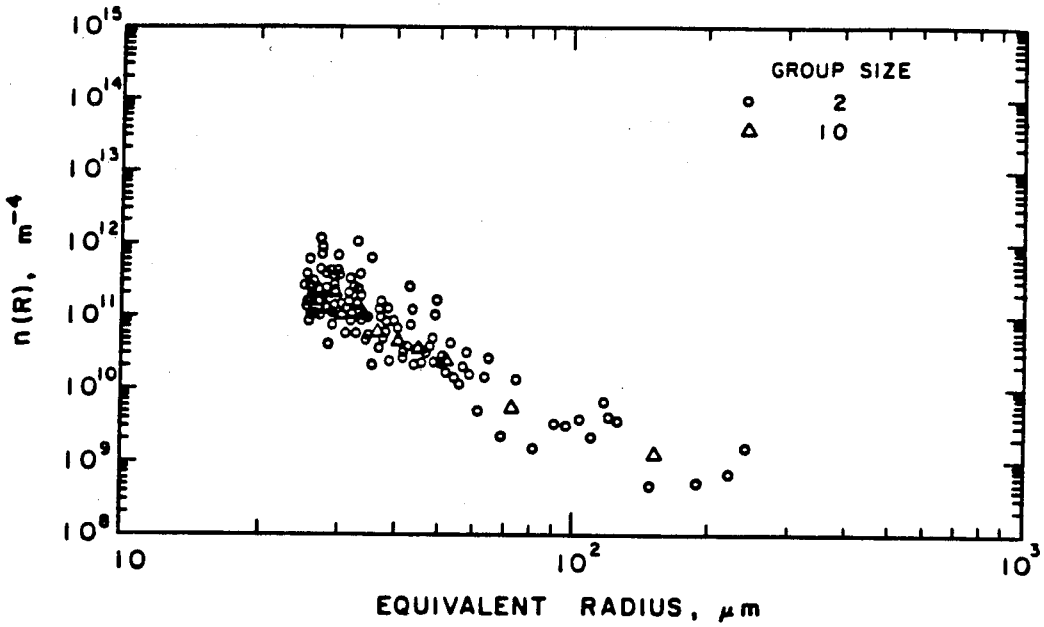

Figure I.3.4. Effect of group size N_g on the number density distribution function $n(R)$. Circles denote data points calculated with N_g=2, yielding an expected r.m.s. error in computation of $n(R)$ of 70%. Triangles indicate N_g=10, for a standard error of 32%.

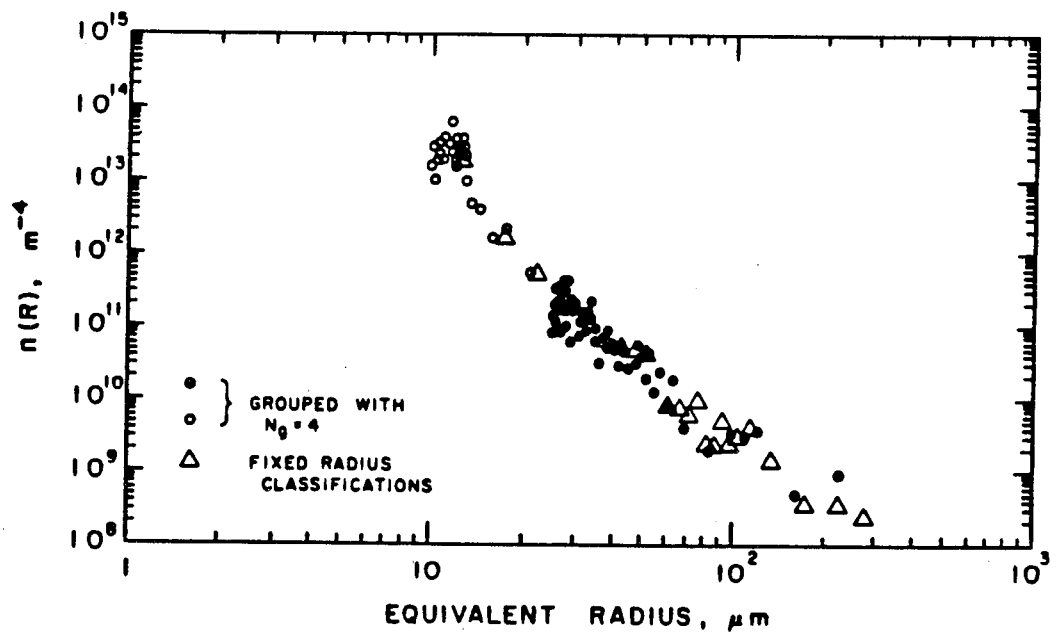

Figure I.3.5. Comparison of two techniques for determination of the number density distribution function $n(R)$. Triangles indicate $n(R)$ determined using fixed size interval "bins," circles indicate grouping of adjacent counts with group size N_g=4.

Ocean Holographic Test Stations			
Station	3	4	5
Date	8/24/85 (A)	8/24/85 (B)	8/27/85
Site	off Long Point, Catalina Island	off East Catalina Island	L.A. County Whites Point Sewage Outfall
Longitude	33°24'48"	33°18'30"	33°41'30"
Latitude	118°21'48"	118°17'16"	118°18'54"
Wind	calm	calm	calm
Visibility (Secchi Disk)	17m	19m	9.14m
Sea State	0–1	0–1	0–1
Waves (m)	0–1	0–1	flat
Bottom Depth (m)	132–228	93	55
Hologram Depths (m)	3 6 15 23 30 32	27 32	1 3 6 12 15 21 27 34

Table I.3.1. Conditions and test depths at holographic test Stations 3, 4 and 5.

CHAPTER I.4
RESULTS

These experiments produced the first ever pulsed holograms recorded in the sea. This chapter will describe the quantitative results of analysis of reconstructed holographic images. A full discussion of these results will be made in Chapter I.5.

In terms of cavitation inception, the most important nuclei are the largest ones, which generally have smaller critical tensions and whose effects therefore dominate those of smaller, less susceptible nuclei, at least in the case of bubble nuclei as shown in Equation I.1.7. For this reason the results here are for nuclei of relatively large radius (more than about 2 μm), unlike many previous investigations of particulate content of the ocean, which used optical or electrical detection techniques to examine the submicron particulates important for optical characteristics of the water.

I.4.1 Bubble Concentrations

Bubbles are known to be primary cavitation nuclei, and the critical tension required for bubble instability and growth is well known on both theoretical and experimental grounds. Therefore, the bubble concentrations in ocean waters are of special importance, and so were measured at all of the ocean test sites. Figure I.4.1 presents images of three bubbles of different radii recorded during these examinations.

As discussed in Chapter I.3, no attempt was made to determine the nature of small particles and bubbles with radii less than 10 μm because of the limitations of the holographic recording and reconstruction processes. However, most of

these small objects are assumed to be particles, and their concentration will therefore be listed along with the particle data. In all of the data plots these objects will be indicated by a different symbol than either the bubble or the solid particle data points.

Few data were gathered in the first series of ocean tests at Stations 1 and 2 (see Chapter I.3 for a full description of the stations). Failure of the Pockels cell Q-switch led to intermittent laser performance, and hence to an extremely limited number of holograms containing significant reconstructable volumes. The results presented here are based on detailed examination of just three holograms, one recorded at Station 1 inside Los Angeles harbor at 5.2 m submergence depth, and the others recorded at Station 2 in the open water of the San Pedro Channel at 3 m depth. The second hologram recorded at this site was examined only for objects with radii above 25 μm. Figure I.4.2 plots the number density distribution function $n(R)$ as a function of radius R for bubbles detected in these three holograms. The $n(R)$ determination for these cases was done using fairly large fixed size classification intervals rather than grouping together adjacent counts as discussed in Chapter I.3. Tables I.4.1 (a) and (b) show the size intervals, measured concentrations and counted volume for the various nuclei size ranges examined in these holograms. The largest bubble observed in these holograms was in the San Pedro Channel at 3 m submergence, with a radius of 48 μm. The hologram containing this large bubble was not examined for smaller bubbles, and all bubbles seen in the other two holograms had radii in the 10 to 25 μm range.

The second series of open ocean tests was made with full oceanographic data support. Figure I.4.3 presents the temperature and transmissivity data for the two test sites near Santa Catalina Island: Station 3 off Long Point and Station 4 off the East end of the island, and for Station 5 above the Whites Point sewage outfall. Each temperature profile includes the thermocline, or layer of steep temperature gradient, at each test station.

Figure I.4.4 shows $n(R)$ plotted as a function of radius R for bubbles observed in the six holograms examined from Station 3 off of Long Point, Santa Catalina Island. Sparse data counts led to fairly high expected error for these cases, and due to the limited number of data counts the number density distribution function was determined using fixed size intervals instead of grouping adjacent counts. The measured bubble concentrations in discrete size intervals are listed in Tables I.4.2 (a) and (b), which also give the size classification ranges and size of the volume examined in each of these holograms. Only two bubbles with radii above 25 μm were observed, both in holograms recorded below the thermocline. The largest bubble observed had a radius of 50 μm and was recorded at 23 m submergence, and a 28 μm radius bubble was seen in the reconstructed image from 32 m submergence. The remainder of the bubbles observed in the six holograms at this site had radii in the 10 to 25 μm range. Figure I.4.5 shows the concentration of bubbles in the 10 to 25 μm radius range as a function of depth. The bubble distribution in seawater is expected to follow a Poisson distribution, so the expected standard error, or fractional uncertainty, in an observation of N events is equal to $1/\sqrt{N}$ (Herdan 1960; Taylor 1982). Therefore, the single bubble observations commonly made in the radius ranges above 25 μm (see Table I.4.2 (a)) have an expected standard error of 100%, while the average count of 7 bubbles per hologram in the 10 to 25 μm range have an expected error of about 37%.

Figure I.4.6 is a plot of $n(R)$ as a function of radius R for bubbles observed in the two holograms examined from Station 4, the test site off Eastern Santa Catalina Island. As at Station 3, the bubble data counts were sparse, leading to a high expected statistical error for these cases, and a size classification technique was used in determining the number density distribution function. Tables I.4.3 (a) and (b) give the size classifications, measured bubble concentrations and size of the examined volume for these holograms. Both holograms were recorded below the thermocline. The largest bubble observed at Station 4 was at 32 m

submergence with a radius of 45 μm (100% expected error), and three bubbles with radii in the range of 25 to 30 μm (58% expected error) were also seen at this depth. The remaining 4 bubbles seen in the two holograms at this site had radii in the 10 to 25 μm range, giving an expected standard error for these measurements of about 70%.

Figure I.4.3 (c) presents the temperature and transmissivity data for the test site at the Whites Point sewage outfall (Station 5). A higher concentration of large bubbles was observed at this site and the largest bubble observed was in the hologram recorded closest to the surface, at 1 m submergence, with a 40 μm radius. The number density distribution was determined using the same size classifications as for Stations 3 and 4, and is presented in Figure I.4.7. The concentration of small bubbles in the 10 to 25 μm radius range at this station is plotted as a function of depth in Figure I.4.8. The size classification ranges, measured concentrations and sizes of volumes examined in each hologram at this site are given in Tables I.4.4 (a) and (b). The expected standard error for bubbles in the 10 to 25 μm radius range is about 46%, and for larger bubbles where single observations were generally made is approximately 87%.

If the tensile strength is defined simply as the critical tension required for instability of the weakest nucleus, then the critical tension of the waters examined in these tests can be estimated by using the radius of the largest bubble observed as the equilibrium radius R_{eq} in the equation of bubble critical tension, Equation I.1.7, with p_∞ taken as the local hydrostatic pressure at the bubble depth. This has been done for each test station and depth, and the results plotted in Figure I.4.9. The sparse bubble counts are insufficient to determine a statistically significant value of the tensile strength for each water sample, but several important general points can be made. The largest single bubble observed was at 23 m submergence at Station 3 and had a radius of 50 μm, so Equation I.1.7 indicates that this water would be expected to cavitate at least occasionally under an applied tension of about 100 Pa. The bubble data figures

and tables presented above show that all of the waters examined contained some bubbles with radii larger than 10 μm, so Equation I.1.7 shows that an applied tension of about 2000 Pa should be sufficient to initiate cavitation in each case.

Upon completion of the bubble analyses presented above, a concern was raised (R. E. Pieper, 1986, private communication) as to whether some of the bubbles observed in the holographic images may have, in fact, been spherical zooplankton eggs. As discussed in Chapter I.3 the images of bubbles and opaque spherical particles appear substantially different, since the bubble refracts light internally to create a virtual source image and refraction ring pattern visible in the reconstructed image, unlike an opaque solid particle. However, interpretation is not so clear for the case of a translucent egg. In theory, the light scattering properties of an egg and a bubble should be distinctly different, since the index of refraction n of an air bubble is less than that of water, while the opposite is expected to hold for eggs. This should cause an egg to act as a positive lens, focusing the incident light to a point, unlike the bubble, which spreads light as a negative lens as discussed in Chapter I.3 and shown in Figure I.3.3. In order to experimentally determine whether this difference in scattering was sufficient to distinguish bubbles from eggs, holograms were recorded of samples of seawater containing living copepods and their eggs. The concentration of copepods as well as eggs in the original samples was quite high, so they were diluted with filtered sea water, then transferred to a glass sample cell for holography. The transfer was done very carefully so as to avoid bubble entrainment or generation in the process. Holograms were also recorded of aqueous solutions containing low concentrations of polystyrene spheres of known size as models of expected egg behavior with known refractive index (polystyrene has refractive index $n \simeq 1.6$, pure water $n \simeq 1.3$ and air $n = 1.0$). Several of the copepod eggs were examined with a light microscope as well.

The mean radius of the eggs examined was 70 μm. In general, the images of eggs presented a somewhat elliptical outline rather than the purely circular

outline of bubbles; however, there were numerous exceptions to this observation. In addition, the focused images of eggs showed a rather inhomogeneous internal organization, quite unlike the uniformly bright appearance of bubble images. However, in terms of the light scattering properties critical for bubble identification, many of the copepod egg and polystyrene sphere images appeared similar to those of bubbles. Samples of some of the reconstructed holographic images demonstrating this are given in Figure I.4.10. Photographs (a) and (b) of this figure show, respectively, the focused and slightly defocused images of a 125 μm radius air bubble in tap water, (c) and (d) show the focused and unfocused images of a 50 μm radius egg in sea water, and (e) and (f) show the focused and unfocused images of a 50 μm radius polystyrene sphere in tap water. The hologram containing images (c) and (d) can be seen to contain a fairly high background optical noise due to interference of the high concentration of copepods, eggs and feces with the in-line reference beam, but this did not affect interpretation of the egg images. Several holograms were recorded of a further diluted batch of copepods and eggs, with no substantial difference in the appearance of the egg images. The key points of Figure I.4.10 are that both the egg and polystyrene sphere images appear fairly circular when focused and indicate the presence of some sort of dark central spot when slightly unfocused, very similar to the virtual source image used as one of the determining characteristics of a bubble image. However, in most cases this spot was not centered within the egg image (see Figure I.4.10 (b)), probably due to inhomogeneity of the egg contents. In addition, neither the egg nor the polystyrene sphere images showed evidence of a clear internal ring pattern, although one may be expected since these two objects do act to refract the light incident on them.

It was concluded that in general bubbles *can* be distinguished from eggs by the symmetry of their virtual source image and internal refractive rings, although there is significant potential for error in this determination. In addition, the typical size range of marine organism eggs seems to be unknown, though

generally they seem to have radii greater than 50 μm.

The light microscope study of copepod eggs was quite informative as well, showing an unexpectedly strong specular reflection from the egg surface, and a slightly blue tinged translucent appearance to the egg itself. The microscopic examination verified the holographic observation that most of the eggs were somewhat elliptical. In some cases the eggs clearly contained an inhomogeneous mass of objects, possibly indicating a further stage of development of the egg contents.

The results of this investigation led to reanalysis of all bubble images in the ocean holograms, and several borderline images that could not confidently be classified as bubbles were dropped from the bubble counts and added to the particle counts. Each remaining bubble image reported here has been checked several times, and it is felt that they all represent actual bubbles. It should be pointed out that a significant number of circular images were observed that were never considered as bubbles because they did not meet the requirements of the presence of a virtual source image and clear internal interference rings.

I.4.2 Particle Concentrations

Microparticulates and organisms greatly outnumber bubbles over all size ranges and depths in all of the ocean waters examined. The potential importance of these objects as cavitation nuclei was discussed in Chapter I.1. For most of the results presented in this section, the term "particle" will be used to indicate all non-bubble matter, including sediments, detritus, and living organisms. During analysis of the reconstructed holographic images, attempts were made to classify the larger non-bubble objects (maximum measured dimension above 25 μm) as either solid particles or biological organisms. This process was somewhat arbitrary and consisted primarily of examining each object for such distinguishing features as legs or antennae indicative of an "organism." The rel-

ative composition of "organisms" in the total particulate distribution at some of the test sites will be discussed below. The data for objects with equivalent radii less than 10 μm are also included in this section, since most of these objects are expected to be particles rather than bubbles, as in all other size ranges.

Examples of some of the images seen in this analysis are presented in Figure I.4.11. Each photograph is of the reconstruction monitor screen showing the focused image of interest. The recording station and depth, and object magnification and tentative identification are given in the figure caption. Figure I.4.11 (a) shows a generic particle, and the other images are all of organisms. A more complete collection of reconstructed holographic images is presented as Appendix III.

Figure I.4.12 presents particle data from the three holograms examined at Stations 1 and 2, expressed in terms of the number density distribution function $n(R)$. These data are also tabulated in Table I.4.5. The second hologram at Station 2 was examined only for larger particles (radius $\geq 25\mu m$). The "diameter" in these results is defined as the maximum length of the object, and the "radius" is simply one-half of this value. This definition differs from that used for the data of Stations 3, 4 and 5, so the two sets of results cannot be directly compared. In addition, the particle $n(R)$ determination for Stations 1 and 2 was made using the fairly wide size classifications shown in Table I.4.5, while those of Stations 3, 4 and 5 were made using the grouping method. The bubble data from the previous section are also included on the present $n(R)$ plots to indicate the much higher concentration of particulate matter. The data points corresponding to objects with less than 10 μm radius are indicated by a triangle to indicate that no attempt was made to distinguish bubbles from particles in this range, so the results could include some bubble counts.

The reconstruction procedure given in Chapter I.3 was followed for the particle data of Stations 3, 4 and 5, recording a major and minor particle diameter and using these two lengths to calculate a volume. For long, thin objects (major

diameter greater than 3 times minor diameter) the volume was assumed to be that of a cylinder with a base of the minor diameter and a length of the major diameter. For all other objects the volume was assumed to be that of an ellipsoid with its third axis given by the geometric mean of the two measured lengths. A spherical equivalent radius was then computed from this volume and used in determination of the number density distribution function. The grouping method of producing the $n(R)$ plot was used for these particle examinations, with the group size N_g taken to be 4, which gives an expected sampling error of 50%. This method could not be used for the smallest objects, those with radii less than 10 μm, because their exact sizes were not recorded. These data points may include bubbles as well as particles, and in the $n(R)$ plots are indicated by a triangle symbol.

The particle data for the six depths examined at Station 3 are presented in Figure I.4.13 and Table I.4.6, and the particle data for the two depths examined at Station 4 are presented in Figure I.4.14 and Table I.4.7. For both stations the bubble data points presented in the previous section are included in order to demonstrate the much higher particle concentrations.

The total particle concentration for various depths at the two Catalina test sites (Stations 3 and 4) are presented in Figure I.4.15. Only objects with radii less than 10 μm and particles in the 10 to 50 μm equivalent radius range are shown (see Tables I.4.6 and I.4.7). Results are based on the analysis of six holograms from the Long Point site and two from off east Santa Catalina Island.

As part of the study of the particle content of the waters of Stations 3 and 4, water samples were collected with Nansen bottles and returned to the laboratory for Coulter Counter analysis. Detailed results and discussion of this study are presented in Appendix II.

The total particle concentrations for eight depths at Station 5 (above the sewage outfall at Whites Point) are presented in Figure I.4.16 and Table I.4.8. Again the bubble data points are included in order to demonstrate the much

higher concentration of particles. The total particle concentration as a function of depth for objects with radii less than 10 μm and for particles in the 10 to 50 μm radius range is presented in Figure I.4.17. The sharp increase in concentration for both size ranges correlates well with the decrease in transmissivity at a depth of roughly 25 m and indicates the edge of the plume of sewage particles. Note that the particle concentrations in the waters above the plume are similar to those found in the clean waters of the Long Point test site (Station 3) as shown in Figure I.4.15.

As mentioned at the beginning of this section, the "particle" examinations included attempts to classify each object as an organism or a solid sediment or detritus particle. Examples of the relative composition of the total particle concentration at two depths examined at Station 3 are given in Figures I.4.18 (a) and (b), which show that the relative concentration of organisms seemed to increase with depth from about 20% at 3 m submergence to over 50% at 30 m. The majority of organisms seen at all stations and depths were long, thin diatoms (phytoplankton) with average major and minor diameters roughly 60 and 15 μm, respectively, but sometimes reaching lengths up to 500 μm. It should be stressed that distinctions between "organisms" and "particles" were attempted only for objects with maximum measured lengths above 25 μm, and cannot be considered as much more than speculation since they were made by operators with no formal training in marine biology. These determinations were made conservatively and probably should be considered as a lower bound on the true percentage of organisms in the total particle count. The most commonly observed large and easily identifiable zooplankton type seen in the waters of the Catalina test sites (Stations 3 and 4) were the copepods (see Figure I.4.11 (c) and (d) and Appendix III). This is in agreement with the observations of Holliday & Pieper (1980) that "the size range 0.1 to 10 mm encompasses and is dominated by the copepods." In several of the holographic reconstructions the total number of copepods of all sizes and species were recorded. For example, at

Station 4 off East Catalina, five very clear adult copepod images were observed, along with at least two immature (nauplius) stages, in the 45 cm^3 examined in the hologram recorded at 27.4 m submergence (Figure I.4.14 (a)), yielding an adult copepod concentration on the order of $10^5/m^3$. Similar copepod concentrations were found in the other deep water holograms of Stations 3 and 4. This concentration is comparable to that given by Holliday & Pieper (1980), who state that copepods are often found in concentrations greater than $5 \times 10^4/m^3$ in biologically productive areas.

As mentioned above, another common identifiable organism type was the diatom, sometimes seen in concentrations up to about $4 \times 10^6/m^3$. Several examples of these are shown in Appendix III. At several test sites a fairly high number of coiled organisms were seen (see Figure I.4.11 (f) and Appendix III); for example, five of these "springs" were seen in the 170 cm^3 sample recorded at 30 m submergence at Station 3 off Long Point, Santa Catalina Island. Identification of these organisms is difficult, as they had not been observed previously in these waters (R.E. Pieper, 1986, private communication). They have tentatively been identified as *Chaetoceros* diatoms.

A full discussion of the present results, comparison with previous investigations and implications in terms of cavitation inception in the sea will be given in the next chapter.

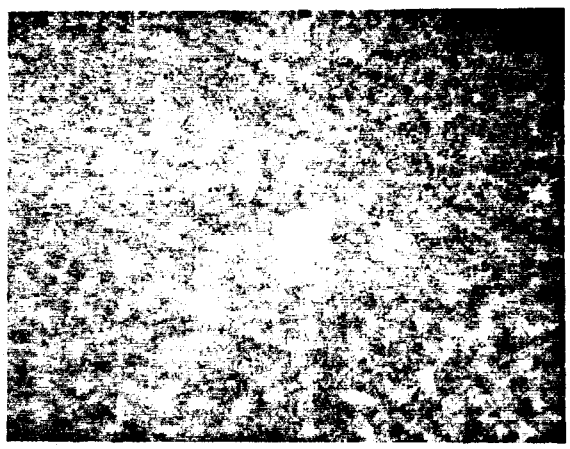

(a)

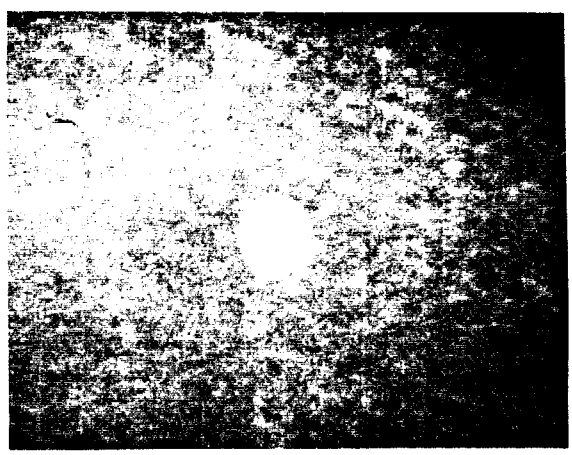

(b)

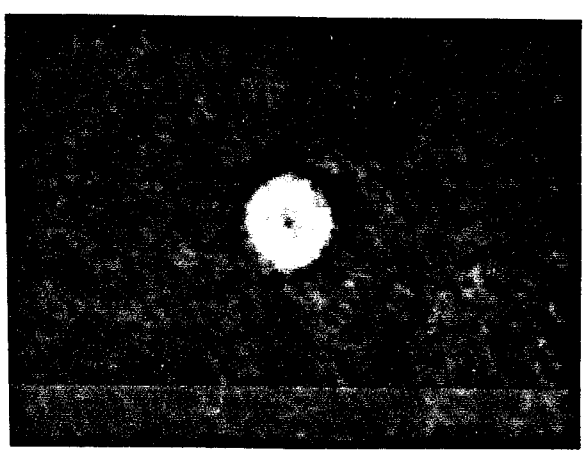

(c)

Figure I.4.1. Reconstructed holographic bubble images.
(a), (b) 22 μm and 30 μm radius bubbles, respectively, Station 5, 3 m.
(c) 45 μm radius, recorded at 32 m submergence at Station 4.

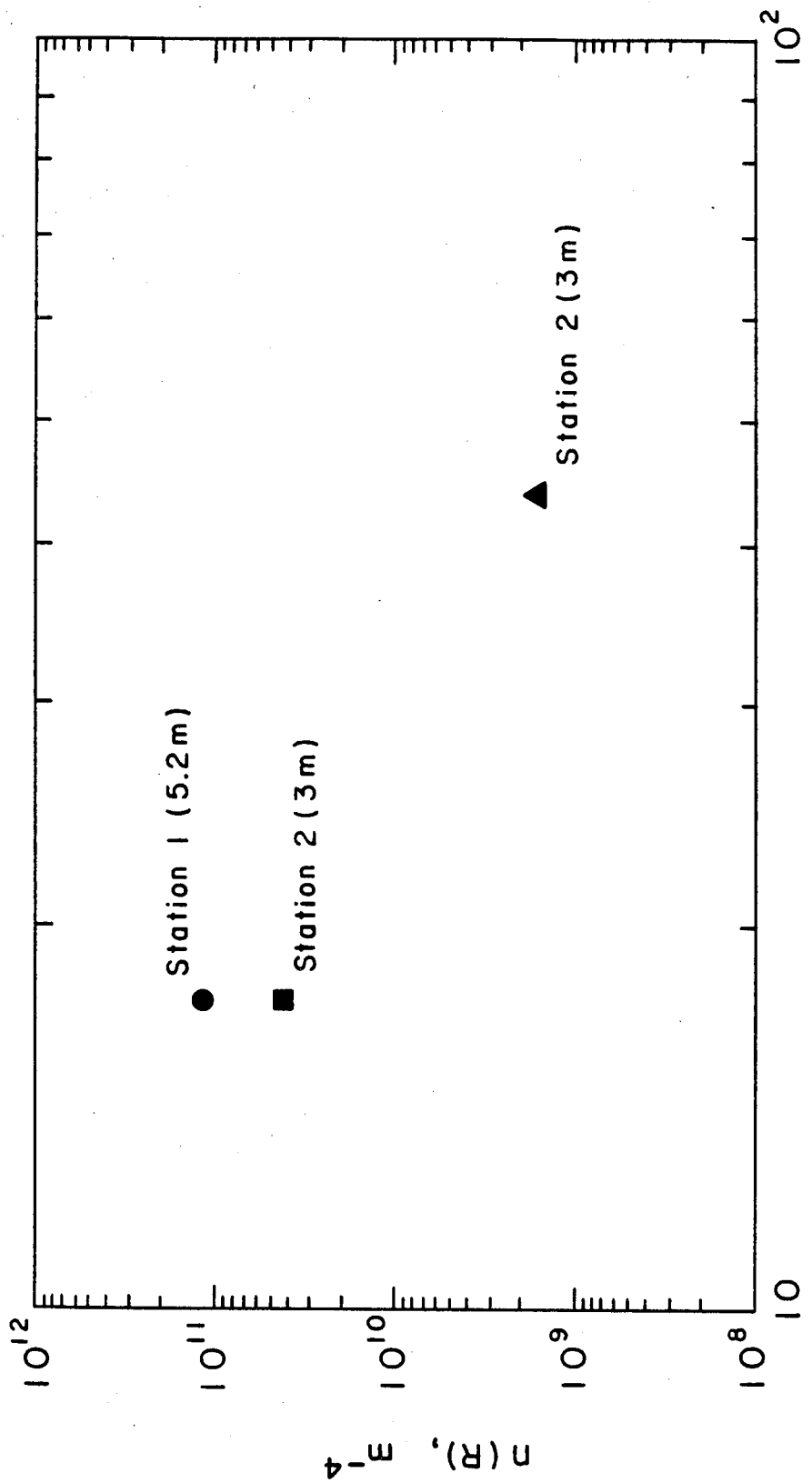

Figure I.4.2. Number density distribution function $n(R)$ as a function of bubble radius R for bubbles observed at Stations 1 and 2.

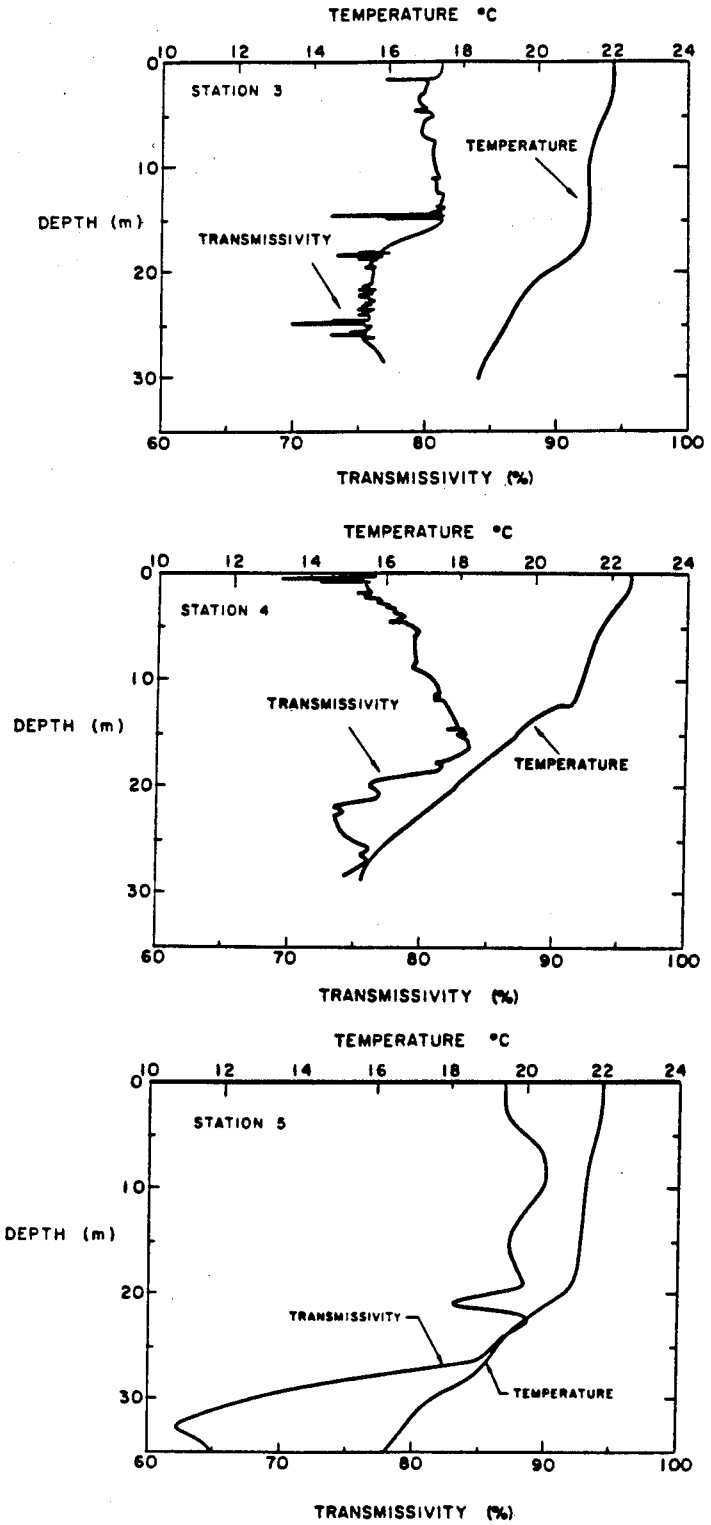

Figure I.4.3. Temperature and transmissivity profiles for the various test sites.
(a) Station 3 off Long Point, Santa Catalina Island
(b) Station 4 off east Santa Catalina Island
(c) Station 5 above the Whites Point sewage outfall.

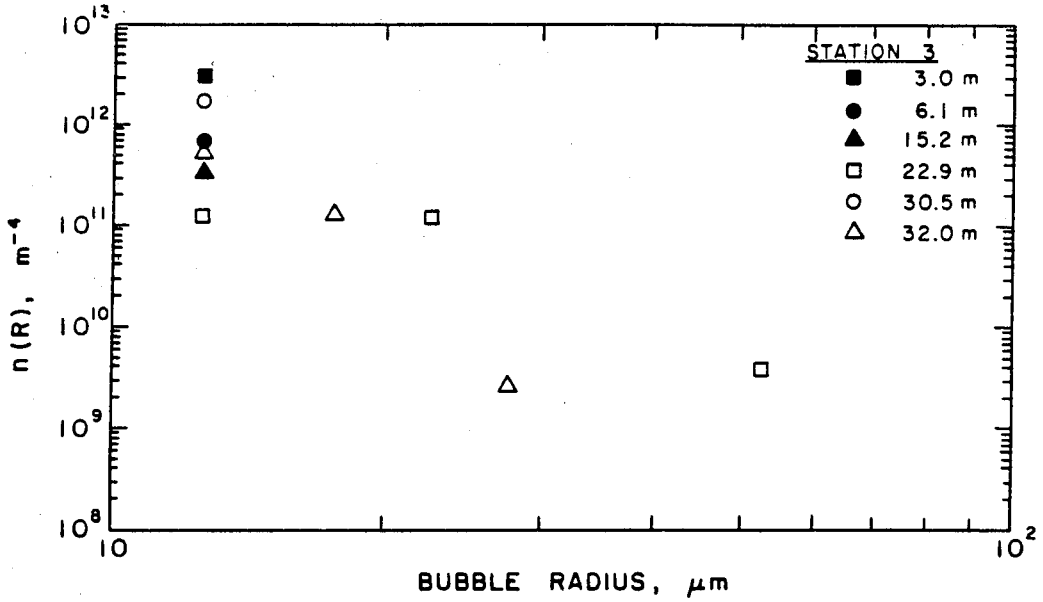

Figure I.4.4. Number density distribution function $n(R)$ as a function of bubble radius R for bubbles observed at Station 3.

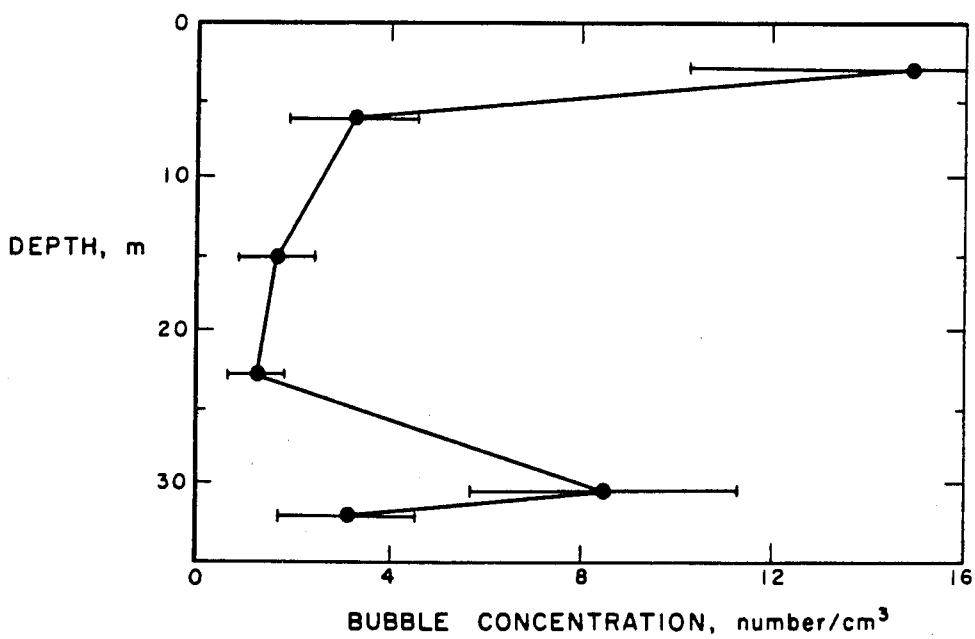

Figure I.4.5. Concentration of small bubbles (10 to 25 μm radius range) as a function of depth at Station 3. Error bars indicate the fractional uncertainty ($\pm 1/\sqrt{N}$) based on the limited number of bubbles observed.

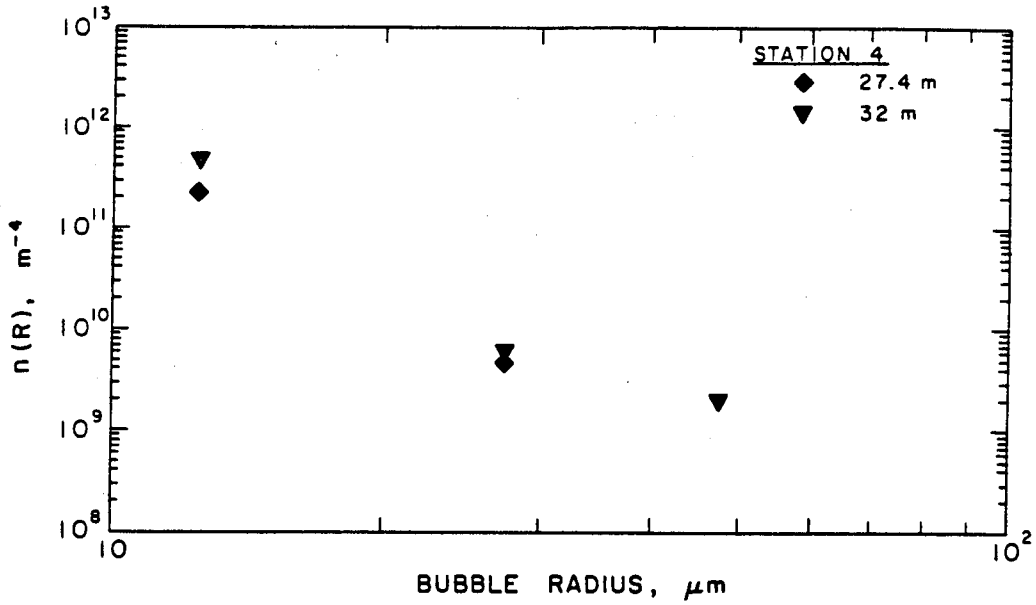

Figure I.4.6. Number density distribution function $n(R)$ as a function of bubble radius R for bubbles observed at Station 4.

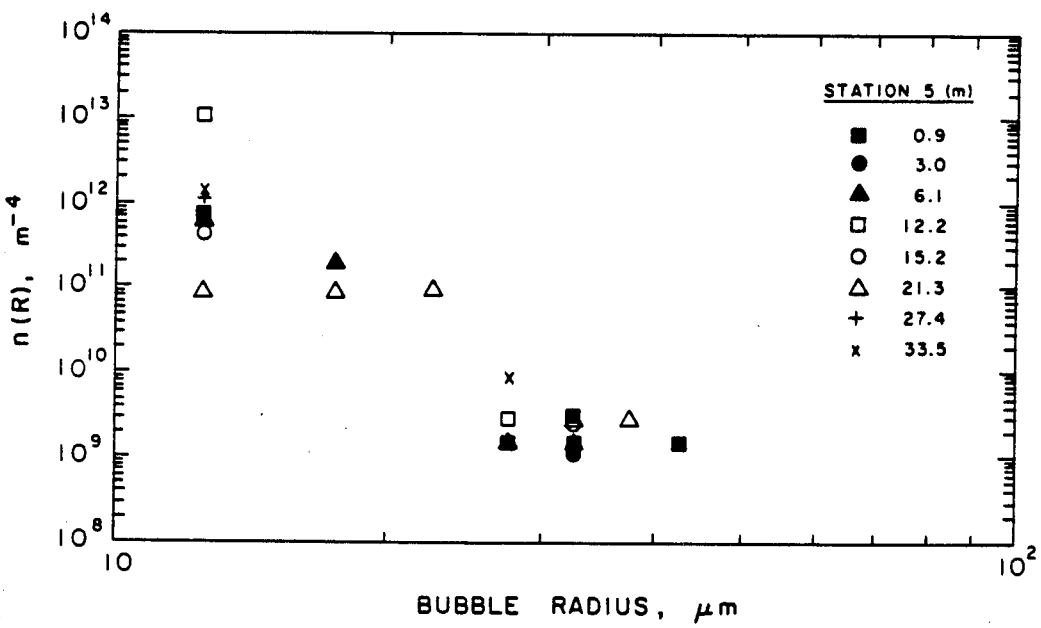

Figure I.4.7. Number density distribution function $n(R)$ as a function of bubble radius R for bubbles observed at Station 5.

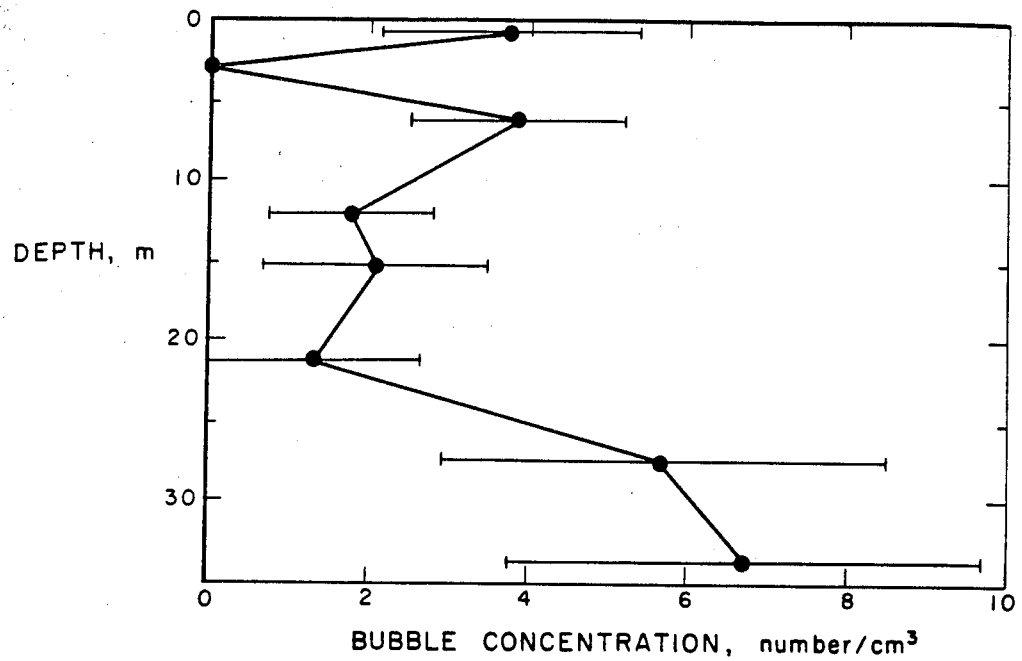

Figure I.4.8. Concentration of small bubbles (10 to 25 μm radius range) as a function of depth at Station 5. Error bars indicate the fractional uncertainty ($\pm 1/\sqrt{N}$) based on the limited number of bubbles observed.

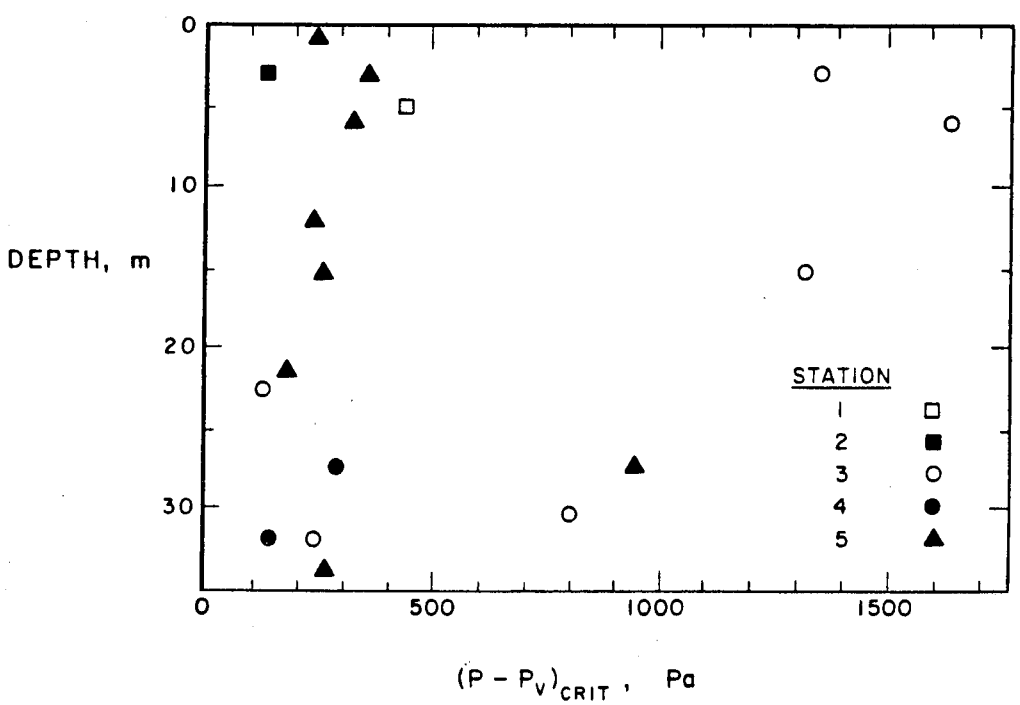

Figure I.4.9. Expected tensile strength of ocean waters based on largest bubbles observed at various Stations and depths, from Equation I.1.7.

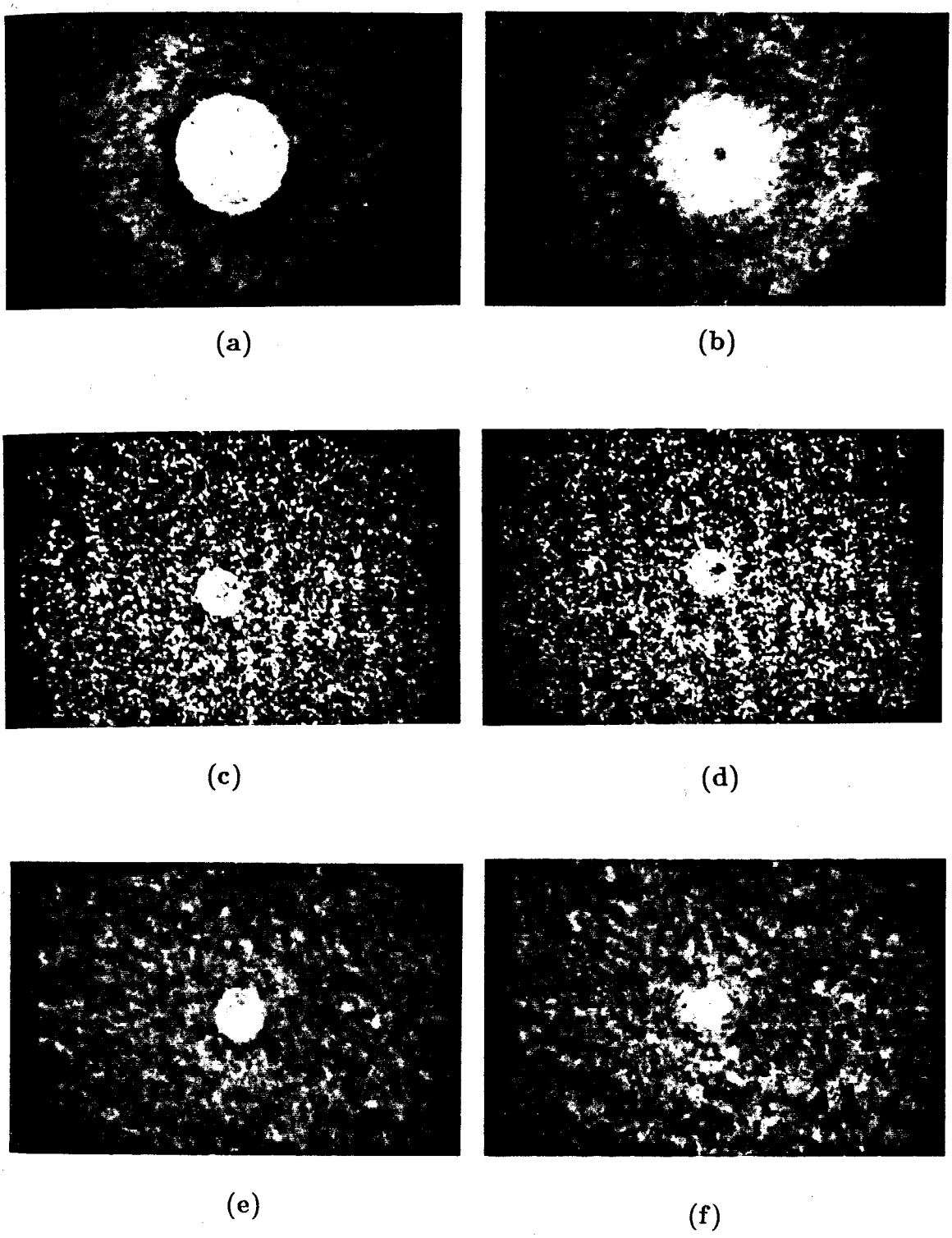

Figure I.4.10. Focused and slightly unfocused reconstructed images
(a), (b) 125 μm radius bubble in tap water;
(c), (d) 50 μm radius copepod egg in seawater;
(e), (f) 50 μm radius polystyrene sphere in tap water.

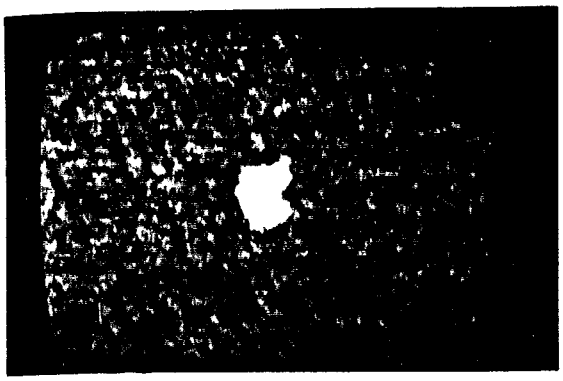

(a) Station 2, 3 *m*. 1/2 inch = 150 μm. Generic particle.

(b) Station 3, 30 *m*. 1/2 inch = 150 μm. *Chaetoceros* diatom.

(c) Station 4, 32 *m*. 1/2 inch = 150 μm. Copepod.

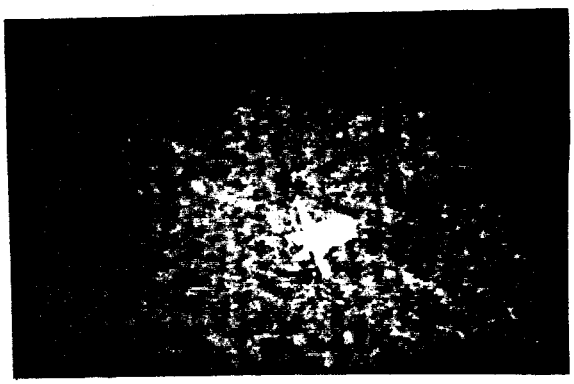

(d) Station 5, 6 *m*. 1/2 inch = 150 μm. Nauplius (immature stage) of copepod.

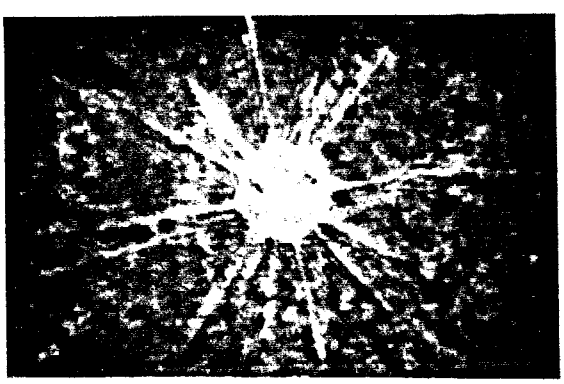

(e) Station 5, 12 *m*. 1/2 inch = 150 μm. Radiolarian.

(f) Station 5, 3 *m*. 1/2 inch = 150 μm. Dinoflagellate *Ceratium*.

Figure I.4.11. Reconstructed "particle" images from various stations and depths.

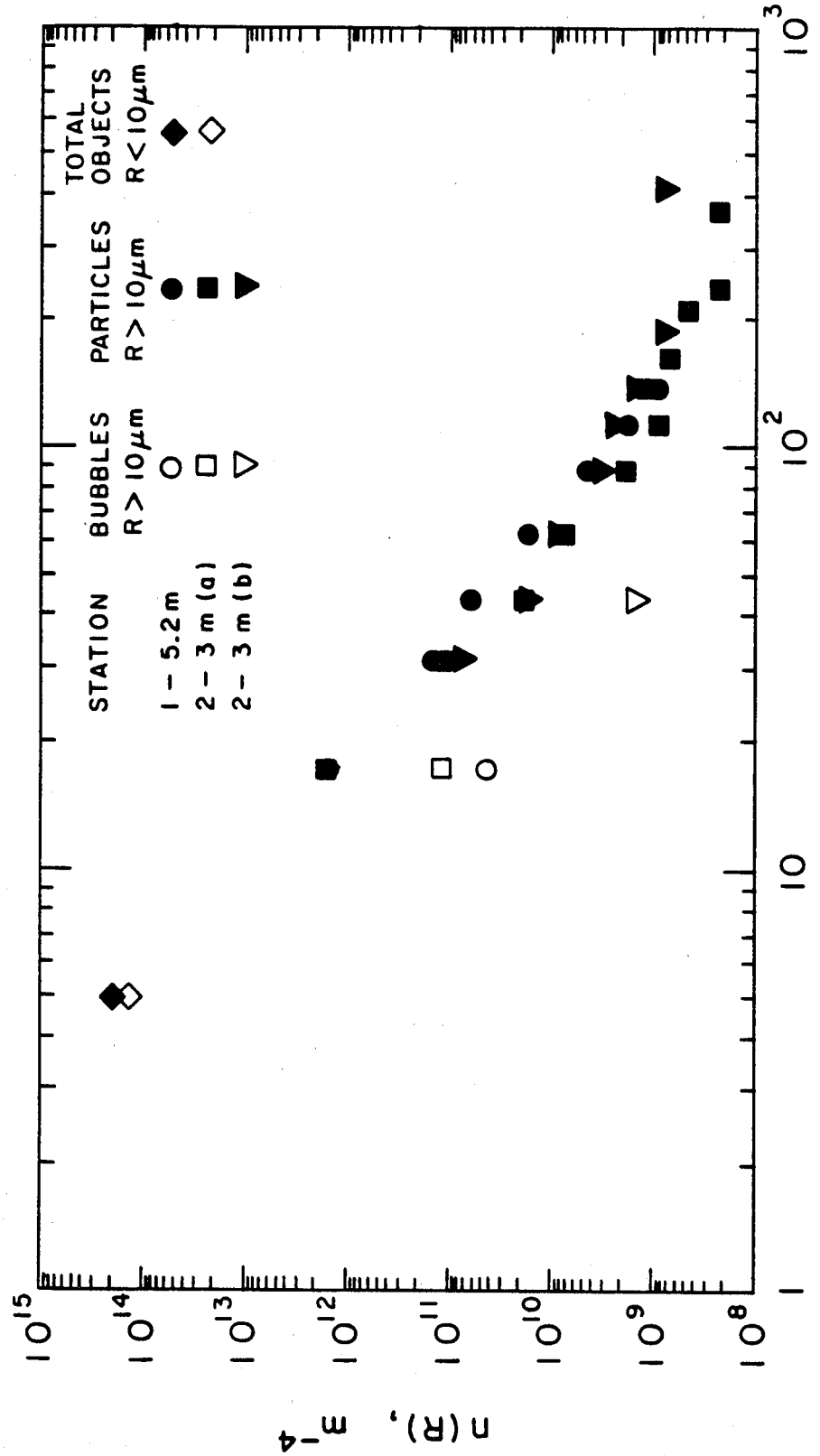

Figure I.4.12. Number density distribution function $n(R)$ as a function of equivalent radius R for total particles observed at Stations 1 and 2. Bubble data from Figure I.4.2 are also included. Diamonds indicate objects with radii less than 10 μm for which no distinction as to type was attempted.

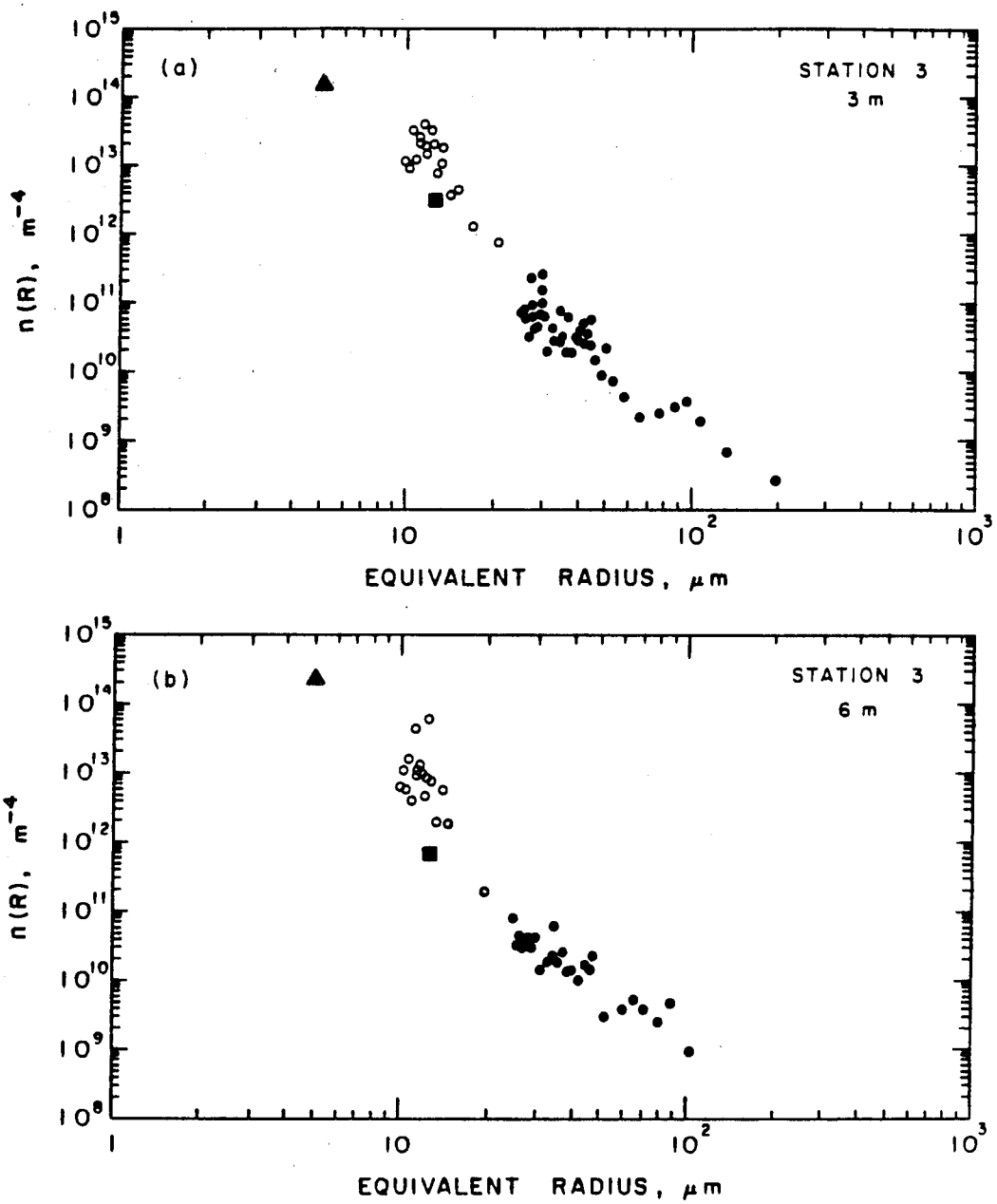

Figure I.4.13. Total particle number density distribution function $n(R)$ vs. equivalent radius R for Station 3. (a) through (f) show the six depths examined, as indicated on the legend of each plot. Circles give the particle data, open and closed indicating a change in volume examined. Bubble data from Figure I.4.4 are also included as solid squares in order to show their relative abundance. Triangles indicate objects with radii less than 10 μm for which no distinction as to type was attempted.

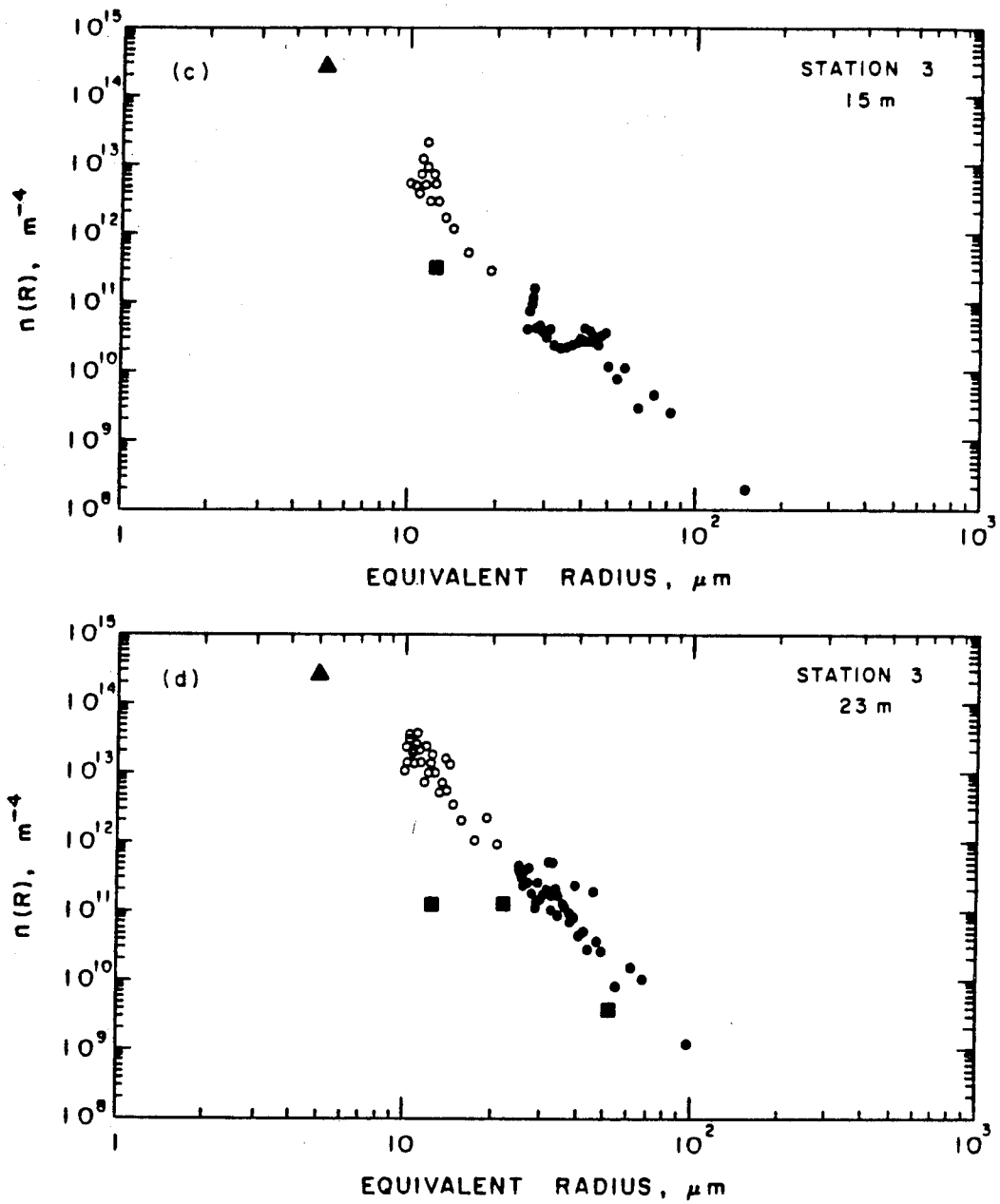

Figure I.4.13 (c), (d). See caption on p. 90.

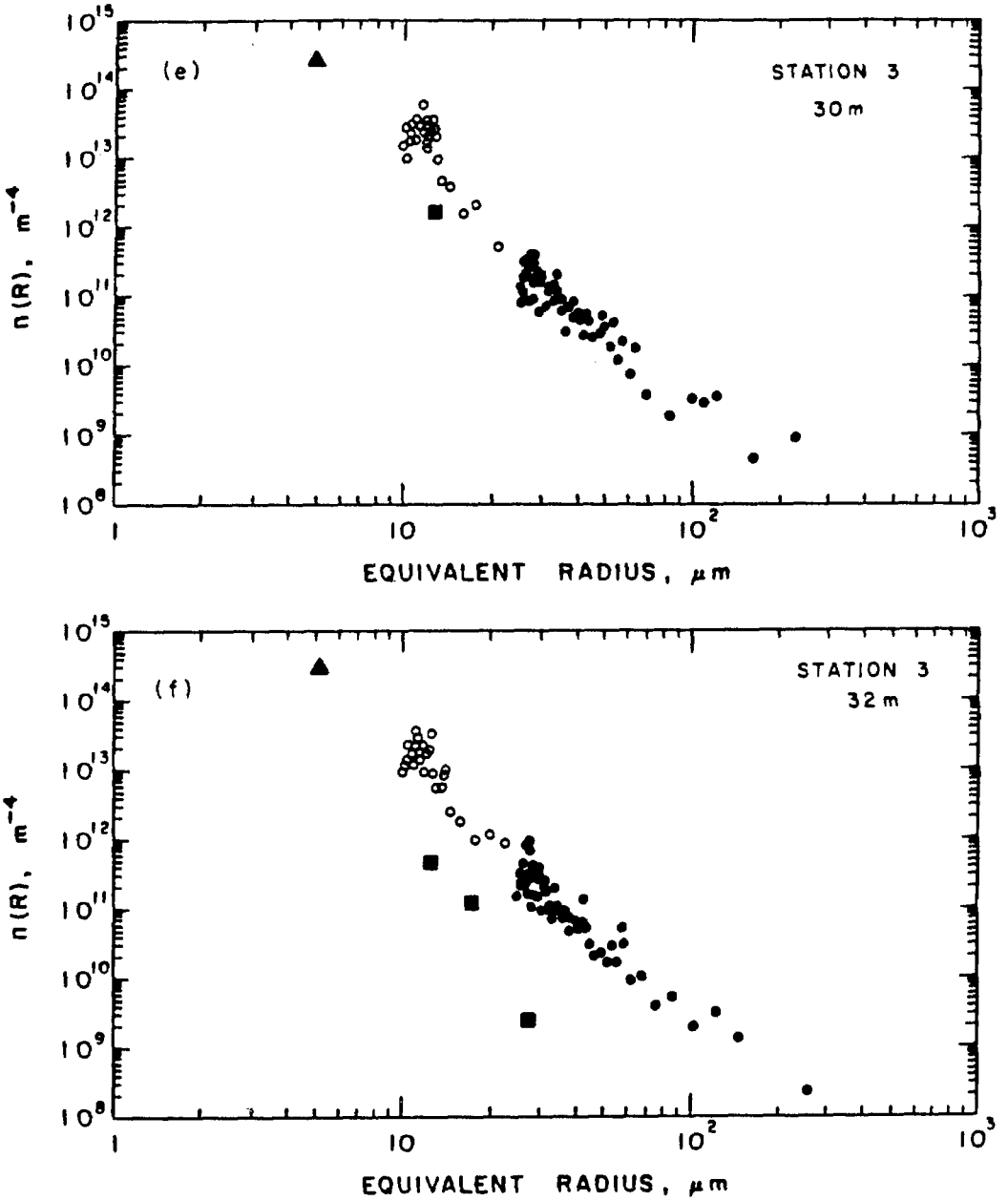

Figure I.4.13 (e), (f). See caption on p. 90.

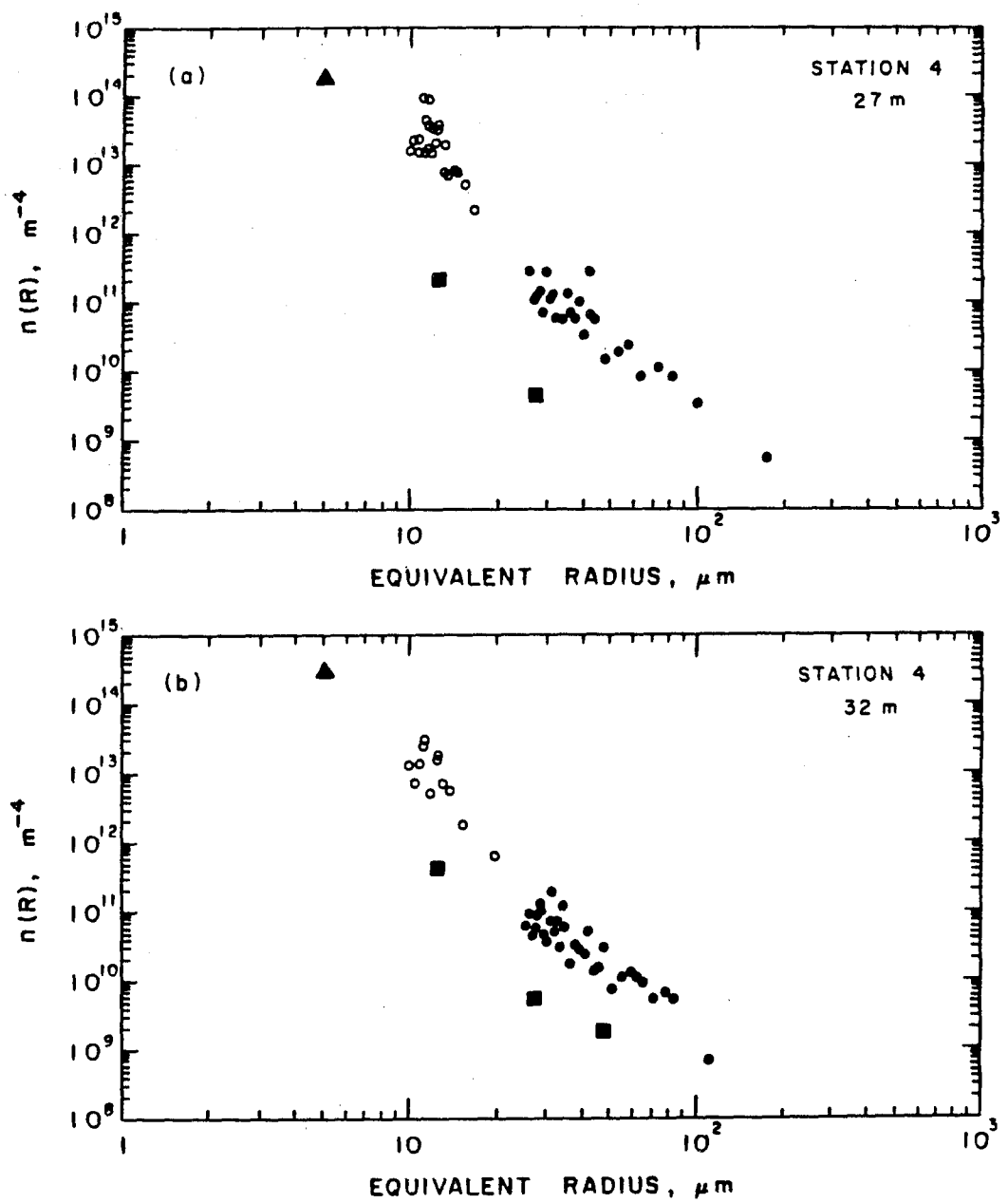

Figure I.4.14. Total particle number density distribution function $n(R)$ vs. equivalent radius R for Station 4. (a) and (b) show the two depths examined, as indicated on the legend of each plot. Circles give the particle data, open and closed indicating a change in volume examined. Bubble data from Figure I.4.6 are also included as solid squares in order to show their relative abundance. Triangles indicate objects with radii less than 10 μm for which no distinction as to type was attempted.

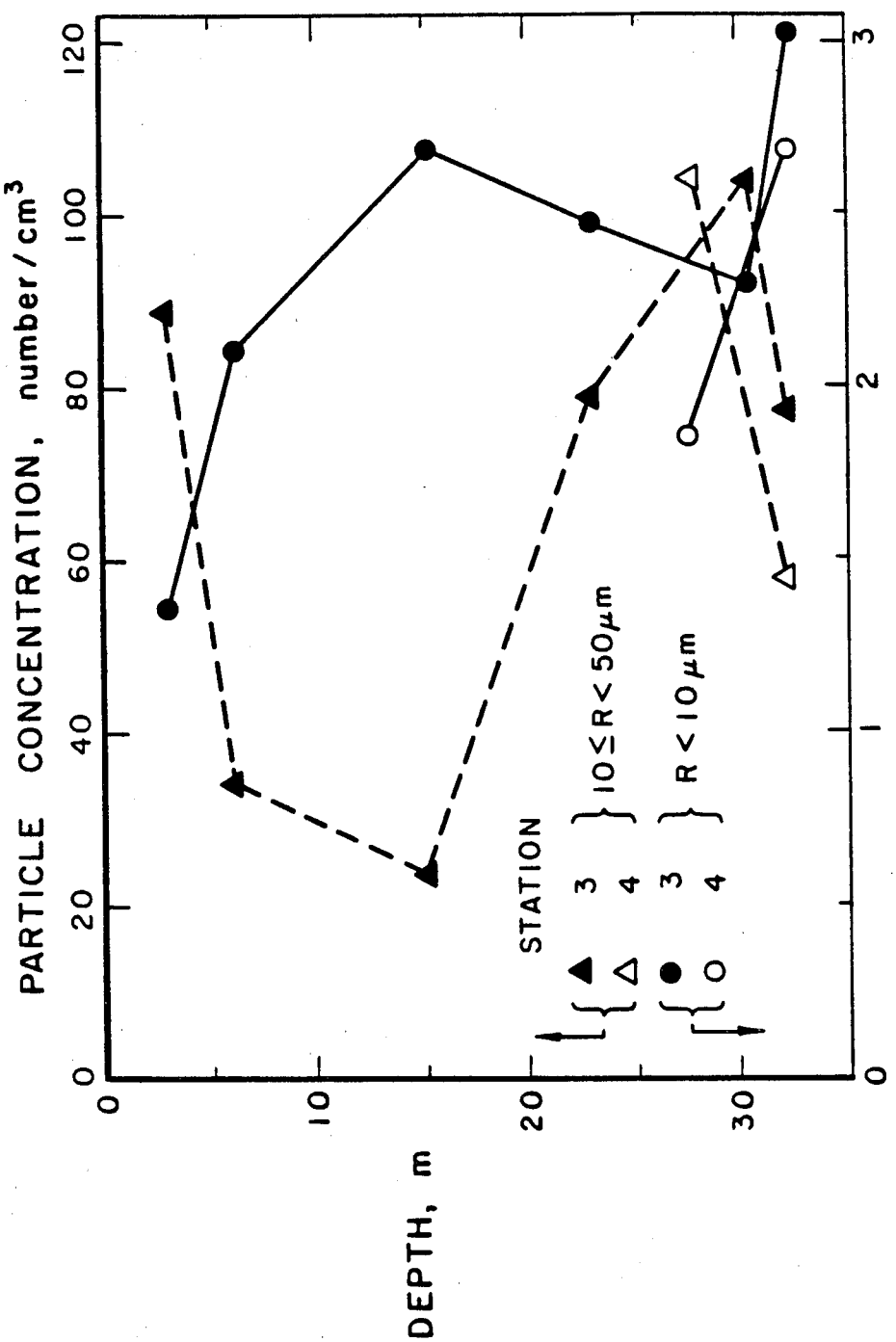

Figure I.4.15. Total concentration of objects with radii less than 10 μm and of particles in the 10 to 50 μm equivalent radius range at Stations 3 and 4 as a function of depth.

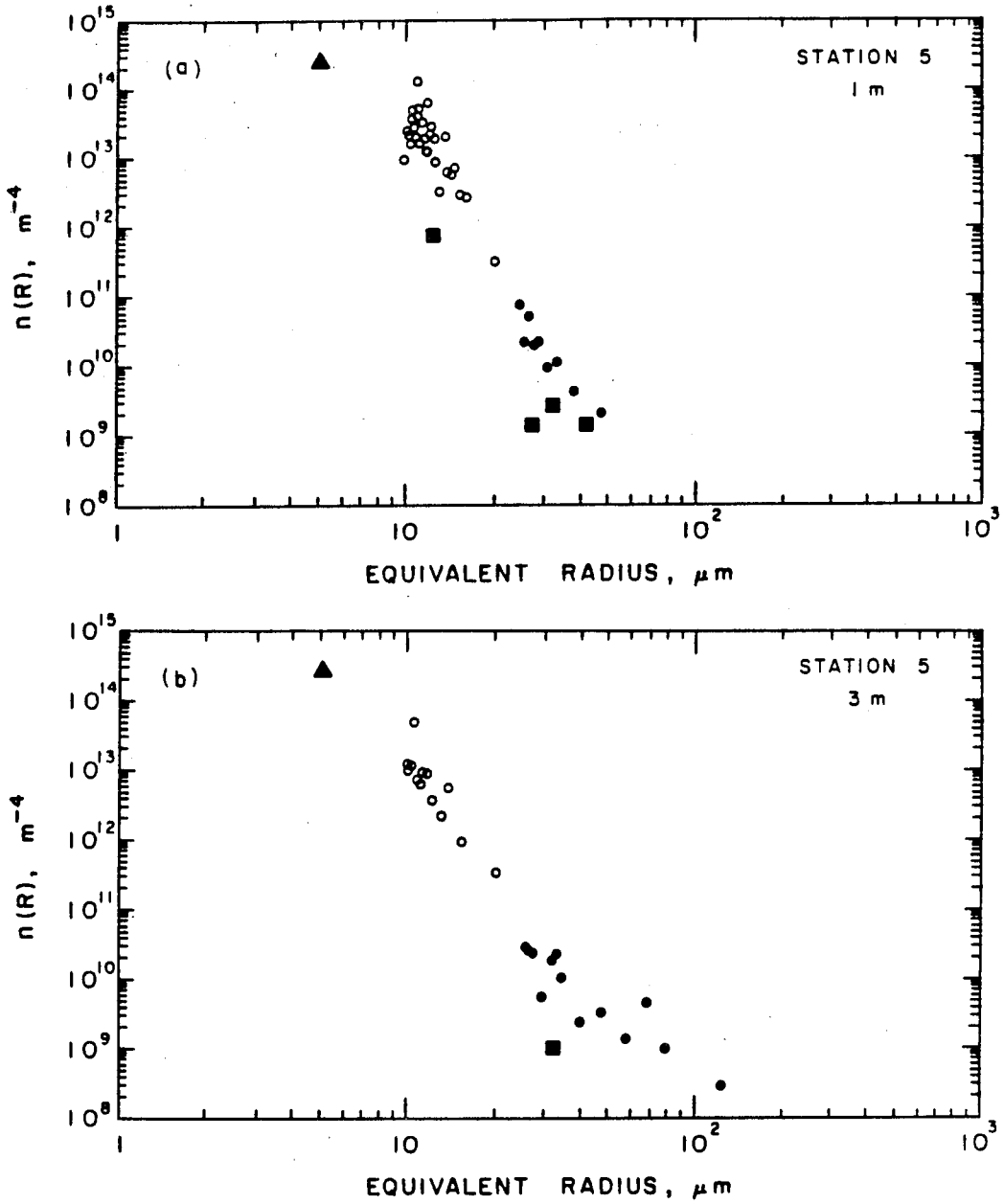

Figure I.4.16. Total particle number density distribution function $n(R)$ vs. equivalent radius R for Station 5. (a) through (h) show the eight depths examined, as indicated on the legend of each plot. Circles give the particle data, open and closed indicating a change in volume examined. Bubble data from Figure I.4.7 are also included as solid squares in order to show their relative abundance. Triangles indicate objects with radii less than 10 μm for which no distinction as to type was attempted.

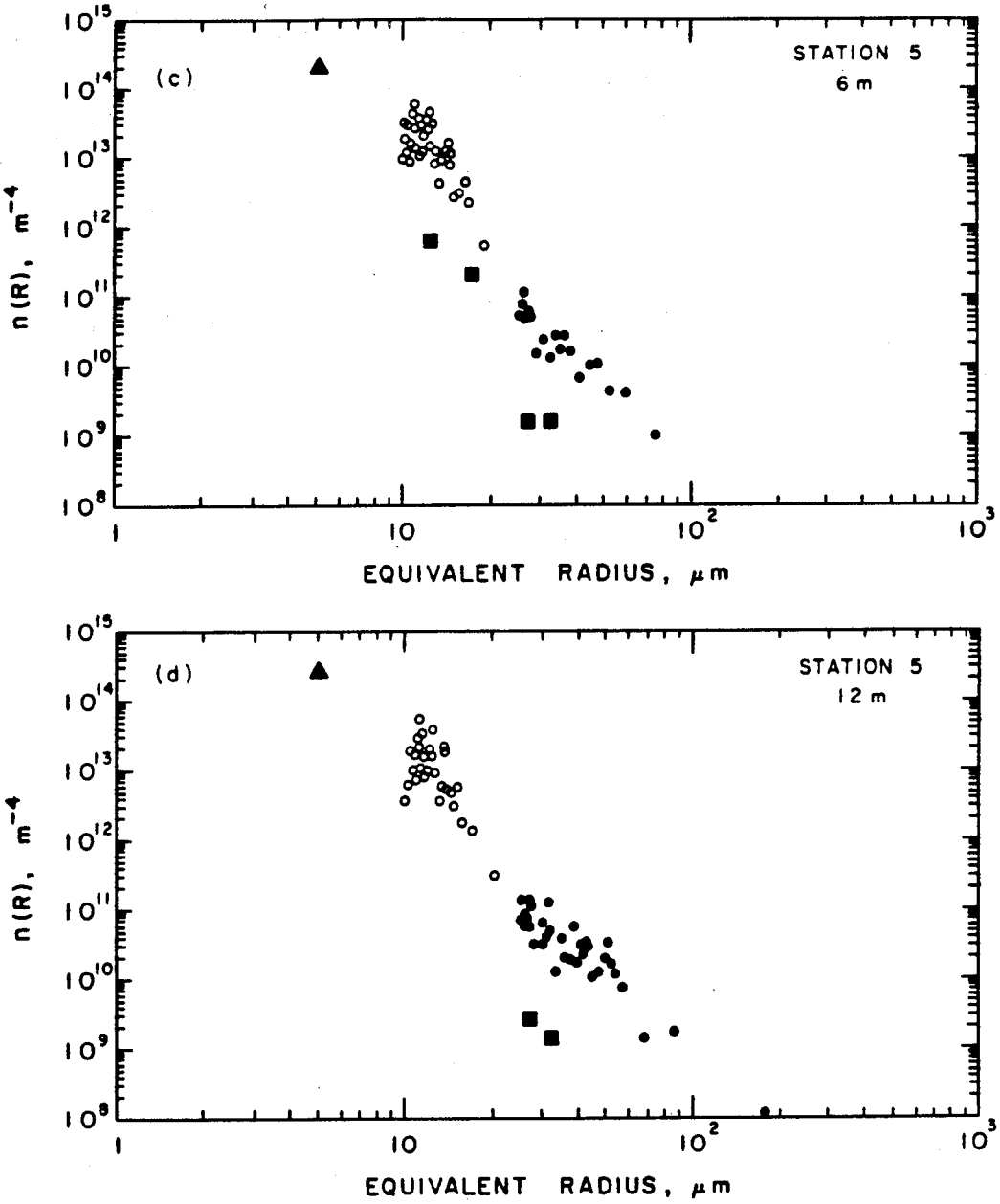

Figure I.4.16 (c), (d). See caption on p. 95.

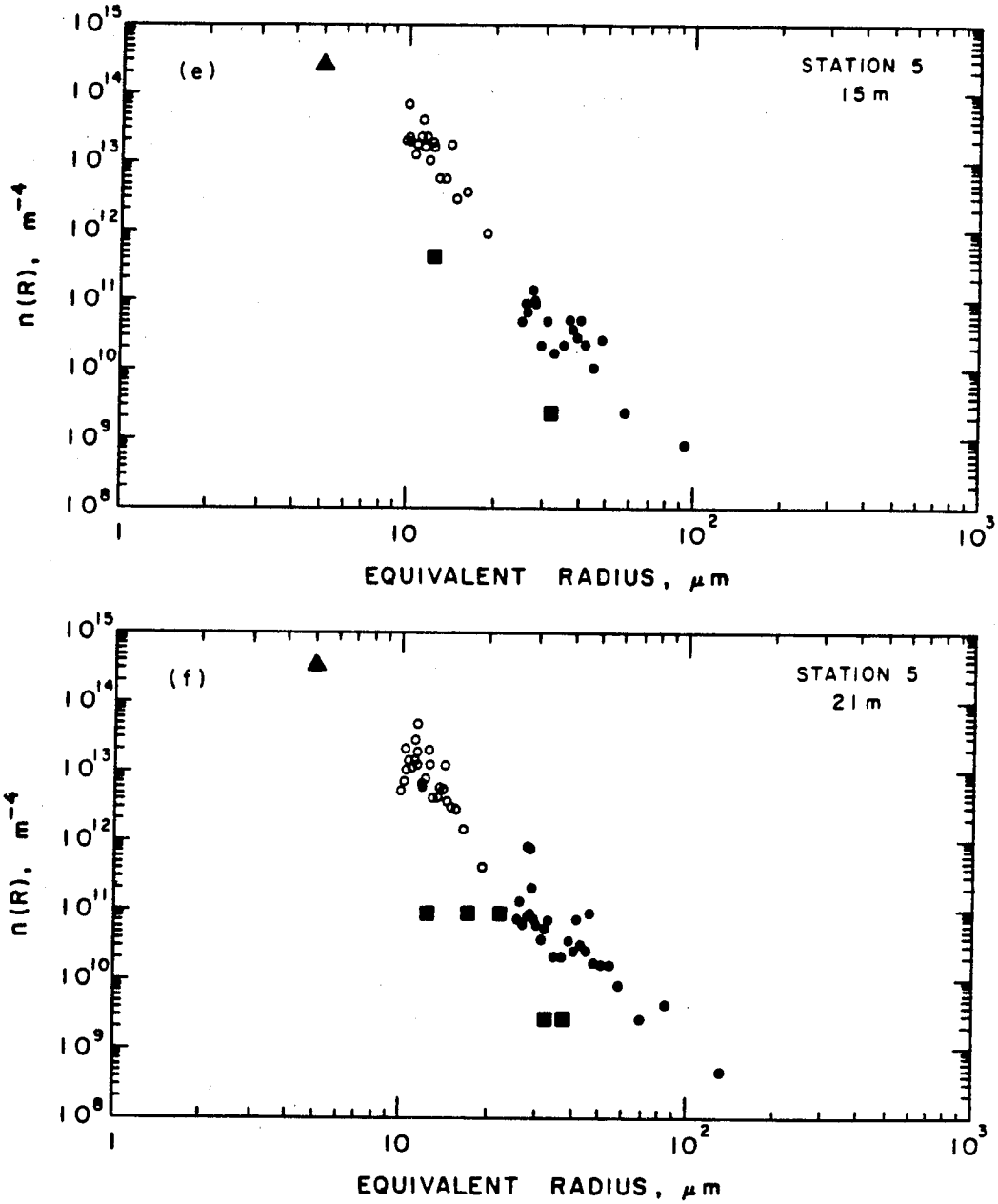

Figure I.4.16 (e), (f). See caption on p. 95.

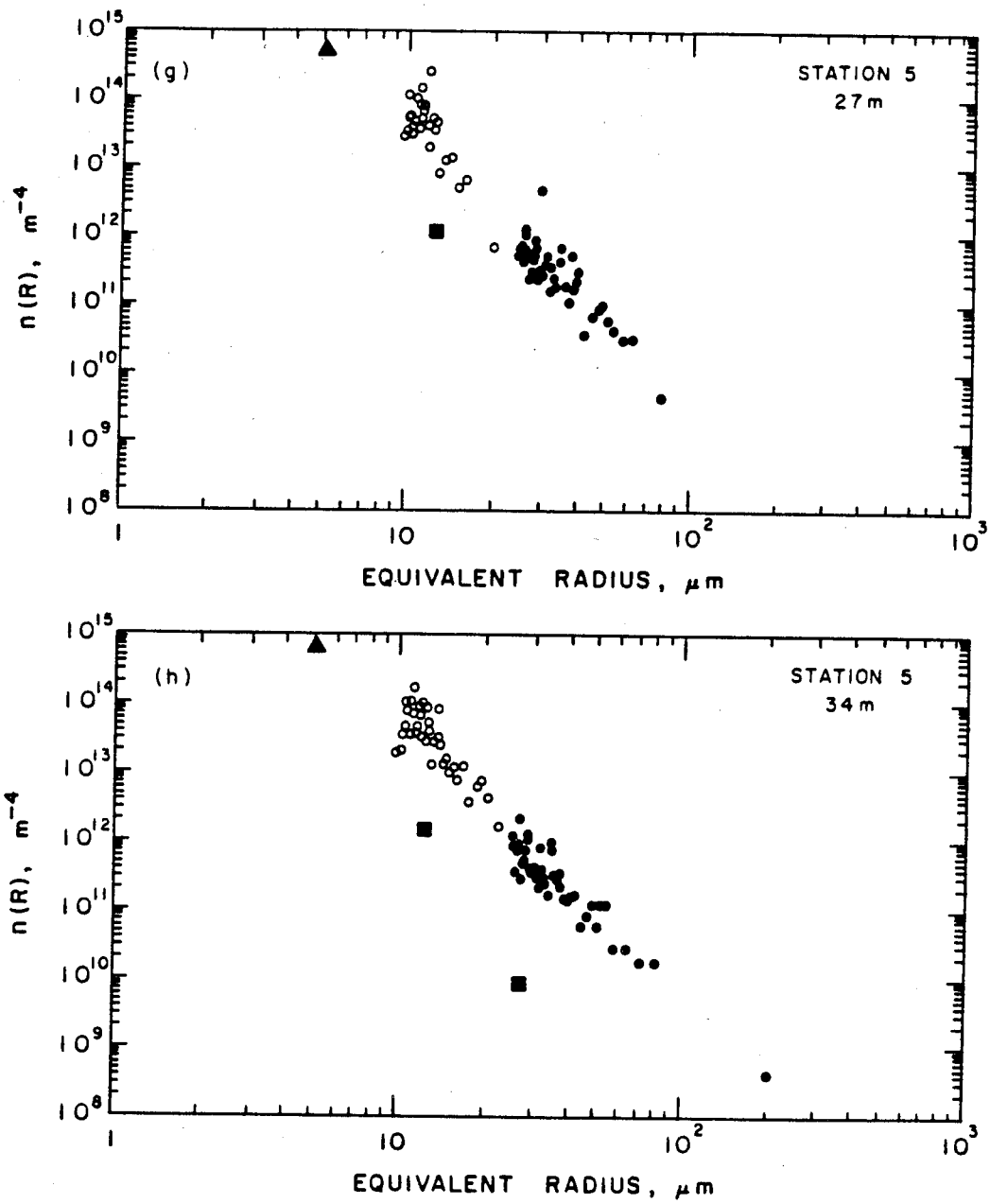

Figure I.4.16 (g), (h). See caption on p. 95.

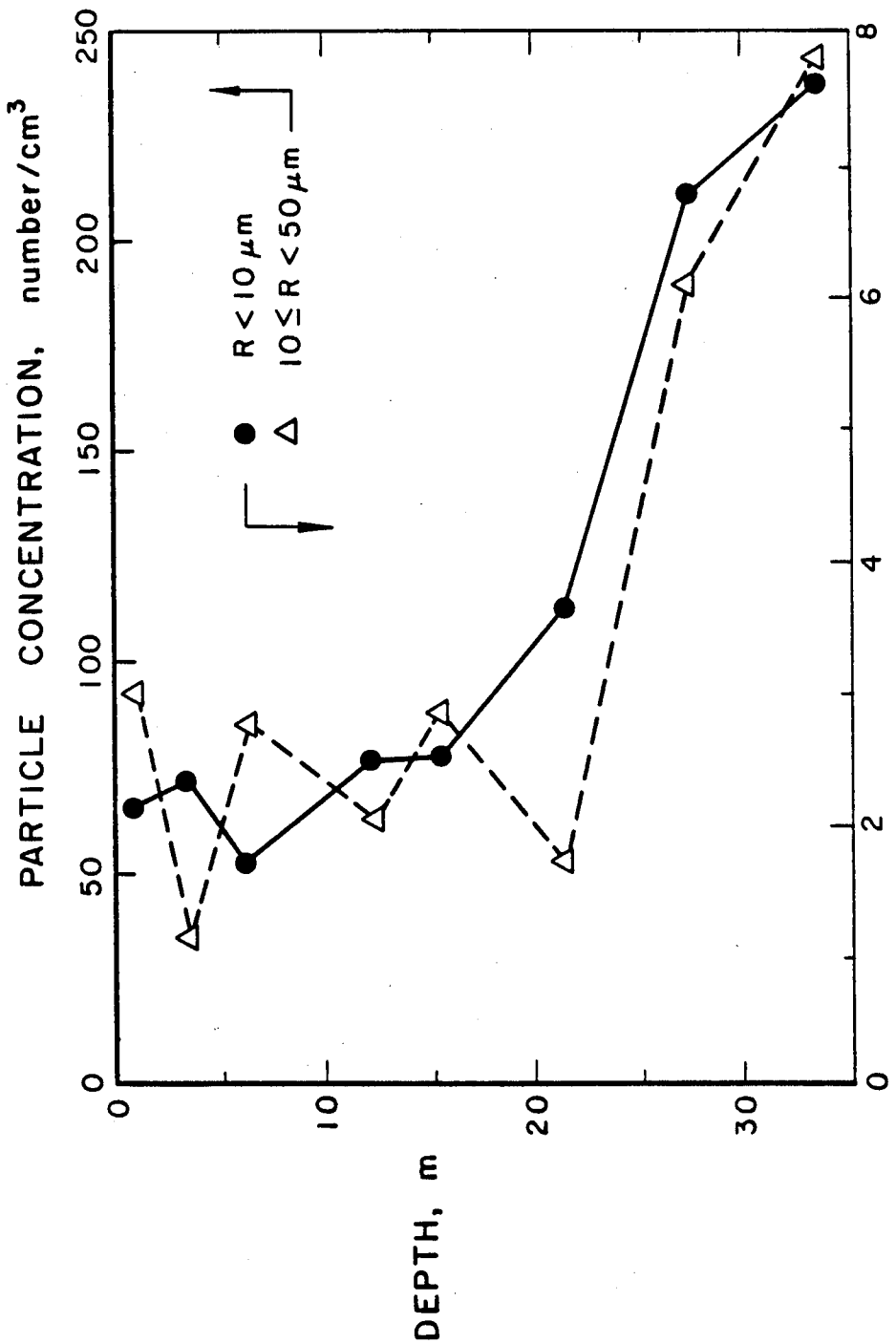

Figure I.4.17. Total concentration of objects with radii less than 10 μm and of particles in the 10 to 50 μm equivalent radius range at Station 5 as a function of depth.

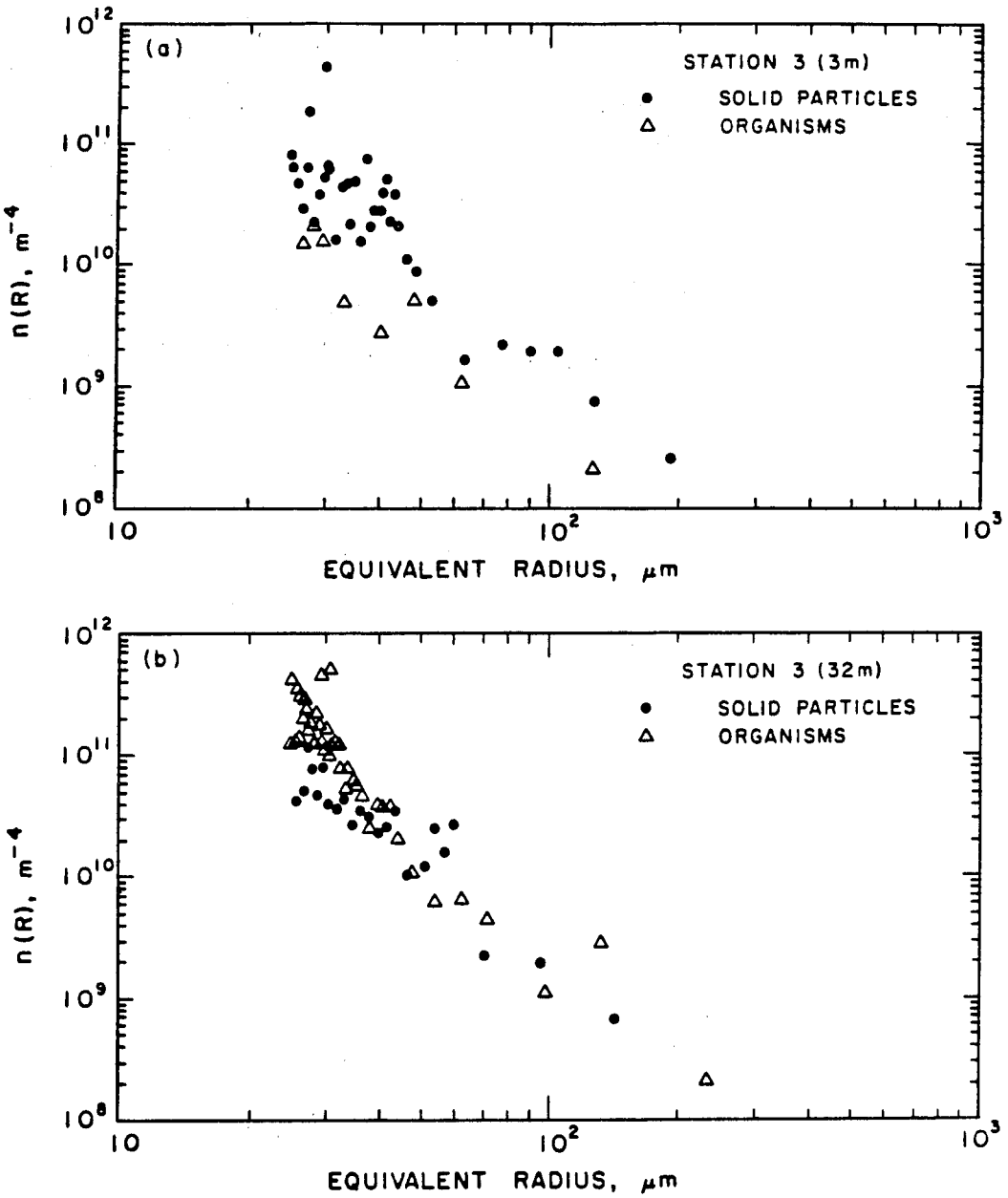

Figure I.4.18. Relative concentration of organisms at two depths from Station 3. Solid particles are indicated by circles and organisms by triangles. (a) 3 m submergence; (b) 32 m submergence.

Bubble Concentrations ($number/cm^3$) Station 1 - Los Angeles Harbor Station 2 - San Pedro Channel			
Radius Range (μm)	Hologram Site Station 1 5 m	Station 2 3 m	Station 2 3 m
$10 \leq R < 25$	0.63	1.73	*
$25 \leq R < 37.5$	0	0	0
$37.5 \leq R < 50$	0	0	0.02

* not counted

(a)

Examined Volume (cm^3) Station 1 - Los Angeles Harbor Station 2 - San Pedro Channal			
Hologram Location	Radius Range Studied $R_{eq} < 10\mu m$	$10 \leq R_{eq} < 25\mu m$	$R_{eq} \geq 25\mu m$
Station 1 (5 m)	0.30	3.18	43.75
Station 2 (3 m)	0.92	9.25	84.69
Station 2 (3 m)	*	*	48.97

* not counted

(b)

Table I.4.1. Data table for bubble distributions at Stations 1 and 2.
(a) Measured bubble concentrations in discrete size intervals. Heavy line indicates change in size of volume examined.
(b) Volumes examined for both bubbles and particles in each size range.

Station 3 - Long Point, Santa Catalina Island Bubble Concentrations ($number/cm^3$)						
Radius Range (μm)	Hologram Depth (m)					
	3	6	15	23	30	32
$10 \leq R < 15$	15	3.3	1.6	0.6	8.6	2.5
$15 \leq R < 20$	0	0	0	0	0	0.6
$20 \leq R < 25$	0	0	0	0.6	0	0
$25 \leq R < 30$	0	0	0	0	0	0.01
$30 \leq R < 35$	0	0	0	0	0	0
$35 \leq R < 40$	0	0	0	0	0	0
$40 \leq R < 45$	0	0	0	0	0	0
$45 \leq R < 50$	0	0	0	0	0	0
$50 \leq R < 55$	0	0	0	0.02	0	0

(a)

Examined Volume (cm^3) Station 3 - Off Long Point, Santa Catalina Island			
Hologram Depth (m)	Radius Range Studied		
	$R_{eq} < 10\mu m$	$10 \leq R_{eq} < 25\mu m$	$R_{eq} \geq 25\mu m$
3	0.21	1.00	149.97
6	0.26	2.13	145.43
15	0.16	3.14	126.96
23	0.25	1.66	53.85
30	0.20	1.17	170.36
32	0.15	1.61	79.47

(b)

Table I.4.2. Data table for bubble distributions at Station 3.
(a) Measured bubble concentrations in discrete size intervals. Heavy line indicates change in size of volume examined.
(b) Volumes examined for both bubbles and particles in each size range.

Station 4 - East of Santa Catalina Island Bubble Concentrations ($number/cm^3$)		
Radius Range (μm)	Hologram Depth (m) 27	32
$10 \leq R < 15$	1.1	2.2
$15 \leq R < 20$	0	0
$20 \leq R < 25$	0	0
$25 \leq R < 30$	0.02	0.03
$30 \leq R < 35$	0	0
$35 \leq R < 40$	0	0
$40 \leq R < 45$	0	0
$45 \leq R < 50$	0	0.01

(a)

Examined Volume (cm^3) Station 4 - Off East Santa Catalina Island			
Hologram Depth (m)	Radius Range Studied $R_{eq} < 10\mu m$	$10 \leq R_{eq} < 25\mu m$	$R_{eq} \geq 25\mu m$
27	0.25	0.93	45.24
32	0.25	0.91	100.41

(b)

Table I.4.3. Data table for bubble distributions at Station 4.
(a) Measured bubble concentrations in discrete size intervals. Heavy line indicates change in size of volume examined.
(b) Volumes examined for both bubbles and particles in each size range.

Station 5 - Whites Point, Palos Verde Peninsula Bubble Concentrations ($number/cm^3$)								
Radius Range (μm)	Hologram Depth (m)							
	1	3	6	12	15	21	27	34
$10 \leq R < 15$	3.78	0	2.92	1.77	2.11	0.44	5.66	6.75
$15 \leq R < 20$	0	0	0.97	0	0	0.44	0	0
$20 \leq R < 25$	0	0	0	0	0	0.44	0	0
$25 \leq R < 30$	0.01	0	0.01	0.01	0	0	0	0.04
$30 \leq R < 35$	0.01	0.01	0.01	0.01	0.01	0.01	0	0
$35 \leq R < 40$	0	0	0	0	0	0.01	0	0
$40 \leq R < 45$	0.01	0	0	0	0	0	0	0

(a)

Examined Volume (cm^3) Station 5 - Whites Point Sewage Outfall			
Hologram Depth (m)	Radius Range Studied		
	$R_{eq} < 10\mu m$	$10 \leq R_{eq} < 25\mu m$	$R_{eq} \geq 25\mu m$
1	0.26	1.58	145.24
3	0.29	1.57	189.53
6	0.40	2.06	138.37
12	0.38	2.26	146.22
15	0.25	0.95	86.10
21	0.25	2.29	75.92
27	0.10	0.71	26.45
34	0.11	0.74	24.40

(b)

Table I.4.4. Data table for bubble distributions at Station 5.
(a) Measured bubble concentrations in discrete size intervals. Heavy line indicates change in size of volume examined.
(b) Volumes examined for both bubbles and particles in each size range.

Particle Concentrations ($number/cm^3$) Station 1 - Los Angeles Harbor Station 2 - San Pedro Channel			
Radius Range (μm)	Hologram Site Station 1 5 m	Station 2 3 m	Station 2 3 m
$R < 10$	1960	1310	*
$10 \leq R < 25$	22.32	24.12	*
$25 \leq R < 37.5$	1.90	1.44	0.96
$37.5 \leq R < 50$	0.78	0.23	0.24
$50 \leq R < 75$	0.43	0.18	0.22
$75 \leq R < 100$	0.11	0.04	0.08
$100 \leq R < 125$	0.04	0.02	0.06
$125 \leq R < 150$	0.02	0.03	0.04
$150 \leq R < 200$	0	0.03	0.02
$200 \leq R < 250$	0	0.02	0
$250 \leq R < 300$	0	0	0
$300 \leq R < 350$	0	0	0
$350 \leq R < 400$	0	0.01	0
$400 \leq R < 500$	0	0	0.02

* not counted

Table I.4.5. Measured concentrations of total particles in discrete equivalent radius intervals examined for Stations 1 and 2. Heavy lines indicate change in size of volume examined. Volumes examined in each size interval are given in Table I.4.1 (b).

Station 3 - Long Point, Santa Catalina Island Particle Concentrations ($number/cm^3$)						
Radius Range (μm)	Hologram Depth (m)					
	3	6	15	23	30	32
$R < 10$	1370	2110	2650	2480	2300	3050
$10 \leq R < 15$	75.92	31.95	20.36	65.26	90.68	61.57
$15 \leq R < 20$	8.99	2.35	1.59	9.67	7.70	8.08
$20 \leq R < 25$	3.00	0	0.95	1.81	2.57	3.73
$25 \leq R < 30$	0.33	0.22	0.32	1.24	0.92	1.36
$30 \leq R < 35$	0.24	0.12	0.13	0.82	0.70	0.67
$35 \leq R < 40$	0.11	0.10	0.09	0.54	0.35	0.35
$40 \leq R < 45$	0.18	0.07	0.17	0.24	0.28	0.26
$45 \leq R < 50$	0.07	0.08	0.13	0.22	0.23	0.11
$50 \leq R < 55$	0.05	0.01	0.05	0.07	0.19	0.14
$55 \leq R < 60$	0.03	0.01	0.06	0.04	0.12	0.11
$60 \leq R < 65$	0.01	0.03	0	0.06	0.04	0.06
$65 \leq R < 70$	0.01	0.02	0.01	0.04	0.04	0.05
$70 \leq R < 75$	0.01	0.02	0.02	0.06	0.03	0.02
$75 \leq R < 80$	0.02	0.01	0.01	0	0.05	0.02
$80 \leq R < 85$	0	0.02	0.01	0.02	0.01	0.01
$85 \leq R < 90$	0.02	0.02	0.02	0	0.01	0.01
$90 \leq R < 95$	0.02	0.01	0.02	0	0.02	0.04
$95 \leq R < 100$	0.01	0.01	0.01	0	0.01	0.01
$100 \leq R < 110$	0.02	0.01	0	0.04	0.03	0.02
$110 \leq R < 120$	0.03	0	0.01	0	0.04	0.01
$120 \leq R < 150$	0.01	0.01	0.01	0.02	0.04	0.08
$150 \leq R < 200$	0.02	0.01	0	0	0.02	0.05
$200 \leq R < 250$	0.01	0.01	0	0	0.02	0.01
$250 \leq R < 300$	0.01	0	0.01	0	0.01	0
$400 \leq R < 500$	0	0	0	0	0	0.01
$700 \leq R < 800$	0	0.01	0	0	0	0

Table I.4.6. Measured concentrations of total particles in discrete equivalent radius intervals examined for Station 3. Heavy lines indicate change in size of volume examined. Volumes examined in each size interval are given in Table I.4.2 (b).

Station 4 - East of Santa Catalina Island Particle Concentrations ($number/cm^3$)		
Radius Range (μm)	Hologram Depth (m) 27	32
$R < 10$	1570	2670
$10 \leq R < 15$	90.4	48.6
$15 \leq R < 20$	11.8	4.4
$20 \leq R < 25$	0	1.1
$25 \leq R < 30$	0.53	0.36
$30 \leq R < 35$	0.44	0.33
$35 \leq R < 40$	0.35	0.13
$40 \leq R < 45$	0.31	0.12
$45 \leq R < 50$	0.11	0.07
$50 \leq R < 55$	0.11	0.06
$55 \leq R < 60$	0.07	0.04
$60 \leq R < 65$	0.04	0.09
$65 \leq R < 70$	0.07	0.03
$70 \leq R < 75$	0.04	0.03
$75 \leq R < 80$	0.07	0.04
$80 \leq R < 85$	0.04	0.01
$85 \leq R < 90$	0.02	0.04
$90 \leq R < 95$	0.04	0
$95 \leq R < 100$	0.04	0
$100 \leq R < 110$	0	0.01
$110 \leq R < 120$	0.04	0.02
$120 \leq R < 150$	0.02	0.01
$150 \leq R < 200$	0.02	0
$200 \leq R < 250$	0	0
$250 \leq R < 300$	0.02	0

Table I.4.7. Measured concentrations of total particles in discrete equivalent radius intervals examined for Station 4. Heavy lines indicate change in size of volume examined. Volumes examined in each size interval are given in Table I.4.3 (b).

Station 5 - Whites Point, Palos Verde Peninsula Particle Concentrations ($number/cm^3$)								
Radius Range (μm)	Hologram Depth (m)							
	1	3	6	12	15	21	27	34
$R < 10$	2070	2290	1740	2350	2460	3670	6840	7540
$10 \leq R < 15$	82.6	32.6	75.4	51.3	77.2	43.6	167.1	180.8
$15 \leq R < 20$	8.83	1.92	8.75	8.40	9.51	7.41	12.8	41.8
$20 \leq R < 25$	0.63	1.28	1.46	0.88	1.06	0.44	2.83	10.80
$25 \leq R < 30$	0.15	0.09	0.20	0.36	0.44	0.59	2.50	3.11
$30 \leq R < 35$	0.06	0.06	0.10	0.17	0.09	0.22	1.70	1.68
$35 \leq R < 40$	0.01	0.03	0.08	0.10	0.17	0.12	1.02	1.02
$40 \leq R < 45$	0.03	0.02	0.04	0.12	0.13	0.16	0.42	0.53
$45 \leq R < 50$	0	0.01	0.04	0.06	0.08	0.18	0.38	0.45
$50 \leq R < 55$	0.01	0.02	0.02	0.08	0.02	0.07	0.38	0.41
$55 \leq R < 60$	0	0	0.02	0.04	0	0.05	0.11	0.12
$60 \leq R < 65$	0	0.01	0.02	0.01	0.01	0.03	0.15	0.08
$65 \leq R < 70$	0	0.01	0	0.01	0.02	0.01	0.08	0.12
$70 \leq R < 75$	0	0.02	0	0.01	0.01	0	0	0.12
$75 \leq R < 80$	0	0.01	0	0.01	0.01	0.01	0.04	0.04
$80 \leq R < 85$	0	0.01	0	0.01	0.01	0.04	0	0.12
$85 \leq R < 90$	0	0	0.02	0	0	0.01	0	0.04
$90 \leq R < 95$	0	0.01	0.01	0.01	0	0.01	0.04	0.08
$95 \leq R < 100$	0	0.01	0	0.01	0	0	0.04	0.04
$100 \leq R < 110$	0	0	0	0.01	0	0.03	0.04	0
$110 \leq R < 120$	0.01	0	0	0	0	0.01	0	0
$120 \leq R < 150$	0	0	0	0.01	0	0	0	0
$150 \leq R < 200$	0.01	0.01	0	0	0	0	0	0
$200 \leq R < 250$	0	0	0	0	0.01	0.01	0	0
$250 \leq R < 300$	0	0	0	0.01	0	0	0	0
$300 \leq R < 350$	0.01	0	0	0	0	0	0	0
$350 \leq R < 400$	0	0	0	0	0	0	0	0
$400 \leq R < 500$	0	0	0	0.01	0	0	0	0.04

Table I.4.8. Measured concentrations of total particles in discrete equivalent radius intervals examined for Station 5. Heavy lines indicate change in size of volume examined. Volumes examined in each size interval are given in Table I.4.4 (b).

CHAPTER I.5
DISCUSSION

I.5.1 Bubble Availability at Various Sites

As shown in the previous chapter, at least one bubble was observed at each station and depth examined in this study. The presence of bubbles in the ocean under calm conditions is of great interest because it implies that some other method of bubble production besides the usual surface mechanisms of breaking waves or whitecaps may be active.

Very few bubble data were collected in the examinations of Stations 1 and 2. The surveys of Stations 3, 4 and 5 were much more extensive and provided considerable new information. The single largest bubble observed at any of the 5 test sites had a radius of 50 μm and was observed at 23 m submergence at Station 3. Several observations can be made based on the bubbles seen in the holographic images, even though the total bubble count was fairly low. The concentration of small bubbles (10 to 25 μm radius) at Station 3 seems to be very high near the surface, then to decrease with depth until the thermocline is reached, at which point the concentration increases, as shown in Figures I.4.3 (a) and I.4.5. Larger bubbles (25 to 50 μm radius) are found only below the thermocline at this site. The bubble data for Station 4 are sparse and represent water below the thermocline only, indicating a fairly high concentration of larger bubbles at the 32 m depth. The expected standard error for each bubble size interval is expected to be equal to $1/\sqrt{N}$, where N is the corresponding number of counts. This error is often large, especially for those size ranges with sparse bubble observations, as was shown in the previous chapter. The existence of microbubbles

down to 32 m and the apparent population inversion below the thermocline are surprising since most bubble formation mechanisms involve surface creation and predict bubble penetration depths of only a few meters.

The results of several previous ocean bubble investigations tend to support the present results to some extent. Figure I.5.1 displays the present bubble number density distribution data from Station 3 along with those of several other investigators. Solid lines are drawn only for clarity in connecting the appropriate data points, not as an indication of a continuous distribution. The bubble concentrations measured at Station 3 are generally higher than those seen in the other studies. However, in consideration of the high expected error for the present measurements, as well as the known wide variability of the ocean, the quantitative agreement between the bubble distributions must be considered satisfactory. Shen et al. (1986), using a light scattering technique, apparently detected microbubbles to 200 m depth at their test site in the Exuma Sound and to 150 m at their Gulf Stream site. Their results, a few of which are shown in Figure I.5.1, indicate an overall decrease in bubble concentration with depth, with no increase in bubble concentration observed below the deep subtropical thermocline at the Exuma Sound test site, and no measurements reported below the very deep thermocline at the Gulf Stream test site. The fact that bubble existence at depths as great as 200 m had not been reported previously and cannot be explained without use of an unproven bubble stabilization hypothesis led Shen et al. to generically classify the objects detected by the light scattering device as "nuclei" but to conclude that "the possible existence of gas bubbles at deep depths is ... strongly suggested." The existence of nuclei at all of their sampled depths was verified by venturi cavitation susceptibility measurements, which showed that the ocean waters examined to depths of 200 m all cavitate easily. The acoustic attenuation measurements of Medwin (1977) indicate the presence of bubbles as deep as 36 m in the ocean, and under a windrow peak bubble concentrations were reported at that depth. Medwin speculates that the

Langmuir cells under the windrow acted to deplete the upper waters without affecting the deep water bubbles, which are postulated to be of biological origin. In addition he found that the summer concentration of bubbles was an order of magnitude higher than the winter concentration at the same location and conditions, providing additional support to the biological bubble production mechanism. Windrows were not present at the stations examined in the present study, but a strong correlation between bubble and organism concentrations was observed, particularly below the thermocline, so bubbles of organic origin may play an important role in the present observations.

The depth dependence of the bubble population density spectra seems to vary considerably. Medwin (1970) found a $z^{-1/2}$ dependence for bubbles with radii greater than 60 μm and $e^{-z/L}$ for smaller bubbles, with $L \simeq 5$ to 9 m, in waters off San Diego. Farmer & Lemon (1984) also found an exponential dependence of bubble concentration on depth, although they found a characteristic length $L \simeq 1.0$ m. The present results cover only a few discrete depths but do not show any agreement with such drastic decreases in bubble concentration with depth, but in fact show a local peak concentration at depth.

The sparse bubble data counts and the inability to distinguish bubbles from particles with radii below 10 μm make it difficult to say much about the bubble population spectrum. However, in all cases the most bubbles are found in the smallest radius ranges. This observation is supported by the results of Medwin (1970, 1977) shown in Figure I.5.1, which indicate a dependence like $n(R) \simeq R^{-4}$ for bubbles less than 60 μm radius, and $n(R) \simeq R^{-2}$ for larger bubbles. The results of Shen et al. indicate similar behavior, with a trend which can be approximated as $n(R) \simeq R^{-4}$ for all of their ocean data. It is interesting to note that the results of Gavrilov (1970) shown in Figure I.1.1 reveal this same spectra for the bubble population in long-standing tap water. On the other hand, the photographic results of Johnson & Cooke (1979) indicate a peak in the ocean bubble spectra at about 50 μm radius. Their photographic technique

could not detect small bubbles with radii less than 17 μm, and their testing was performed in rough seas. They speculate that the peak in their measured bubble spectra may be attributed to a high production rate of large bubbles by breaking whitecaps at the surface.

The overall high bubble concentrations, particularly near the surface at Station 3, are surprising in view of the calm windless conditions at the time these holograms were recorded, as well as for several previous days. Strong increases in bubble concentration with increasing wind speed have been reported in many cases. The results of Medwin (1977), shown in Figure I.5.1, indicate approximately a factor of two increase in bubble concentration at 4 m depth for an increase in wind speed from 3.3 m/s (6 knots) to 5.5 – 6.1 m/s (10 – –11 knots). The results of Johnson & Cooke (1979) show a 20 fold increase in bubble production for an increase in wind speed from 8.6 – 10.7 m/s to 11.8 – 13.9 m/s. Similar trends are reported in Thorpe (1982). The effect of weather, particularly wind speed, on the bubble population is clearly an important topic but one that could not be studied in the present examination, where all experiments were performed on calm days with flat seas.

The bubble concentrations measured at Station 5 are discussed separately here because of the unusual testing environment. As can be seen in Figures I.4.7 and I.4.8, the magnitude of the bubble concentrations as well as their depth behavior at this station seem similar to those found at Station 3, even showing a similar increase in small bubble concentration below the thermocline. However, an overall higher concentration of larger bubbles is found at Station 5. The increase of bubble concentration below the thermocline cannot be expected to relate to an increase in biological activity as is speculated for the results at Station 3, however, because at Station 5 the thermocline depth was fairly close to the sewage plume depth as indicated by the transmissivity profile of Figure I.4.2 (c). Expected bubble concentrations in the outfall of a sewage treatment plant could not be found in the literature. Very high particle concentrations deep in

the sewage plume disturbed the in-line reference beam of the holographic camera to the extent that some of the images recorded at these depths appear somewhat foggy, so the distinction of "organisms" from "particles" was not attempted. The large majority of particles seen in these waters appeared to be amorphous sludge particles. No meaningful estimates could be made of relative concentrations of organisms at this site, so it is impossible to determine whether the bubbles seen here were transported to sea with the sludge or created by biological activity or some other mechanism.

Several mechanisms were proposed and discussed in Chapter I.1 for the existence of stable equilibrium microbubbles. The results of the present study do not support one of these mechanisms over another, but the presence of bubbles at depth and without the action of the usual surface bubble generation mechanisms of breaking waves or whitecaps may indicate that the observed bubbles had somehow become stabilized. However, there is no means to determine whether the observed bubbles were in a state of equilibrium or in a transient state, possibly en route from a bottom or volume source location to the surface.

A very large number of particles and organisms were observed in all waters sampled, especially below the thermocline depth, as will be discussed below. The correlation between the depths of high bubble concentrations and high organism concentrations indicates that a biological bubble production mechanism may be in action. This observation tends to agree with the biological bubble creation hypothesis proposed by Medwin (1970, 1977) to explain his measured bubble populations, and it is supported by the results of Shen et al. (1986), who found bubble concentrations to correlate well with areas of higher ocean biological activity.

As discussed in Chapters I.3 and I.4, some operator decisions are required during the reconstruction process, for example whether a circular image should be counted as a bubble or as a particle. There is some potential for error in this step, although all reconstruction was performed by well-trained and practiced

operators. In fact, the present concentration values should be considered minimum values as any unclear images were not counted. Independent verification by two examiners was used over much of each hologram, minimizing error due to operator judgment.

Higher bubble counts would give more certainty in the estimates of concentration and therefore of the expected tensile strength, but could not be made because of the time-intensive nature of the reconstruction process. However, the fact that bubbles were seen and clearly identified at these depths and under these conditions is a very significant result by itself. The present results tend to support the recommendation of Billet (1985), that a concentration of at least 3 bubbles per cm^3 in the 5 to 20 μm radius range is needed in test facility water in order to model marine conditions.

I.5.2 Particle and Organism Concentrations

The particles observed here were only a minor portion of the total number of particles present in each sample volume. Numerous investigations have shown that the majority of particles in seawater have diameters of less than about 5 μm, below the resolution limit of the holographic system. However, for purposes of cavitation nuclei the larger particles should be most important. In most of the discussion in this section, total particulate matter will be understood to include both solid particles and organisms.

The results of the first ocean tests at Stations 1 and 2 shown in Figure I.4.12 and Table I.4.5 indicate that the harbor water (Station 1) has considerably higher particle concentrations than those found in the open ocean measurements at Station 2. This is not surprising, as water in an industrial harbor typically has fairly high pollution levels. Very high $n(R)$ values for total particle matter are observed, especially at Station 1. The high concentrations measured at Station 2 are surprising in consideration of the excellent visibility at the time of hologram

recording. The high values of $n(R)$ may be due to the fact that only holograms of surface waters were examined, so contamination by storm-swept shoreline debris was possible, as the test period for these early experiments followed several days of heavy storms.

Figure I.5.2 shows some of the results of Pieper & Holliday (1984) plotted along with those found holographically at Stations 1 and 2. It can be seen that the acoustic measurements of zooplankton populations made by Pieper & Holliday basically extend the present particle results to higher radius range. It appears that their zooplankton concentration measurements fall within the trends that were observed in the holographic testing but are much fewer in the intermediate size range around 50 μm. This comparison also supports observations made during the reconstruction process, that most of the larger particles observed seem to be zooplankton. These large zooplankton may be too few to be important for cavitation even if they turn out to be efficient nuclei.

The total particle concentration depth profiles for Stations 3 and 4 are given in Figure I.4.15. Only small objects with radii less than 10 μm and particles with equivalent radii in the 10 to 50 μm radius range are shown, as very few larger particles were observed. The data indicate higher total particulate concentrations in these radius ranges than those typically reported in the literature for either ocean or laboratory waters (see, for example, Sheldon et al. 1972; Billet 1985). The samples recorded at greater depth contain a higher number of large particles. As with the bubble concentration data shown in Figure 1.4.5, the total particle data at Station 3 indicate an increase in particle concentration near the bottom of the thermocline and correlate well with the transmissometer trace of Figure I.4.3 (a), which shows a drop in transmissivity near the thermocline depth of about 20 to 25 m. As was shown in Figure I.4.18 and discussed briefly when that figure was presented, the primary components of the total particulate count below the thermocline were organisms, especially diatoms and copepods. Similar increases in particle concentration below the thermocline were

seen at Station 4, as indicated by the transmissometer trace of Fig. I.4.3 (b), as well as by the Coulter Counter results presented in Appendix II, although the holographic results at this site are too sparse to indicate any trend with depth.

The overall shape of the number density distribution curves are very similar at the six test depths of Station 3 and the two depths of Station 4, with a trend given approximately by $n(R) \simeq R^{-4}$ over the observed size range. Similar dependence has been reported in the literature for the population of particles in many natural environments including seawater (Bader 1970) as well as for the population of comparable size bubbles in the ocean as was seen in the previous section.

The observation of an increase in particle concentration near the bottom of the thermocline is supported by the data of Pieper & Holliday (1984), who present zooplankton concentrations determined by microscopic examination of organisms deposited on filters as sea water samples were pumped through from various depths. This testing was done in May, 1978, at a location and at depths very similar to those examined at Station 3. The thermoclines were similar in each test, with the top at about 18 m and the bottom at about 30 m, although that reported by Pieper & Holliday was stronger ($5°C$) and the surface temperature was lower ($17°C$). Their results show peak zooplankton concentrations near the bottom of the thermocline, in agreement with other biological investigations. The present holographic results show similar behavior, since a large percentage of the "particles" observed, especially below the thermocline, were determined to be living organisms. Pieper & Holliday (1984) found secondary acoustic scattering peaks, indicative of high organism concentrations, which tended to correlate well with the ocean thermal microstructure. The present holographic measurements are too sparse to determine whether or not corresponding localized particulate or organism concentration peaks were present.

The types of organisms observed in the holographic images seem to agree with the comments of Stewart et al. (1973), that copepod crustaceans are the

principal zooplankton in many ocean regions and with Holliday & Pieper (1980), who observed such zooplankton types as copepods, larvacean (*Oikopleura*) and euphasiid larvae in their May 1978 pump samples just mentioned. Appendix III presents photographs of some of the present holographic images showing some of these same organisms. The finding of high zooplankton counts in deeper waters should be of interest in cavitation studies since zooplankton, with their metabolic gases, may presumably act as cavitation nuclei as discussed in Chapter I.1.

As in the presentation of bubble data, the particle results of Station 5 at the Whites Point sewage outfall must be discussed separately, since they clearly represent atypical ocean particle concentrations. The waters above the sewage plume were fairly clear, but at about 25 m the particle concentrations increased by at least a factor of 4 across all measured size ranges. This significant increase in particle concentration can be attributed to the presence of the sewage plume, which is shown distinctly in the transmissometer trace of Figure 1.4.2 (c). As mentioned in the previous section, the relative concentration of organisms in the plume was not determined. The presence of some organisms in the plume was noted however, and several of the organism photographs in Appendix III were recorded there. Peterson (1974) made Coulter Counter examinations of samples taken from the same waters, although his interests were in optical properties of seawater, so his particle measurements covered only the "optically important" radius range from 0.35 to 10 μm. Peterson found that a $4°C$ thermocline was sufficient to prevent intrusion of effluent to the water above the thermocline, but that a weak winter thermocline of $1°C$ was insufficient. The present results are in qualitative agreement with those of Peterson in that the roughly $6°C$ thermocline present during the present testing was sufficient to restrict the vertical transport of effluent sludge particles. In fact, comparison of Figures I.4.15 and I.4.17 shows that the particle concentrations in the upper 20 m were comparable at Stations 3 and 5.

I.5.3 Expected Tensile Strength of Ocean Waters

The relationship between the number density distribution of total bubbles and particulates in a liquid and the tensile strength of the liquid remains an elusive problem in cavitation research. Little can be said about the role of particulates as cavitation nuclei apart from the obvious consideration that larger concentrations of particulates are likely to lead to higher active cavitation nuclei populations. On the other hand, the dynamic properties of gas bubbles are related to their size by the Rayleigh-Plesset equation (Equation I.1.1). Even in this case cavitation results from the combination of the dynamic and interference effects among developing cavities with the statistical occurrence of bubble nuclei and depends significantly on the specific flow conditions. Therefore, a constant relation between the tensile strength of liquids and their bubble population can be established only in an idealized situation where dynamic and interference effects are neglected by considering only the static equilibrium of individual bubbles. Then a lower bound for the tension required to cause cavitation is given by the critical tension of a spherical gas bubble which, in the absence of viscosity, mass diffusion and thermal effects, is given by Equation I.1.7.

The sparse bubble data collected in the present experiments are insufficient to determine a statistically significant value of the tensile strength for each water sample examined, but several important points can still be made. As shown in Figure I.4.9, the test seawater would be expected to cavitate at least occasionally under an applied tension of about 100 Pa and in general would be expected to cavitate under an applied tension of about 2000 Pa. These values can be compared with several determined by different techniques and reported in the literature. Shen et al. (1986) present tables of tensile strength values for various sea waters using venturi systems. These data indicate critical tensions ranging from -5.8×10^4 Pa (compression) at 200 m submergence at Exuma Sound to 2.1×10^5 Pa at 65 m off the Britton coast, with an average tensile

strength of all waters examined of about 6×10^4 Pa. Akulichev & Ilyichev (1986) used an acoustic resonator to determine the maximum acoustic amplitude that could be applied to seawater samples at various frequencies without causing cavitation. This threshold amplitude was taken to be the local tensile strength. This technique was used in a variety of sea waters worldwide, and the measured tensile strengths ranged from 1.35×10^5 Pa in the North Sea to 5.6×10^5 Pa in the Arctic Ocean, with an average of about 3×10^5 Pa. They attribute the localized differences in tensile strength to differences in concentration of gas bubbles and plankton.

The effectiveness as cavitation nuclei of the large number of particles and organisms observed cannot be determined by any device that simply counts and measures them. The present particle results therefore provide an upper bound on the total number of potentially available nuclei, without determining what percentage of these potential nuclei may actually be active in a given pressure field. This difficulty can be overcome only by direct observation of cavitation induced by the particulates under controlled circumstances, for example, through use of a venturi cavitation susceptibility meter. While the percentage of total particles that will become active must be expected to vary depending on the exact composition of the total population, it will be instructive to consider the results of several previous investigations into this problem. For laboratory waters, Lecoffre & Bonnin (1979) reported that often less than one particle per million acts as an active nucleus, and Godefroy et al. (1981) showed venturi results indicating that the concentration of active cavitation nuclei is several orders of magnitude lower than the total concentration of all particles suspended in the liquid. Billet (1985) reports the results of Wushansky & Baiter, who made electron microscope and venturi examinations of the water in Lake Ammer and found that the total particulate concentration in the 0.05 to 50 μm radius range was on the order of $10^5/cm^3$ but that the concentration of active nuclei was only about $1.5/cm^3$, with an equivalent bubble radius of 1.5 μm or less.

Overall, large variations are seen in the results of various investigations into bubble and particle concentrations as well as the tensile strength of seawater. At present, the number of comparative simultaneous investigations into these properties of the ocean are too few to allow determination of whether the differences are due to experimental technique or to inherent variability of the ocean. The waters of the ocean are known to exhibit widely differing physico-chemical properties such as gas content, salinity, temperature and the like, and the effect atmospheric conditions on the sea is also very strong.

I.5.4 Holography for Marine Nuclei Examinations

Since one of the primary goals of this investigation was to determine feasibility of a holographic system for study of marine nuclei, a few comments are in order as to the practical applicability of such a device. The holocamera was successfully deployed at several test stations to depths of 34 m in the course of this investigation. A considerable number of high quality holograms were recorded *in situ*, allowing reconstruction and analysis of clear images with resolution down to about 5 μm. Each hologram contained a fairly large reconstructable volume, on the order of 800 cm^3. Examination of the reconstructed images under high magnification allowed clear visual determination of object type, and the short exposure time gave sharp unblurred images. This technique seems to be particularly useful for the study of delicate organisms or aggregate particles including "marine snow," since the objects are viewed in an essentially undisturbed environment. The permanent record stored in each hologram allows later reanalysis with a different goal (for example, to determine concentration of a particular organism) or double-checking of results, possibly by another operator.

There are some drawbacks to the application of holography in such a study, including the practical difficulties of handling in the field while maintaining the various optical components in perfect alignment. The present examinations

were all made under very calm sea conditions, and even so considerable problems arose in the areas of handling and transport. Future marine holographic investigations could be more comfortably made, and possibly extended to a wider range of ocean conditions, if the holographic system were smaller and easier to handle. A high-power continuous wave gas laser would require considerably fewer electronics and when used in conjunction with a very short-opening shutter should be able to produce satisfactory holograms.

The reconstruction process is difficult and time-consuming, and must be performed by a trained operator. Even with detailed analysis of the full sampled volume (requiring at least 5 man-days) the statistical error for bubble measurements will be high because of their relatively low concentration in the sea. As pointed out in Chapter I.4, there remains some question as to whether some of the "bubbles" counted may actually have been organism eggs, although reanalysis was done, and only objects containing both a clear central virtual source image when slightly off-focus and an internal refraction ring pattern were included as bubbles. Although improper identification seems unlikely in the present results, it could explain the correlation between organism and bubble concentrations. The holographic reconstruction procedure should be able to benefit greatly from the current increases in availability and capability of computer image analysis systems. A great deal of work has been done in this field by investigators such as Hausmann & Lauterborn (1980), but as yet no standard automated reconstruction system has been fully proven. Such a device would be a considerable improvement in the field of holographic measurement, since the time required for reconstruction is currently the major prohibition to obtaining statistically significant numbers of counts over all nuclei size ranges. In addition, a dependable and indisputable means of distinguishing bubbles from particles could conceivably be implemented in such a system.

Finally, the major drawback of using any total bubble and particle counting technique is that it cannot tell which of the objects observed will be active in

the cavitation inception process. Further *in situ* holographic examinations of seawater in conjunction with simultaneous testing with a device such as the venturi cavitation susceptibility meter would be very useful in determining of how many of the large number of potential nuclei seen holographically are indeed active nuclei under a known pressure field. In particular, the effect of marine organisms on the cavitation process must be clarified. As a simple laboratory experiment, it should be possible to use one of the standard bubble detection devices to monitor populations of typical plankton and to observe whether the biological bubble production speculated upon in this thesis is actually a viable mechanism in the ocean.

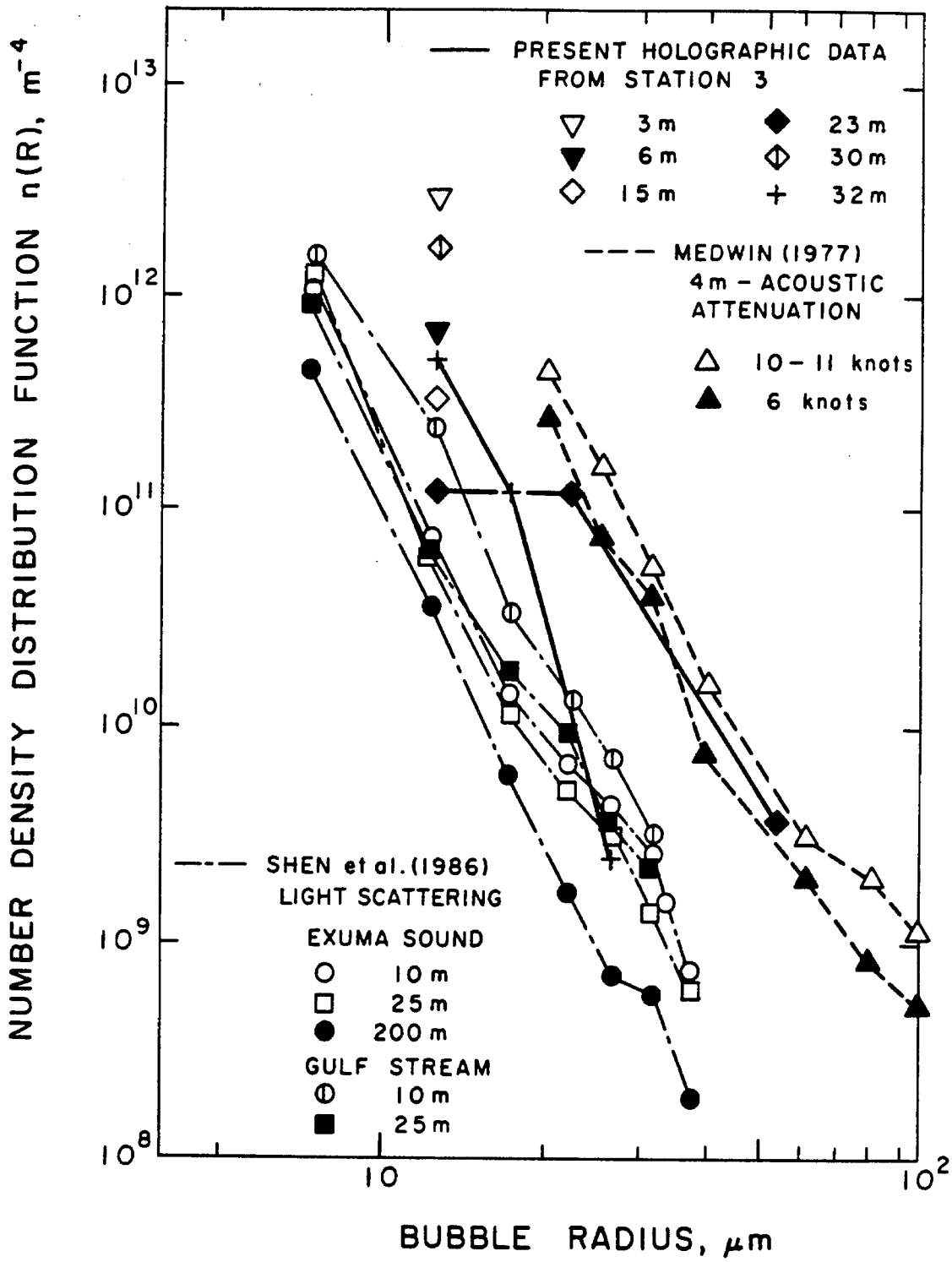

Figure I.5.1. Present bubble number density distribution data from Station 3 plotted along with some of those of Medwin (1977) using acoustic attenuation in Monterey Bay and Shen et al. (1986) using a light scattering technique in waters of the Gulf Stream and Exuma Sound.

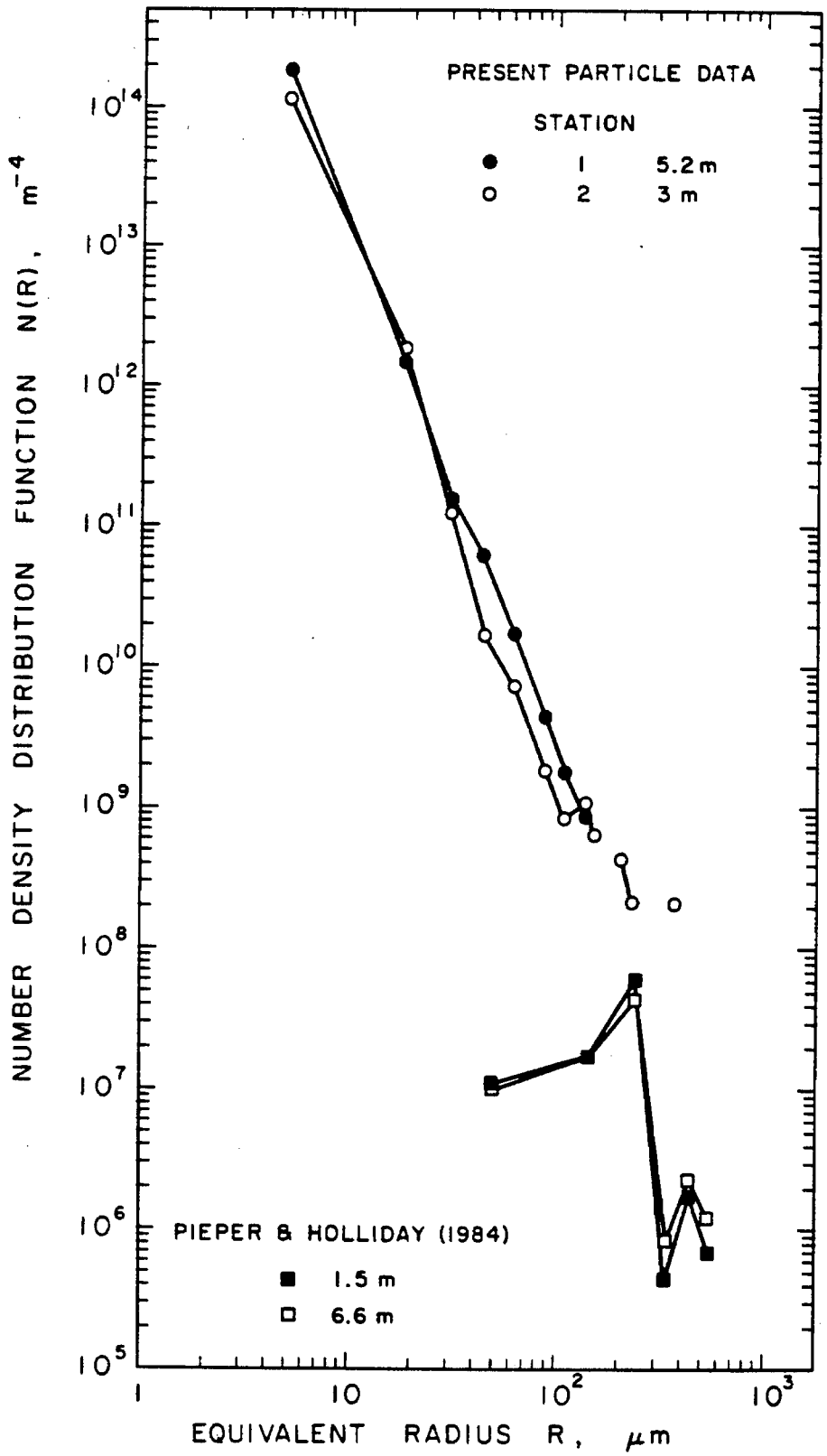

Figure I.5.2. Total particle results of Stations 1 and 2 plotted with those of Pieper & Holliday (1984) using acoustic scattering to detect zooplankton distributions.

CHAPTER I.6
SUMMARY AND CONCLUSIONS

A pulsed ruby laser in-line holographic system was constructed and deployed for measurement of bubble, particle and organism concentrations in the ocean. Holographic detection was shown to be a reliable method of measuring the nuclei number concentration density distributions. The unique capability of holography to provide discrimination between bubbles, particles and organisms is of great value for *in situ* sea water analysis.

Overall very high concentrations of the various types of potential cavitation nuclei were observed at all of the test sites and depths examined, although the statistical significance of these results is strong only in the smaller size ranges, where a significant number of counts were made. The relatively high bubble concentrations and their population inversion below the thermocline where organism activity was high indicate a possible biological source of bubble production rather than the usual surface mechanisms of breaking waves and whitecaps. The measured population of particulates is somewhat higher than previous comparable data. The number density distribution of particulates decreases approximately as the fourth power of the particle size, as often reported in the literature. An increase in particle concentration near the bottom of the thermocline in clear coastal waters is observed, in agreement with zooplankton population measurements made by Pieper & Holliday (1984). The particulate measurements above a sewage outfall clearly indicate the presence of the effluent plume, and verify observations of Peterson (1974) that a normal summer thermocline is sufficient to prevent intrusion of the plume into surface waters.

Further study is needed to clarify the dependence of the tensile strength of liquids on their nuclei content and therefore to deduce scaling laws for cavi-

tation phenomena. This is especially true in the case of particles, whose effect on the liquid susceptibility is not yet fully understood. However, the total concentration of particles and bubbles in a liquid still provides an upper bound for the number of potentially active cavitation nuclei. Much higher concentrations of particles were detected in the ocean than in typical cavitation test facilities. These differences must be taken into consideration when trying to relate laboratory results to prototype operation. The measured bubble sizes can be used to indicate that the average tensile strength of the ocean waters examined in this study should be on the order of a few thousand Pascals, with a minimum expected value of about one hundred Pascals. The present results tend to support the recommendation of Billet (1985) that a concentration of at least 3 bubbles per cm^3 in the 5 to 20 μm radius range is needed in test facility water in order to model marine conditions.

PART II
CAVITATION INCEPTION IN A TURBULENT SHEAR FLOW

CHAPTER II.1
INTRODUCTION

Turbulent shear flows are common in many cases of engineering importance, including submerged jet slipstreams and the separated wake flows behind "bluff" or non-streamlined bodies. These simple flows are a vital component of the complicated separated flow fields associated with such practical devices as gate valves, hydrofoils, propellers, pumps and turbine runners. Cavitation in these devices is of great practical interest because of the generally harmful effects of noise, erosion and vibrations associated with cavitation.

II.1.1 Cavitation in Turbulent Shear Flows

Most cavitation studies to date have been made on smooth, streamlined bodies (see for example Arakeri & Acosta 1979; Huang 1981), and the basic cavitation characteristics in these cases are now fairly well understood. Although shear flow cavitation is a fairly common phenomenon, understanding and prediction of inception in these flows have not been very extensively pursued because of several analytical and experimental complications. First, the controlling features of the underlying *single phase* flow have yet to be determined, remaining a topic of much basic research interest. Second, cavitation phenomena in these flows are ill-suited to laboratory examination because of their commonly observed strong scaling, with scale effects generally much more significant than those associated with the flows around streamlined bodies. For example, the inception index for the flow around streamlined bodies approaches $-C_{pmin}$ as body size and free stream velocity are increased (e.g., Parkin & Holl 1953). In contrast, the minimum pressure coefficient for the flow around a disk is on the

order of $C_{pmin} = -0.45$, while the inception index is typically in the range of 1 to 2, and several investigators have observed a steady trend of increasing inception index with Reynolds number with no upper bound on σ_i yet established. In general, the inception indices for shear flows are considerably higher than those for flows around streamlined bodies; i.e., shear flows are typically more susceptible to cavitation. Unlike cavitation in flows around streamlined bodies, inception in shear flows occurs in the freestream, usually far from the test body, due to the vortices and associated fluctuating pressure peaks in the free shear layer. Knapp et al. (1970) point out that the vortex cores in a shear flow are the centers of minimum pressure in this flow, as opposed to the minimum pressure points that occur along the body surface of a more streamlined flow.

Turbulent flows exhibit wide fluctuations in velocity and pressure, generally leading to a broad range of inception indices even for constant mean flow conditions. The vortex structure of turbulent flows can lead to very low localized vortex core pressures that can cause cavitation even when the mean flow pressure significantly exceeds the vapor pressure. A bubble nucleus can be expected to cavitate in a vortex core if the core pressure is low enough to satisfy Equation I.1.7 for a time period long enough to satisfy the bubble response time.

Pioneering work on cavitation inception and scaling in turbulent shear flows was performed by Kermeen & Parkin (1957) in their study of cavitation inception in the separated wakes behind a series of sharp edged disks. They found that inception consistently occurred in the turbulent shear layer of the disk wake, and a steady monotonic increase of the inception index was observed with increasing body Reynolds number, with no limiting upper bound evident. Inception could not be related to the minimum pressure measured on the body, the cavitation inception index σ_i always being much larger than $-C_{pmin}$. The distinct shear layer vortices led Kermeen & Parkin to speculate that inception occurred in the vortex cores, and to develop a semi-empirical model of the roll-up of two-dimensional vortices that could be used to predict the inception index. This

analysis gave proper order of magnitude values for the inception indices, as well as their velocity dependence, but could not explain the observed dependence of σ_i on body size. Arndt (1978) conducted cavitation experiments in the wake of sharp edged disks with similar results. The inception index σ_i was always much higher than the measured value $-C_{pmin} = 0.44$. In addition Arndt (1976) developed a semi-empirical model of inception in the vortex cores, which fit the data for magnitude and Reynolds number dependence of the inception indices fairly well up to body Reynolds number up to about 2×10^5. However, several of the assumptions used in derivation of this model may be debatable (Katz 1981; Katz & O'Hern 1986). In particular, the assumption that the vortex size depends directly on the disk boundary layer thickness and thus on the freestream velocity is at odds with numerous studies of plane shear flows (to be discussed below), which demonstrate that the size of the mixing layer eddies, or thickness of the mixing layer, depends only on the downstream distance from separation, not on the velocity above the layer. Thus, the scaling trend of the cavitation inception indices remains to be fully explained.

As mentioned above, the experimental study of cavitation in shear flows is complicated by the freestream occurrence of inception due to pressure peaks in the flow that occur far from the test body. Katz (1981, 1984) conducted a study of cavitating flows around several axisymmetric bodies, including blunt circular cylinders (zero caliber ogives), and found that inception in the flows around these cylinders occurred in the turbulent separated shear layer, and that pressure fluctuations measured on the cylinder surface could not explain either the large numerical values of the inception indices or their Reynolds number dependence.

A few of the additional investigations into cavitation in turbulent shear flows are those of van der Muelen (1980), who examined cavitation phenomena in the flow past hydrofoils at various angles of incidence, Ooi (1981, 1985), who studied scale effects in submerged water jets, and Franc & Michel (1983), who

looked at the effect of cavitation on vortex shedding in the wake of wedges. All of these investigations indicate that a better understanding of cavitation in the turbulent shear layer is needed to explain inception in free shear flows or large scale separated flows.

II.1.2 Turbulent Structure of Shear Flows

Turbulent shear flows have been a topic of great research interest in the international turbulence community since the early 1970's because they clearly demonstrate the existence of a coherent vortex structure, allowing these turbulent flows to be described in a more deterministic manner. Brown & Roshko (1974) were among the first to note the significance of large organized vortical structures existing up to high Reynolds numbers in a turbulent mixing layer. The coherence of the organized structure was evident even when small scale turbulence was present, that is, in flows meeting the classical definitions of turbulence. The mean velocity profiles in these flows closely matched those measured in earlier investigations into turbulent shear flows, and a broadly distributed energy spectrum was observed, further demonstrating the true turbulent nature of the flow. Existence of quasi-deterministic coherent structures in fully turbulent flows seemed surprising, since this well-defined mechanism appears to contrast with the classical random, stochastic concept of turbulence. Early claims that the vortex structure was just the lingering effect of transition, and that the final state of the flow would be chaotic (e.g., Chandrsuda et al. 1978) have been disproved by numerous subsequent investigations into various turbulent flows that have supported the observations of Brown & Roshko in high Reynolds number, classically turbulent flows. These investigations have established that the initial plane vortex sheet separating the two streams of a plane mixing layer is unstable and quickly rolls up into discrete line vortices by action of the Kelvin-Helmholtz instability mechanism. Winant & Browand (1974) performed dye visualization

in a water mixing layer to show that shear layer growth, which by dimensional reasoning has to be linear, is principally achieved by vortex coalescence rather than by their individual growth. The pairing process involves rotation of adjacent vortices about each other because of their induced velocity fields, until they coalesce into a single vortex of larger scale. This process leads to a discontinuous change of both eddy diameter and spacing, but the mean layer growth remains linear in x as predicted by similarity in the far-field or self-preserving region. Dimotakis & Brown (1976) provided higher Reynolds number verification of this pairing mechanism. However, other investigators such as Moore & Saffman (1975) and Bernal (1981) have disagreed with the idea that the primary growth was due to pairing, arguing instead that it must be due to a large extent on growth of the individual vortices during their lifetimes between pairing events. Numerous investigations have established that the characteristic spanwise vortex size and spacing grow linearly with distance from the mixing layer virtual origin, and that typical spanwise vortex convection velocities are roughly equal to the average of the high and low speed streams above and below the mixing layer.

The existence of secondary, longitudinal or streamwise oriented vortices as part of the shear layer turbulent structure was suggested by some of the shadowgraph flow visualization of Brown & Roshko (1974) in which distinct "streaks" could be seen in plan views of the flow. Several subsequent examinations of the coherent structure of plane mixing layers have provided a great deal more insight into this secondary structure. Konrad (1976) used shadowgraph flow visualization and concentration measurements to show that a "mixing transition" occurred in the plane mixing layer between two gas streams carrying reactive species. Mixing increased by 25% across the transition, and high frequency concentration fluctuations increased by more than two orders of magnitude. Downstream of the transition region a great deal more three-dimensional structure became visible in the shadowgraph pictures. The three-dimensional struc-

ture appeared to be composed of streamwise oriented vortices, which started upstream as tiny hairpin vortices. Briedenthal (1979, 1981) made similar observations in a water shear layer using a chemical dye visualization technique, with even more dramatic increases in mixedness seen across the mixing transition. He found that three-dimensional motion was required to explain the order of magnitude increases in mixing, and that pairing of spanwise vortices did not have this strong effect on the mixing. He also noted the existence of a spanwise instability wave ("wiggle"), which appeared early in the flow and apparently was amplified by stretching to form the "streaks" visible further downstream. Both Konrad and Briedenthal noted that the three-dimensional structure appears superimposed on the primary two-dimensional large eddies without destroying the underlying primary coherence, even well beyond the mixing transition. Bernal (1981) and Bernal & Roshko (1986) made detailed measurements and flow visualization studies that have allowed them to develop a model of the turbulent shear flow including the three-dimensional structure. Persistent streaks were observed for all flow conditions, even at the downstream end of the test section. The spanwise spacing of the streaks fluctuated very little at a fixed downstream location for constant flow conditions. The persistence of the streaks at fixed spanwise positions suggested a dependence on disturbances originating upstream in the settling chamber, and this conjecture was supported by the fact that changes of flow-conditioning screens upstream caused a change in the spanwise streak spacing. Further, the number of streaks across the span and their downstream point of visibility could be shifted by changing the velocity or velocity ratio. The onset Reynolds number (Reynolds number of first streamwise vortex visibility) was strongly dependent on the velocity difference across the mixing layer. A high speed motion picture investigation using laser-induced fluorescence and sheet illumination showed conclusively that the axial "streaks" were actually pairs of counter-rotating vortices, as had been previously speculated by Konrad and Briedenthal. Analysis of the high speed movies

allowed Bernal to develop the mixing layer model shown in Figure II.1.1, in which the braid region between adjacent spanwise vortices contains an array of longitudinal vortices. Each streamwise vortex is part of a continuous vortex line, which snakes between neighboring spanwise eddies. The secondary vortices are superimposed on the periphery of the primary structure in such a way that the basic coherence of the spanwise vortices is not destroyed. This model fits the high speed motion picture observations as well as more quantitative data such as concentration measurements that show fluid from the high and low speed streams being entrained at different spanwise positions. It also gives a zero net longitudinal vorticity in the flow due to the alternating signs of vorticity of each spanwise vortex pair, as expected, since there are no known means to introduce streamwise vorticity into the flow (Jimenez et al. 1985). The secondary vortices act to considerably increase the interface, possibly explaining the mixing transition. Lasheras et al. (1986) performed a low Reynolds number flow visualization of the interface between the two streams of a plane mixing layer and found that the first appearance of streamwise vortices always took place in the high strain braid regions. They agree with Bernal that the plane mixing layer is unstable to three-dimensional perturbations, which are introduced in the upstream conditions.

The results of the investigations mentioned above, along with those of Jimenez (1983); Jimenez et al. (1985) and others provide a great deal of insight into the organization of the turbulent structure in plane mixing layer flows. The turbulent structure of the plane two-stream mixing layer is seen to consist of the primary two-dimensional vortices resulting from the Kelvin-Helmholtz instability and containing the basic component of vorticity, while three-dimensional secondary vortices introduce the other two components of vorticity into the flow. The Reynolds stress and the growth of the layer are controlled mainly by the primary vortices, while the secondary structure provides internal mixing, and possible modifies the stress (Roshko 1980). Secondary vortices are superim-

posed on the primary structure such that the primary structure maintains its basic coherence. The clear, orderly vortex structure remains visible even in high Reynolds number, fully turbulent flows. It should be pointed out that a similar streamwise vortex structure has been observed in many investigations into the structure of the turbulent boundary layer, where the Taylor-Görtler instability is the mechanism for production of longitudinal vortices in the sublayer (Liepmann 1979; Cantwell 1981; Taneda 1983). The mechanism of production of streamwise vortices in turbulent shear flows is as yet unknown. Longitudinal vortices in the braid can be theoretically predicted by considering that any streamwise vorticity "accidentally" injected into the braid would be stretched into longitudinal vortices by the straining field produced by the primary vortices (Corcos 1979). The data of Bernal (1981) and Lasheras et al. (1986) indicate that streamwise vortices are caused by upstream flow perturbations. Once formed, the instability waves are amplified by stretching in the mixing layer braid regions until they become strong enough to be detected. The initial linear phase of instability was given by Pierrehumbert & Widnall (1982) as a wave-like deformation along the span of a two-dimensional vortex, similar to the experimental observations of Briedenthal that the first sign of three-dimensional instability was the "wiggle" of the spanwise cores. Once begun in this way, the vorticity is stretched in the braids by the mechanism proposed by Corcos (Jimenez et al. 1985), so the upstream disturbances essentially act as a means of "injecting" streamwise vorticity in the braid region (Bernal 1981; Jimenez 1983; Lasheras et al. 1986).

This discussion of the role of coherent structures in turbulent shear flows has been very brief and therefore necessarily incomplete. Several review articles are available which can provide further background in this field. Cantwell (1981) reviews coherent structures in turbulent boundary layers as well as free shear layers, and Ho & Huerre (1984) provide a thorough review of work done on mixing layer instability, vortex dynamics and coherent vortex structure. In addition, the introductory sections of Bernal & Roshko (1986) and Lasheras

et al. (1986) review investigations into the streamwise vortex component of the turbulent shear layer.

II.1.3 Scope of the Present Work

Previous investigations of the cavitation characteristics of various types of shear flows by Kermeen & Parkin (1957); Arndt (1976, 1978); van der Muelen (1980); Ooi (1981) and Katz (1981, 1984) have demonstrated the importance of detailed examination of the cavitation process in the turbulent shear layer. In particular, the results of Katz point out the importance of the separated shear layer on inception in the turbulent flows around bodies with large separation regions. Basic understanding of the conditions required for inception in terms of known flow parameters is needed as a fundamental step toward predicting inception in more complex shear flows.

An experimental investigation into cavitation in the wake of a sharp edged plate was performed in order to examine a turbulent shear layer in more detail than was possible in previous, smaller scale experiments. In particular, the large physical dimension of the separated shear flow in the present study allows detailed optical flow observations. The location and appearance of inception have been examined under a variety of flow conditions. Detailed measurements of the inception index over a wide range of flow conditions were also undertaken. The adjustable flow parameters were the mean static pressure and velocity above the shear layer, and the dissolved air content and nuclei distribution. Since the physical dimension of the flow was fixed, the scale effects studied were only those due to changes in velocity and changes in the liquid susceptibility (nuclei content). The role of Reynolds number scaling was examined at higher values of the Reynolds number than those achieved in previous investigations of shear flow cavitation. Photographic and holographic examinations were undertaken in order to relate the observed cavitation phenomena to the underlying turbulent vortex structure of the layer. Detailed holographic measurements of

pressure fluctuations and instantaneous three-dimensional velocity components were made within the free shear layer. Finally, the effect of nuclei availability on the cavitation characteristics was examined.

The lack of understanding of single-phase turbulent shear flows clearly hinders the understanding of cavitation in these flows. The aim of this thesis is to present the results of this investigation and to interpret them according to their effect on cavitation as well as to provide insight into the underlying flow field.

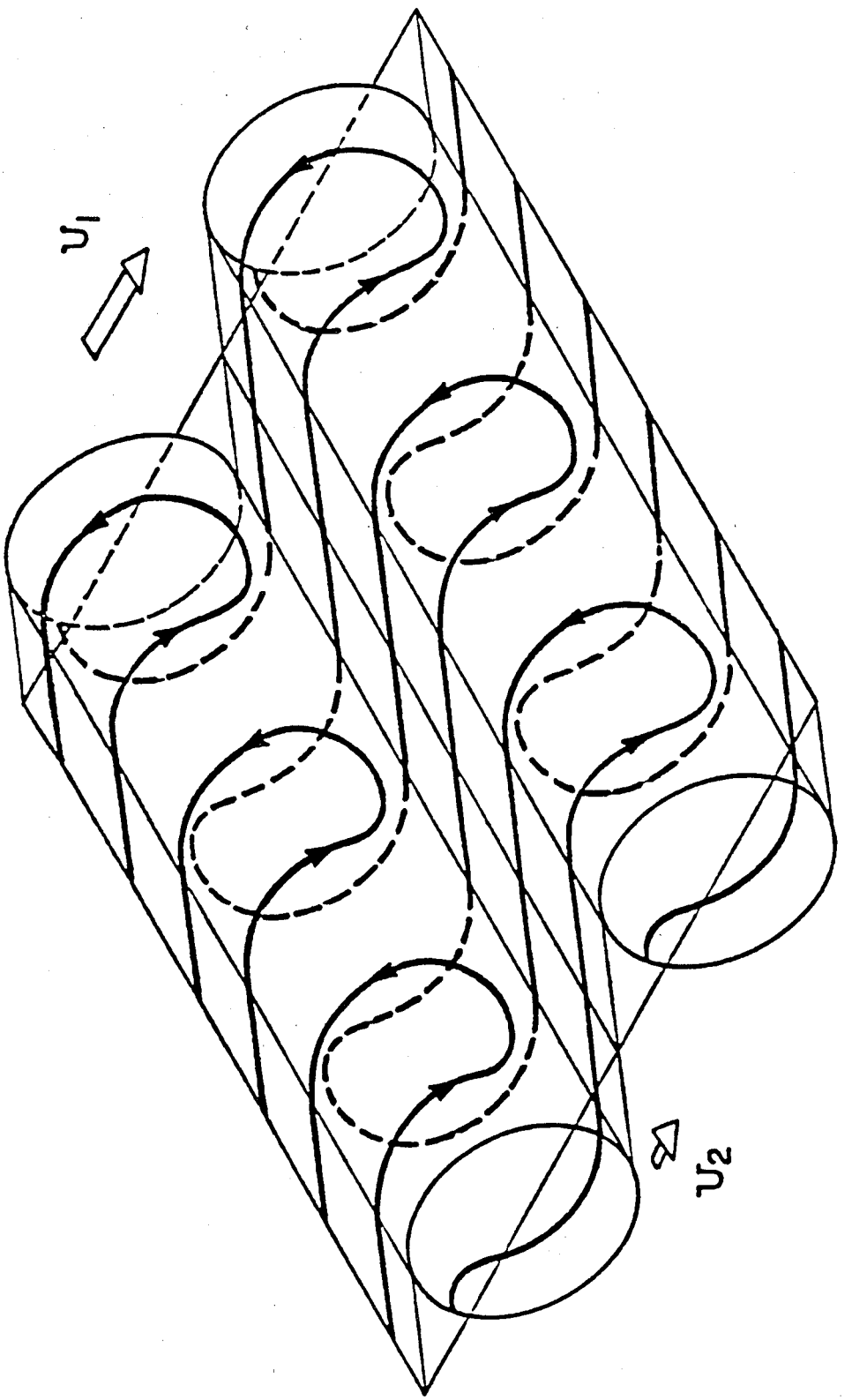

Figure II.1.1. Schematic model of turbulent structure of plane mixing layer (from Bernal 1981).

CHAPTER II.2
EXPERIMENTAL APPARATUS

This chapter describes the water tunnel and test body used for shear layer experiments, and briefly describes application of the holographic camera system to this experiment. Special equipment used only in specific tests (e.g., photographic equipment, air bubble injectors, etc.) will be explained in Chapter II.3, when the experiments are described.

II.2.1 Low Turbulence Water Tunnel

Experiments were conducted in the the Low Turbulence Water Tunnel (LTWT), which has been described in detail by Gates (1977) and is sketched in Figure II.2.1. This tunnel has been specifically equipped as a cavitation test facility, and only those special features needed for cavitation experiments will be described here.

The tunnel water is recirculated by a mixed-flow type pump driven by a 30 HP DC electric motor through a belt drive. The rectangular test section is 2.5 m long and has a cross section that expands from 0.3 by 0.3 m at the inlet to 0.3 by 0.36 m at the outlet, with the spanwise distance remaining constant. Only the upstream 1.25 m are used in the present experiments. The test section is enclosed by ground, polished glass side windows and transparent plexiglass top and bottom windows. Maximum unblocked test section velocity is 7.3 m/s. A low freestream turbulence level of less than 0.04% is maintained over the full tunnel velocity range (Gates 1977) through use of vaned turning elbows and a settling chamber containing two honeycombs and three turbulence damping screens. A nozzle transition from the settling chamber to the test section entrance accelerates the flow through a 16:1 contraction ratio. A pressure control

tank connected to a 5 HP vacuum pump allows control of tunnel mean static pressure from 1.2 *atm* to 0.1 *atm*. The LTWT does not contain a resorber, and at maximum velocity the water recirculation time is about 30 seconds.

The LTWT contains approximately 23 m^3 of tap water, half of which is pumped to storage tanks when the tunnel is not in use. Water quality is maintained through use of filtration and deaeration systems. The deaeration system allows control of the tunnel water dissolved air content from 15 *ppm* molar (saturated) to 3 *ppm* (Ooi 1981). Dissolved air content is measured using a van Slyke Blood Gas Analyzer (van Slyke & Neill 1924). Suspended particulate concentration is controlled using a diatomaceous earth filtration system to remove particles above about 20 μm diameter. Deaeration and filtration procedures are carried out between cavitation experiments. No measurable change in dissolved air content is seen over the course of a typical experiment. Similarly, the water bulk temperature is taken to be constant and equal to the controlled laboratory air temperature of 20 $^\circ C$, and differs only negligibly from this value over the 1 to 2 hours of a typical experiment. For purposes of corrosion control, a weak concentration of about 700 *ppm* sodium chromate (Na_2CrO_4) is maintained in the tunnel water. Efficient use of sodium chromate requires a basic environment, so the tunnel water pH is maintained at 9.5 through addition of potassium hydroxide (KOH). The weak chemical concentrations have a negligible effect on the physical properties of the water.

Velocity and pressure measurements can be made either with mercury-water manometers or with absolute and differential pressure transducers. The transducer digital displays can be remotely "frozen" to allow instantaneous recording of a specific pressure and velocity of interest during a dynamic process. The nominal accuracy of the velocity and pressure transducers is 0.5%. The manometers are bled and zeroed and a transducer calibration check is performed prior to each test.

II.2.2 Test Body: Shear Layer Generator

The test body for these experiments is a sharp edged aluminum plate extending vertically into the flow, as sketched in Figure II.2.2. The tip of the 2.5 cm thick plate is chamfered to a 30° angle in order to give a clean sharp edge for flow separation. The plate spans the full 0.3 m width of the test section and is sealed to the side walls to prevent leakage flow around the edges. A 2.5 cm stand-off above the floor of the test section prevents boundary layer contamination of the shear layer, and a 50 cm long horizontal bypass plate separates the two flow regions. The plate blocks half of the oncoming flow, and the maximum velocity that can be reached above the shear layer is about 12 m/s, measured at a pressure tap located 35 cm downstream of the sharp edge (see Figure II.2.2). The plate is machined to provide ports for injection or pressure measurement at several sites on the front and back faces and along the oblique edge.

II.2.3 Holographic Camera

The holographic camera described in detail in Part I has been used extensively in the LTWT for various purposes, including measurement of cavitation nuclei distributions, flow visualization (Katz 1981, 1984) and pressure fluctuation measurements using injected air bubbles as pressure sensors (Ooi 1981). The holocamera was used for measurement of nuclei density distributions as well as three-dimensional velocity components and local pressure fluctuations in the shear layer during the present investigation. Detailed descriptions of the holographic camera and reconstruction systems can be found in Chapter I.2.

Figure II.2.3 is a schematic diagram, and Figure II.2.4 a photograph, showing the holographic system mounted on an optical bench for measurements in the water tunnel test section. The Pockels cell Q-switched ruby laser is an ideal light source for water tunnel investigations because its short (20 to 50 nanosecond) pulses effectively freeze the images of small objects streaming through the region of interest at fairly high speeds.

Although the initial holographic setup was in the off-axis or reference beam configuration in order to gain the advantages of this technique discussed in Chapter I.2, the Fraunhofer or in-line technique was eventually chosen for the present set of experiments (see Figure II.2.3) because of its simplicity and requirement of fewer optical components. The Fraunhofer holographic technique is limited to cases in which the sample is composed of a dilute concentration of small particles, in order to maintain a sufficiently strong undiffracted reference beam. This is not a serious limitation for the cases of interest here.

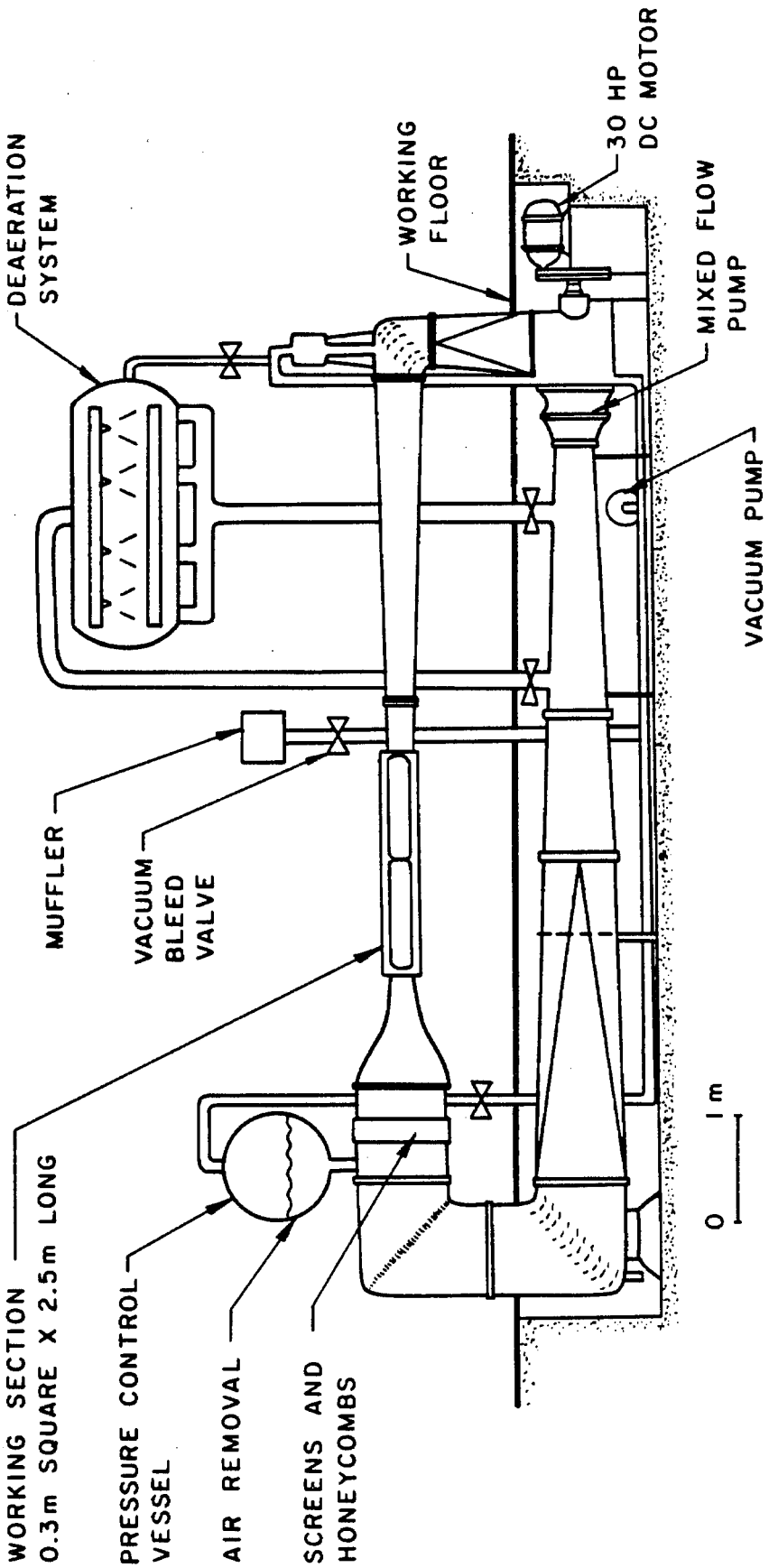

Figure II.2.1. Diagram of the Low Turbulence Water Tunnel (LTWT) (not to scale).

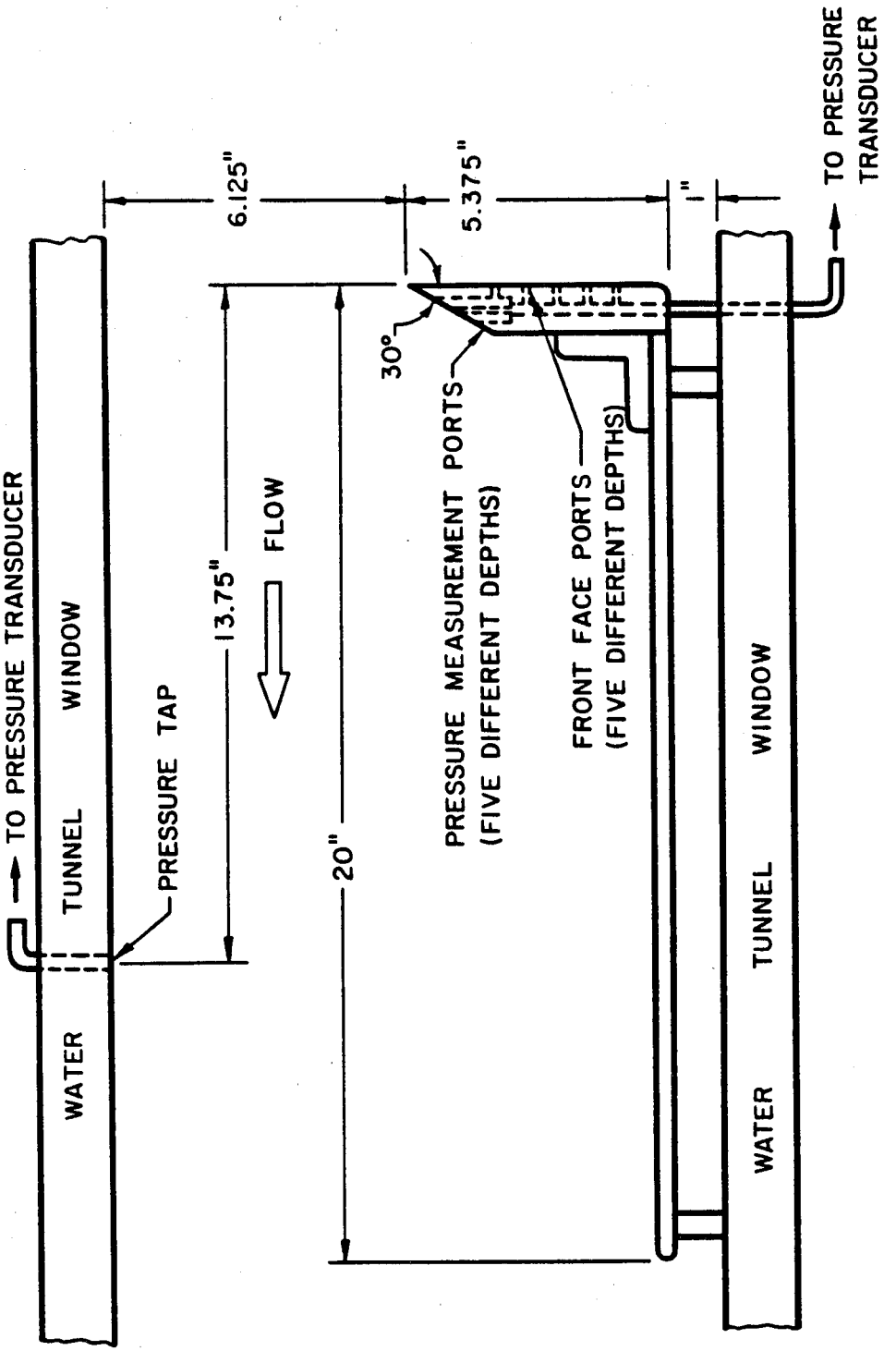

Figure II.2.2. Diagram of the sharp edged plate installed in the LTWT test section. The one inch stand-off distance allows boundary layer fluid to escape underneath the plate to avoid contamination of the flow over the sharp edge.

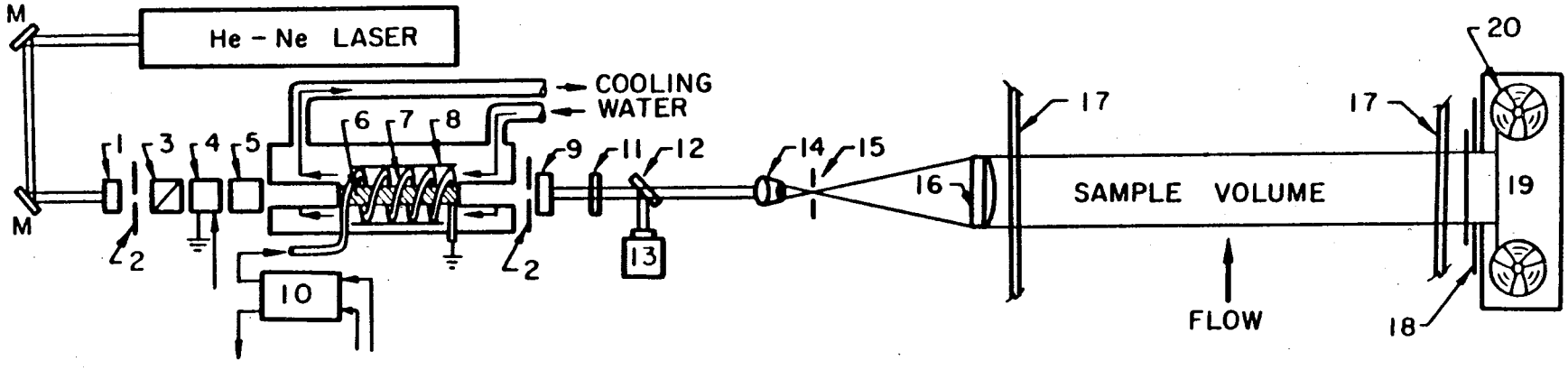

1. BACK MIRROR
2. IRIS APERTURE
3. POLARIZER
4. POCKEL S CELL
5. POLARIZER
6. RUBY ROD
7. XENON FLASH LAMP
8. REFLECTOR
9. FRONT MIRROR-SAPPHIRE ETALON
10. TRIGGER TRANSFORMER
11. NEUTRAL DENSITY FILTER
12. BEAM SPLITTER (4% REFLECTIVITY)
13. PIN DIODE
M. MIRROR
14. MICROSCOPE OBJECTIVE
15. SPATIAL FILTER-10μ PIN HOLE
16. COLLIMATING LENS
17. GLASS WINDOWS OF THE TUNNEL
18. SHUTTER
19. AUTOMATIC FILM DRIVE
20. HOLOGRAPHIC FILM

Figure II.2.3. In-line holographic camera system mounted on optical bench for LTWT experiments. The legend identifies the major components.

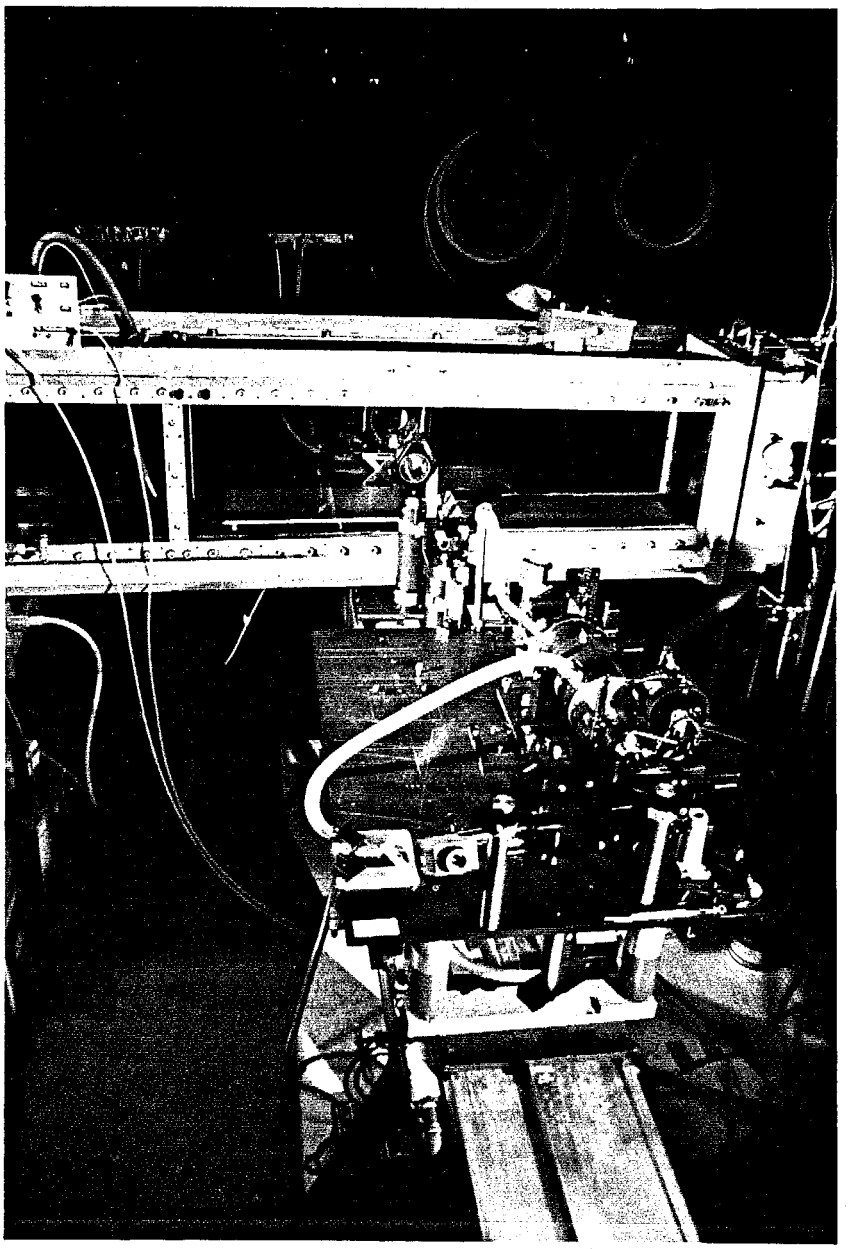

Figure II.2.4. Photograph of in-line holographic system mounted on optical bench for LTWT experiments. The sharp edged plate is visible in the LTWT test section.

CHAPTER II.3
EXPERIMENTAL TECHNIQUES

This chapter will describe the specific experimental procedures used during the present set of experiments. The experimental apparatus described in Chapter II.2 was used in most of these experiments.

II.3.1 Test Conditions Studied

A fairly wide range of test conditions was examined in the course of the present investigations. Testing was performed at freestream velocities above the shear layer (U_L) up to about 12 m/s (or maximum Re_L of about 2×10^6, since h was fixed at 8.8 cm). The minimum local static pressure above the shear region (p_L) was 1×10^4 Pa. The minimum cavitation index that could be achieved at minimum pressure and maximum velocity was $\sigma = 0.16$. Since the primary interest of this investigation is cavitation *inception*, this low σ value was never reached during data recording experiments but only during flow visualization and general observations. The dissolved air content α was varied from saturation (about 15 ppm) to as low as 3 ppm.

II.3.2 Surface Flow Visualization

Flow visualization studies using paint droplets and tufts attached to the front surface of the sharp edged plate were performed in order to determine the nature of the flow and position of the stagnation line on the front face. Figure II.3.1 shows that the flow on the face is two-dimensional, with the corner vortices at the junction of the plate with the tunnel side windows causing only a minor disturbance over a very limited region. This observation was made during both the tuft visualization shown in Figure II.3.1 and the paint visualization studies.

These studies also clearly showed the location of the stagnation line on the front face of the sharp edged plate, allowing measurement of the distance h from the stagnation line to the sharp edge separation point, which was determined to be 8.8 cm. This characteristic length scale was used in determining the body Reynolds number and as a normalization factor in much of the description to follow. The value of h was verified by numerous observations of the pathlines of freestream particles and bubbles as well as of the streaklines of injected dye impinging on the surface of the plate, and by the direction of motion of small air bubbles released on the face surface.

II.3.3 Cavitation Inception Testing

The LTWT test section is enclosed by high quality glass side windows and clear plexiglass top windows, allowing direct visual observation of the flow. Cavitation inception testing was made visually, using stroboscopic illumination. The primary goal of inception tests was to determine the pressure required for the onset of cavitation under various test velocities and dissolved air contents. Accordingly, the tunnel velocity and air content were fixed and the water recirculated under steady non-cavitating conditions at high pressure. The cavitation index was then reduced at constant velocity by using a vacuum pump to lower the tunnel static pressure until the first traces of cavitation became visible. A sharp increase in noise was used as a secondary indication of inception. The pressure transducer reading was frozen at the moment of inception and recorded together with the tunnel velocity to allow calculation of the inception index. The location of the tap for making velocity and pressure measurements (defined as the "local" values) is shown in Figure II.2.2. Since the LTWT does not include a resorber, it was necessary to recirculate the water at atmospheric pressure (high steady-state σ) for at least ten minutes after each inception test in order to maintain a steady population of freestream bubbles (see Katz 1984; Ooi 1985). This time period seems sufficient to allow newly formed bubbles either to rise

because of buoyancy to collect in pockets at the top of the tunnel or to be forced back into solution by their surface tension.

II.3.4 Photographic Studies

Flow visualization is an important means of identification of many key flow features in complicated flows, and has been particularly useful in demonstrating the coherent structure of turbulent flows. Detailed observations of cavitation, or cavitation flow visualization, is an especially useful technique, since it provides some quantitative data on the pressure field as well. The clear glass LTWT windows provide optical access for photographic recording of the flow. Two photographic examinations were performed, first recording a series of simultaneous top and side view short exposure photographs of various stages of cavitation in the shear layer, followed by the recording of high speed motion pictures of the flow in order to follow the convection and evolution of the flow structures identified in the still photographs.

II.3.4.1 Simultaneous Top and Side Photography

The simultaneous top and side photographs were recorded by mounting two 35 *mm* cameras on tripods above and beside the test section. The shutter opening times were electronically synchronized with a high speed flash unit (approximately 8 μs), which was pulsed in the middle of the cameras' shutter opening period. The side view photographs record back-lit cavitation bubbles whose refractive and reflective properties cause them to appear dark against the bright background of the diffuse light sources, while the top view records bright reflections from the side-illuminated cavitation bubbles, providing sharp contrast from the dark background of the black anodized aluminum test body. In both the top and side photographs, the field of view spans the full test section window and the full length of the test body horizontal splitter plate. Flow conditions in the photographic studies cover a wide range of freestream velocities, cavitation numbers and air content levels. Long exposure photographs (up to

1 *sec* exposure time) were also recorded in order to provide a time-averaged view of the shear layer envelope.

II.3.4.2 High Speed Motion Pictures

High speed movies were recorded with an Eastman Kodak High Speed camera at framing rates up to 2600 frames/sec, using 100 foot rolls of Kodak 7250 400 ASA High Speed color motion picture film. The short exposure times (about 200 μs for a framing rate of 2000 frames/sec) required use of up to 10 kW illumination from quartz lamps (3200 K color temperature). Top, side and simultaneous views were recorded under conditions similar to those used for the simultaneous photographs. The configuration of the light sources and camera was essentially the same as in the simultaneous photographs, although a mirror had to be used for shooting the top view motion pictures. Detailed frame by frame analysis of the motion picture film was performed using an NAC Film Motion Analyzer. The film speed for each frame was determined using timing marks automatically recorded on the edge of the film during exposure, and measured velocities were determined to be accurate to within about 10%, based on tracking of freestream particles in a constant velocity stream. Fluctuations of the film registration in the camera led to an uncertainty in determination of object location of up to 3 mm in the cross-span views but only about 1/2 mm in the downstream location, both quite small. The smallest objects that could clearly be identified and followed in the high speed motion pictures were about 1.5 mm diameter.

II.3.5 Holographic Experiments

The holographic camera system was used for a variety of water tunnel measurements, as mentioned in Chapter II.2. Although off-axis holograms were successfully recorded in the tunnel test section, the Fraunhofer or in-line holographic technique was eventually used for all water tunnel experiments. Figure II.2.4 is a photograph of the holographic system mounted for measurements in the water

tunnel test section.

II.3.5.1 Cavitation Nuclei Measurements

Nuclei measurements are needed to characterize the conditions at the moment of inception. As was discussed in Section I.1.2, various devices have been developed for making standard nuclei distribution measurements. Holography has been specifically applied for cavitation nuclei measurements in such studies as Peterson (1972); Feldberg & Shlemenson (1973); Ooi (1981); and Katz (1981, 1984). Several of these investigations were made in the present test facility (LTWT) and have established expected ranges of nuclei for various flow conditions. In the present study, holographic nuclei measurements were made at the sharp edge of the test body in order to record nuclei concentrations in the flow regions above and below the dividing streamline at non-cavitating and incipient cavitation conditions.

II.3.5.2 Holographic Velocity Measurements

The use of holography for determination of velocity components has been demonstrated in numerous investigations, such as the particle tracking study of Crane et al. (1982), who presented 2 and 4 pulse images of 79 μm pollen particles.

Holographic measurement of local three-dimensional velocities is done by using the ruby laser in a double-pulsed mode, in which two Pockels Cell pulses are applied, opening the laser cavity for emission of two laser pulses with a precisely determined pulse separation period in the range of 20 to 500 μs. The two laser pulses form two holograms superimposed on a single film frame, so the reconstructed image displays the three-dimensional displacement of particles and bubbles in the flow. The displacement of these flow tracing objects can then be accurately measured and combined with the known pulse separation times to calculate directly the local three-dimensional velocities in the region of interest. Figure II.3.2 demonstrates double-pulsed holographic velocity determination in

a simple flow, as well as the three-dimensional nature of the reconstructed image. Measurement of the relative strength of the two laser pulses is needed in order to determine the direction of motion and therefore of the velocity vector. The two pulses must be of comparable intensity for clarity of the two reconstructed images, with brighter images corresponding to the more intense laser beam.

Double-pulsed holography was used to measure local velocities at specific regions of interest in the flow, specifically in the vicinity of the first cavities seen at inception. Naturally occurring bubbles and particles in the flow were employed as tracers, since it is desirable to maintain a low tracer concentration, both to allow efficient use of Fraunhofer holography and to ensure accurate matching of image pairs. In addition, the presence of tracer particles in a closed-loop flow facility such as the LTWT can lead to difficulties when determining cavitation nuclei concentrations. Double-pulsed holography can record three-dimensional motions of objects in a fairly large volume (about 1 l in the present case), and so is particularly useful in flows in which the region of interest is not well defined and therefore not well suited to such point-measuring techniques as Laser Doppler Velocimetry. However, as discussed by Crane et al. (1982), there are practical problems of image overlap, as well as difficulty measurement of the z (out of film plane) displacement. The potential for making velocity measurements in the transform plane of the hologram was also discussed by Crane et al.; however, at present this technique cannot be applied to three-dimensional motions.

II.3.5.3 Pressure Fluctuation Measurements

Knowledge of the local fluctuating static pressure field is required for full understanding of a turbulent flow and especially of its cavitation characteristics. The mean pressure variations in a turbulent shear flow are often small, but the instantaneous peak pressures have been shown in several studies to vary significantly from the mean (see, for example, Arndt & George 1979; Ooi 1981;

and Ooi & Acosta 1983). These pressure peaks are responsible for the relatively large cavitation inception indices commonly measured in turbulent shear flows. Numerically large indices show that inception occurs under *mean* pressures much larger than the vapor pressure, but do not provide any information on the response of a nucleus to the *localized* pressure peaks it is exposed to. Measurements of mean and fluctuating pressures on a test body surface are standard and relatively simple procedures, but these same measurements become difficult in a free shear flow. Intrusive probes are unsuitable for detailed fluctuating pressure measurements because of the flow disturbances they cause, the fact that their size inevitably leads to spatially averaged pressure measurements, the directionality of their response, and the fact that premature vortex bursting is known to occur when even a miniature probe is placed in a vortex core, leading to inaccurate measurements of the true core pressure (Arndt 1981).

The concept of using specially "tailored" air bubbles as Lagrangian pressure indicators was introduced by Ooi (1981), and only a few key features of this technique will be presented here. The basic equation of bubble dynamics is the Rayleigh-Plesset equation (Equation I.1.1), which can be rewritten as

$$p_\infty = \left[p_g + p_v - \frac{2S}{R} - \frac{4\nu\dot{R}}{R}\right] - \rho\left[R\ddot{R} + \frac{3}{2}\dot{R}^2\right] \qquad \text{(II.3.1)}$$

The reference pressure $p_\infty(t)$ can be taken to be the local pressure $p_x(t)$ that a bubble at position x in the flow would be exposed to. Therefore, the local static pressure near a bubble can be determined when all quantities on the right-hand side of Equation II.3.1 are known.

It can be shown (Ooi 1981; Ooi & Acosta 1983) that the inertial and viscous terms on the right-hand side of Equation II.3.1 are negligible when the bubble response time is short relative to the time scale of typical pressure fluctuations, so that the bubble responds instantaneously to the pressure fluctuations. In this "quasi-static" case, Equation II.3.1 simplifies to:

$$p_\infty(t) = p_x(t) = p_g + p_v - \frac{2S}{R} \tag{II.3.2}$$

When a bubble of initial radius R_o and internal gas pressure p_{go} undergoes a polytropic expansion or compression, with a resulting radius of R_x, the final gas pressure p_{gx} is given by:

$$p_{gx} = p_{go}\left(\frac{R_o}{R_x}\right)^{3\gamma} \tag{II.3.3}$$

where γ is the polytropic constant. Further, the bubble gas reference pressure p_{go} at static equilibrium is given by:

$$p_{go} = p_o + \frac{2S}{R_o} \tag{II.3.4}$$

where p_o is the mean static pressure in the vicinity of the bubble and R_o the bubble radius. Applying this in Equation II.3.3 gives:

$$p_{gx} = \left(p_o + \frac{2S}{R_o}\right)\left(\frac{R_o}{R_x}\right)^{3\gamma} \tag{II.3.5}$$

Therefore, for known reference bubble size R_o and static pressure p_o, as well as for surface tension S, the local bubble gas pressure can be determined wherever the local bubble size R_x is known.

The use of "tailored" air bubbles involves injection of a uniform stream of known size bubbles containing only dry air into the flow, then monitoring the size of these bubbles as they pass through the pressure field of interest. The vapor pressure term of Equation II.3.2 can then be neglected, since initially the bubble contains only dry air, and the time between injection and measurement is short enough so that evaporation of water vapor to the bubble interior is negligible. Also, the bubble gas pressure term is given by Equation II.3.5, so that from Equation II.3.2:

$$p_x(t) = \left(p_o + \frac{2S}{R_o}\right)\left(\frac{R_o}{R_x}\right)^{3\gamma} - \frac{2S}{R_x} \qquad \text{(II.3.6)}$$

where R_o and p_o are bubble radius and pressure values established at some reference location, and R_x is the bubble radius at location x. Injection of a bubble of known radius and following it as it traverses the flow field of interest, instantaneously recording any changes in its radius, could be done to determine the local pressure values for that single realization. In practice, rather than follow a single bubble, recording its size as a function of downstream position, we record holograms of the flow field containing a large number of injected air bubbles of uniform initial size. The local instantaneous pressures p_x at numerous sites in the flow field can then be determined by measuring each bubble and using the local R_x values in Equation II.3.6, where p_o and R_o are known from the bubble reference conditions.

There are several restrictions on the flow conditions and bubble size for which this technique is applicable. First, quasi-static bubble response requires that the bubble natural frequency be much less than the exciting frequency, or frequency of the pressure fluctuations. Bubble natural frequencies can be determined from Equation I.1.4, or a convenient approximation for the characteristic bubble response time can be used, for example, the expression derived from the Rayleigh-Plesset equation by Arndt & George (1979) and given by Ooi (1981) as:

$$T_b = 1.06\sqrt{\frac{\rho {R_o}^3}{S}} \qquad \text{(II.3.7)}$$

The expected time scale for pressure fluctuations in a free turbulent jet are given by Ooi (1981) to be on the order of 1 ms, and it is assumed that this same order of magnitude holds for the free shear flow. Equation II.3.7 shows that a bubble with a 100 μm radius will have a characteristic response time of about 100 μs, an order of magnitude shorter than the expected pressure fluctuation

time scales. Clearly, even smaller bubbles with shorter response times would easily satisfy the quasi-static requirement for even shorter pressure fluctuation times. However, a practical limitation arises in trying to measure accurately the radii of very small bubbles scattered throughout a significant volume. A compromise between these requirements leads to injected bubble radii of 50 to 100 μm being ideal. The present investigations were made with injected bubble radii ranging from 60 to 80 μm.

Ooi (1981) took the reference location for bubble injection to be the injection point, but in the present investigation the reference location is taken to be the flow region just above the back angled face of the sharp edged plate. The reference static pressure p_o at this location is known from base pressure measurements, and the reference bubble radius is determined by averaging the radii of several bubble images holographically observed in this region. Details of these measurements will be given with the results in the following chapter. Measurements of turbulent pressure fluctuations under non-cavitating conditions using injected air bubbles were made at two freestream velocities, $U_L = 4.9$ and $8.4\ m/s$ ($Re_L = 9.57 \times 10^5$ and 1.63×10^6, respectively). All injection was done with tunnel water at an air content just below saturation. Relatively high mean static pressure was maintained in order to avoid cavitation and the subsequent generation of vapor bubbles, which would make identification of the injected air bubbles difficult. The bubble injectors were glass pipettes with about 45 μm internal diameter, formed from 1.6 mm tubing stock, using a David Kopf Instruments Vertical Pipette Puller. A constant pressure feed of dry, filtered air was supplied to the finished injectors through plastic tubing. There was considerable difficulty in positioning the injectors in such a manner so as to achieve stable uniform injection into the flow region of interest, with the final configuration being that the injectors were taped to the front face of the test body, with the injector tip located 1 cm below the sharp edge. Figure II.3.3 is a photograph of the front surface of the sharp edged plate with injectors

in place, and Figure II.3.4 is a diagram of the air injection system.

Reference holograms were recorded at the injection point to verify uniformity of the injected bubbles and to determine their initial size accurately. Only one injector, located on the test section centerline, was used during testing. Careful examination of the holograms recorded at the injector tip indicated that the injected bubble size was very uniform, and that the bubbles clearly followed the accelerating flow up the plate face. Figure II.3.5 shows the reconstructed holographic image of several injected air bubbles just after leaving the injector tip. When the bubbles reached the high shear region at the sharp edge, many of them were sheared to a highly ellipsoidal shape, but bubble breakup was never observed. Those bubbles that were badly sheared as they entered the high shear region recovered to a more spherical shape within a few centimeters downstream, well before their sizes were holographically recorded. Figure II.3.6 shows reconstructed holographic images of several of the injected air bubbles as they passed over the sharp edge of the plate into the high shear region. Data holograms were recorded centered at the downstream position $x/h = 3.0$, $y/h = 0.22$ in order to record conditions in the nominal center of the shear layer.

II.3.6 Total Pressure Survey

Wake surveys were made with a total pressure probe at several downstream positions from $x/h = 1/2$ to $x/h = 6$. A shielded total pressure probe was used, with the probe internal diameter 1 mm and the shield internal diameter about 4 mm. The shielded probe was selected since it tends to minimize directional dependence of the pressure measurement (Holman 1966). The total pressure probe was held in a vernier mount, allowing accurate positioning of the probe at any point in the flow from the top window (above the shear layer) to 15.7 cm down into the flow, approximately the height of the test section centerline and the sharp edge of the plate. The probe was connected into the LTWT standard manometers and transducers for data recording. The maximum freestream

working velocity U_L for the total pressure surveys was limited to about 7 m/s because of excess vibrations of the probe at higher velocities. Two surveys were made, one at 3.0 m/s and the other at 7.0 m/s.

II.3.7 Body Pressure Measurements

Body static pressure measurements were made at several locations on the sharp edged plate in order to determine the base pressure coefficient, C_{pb}. Static pressure taps were located along the back of the plate and on the angled face (see Figure II.2.2), as well as on the upper surface of the horizontal "splitter plate" behind the sharp edged plate. The static pressure taps could be connected to the standard tunnel manometers and transducers for pressure measurement.

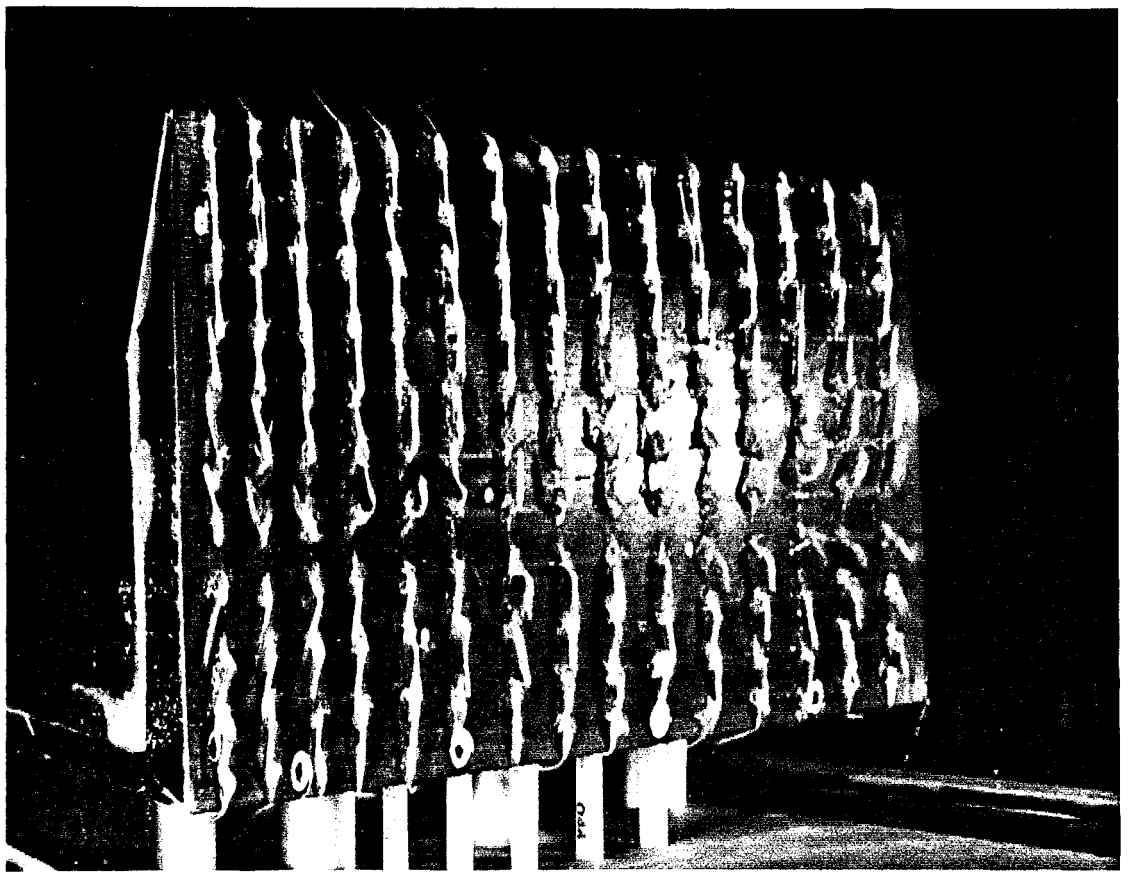

Figure II.3.1. Photograph of tuft test on face of sharp edged plate showing that the flow on the front face is two-dimensional and that wall effects do not extend very far into the flow. $U_L = 9.8\ m/s$, $Re_L = 1.78 \times 10^6$, $\sigma_L = 1.33$. The distance h from the stagnation line to the separating edge was determined to be 8.8 cm from these observations.

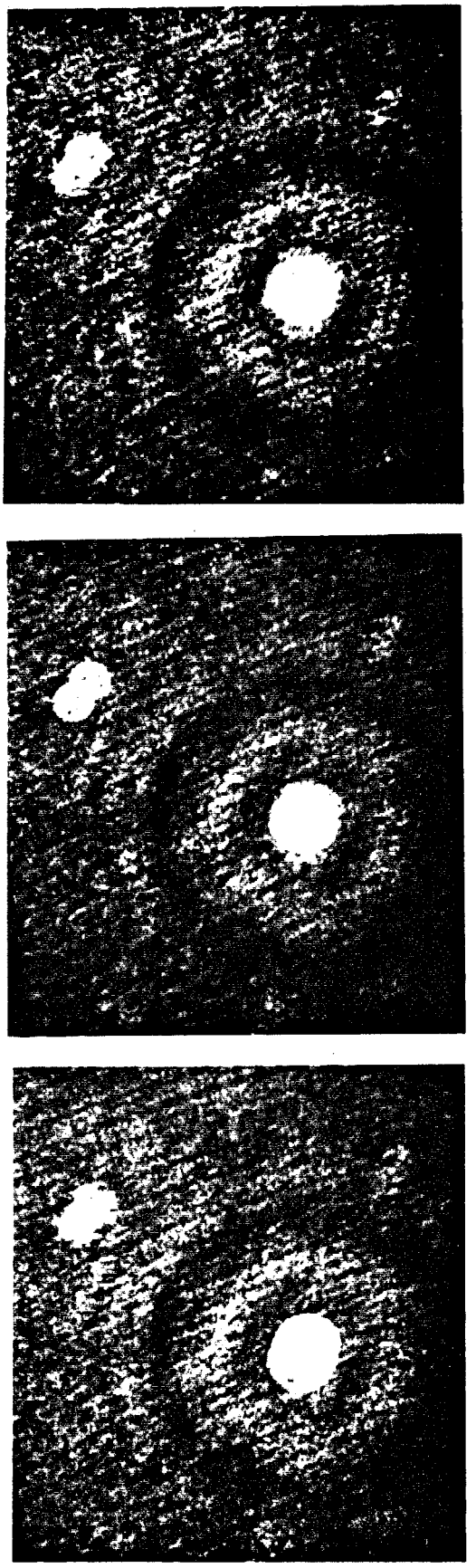

Figure II.3.2. Object location and velocity determination using double-pulsed holographic technique in a simple two-dimensional flow. Three bubble pairs can be seen in each reconstructed plane, with a pulse separation of 200 μs between the two image recording times. In left photograph the large bubble pair is focused ($z = 25.20\ cm$), in center the intermediate size bubbles are focused ($z = 25.35\ cm$), and at right the two small images are in focus ($z = 25.55\ cm$). Average indicated velocity is 0.3 m/s.

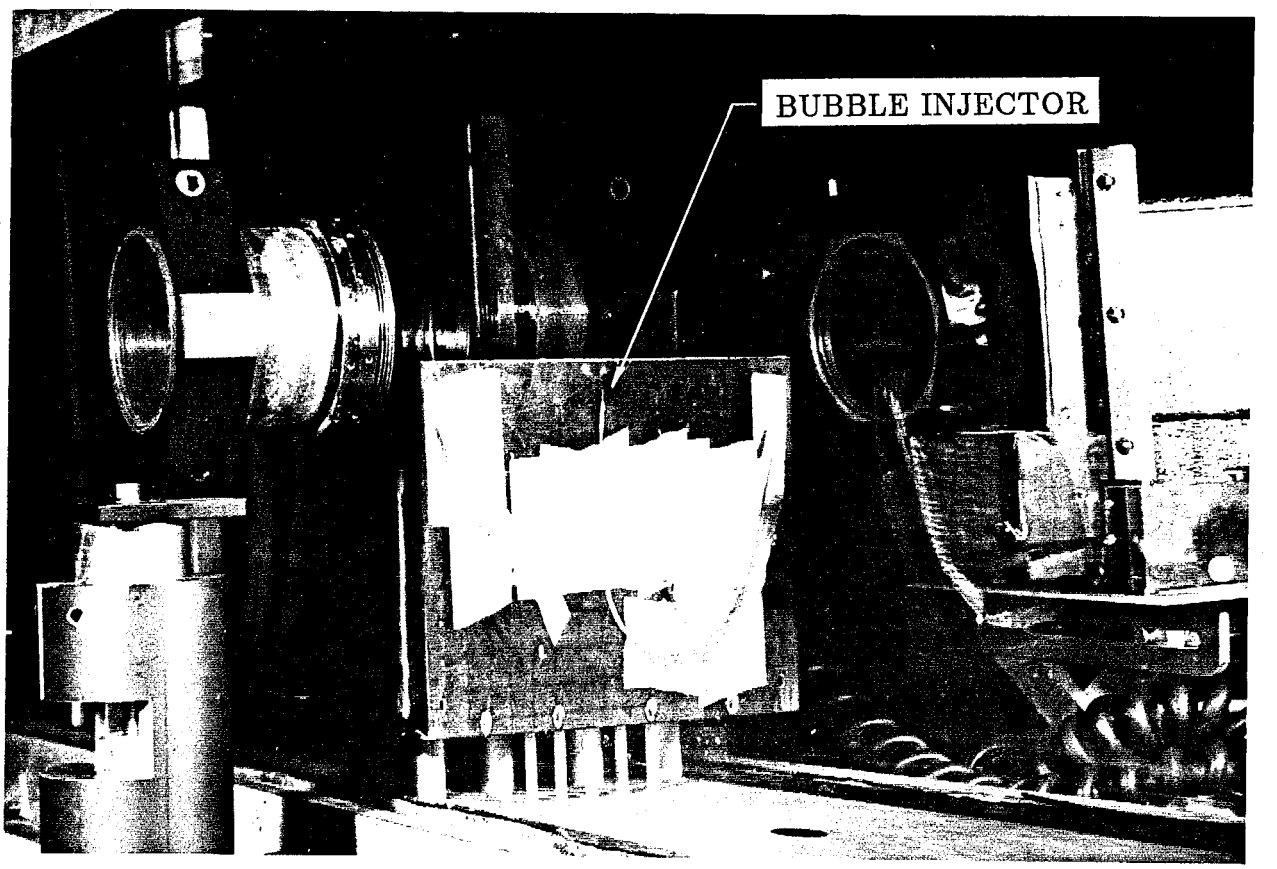

Figure II.3.3. Photograph of air bubble injector attached to front face of the sharp edged plate in LTWT test section. Collimating lens and film drive of holographic system are also visible.

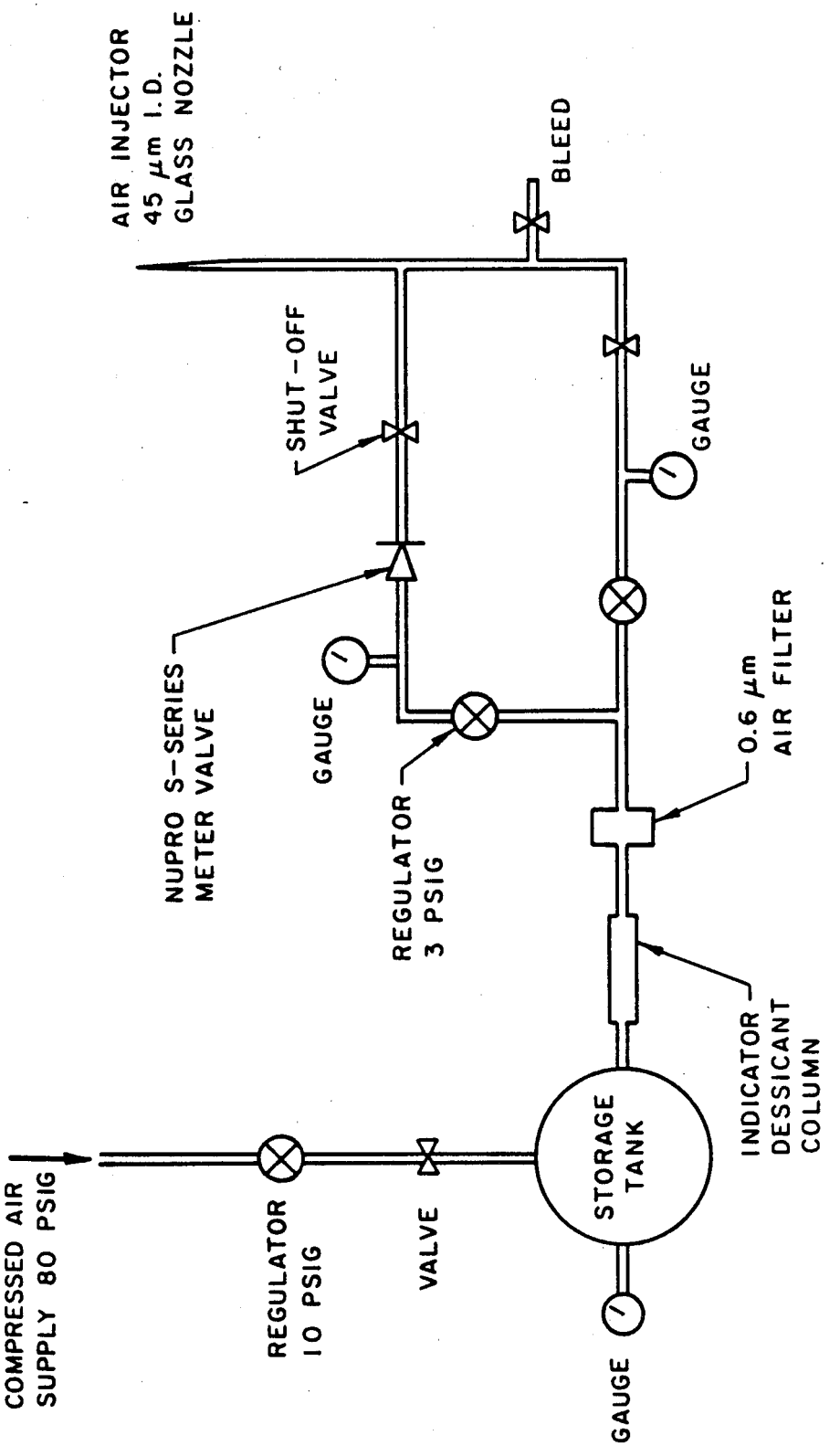

Figure II.3.4. Sketch of the air bubble injection system.

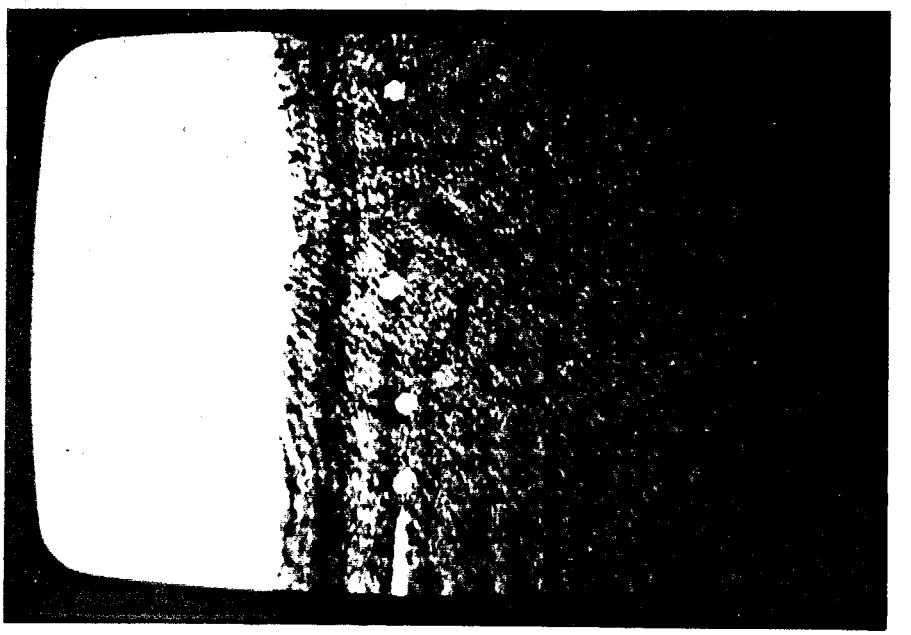

Figure II.3.5. Reconstructed holographic images of air bubbles near injection point on face of sharp edged plate. Mean bubble diameter at tip of injector is about 119 μm. Freestream velocity above the shear layer is 8.4 m/s.

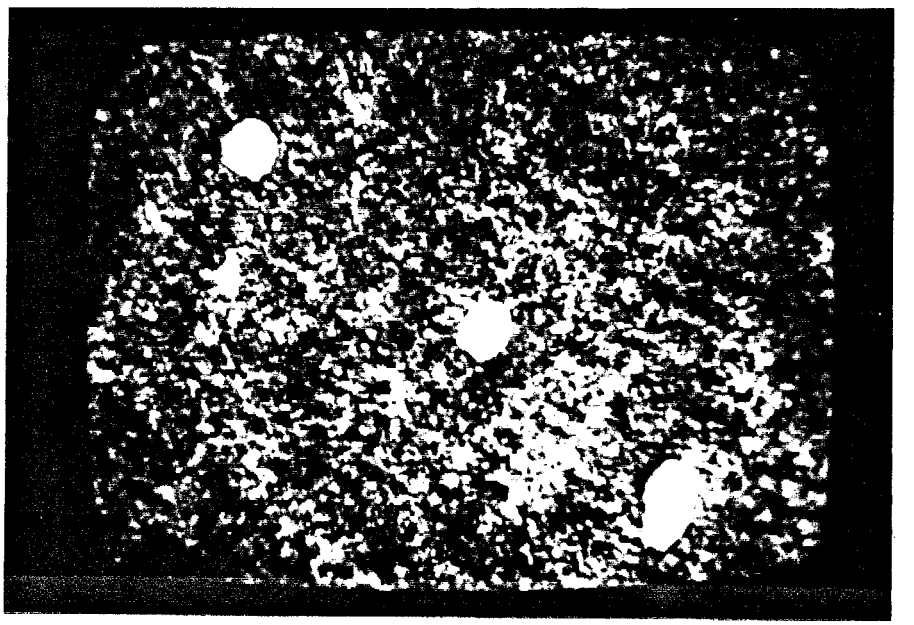

Figure II.3.6. Reconstructed holographic images of injected 119 μm diameter air bubbles as they pass over sharp edge into high shear region. Shearing is evident, but no bubble breakup was observed at freestream velocities up to 8.4 m/s. Bubbles have geometric mean diameters ranging from 157 μm (highly sheared bubble at lower right) to 130 μm (upper left).

CHAPTER II.4
DATA ANALYSIS AND RESULTS

Numerous observations and flow measurements were made in the course of this study. This chapter will present the results of these investigations, and a full discussion of them will be made in Chapter II.5. The present chapter is divided into two sections, the first concentrating on basic flow characteristics, excluding (as much as possible) specific cavitation behavior. The second section focuses on the cavitation characteristics and their relation to the underlying flow structure.

II.4.1 Flow Field

Before presenting the detailed quantitative results, it will be useful to qualitatively describe several aspects of the overall non-cavitating flow field. As discussed in Chapter II.3, surface flow visualization was performed using paint droplets and yarn tufts, and an example of one of these visualizations was given as Figure II.3.1. These investigations clearly established the two-dimensional nature of the boundary layer flow on the front face of the test body. The oncoming stream splits at the front face stagnation line, and laminar boundary layers accelerate from that line under highly favorable pressure gradients toward the top and bottom plate tips. The upper boundary layer separates at the sharp edge and forms a "vortex layer" separating the freestream flow above from the recirculating wake region below. The separation streamline undergoes very strong curvature for about one characteristic length h downstream, then begins to "flatten out" farther downstream. Distinct spanwise vortices roll up in the layer, forming a large spanwise eddy structure, which maintains its clarity for at least the length of the splitter plate, a downstream distance of about $x/h = 6$,

beyond which point the shear flow becomes disturbed by mixing with the flow from beneath the splitter plate and observations are discontinued. A sketch of some of the key flow components and definitions is given in Figure II.4.1, and the long exposure photograph of Figure II.4.2 provides an overall view of the time-averaged flow patterns. Streamline mapping by hot-wire anemometry or other techniques was not made in the present testing, but qualitative flow observations indicate fairly good agreement with the overall streamline patterns measured by Arie & Rouse (1956); Carmody (1964); and Bradbury (1976) in similar flows.

The turbulent mixing layer entrains fluid from the recirculating wake region, thus maintaining a base pressure p_B on the back of the plate, which is lower than the freestream static pressure p_∞. The base pressure coefficient, C_{pb}, can be defined in several different ways, depending on the location of measurement of the "base" pressure and on the location of the reference "freestream" velocity and pressure. Base pressure measurements were made at three locations: two on the back face of the sharp edged plate, just behind the sharp edge on the angled portion of the plate and at a port 6 cm below the sharp edge on the test section centerline (see Figure II.4.1), and one on the upper surface of the horizontal splitter plate. Within experimental accuracy, the mean static pressures measured at these three locations were identical over the full range of tunnel velocities, although fairly large temporal fluctuations were observed at each one. The average base pressure coefficient with relation to the local conditions p_L and U_L above the shear layer (see Figure II.4.1) was -0.01 over the range $U_L = 3.4$ to 9.8 m/s. For a choked flow, the appropriate reference conditions in defining the base pressure coefficient are the undisturbed freestream conditions upstream of the flow constriction (U_∞ and p_∞ in Figure II.4.1). The high blockage ratio of the present test apparatus creates a choked flow, and the base pressure coefficient using the upstream reference quantities and the measured base pressure ranges from -4.3 to -5.2 over the range $U_L = 3.4$ to 9.8 m/s, with an average

value of $\overline{C_{pb}} = -4.95$. This value is in good agreement with a simple choked flow analysis, assuming a stagnant wake and frictionless, incompressible flow. A more complex free streamline model that can be applied to determine the pressure distributions, base pressure coefficient and drag coefficient for bluff-body flows with various blockage ratios was developed by Modi & El-Sherbiny (1977). The blockage ratio in the present case (ratio of model to test section cross-sectional areas) is 0.43 (see Figure II.2.2). With this blockage ratio, the model of Modi & El-Sherbiny predicts a base pressure coefficient of -5.0, in good agreement with the measured value, and a drag coefficient $C_D = 5.5$. Drag was not measured during the present testing. However, Hoerner (1958) gives the drag coefficient for a normal flat plate with a splitter downstream as $C_D \simeq 1.6$ (showing the effect of the splitter plate on the wake vortex structure, since its addition reduces the drag coefficient from the value of 1.9 to 2.0 commonly measured for a normal flat plate without a splitter). The drag predicted by Modi & El-Sherbiny for the present test apparatus is considerably higher than that given by Hoerner, because of the high blockage ratio. All of these drag coefficient values are significantly higher than the value $C_D = 0.88$ determined using the Kirchoff free-streamline theory, due to the theoretical requirements that the free streamline velocity be equal to the freestream value or, equivalently, that the base pressure be equal to the freestream pressure (Roshko 1954). The drag on a normal flat plate can be attributed entirely to the pressure drag component, with viscous drag negligible. The separation points are fixed, so the drag coefficient is essentially independent of Reynolds number above the creeping flow regime.

The overall shape and apparent structure of the shear layer are fairly similar to those seen in numerous studies of the turbulent structure of plane two-stream mixing layers behind a splitter plate (e.g., Brown & Roshko 1974; Winant & Browand 1974; Dimotakis & Brown 1976). Detailed comparison of typical characteristics of several different shear flows will be made in Chapter II.5.

II.4.1.1 Cavitation Flow Visualization

Photographs and high speed motion pictures of the flow taken under various stages of cavitation contain information not only on the cavitation behavior but also on the flow field itself. Cavitation in this flow is very closely related to the turbulent structure, the cavities acting to visualize the flow and allowing examination of the shape and pattern of the coherent vortices. Figure II.4.3 presents six side-view photographs of varying levels of cavitation in the shear layer, indicating the effect of cavitation number on the state of development of cavitation and providing an overall view of the large vortex structure. The shear flow is fully turbulent for all conditions visualized ($1.2 \times 10^6 < Re_L < 2.1 \times 10^6$). The unexpected filamentous nature of the early stages of cavitation is quite distinct, and the cases with more fully developed cavitation clearly visualize the large eddy structure of the shear layer.

Examination of a large number of simultaneous top and side photographs of various stages of cavitation has been useful in clarifying several of the flow features shown in Figure II.4.3. Visual observations under stroboscopic light, as well as photographic examinations at inception (such as Figure II.4.4), have consistently demonstrated that inception occurs in the form of long, thin "strings" oriented in the streamwise direction when viewed from above, and at roughly 45° to the mean flow direction when viewed from the side. This appearance was consistent over hundreds of photographs and numerous visual observations. These "strings" are the cavitating low pressure cores of the streamwise oriented secondary vortices of the free shear layer, occurring in the high strain braid region between adjacent spanwise or primary vortex cores. Inception is not observed in the primary vortex cores, indicating that the lowest pressures in the flow are found in the streamwise cores. At lower cavitation indices, more fully developed cavitation visualizes both the primary and secondary structures, as shown in Figures II.4.5 through II.4.8. These photographs demonstrate that when both

types of vortex structure are visible, the streamwise vortices are primarily confined to the braid region. It is not possible to tell from such a view whether the spanwise cores are actually cavitating or whether they are made visible by entrainment of bubbles formed in the streamwise vortices. Finally, at very low cavitation numbers the full shear layer is visualized by cavitation bubbles, as shown in Figures II.4.9 and II.4.10. These heavily cavitating conditions were used for most of the flow field quantitative visualization analyses to be described below.

Analysis of high speed motion pictures allows observation of the convection and evolution of structures seen in the still photos. The same general cavitation phenomena are visible in the movies as in the still photographs, that is, inception consistently occurring in the streamwise cores and heavier cavitation indicating both vortex structures. Significant variations in the cavitation level and overall appearance of the cavities can clearly be seen over millisecond time scales in these motion pictures, which record only 1 to 2 "real time" seconds of the flow. Figure II.4.11 is a sequence of frames taken from one of the high speed movies at inception. Note that this sequence provides evidence of inception taking place in longitudinal vortex cores, in that in the 2 ms between frames (iii) and (v) of this sequence two distinct cavities grow together to fill in the streamwise vortex core low pressure region. Analysis of similar movies at inception has shown examples of the growing cavity propagating *upstream* at speeds up to 3.4 m/s against the freestream velocity of 7.8 m/s as the core "fills in" as a cavity. Cavitation inception events occur at random throughout the shear layer, except that they are generally absent within the first plate height downstream. This random occurrence indicates that the secondary vortices are not determined by such constant factors as possible imperfections of the sharp edge (although every effort was made to protect this and keep it uniformly sharp) or mean flow non-uniformities. The appearance of cavitation did not qualitatively change after cleaning and rearranging the order of the flow conditioning screens, or after

removing, reanodizing and reinstalling the test body.

Frame-by-frame motion picture analysis shows that the streamwise oriented cavities occurring at inception are convected some distance downstream before collapsing, but very few travel all the way out of the field of view before this occurs. At very low cavitation indices, the spanwise vortex cores become visible close to the separating edge, appearing as straight linear cavities spanning the test section. Under these extreme conditions, inception is clearly observed in both the spanwise and the streamwise vortices, the first appearance of spanwise cores occurring close to the sharp edge, and the streamwise at a downstream distance of $x/h \simeq 1$ to 3. The spanwise cores generally lose their sharp definition by the time they have been convected about 15 *cm* downstream ($x/h = 1.7$), by which time the braid region is usually filled with thin, longitudinal cavities. Beyond about 20 *cm* downstream ($x/h = 2.3$), the spanwise cores have grown considerably, and have lost the clear cavities filling their cores, now appearing as large rotating bubble clouds. Figure II.4.12 displays a sequence of frames taken from one of the high speed movies showing a fairly well developed state of cavitation in which both vortex structures can be seen. The growth of longitudinal vortices in the braid between spanwise vortex cores is evident, as indicated by the appearance of several cavities in the braid during the 4 *ms* between frames (v) and (vi) of this sequence.

It should be pointed out that cavitation cannot be considered as a purely passive visualization technique. Franc & Michel (1983) noted changes in vortex spacing and Strouhal number in the wake of a wedge due to changes in the cavitation index. They determined that a decrease in cavitation index from 2.0 to 1.1 was sufficient to cause a 20% increase in Strouhal number for fixed Reynolds number. Only a small range of cavitation indices was covered during measurements of the shedding frequency in the present flow (see Figure II.4.19), and no clear dependence of Strouhal number on the cavitation number could be detected.

II.4.1.2 Shear Layer Growth Rate

The developing shear layer is expected to grow through the mechanisms of vortex pairing (Winant & Browand 1974) and engulfment of irrotational fluid and individual vortex growth between pairing events (Moore & Saffman 1975; Bernal 1981). Several complementary methods were used to determine the shear layer thickness as a function of downstream distance, $\delta(x)$. First, measurements were made in several side-view photographs of the "visual" thickness at various downstream distances by measuring the thickness of the cloud of bubbles visualizing each spanwise vortex core, as can be seen in the side-view photographs of Figure II.4.3. Similar measurements were made by tracking large spanwise vortices in the high speed motion pictures, with the results in very good agreement. Results of the detailed growth rate analysis in one of the side-view high speed motion pictures is shown in Figure II.4.13, which shows the average shear layer thickness measured at several fixed downstream stations. Fully turbulent flows are characterized by a broad distribution of scales at any downstream location, and this behavior is observed in the present analysis. Thus, there is a large spread to the measured thickness values as indicated by the error bars in the figure, which show plus and minus one standard deviation from the mean thickness value for each normalized downstream location. However, by averaging over several measurements, the mean growth rates can be determined. The average growth rate determined by fitting a straight line to the measured values is

$$\frac{\delta}{h} = 0.225\left[\frac{x}{h} + 0.25\right] \qquad \text{(II.4.1)}$$

also included in Figure II.4.13. This growth rate was verified by analysis of 20 long exposure photographs (see Figure II.4.2), which gave essentially the same growth rate, and indicated no systematic dependence of the growth rate on freestream velocity over the range $U_L = 7.8$ to $11.3\ m/s$. From this analysis the

average growth rate was determined to be:

$$\frac{\delta}{h} = 0.23\left[\frac{x}{h} + 0.08\right]$$

Determination of growth rate from such long exposure photographs is somewhat subjective, and may give a biased growth rate due to the passage of a single large vortex, so the growth rate determined using the motion pictures is considered to be more reliable.

Measurement of the thickness of vortices visualized by cavitation bubbles in their cores could be made only with a very high cavitation level, or low cavitation index ($\sigma_L = 0.37$ for the motion picture and σ_L ranging from 0.16 to 0.40 in the long exposure photographs). Since this low cavitation index may affect the basic flow structure (as was seen by Franc & Michel 1983), it was decided to perform, for comparison, a total pressure survey of the shear layer under non-cavitating conditions. Total pressure profiles at several downstream locations are given in Figure II.4.14 for two freestream velocities, U_L= 3.0 and 7.0 m/s. The locus of 1% total pressure deficit points at each station are sketched in the figures, and the linear growth rate determined by motion picture examination (Equation II.4.1) is also included. The instantaneous outline of the shear layer and thus the total pressure profiles are expected to fluctuate considerably, but time-averaged signals should indicate the mean envelope of the shear region. In addition, probe measurements in highly turbulent three-dimensional flows are subject to considerable error because of the probe response to the fluctuating velocity components. However, this error is likely to affect only the magnitude of the total pressure measurements, so use of such measurements as an indication of the outer envelope of the shear region seems justified. A discrepancy is seen between the growth rate determined visually and the locus of 1% total pressure deficit values shown in Figure II.4.14. The apparent discrepancy within the first characteristic length h downstream can be easily explained by the high

streamline curvature in that region and the lack of applicability of the linear growth law here. Farther downstream the discrepancy is much smaller and may be attributed to fundamental differences between the measured quantities. The flow visualization experiments gave a growth rate for the "visual thickness" of the layer (after Brown & Roshko 1974), whereas the total pressure profiles gave the 1% total pressure deficit, an arbitrary value chosen to indicate the edge of the shear layer.

II.4.1.3 Coherent Structure

Figure II.4.15 shows the trajectories of spanwise vortices as they travel downstream from the vicinity of the sharp edge. The data points indicate measured locations of the vortex centers from one of the high speed motion pictures. The high initial streamline curvature and downstream "flattening" are evident.

The convection velocity of the large spanwise vortices was measured in the high speed motion pictures by frame-to-frame tracking of several well-defined vortex occurrences. Vortex clarity required a low cavitation index σ, and limited this analysis to just two freestream velocities, $U_L = 10.86$ and $11.71\ m/s$, with four distinct spanwise core tracking sequences made for each velocity. Figure II.4.16 shows the average convection velocity of spanwise vortices as a function of local freestream velocity U_L for each of these sequences. A large jitter was observed in the convection velocity of each individual vortex as a function of downstream location, as shown in the convection velocity frequency distribution of Figure II.4.17. The mean values show that the average convection velocity of spanwise vortices is about 40% of the local freestream velocity for the two velocities examined. The large fluctuations around the mean value may be related to vortex pairing in the shear layer, since velocity measurements for particles and bubbles in the freestream above the shear layer did not exhibit such behavior.

Numerous distinct cases of spanwise vortex pairing were observed in the

high speed motion pictures, in a process similar to that described by Brown & Roshko (1974) and Winant & Browand (1974). Measurements of the downstream location of the first pairing event were made in several films, and the average results are given in Figure II.4.18. There is a wide scatter in the data, but overall the average downstream distance to the first pairing event increases with increasing freestream velocity. Persistence of the basic vortex structure through the pairing process was shown by the existence of well-defined spanwise cavities after pairing. The spanwise cores remained visible and clearly rotational after pairing, but in most cases the bubbles visualizing their cores became more diffuse, making further downstream tracking difficult, particularly beyond the second and third pairing events. Pairing may not have been the only means of interaction of the large spanwise vortices. Also indicated were coalescence of three vortices, "tearing," and partial pairing as predicted by Moore & Saffman (1975) and observed by Dimotakis & Brown (1976), although interpretation of the present observations cannot be definite, since pressure changes during pairing could cause specious changes in the appearance of the flow-visualizing bubbles.

In heavily cavitating flows, spanwise cavities became visible in the first 1 to 3 *cm* downstream from the sharp edge of the plate. Determination of the shedding frequency of these cavities is complicated by the fact that the downstream location of first appearance is not fixed. An average shedding frequency based on 3 shedding sequences from a single movie recorded with $U_L = 10.76\ m/s$ was used to determine an average Strouhal number $(2hf/U_L)$ of 5.28. These measurements were made at a normalized downstream location $x/h = 0.14$ since, as mentioned above, vortices were not observed at the sharp edge proper. Measurements were also made of the passage frequency of distinct spanwise vortices past the fixed downstream locations $x/h = 0.5$, 1 and 2. Strouhal numbers for these measurements are given in Figure II.4.19. The single point for $x/h = 0.14$ is also included in this plot. Figures II.4.20 gives examples of the wide distri-

bution of passage frequencies seen at two downstream locations. The scatter is primarily due to the turbulent nature of the flow, but may to some extent be due to difficulty in defining exactly when the vortex core "passed" the station, especially at x/h=2, where the spanwise cores are quite large and are often beginning to lose their sharp definition. Also shown in Figure II.4.19 is the curve for the measurements of Kermeen & Parkin (1957) of the Strouhal number in the wake of a sharp edged disk. Comparison of these measurements will be made in the next chapter. No apparent dependence of Strouhal number on the Reynolds number was observed over the range $1.95 \times 10^6 \leq Re_L \leq 2.12 \times 10^6$, although the wide scatter and limited number of measurements limits the certainty of this result. However, Kermeen & Parkin (1957) and Clark & Kit (1980) observed Reynolds number independence of the Strouhal number for the wake flow behind a sharp edged disk and a turbulent jet generated by a sharp edged orifice, respectively.

The average spanwise vortex spacing l as a function of downstream position is made from the side-view high speed motion pictures, defining the vortex spacing l as the distance between adjacent braid/x-axis intersections (after Bernal 1981). This measurement could be made only in those film sequences in which the cavitation had reached a sufficiently developed state that it was clearly visible in both the spanwise cores and the braid regions. Approximately 60 measurements were made in a single side-view motion picture at the three fixed downstream locations x/h= 1, 2 and 3, leading to an expression for the average vortex spacing, using a straight line fit to the measured data points as:

$$\frac{l}{h} = 0.50 \left[\frac{x}{h} + 0.20\right] \qquad \text{(II.4.2)}$$

The data points showing average vortex spacing at downstream stations $x/h = 1, 2$ and 3, and the straight line fit to these points, are given in Figure II.4.21. Figure II.4.22 presents an example of the distribution of vortex spacing values

measured at a fixed downstream location.

Measurements of the spanwise location of longitudinal vortices showed that in most cases the visible longitudinal cavities were not uniformly distributed across the span. If the underlying vortex array is uniformly spaced, the cavitating cores do not show it. Figure II.4.23 is a graph of the average spanwise spacing of longitudinal vortices as a function of downstream distance. There is a very large scatter in the data, but overall the spacing increases with downstream distance.

II.4.1.4 Strength of Secondary Vortices

Cavitation observations have pointed out the dominant role of the longitudinal or secondary vortices in the inception process in this flow. As mentioned in Chapter II.1, very little is known of the nature of these vortices, their characteristics or their dependence on flow conditions. In order to gain further insight into these streamwise vortices, estimates of their strength (circulation) were made by modeling them as Rankine vortices, with a core in solid body rotation and an irrotational outer flow acting as a potential vortex. Use of this model allows the vortex strength to be determined from cavitation inception observations and measurements. The vorticity in a Rankine vortex is confined and uniformly distributed within the core, and the minimum pressure occurs at the center of the core. For a Rankine vortex with a strength of $\Gamma_s = \pi\omega {r_c}^2$, this minimum pressure p_c is given by

$$p_c = p_\infty - \rho \left[\frac{\Gamma_s}{2\pi r_c}\right]^2 \qquad \text{(II.4.3)}$$

This core pressure can be used to define a minimum pressure coefficient for the vortex as

$$C_{pmin} = \frac{p_c - p_\infty}{\frac{1}{2}\rho {U_L}^2} = -2\left[\frac{\Gamma_s}{2\pi r_c U_L}\right]^2 \qquad \text{(II.4.4)}$$

If, at the moment of inception, the core pressure is assumed to be equal to the water vapor pressure, then $\sigma_i = -C_{pmin}$. Using this assumption, Equation II.4.4 can be rearranged to give:

$$\Gamma_s = 2\pi r_c U_L \left[\frac{\sigma_i}{2}\right]^{\frac{1}{2}} \qquad \text{(II.4.5)}$$

If the vortex core radius, r_c, is equal to the radius of the visible cavity at inception, then the vortex strength can be determined by measuring the cavity radius from photographs or high speed movies recorded at the moment of inception, such as those shown in Figures II.4.4 and II.4.11, and applying these values in Equation II.4.5, along with the inception index and freestream velocity data measured at the time the photograph or movie was recorded. The validity of the assumptions made will be discussed below, but clearly this model can be used to provide order of magnitude strength estimates. Results of such an analysis performed on a number of streamwise cavities at several different freestream velocities and inception indices are presented in Table II.4.1. This table also includes estimates of the expected strength Γ_p of a primary or spanwise core, if it were located at the same downstream location as the streamwise vortices used in determining the Γ_s values. The spanwise strength is given by (Moore & Saffman 1975; Bernal 1981):

$$\Gamma_p = l(x) \times \Delta U \qquad \text{(II.4.6)}$$

Determination of the mean spanwise vortex spacing l as a function of downstream position was presented above, and led to the expression for average vortex spacing given in Equation II.4.2. Use of this expression in Equation II.4.6 was made to determine the values of Γ_p listed in Table II.4.1. The strength of the secondary vortices is found to be on the order of less than 10% of the spanwise strength, yet inception very consistently occurs in the streamwise rather than in the larger and stronger spanwise structure. A discussion of the expected relative

strengths of primary and secondary vortices will be given in the following chapter. Also listed in Table II.4.1 is a dimensionless vortex circulation $\Gamma_s/(r_c U_L)$ proportional to the vortex minimum pressure coefficient. The values of this parameter indicate that the axial vortices are quite intense, on the order of 50 times stronger than those reported by Billet (1981) for hub vortex cavitation.

Several important assumptions were made in estimating the strength values listed in Table II.4.1. As mentioned, it was necessary to assume that the vortex core pressure at inception was equal to the liquid vapor pressure. There may be significant error here as a considerable gas pressure component will be present if the surrounding water is highly supersaturated at the low vortex core pressures (Arndt 1981; Kuiper 1981). (It should be noted that this approach is at odds with the claim made by Kermeen & Parkin (1957), that vortex cavitation is of the vaporous type since there is little relative motion between each growing bubble in the convecting vortex cores and the surrounding liquid.) It was also assumed that the vortex core size was equal to the measured cavity size, which should be accurate to within a proportionality factor and so suitable for order-of-magnitude estimates. In determining the strength of the spanwise vortices, it was necessary to use the freestream velocity U_L as a measure of the velocity difference across the shear layer, since the velocity of the recirculating region beneath the shear layer was not measured. Again, this assumption should be acceptable for order-of-magnitude analysis, since the recirculating wake velocity was fairly small, with an expected value on the order of 0.035 U_L (Brown & Roshko 1974). Another important error source in this estimation is that some of the photographs used to measure r_c were taken at conditions that were close to, but not precisely at, inception. This can be seen by comparing the σ_L values given in Table II.4.1 with those measured during inception tests (to be presented in Section II.4.2.1 below). Photographs taken at conditions just below inception had to be used in order to measure a significant number of streamwise vortex cores, since it is very difficult to capture the intermittent inception process on

film. When the cavitation index is lowered to a value just below the inception index, the capture of a core very close to inception becomes feasible. Use of a cavitation number slightly too low has a minor effect of decreasing the estimated vortex circulation, since Γ_s is proportional to $\sqrt{\sigma_i}$. The measured core radius values shown in Table II.4.1 have a wide spread, but overall, r_c increases with lower σ, as expected and in agreement with measurements by Kuiper (1981). Therefore, the use of non-inception conditions will tend to overestimate r_c and thus *increases* Γ_s since they are linearly related. These two effects of working with inception indices slightly too low are small and tend to cancel each other to some extent.

If there were an alternate means of determination of Γ_s, Equation II.4.5 could be used to predict the inception index. This led to an attempt to measure the tangential velocity U_θ around the longitudinal vortex cores. The small core size of streamwise vortices indicates that high local induced tangential velocities may occur. Double-pulsed holography was used to make these near-core velocity measurements. Figure II.4.24 shows a double-pulsed hologram from such a test (center) along with photographs of reconstructed images showing displacements over the 200 μs pulse separation period. Velocity components are found by dividing the measured three-dimensional displacements by the known pulse separation period. Table II.4.2 displays several velocity components typical of those measured in this study. Freestream velocity U_L was fixed at 7 m/s, and the cavitation index was varied from 0.4 to 1.0 during testing, but was held at 0.5 for the data shown in the table. Several holograms were recorded under these fixed conditions, including the one shown in Figure II.4.24. U_x is the measured velocity in the downstream direction, U_y is normal (up) and U_z is the cross-span velocity. These velocity components demonstrate the three-dimensionality of the turbulent flow; for example, some of the U_x values indicate motion upstream against the mean flow, and in general the three velocity components are of the same order of magnitude. However, the velocities in the vicinity of the

streamwise cores do not seem high enough to explain the fact that inception occurs in these cores rather than in the stronger, larger primary cores. The true *peak* near-core local tangential velocity values could not be measured with the present experimental technique since too few tracers were observed close to the cavitating cores. In fact, the velocity components listed in Table II.4.2 are typically for tracer bubbles located several *cm* away from the nearest visible cavitating core. Higher tracer concentrations are needed in order to determine the peak tangential velocity or its radial distribution about the core needed for determination of the vortex strength. Increasing the data rate for these velocity measurements is difficult, however, first because particle addition affects the concentration of available cavitation nuclei, and also because the presence of a large number of tracers (even bubbles) complicates the task of matching up the two images seen in reconstruction.

II.4.1.5 Turbulent Pressure Fluctuations

The air bubble injection technique described in the previous chapter was employed to determine the magnitude of turbulent pressure fluctuations presumably due to the presence of streamwise vortices in the shear region. Examination of the reconstructed holographic images provides detailed information on the size range of the injected air bubbles at some distance downstream; specifically, a major and minor diameter can be directly measured from the reconstruction monitor for each bubble. The data analysis for determination of the local pressure in the vicinity of each bubble requires that a characteristic bubble radius be determined. This length was assumed to be the geometric mean of the two measured values, i.e., $R_z = \sqrt{R_x R_y}$, since the reconstruction process does not allow direct measurement of the bubble size in the third (z) dimension. In general, the bubbles in the shear layer were not spherical; however, Ooi (1981) has shown that ellipsoidal bubbles remain valid pressure indicators. The accuracy of bubble radius measurement during holographic reconstruction is better than

1 μm, leading to pressure determination accuracy of about 5%.

Pressure fluctuation determinations were attempted for two freestream velocities, $U_L = 4.9$ and $8.4\ m/s$. High mean static pressures were used to maintain non-cavitating conditions. The reference bubble location was taken to be just downstream of the sharp edge of the test body. The pressure at this location is known from static pressure measurements, and the reference bubble radius is determined by averaging the radii of several bubble images holographically captured in this flow region. Downstream holographic measurements were made in a 5 cm diameter cylindrical sample volume spanning the test section at $x/h = 3.0$, $y/h = 0.22$. Bubble measurements were made only in the cross-span region of highest bubble concentration in the reconstructed image (close to centerline bubble injection location) in order to limit the recorded bubble images to those of injected rather than freestream or recirculating bubbles.

The pressure fluctuation measurements for the lower velocity case ($U_L = 4.9\ m/s$) were made with an injected bubble diameter of 146.7 μm, with standard deviation of 2.9 μm for 24 bubbles measured, and a reference bubble diameter of 165.7 μm with standard deviation of 9.2 μm for 28 bubbles measured. The reference pressure above the sharp edge was $9.98 \times 10^4\ Pa$ and the local pressure p_L above the shear layer was $1.0 \times 10^5\ Pa$. Analysis of three downstream holograms was performed, with 90 bubble diameters recorded in the region of interest, giving a mean diameter of 158.6 μm, with a standard deviation of 18.1 μm and a mode (most frequently counted) diameter of 162 μm. The mean static pressure indicated by these measurements was slightly higher than expected ($p_{mean} = 1.4 \times 10^5\ Pa$), and the peak fluctuating values were also high and skewed toward high positive pressure fluctuations. The reason for these unusual findings is that spurious bubbles were recorded in the holograms along with the bubbles of interest, then measured and used as pressure indicators during analysis, as indicated by the fact that only 60 to 80 bubbles were expected to be found at the downstream measurement site for the measured injection

rate. The problem of spurious bubbles had been anticipated and attempts were made to prevent them from playing a significant role. Air bubble injection times were kept short (approximately one minute) to avoid recirculating injected bubbles in the freestream, and tunnel operation was stopped every few minutes to bleed air out of the system before returning to steady test conditions. (Holograms recorded at the injector tip showed that this procedure did not lead to a change in the injected bubble diameter, since during the time that injection was stopped, the air supply to the bubble injector was maintained at its fixed value but shunted to a bypass line.) Since these precautions were taken, it seems that rather than bubbles traversing the entire flow loop and reentering the region of interest, the problem was more likely one of entrainment of injected bubbles immediately into the recirculating wake region. This is the fundamental difference between the present case and that examined by Ooi (1981), in which water containing the pressure indicating bubbles was injected into a quiescent test section where recirculating bubbles were not a factor. Even so, Ooi had to discard bubbles that were "significantly different from the majority of data in that group." In the present measurements, the high freestream static pressure indicated by the original measured distribution, as well as the mean bubble diameter being less than the mode, indicated that too many small bubbles were counted. Therefore, small bubble counts were neglected in an attempt to recover the distribution due only to injected air bubbles. The goal was to center the bubble distribution about its mean (and mode) diameters, bringing those two measurements of central value closer together while simultaneously lowering the indicated mean static pressure in the shear region, p_{mean}, to a value close to the base pressure, and reducing the total number of counts to that expected for the known injection rate. As bubbles are discarded, the value of p_{mean} changes, and thus so do all of the pressure fluctuation values, since by definition $p' = p_{local} - p_{mean}$. Overall, the 20 smallest bubbles (and 5 largest) had to be neglected to give a final distribution of 65 bubbles centered around a mean di-

ameter of 161.6 μm with a standard deviation of 6.6 μm. Maximum deviations from the mean diameter were 93% and 112%, indicating peak pressures of 64% to 137% of the mean indicated static pressure of 1.1×10^4 Pa. When normalized with the local dynamic pressure (above the shear layer), a very high r. m. s. pressure fluctuation of 153% of the local dynamic pressure was indicated, with peak pressure fluctuations of +344% and −336% of the local dynamic pressure. The normalized pressure fluctuation distribution is given in Figure II.4.25. In consideration of the fact that the bubbles remaining in the distribution were selected from a much larger group, the exact numbers must be considered somewhat arbitrary, since they could be shifted by changing the bubble selection criteria. Therefore, the final result cannot be stated with more precision than that the pressure fluctuations were about ±300% of the freestream dynamic pressure.

The calculations and discussion above were all for the case of polytropic constant $\gamma = 4/3$. Assumption of an isothermal case, i.e., $\gamma = 1.0$, leads to a slightly lower intensity of pressure fluctuations. For example, analysis of the lower velocity case with $\gamma = 1.0$ indicates an r. m. s. pressure fluctuation of 108% of the freestream dynamic pressure and peak pressure fluctuations of +229% and −243% of the freestream dynamic pressure. The histogram of normalized pressure fluctuation values for the isothermal case is given in Figure II.4.26, and comparison with Figure II.4.25 shows the slightly reduced fluctuations of the isothermal case.

In the higher velocity case ($U_L = 8.4$ m/s), the mean bubble diameter at injection was 118.6 μm, with a standard deviation of 3.0 μm for 21 bubbles measured. A large number of bubbles were measured in the region of interest, most of them having diameters well below the expected range. The procedure described above, that is, neglecting the smallest bubbles in order to bring the mean and mode diameters closer together and the mean indicated pressure closer to the base pressure, simply could not be made to work satisfactorily in this case, so the bubble distribution corresponding to the initial injection could not

be recovered without selective neglect of numerous bubble counts. The increased difficulty in determining which bubbles to include in this case may have been the result of a higher bubble entrainment rate into the recirculating wake region due to the higher freestream velocity.

Use of the air bubble injection technique to find the peak pressures in the flow relies on the assumption that some of the injected bubbles are exposed to the low pressure cores of streamwise vortices. The odds of finding an injected bubble in a core is actually fairly low since at the downstream location of hologram recording only 4 to 6 cores were typically visible across the span, so a stream of injected bubbles would at best encounter one of them. Nevertheless, the large indicated pressure fluctuations imply that at least some of the bubbles may have encountered one of the vortex cores.

II.4.2 Cavitation Inception

The photographs and motion pictures used above for quantitative flow measurements also contain valuable information on the cavitation characteristics of the flow. Visual and photographic observations show very clearly that cavitation takes place only in the shear layer behind the sharp edged plate. Newly formed bubbles collapse when they reach a higher pressure flow region, often beyond the end of the test section viewing area. Cavity growth and collapse are generally explosive, and measurements of the growth rate of several developing cavities in the shear layer were made during analysis of the high speed motion pictures, demonstrating cavity wall growth rates up to 18 m/s, and collapse rates up to 8.5 m/s. All of the flows visualized were fully turbulent, and the appearance of cavitation had significant instantaneous variations even for fixed mean flow conditions.

As demonstrated in Figures II.4.4 and II.4.11, the first cavities at inception were always observed to be long thin "strings" oriented in the longitudinal direction, presumably indicating the coincidence of a nucleus with a low pressure

longitudinal vortex core (see Section II.4.1.1). Measurements of the downstream location of inception events did not indicate the presence of an "inception zone." Rather, inception occurred at random sites throughout the shear layer, although generally at least one plate height downstream rather than near the sharp edge in the region of high streamline curvature. In addition, inception was never seen to occur in the corner vortices upstream of the sharp edged plate. In fact, cavitation in these vortices became visible only when very low cavitation indices were reached (lower than those examined during the present tests).

As in the still photos, no clear downstream or spanwise site of most probable occurrence of inception could be detected in the motion picture analysis. Detailed measurements of the x and z location of inception of streamwise cores were made by following top-view motion pictures backwards and tracking the streamwise cavities back to their point of first visibility (core diameter of about 1.5 mm). This was done for approximately 500 streamwise cores in 4 movies covering two flow conditions (U_L = 7.8 and 9.5 m/s, and σ = 1.4 and 1.7, respectively). In each case inception occurred at random sites throughout the shear layer region, although never starting closer than $x/h = 1$, and never occurring within 5 cm of the test section side walls. Measurement of the location of these inception events gave an average downstream distance to inception of 21 cm ($x/h = 2.4$), with a standard deviation of 7.4 cm. The average spanwise location of inception was $z = 0.2$ cm (where z=0 is the tunnel centerline), with a standard deviation of 4.7 cm. The large standard deviations indicate the random nature of the inception locations. There was no statistical difference in the inception location between the two flow conditions examined.

II.4.2.1 Inception Indices

Local cavitation inception indices are plotted against the body Reynolds number in Figure II.4.27. The length scale in the Reynolds number is taken to be $2h$, or twice the distance between the test body stagnation and separation

lines, in order to allow direct comparison of the present results to those made on axisymmetric bodies. The present inception index values are numerically large but do not show any clear Reynolds number dependence although their scatter, and the narrow range of velocities under which inception can be achieved in the tunnel, preclude determination of any universal trend.

Figure II.4.28 compares the present results at high air content to those of Kermeen & Parkin (1957) and Arndt (1978) behind sharp edged disks and those of Katz (1984) in the flow around two different sized flat-faced circular cylinders. The present results extend the upper Reynolds number bound of the data in this plot. The present results are of the local cavitation inception index, based on conditions above the shear layer, while the values of the inception index in the other experiments are based on the pressure and velocity at infinity. In order to compare the results, the axes of Figure II.4.28 were adjusted according to the relation

$$\sigma_L = \frac{\sigma_i + C_{pb}}{1 - C_{pb}}$$

where C_{pb} is the minimum base pressure coefficient, which was measured by both Kermeen & Parkin (1957) and Katz (1984), and the average of these is taken to be -0.6. The values of the Reynolds number were also adjusted to the local velocity. As presented at the beginning of this chapter, the present high blockage flow is essentially choked, and so has a considerably lower base pressure than these cases where the blockage effect is small.

The data of Figures II.4.27 and II.4.28 show that although the present results do not, by themselves, display a clear trend with velocity (Reynolds number), they are in general agreement with the commonly observed overall increase in inception index with increase in Reynolds number.

A large scatter is seen in the data obtained in the present cavitation tests and plotted in Figures II.4.27 and II.4.28. The scatter is larger in the lower

Reynolds number range, 1.0×10^6 to 1.4×10^6. The present measurements were carried out using velocity and pressure transducers with a 0.5% accuracy, so the measurement error is much smaller than the scatter of the data. The major component of scatter is the fact that the onset of cavitation (in any type of flow) requires the coincidence of at least two events, a low enough pressure (occurring in the streamwise cores in this flow) and a freestream cavitation nucleus of such size that it becomes unstable at the local pressure. According to Bernal (1981), the location, spacing and strength of the longitudinal vortices may depend on the velocity (although such dependence could not be determined for the present data; see discussion in Section II.5.3), thus altering the number of possible inception sites. As a result, the probability of inception is expected to vary with the freestream velocity, providing an explanation for some of the observed scatter in the inception data.

The high air content inception data of Figure II.4.27 exhibit particularly large scatter, due in part to uncertainty in the definition of inception in high air content cases. The appearance and sound of cavitation are distinctly different for very high dissolved air contents (at or near saturation). At lower α, the occurrence of inception is very sharp and clear, almost always appearing in the form of a long streamwise cavity that erupts into view suddenly, accompanied by a "snapping" noise. At high α, the moment of inception becomes more difficult to define since the entire shear layer and eventually the recirculating wake often begin to support a large number of small bubbles before any "macroscale" vortex cavitation becomes visible (this is not always the case however; see Figure II.4.4 with the relatively high $\alpha = 9.9$ *ppm*). Air content effects on cavitation and limitations of visual detection of inception will be discussed in the next chapter.

II.4.2.2 Nuclei Availability Effects

Significant nuclei measurement studies have been performed in the LTWT over the last 10 years, primarily relying on holographic measurement (see, for

example, Billet & Gates 1979; Katz 1981; Ooi 1981; Katz et al. 1983). A representative sample of "typical" bubble number density distribution functions in this facility is given in Figure II.4.29 (from Katz 1981; also Katz & O'Hern 1983). The population of freestream bubbles in the LTWT has been shown to depend on cavitation index, dissolved air content, and test procedures. The pure nuclei measuring portions of the present work were kept to a minimum, consisting of determination of the relative bubble populations above and below the shear layer prior to, and at the moment of, inception. Representative samples of the bubble populations measured in one of these examinations are given in Figure II.4.30, which shows the number density distribution function $n(R)$ for bubbles above and below the shear layer for two holograms recorded at the same freestream velocity and dissolved air content, the only difference being that one was recorded at steady conditions ($\sigma_o = 3.11$), while the second was recorded after lowering the static pressure until inception was observed ($\sigma = \sigma_i = 2.06$). The bubble populations above and below the shear layer are essentially the same in the steady case. However, at the moment that the first macroscopic inception event has occurred, the population of microscopic bubbles in the recirculating wake below the shear layer has increased by up to an order of magnitude above the freestream values over all size ranges, while the freestream concentration remains at its steady value. The increase in bubble concentration is particularly pronounced for the larger bubbles (25 to 50 μm radius). Vertical traverses through the reconstructed image at inception indicate that the highest bubble concentrations occur at and just below the estimated location of the dividing streamline, with the bubble population more than several cm below the dividing streamline being essentially the same as that in the freestream above the layer. The results shown are for a high air content test, but similar trends hold for lower air contents, although the magnitude of the difference between the two regions becomes much less marked, never exceeding a factor of two. These measurements were made only for bubbles with radii above 10 μm, since the interest was in

relative populations in the two regions rather than the absolute concentration in either one. It is expected that the population of smaller bubbles will follow the same trends as the larger ones, based on numerous previous studies showing shifts of the entire population as flow conditions are changed.

There are also a significant number of particles always present in the LTWT under all operating conditions that may be important as cavitation nuclei (see Section I.1.1). Despite the fact that the tunnel water is frequently filtered, in many cases particle concentrations are comparable to those of bubbles. Figure II.4.30 includes the results of an examination of LTWT water, using a HIAC optical particle counter (performed by J. Goldish, 1984, private communication) which showed that 82% of particles sampled were less than 10 μm, 0.2% above 50 μm, and none greater than 100 μm. A total of 92 particles/ml were determined by this process, in tunnel water which had not been filtered for some time. Examination with a Coulter Counter showed a total of 2640 particles/ml, with about 75% of them less than 10 μm. While the two spectra were similar, the Coulter Counter indicated more than an order of magnitude higher particle concentrations. Typical holographic results in unfiltered LTWT water tend to support the high Coulter Counter measurements, although many of these small particles are below the resolution limit of the holographic system (about 5 μm).

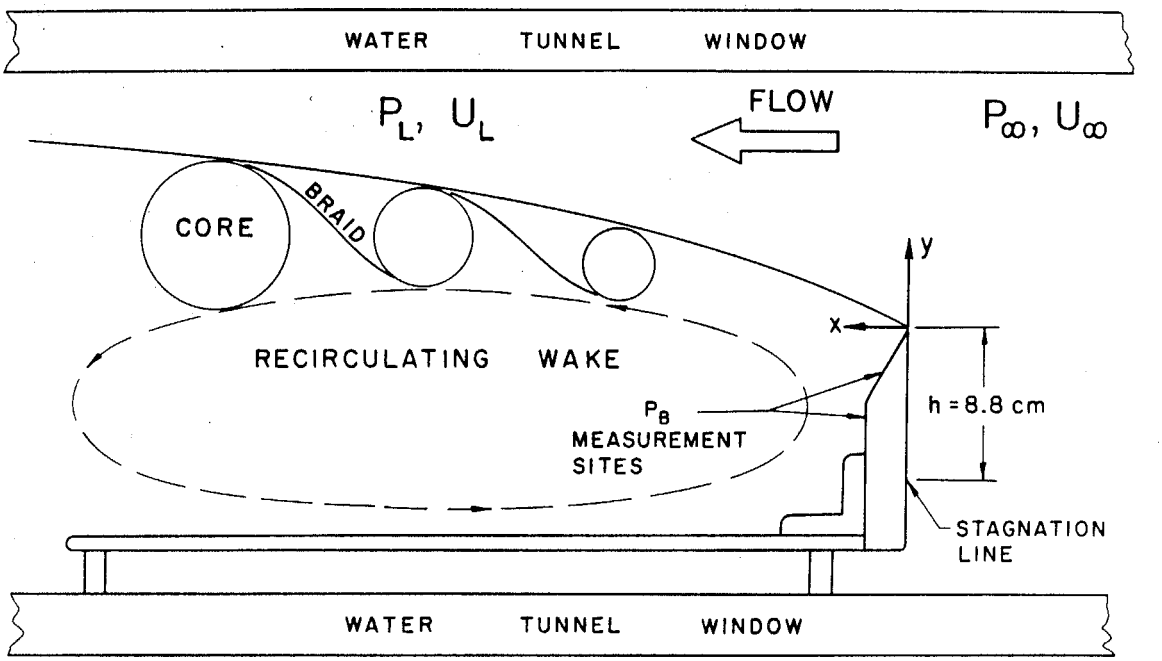

Figure II.4.1. Sketch indicating overall mean shape of the separated flow.

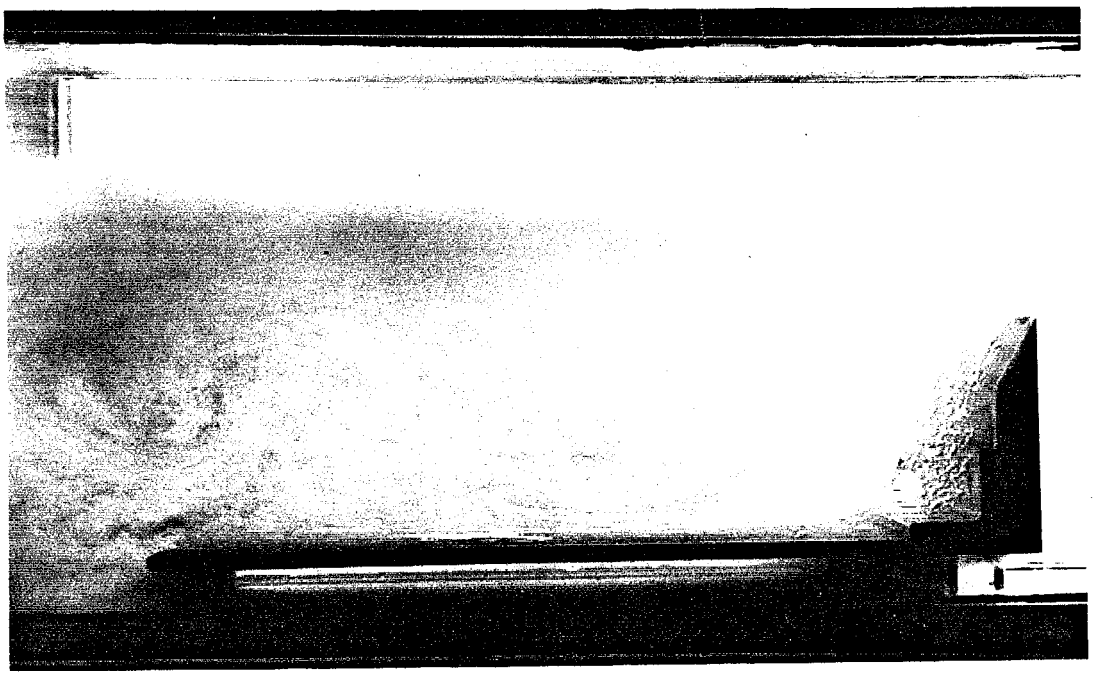

Figure II.4.2. 1/4 *sec* exposure photograph showing time-averaged growth rate of the turbulent shear layer. $U_L = 7.81\ m/s$, $Re_L = 1.52 \times 10^6$, $\sigma_L = 0.16$.

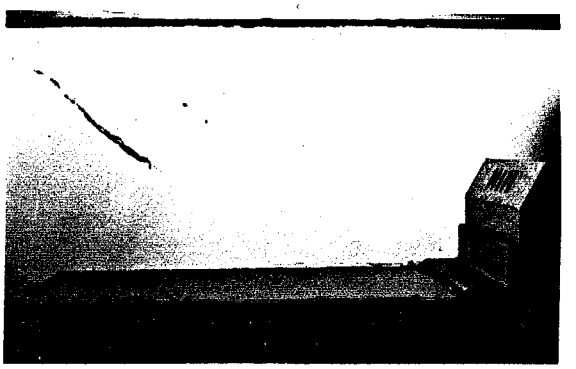

(a) Re_L=1.5 × 10^6, σ_L=0.87

(b) Re_L=2.0 × 10^6, σ_L=0.78

(c) Re_L=2.1 × 10^6, σ_L=0.65

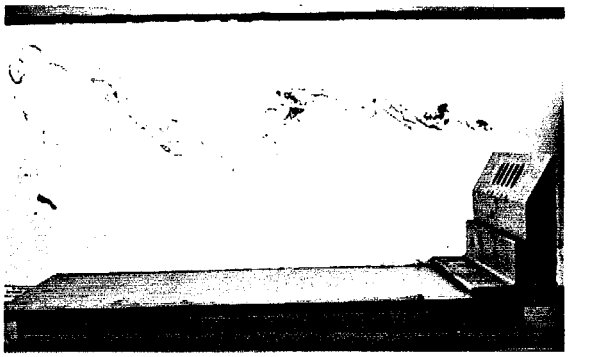

(d) Re_L=2.1 × 10^6, σ_L=0.65

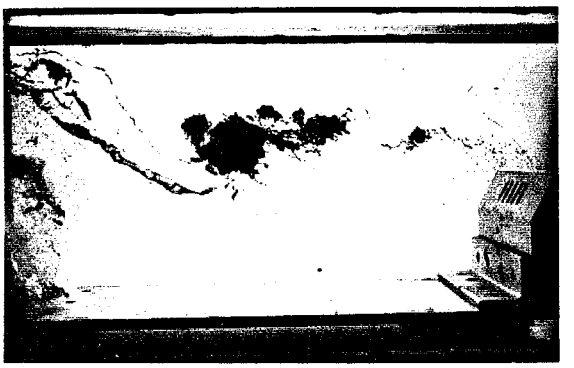

(e) Re_L=2.1 × 10^6, σ_L=0.41

(f) Re_L=2.1 × 10^6, σ_L=0.40

Figure II.4.3. Side view photographs showing change in cavitation behavior with decreasing cavitation index σ. A different lighting scheme was used for (b).

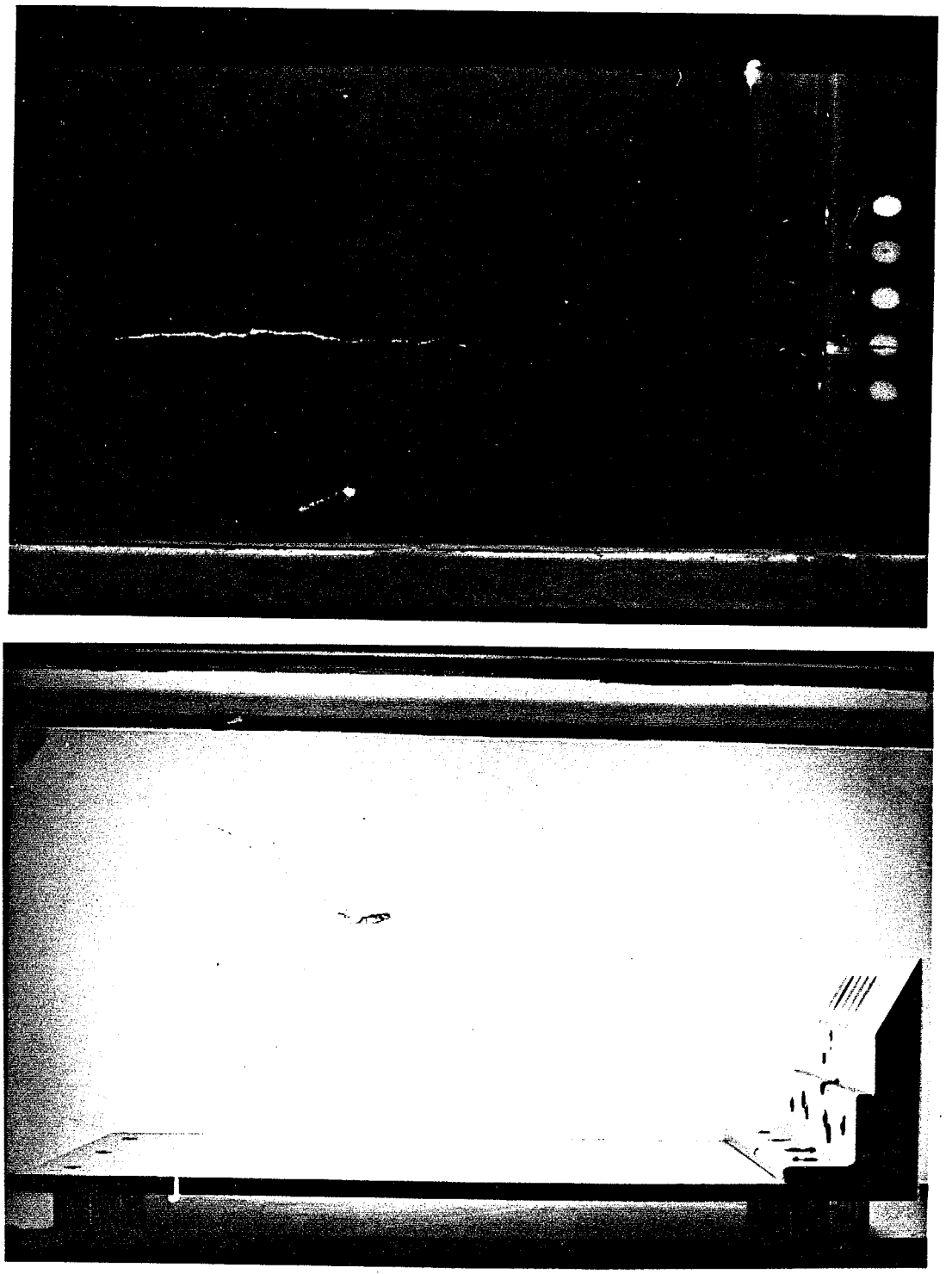

Figure II.4.4. Simultaneous top and side photographs of free shear layer cavitation inception. $U_L = 7.81\ m/s$, $\sigma_L = \sigma_i = 1.52$, $Re_L = 1.42 \times 10^6$, $\alpha = 9.9\ ppm$.

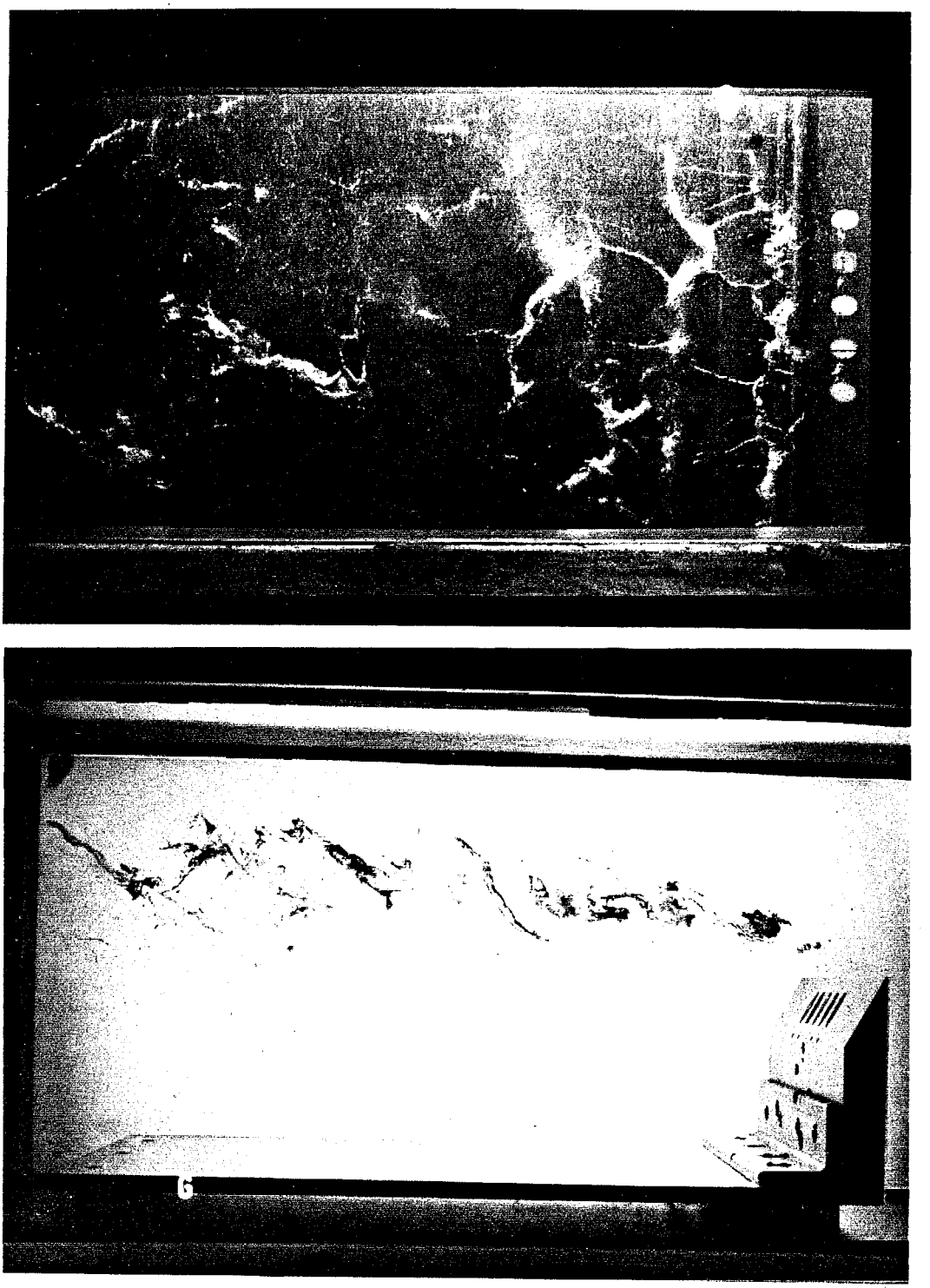

Figure II.4.5. Simultaneous top and side photographs of early stage of cavitation in the free shear layer. $U_L = 11.38\ m/s$, σ_L=0.65, $Re_L = 2.06 \times 10^6$, $\alpha = 9.9\ ppm$.

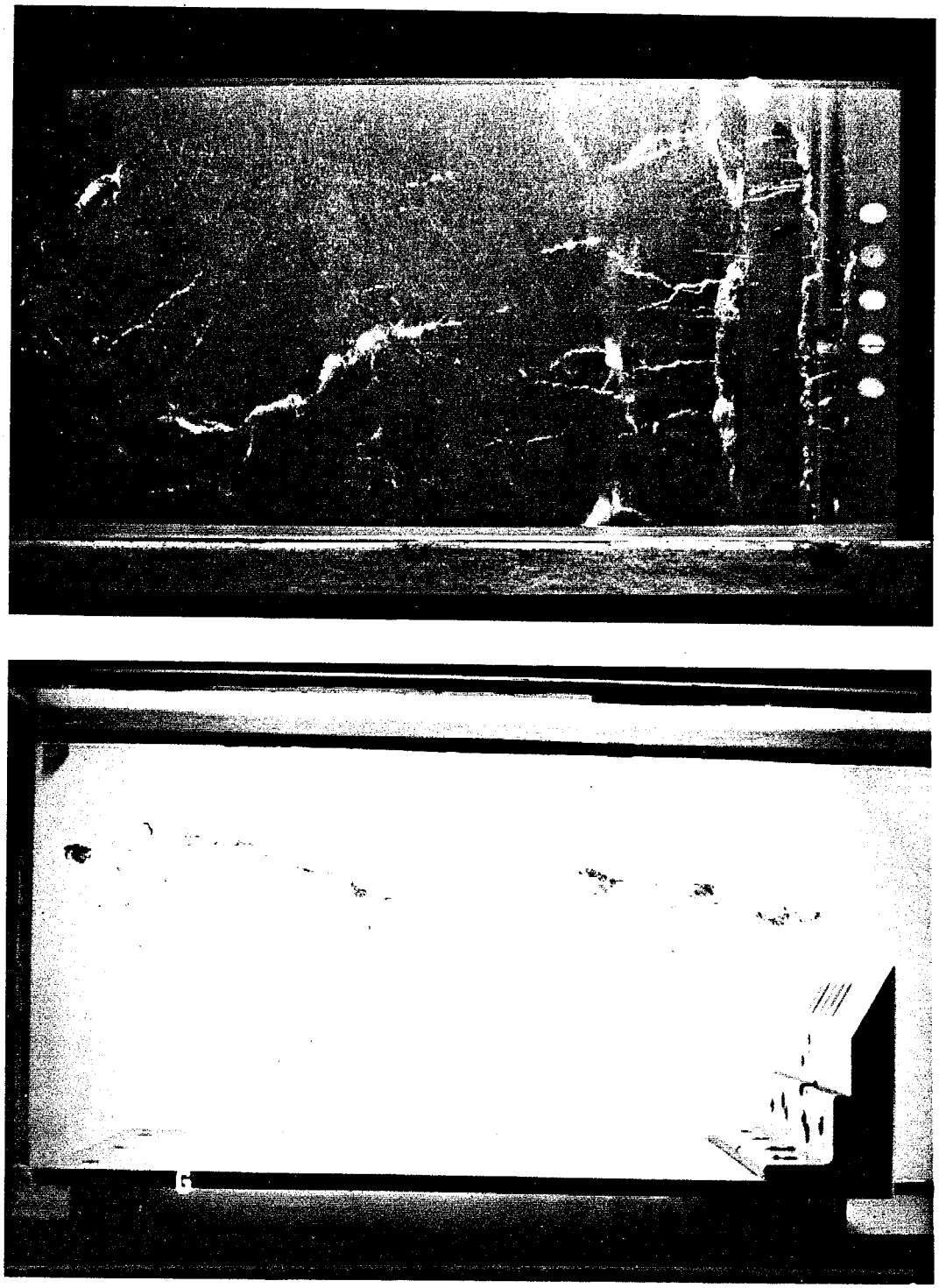

Figure II.4.6. Simultaneous top and side photographs of early stage of cavitation in the free shear layer. $U_L = 11.38\ m/s$, σ_L=0.65, $Re_L = 2.06 \times 10^6$, $\alpha = 9.9\ ppm$.

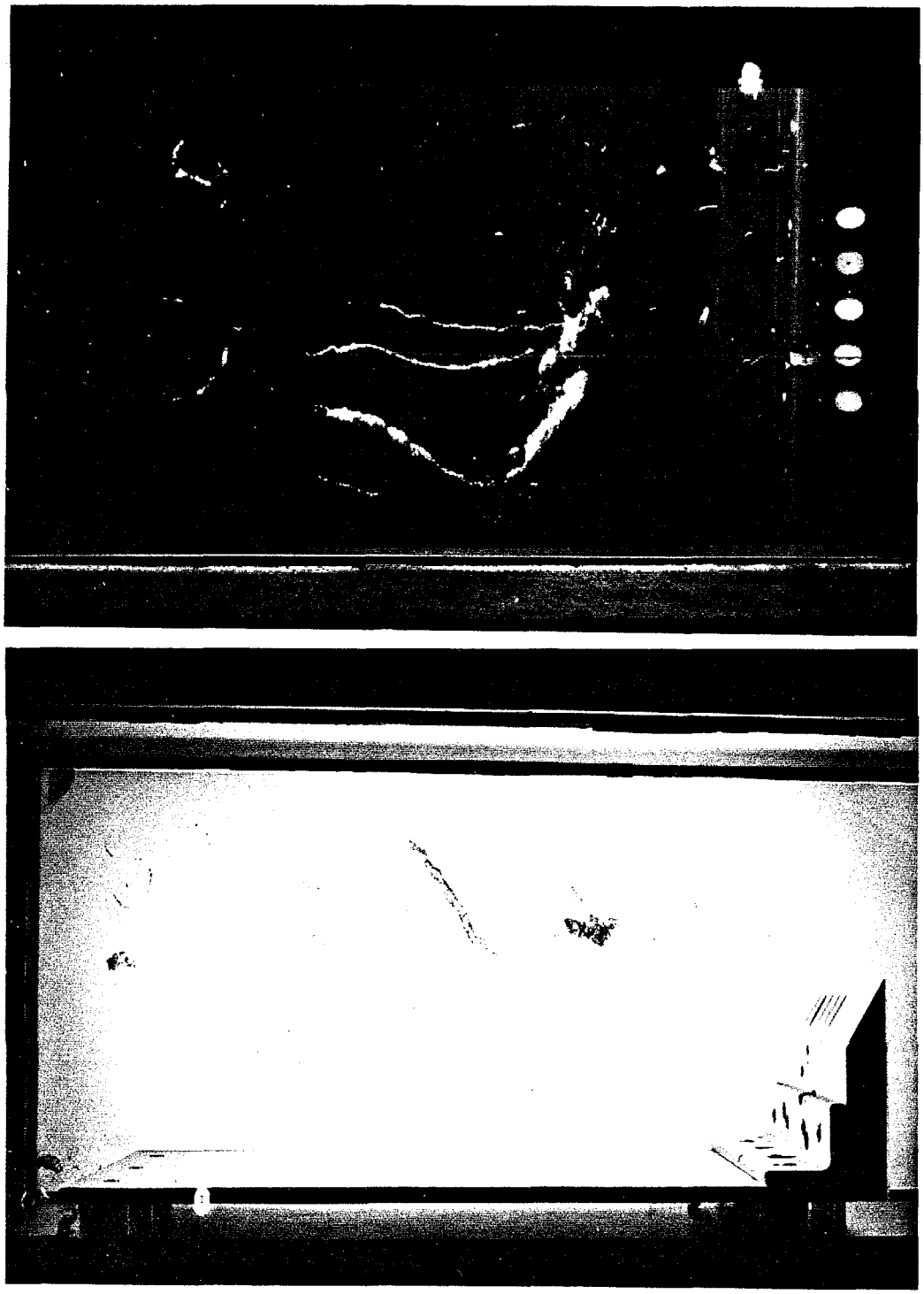

Figure II.4.7. Simultaneous top and side photographs of early stage of cavitation in the free shear layer. $U_L = 11.75\ m/s$, σ_L=0.62, $Re_L = 2.13 \times 10^6$, $\alpha = 4.2\ ppm$.

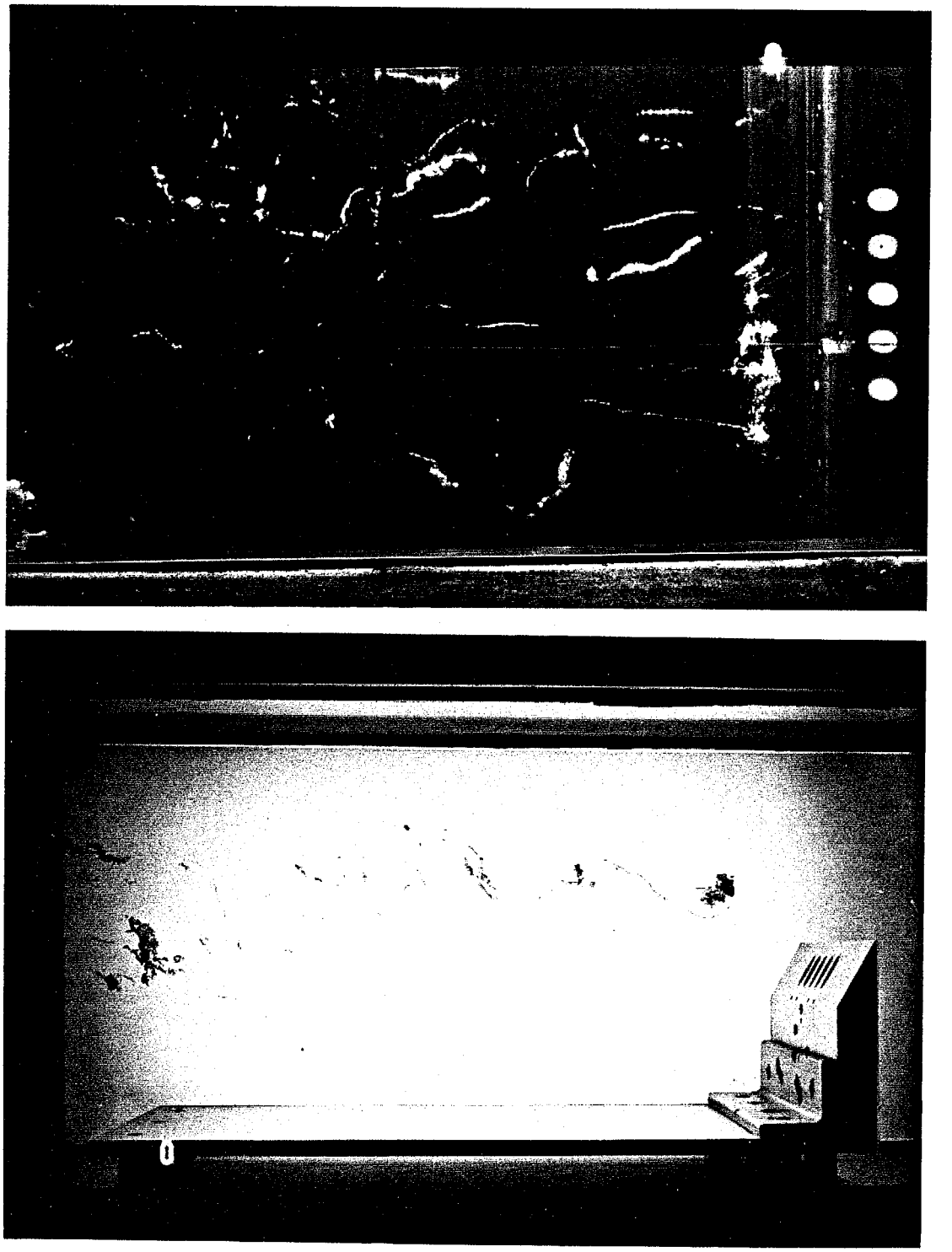

Figure II.4.8. Simultaneous top and side photographs of early stage of cavitation in the free shear layer. $U_L = 11.75\ m/s$, σ_L=0.62, and Re_L=2.13×10^6, $\alpha = 4.2\ ppm$.

Figure II.4.9. Simultaneous top and side photographs of well-developed cavitation in the free shear layer. $U_L = 10.14\ m/s$, σ_L=0.39, $Re_L = 1.84 \times 10^6$, $\alpha = 10.1\ ppm$.

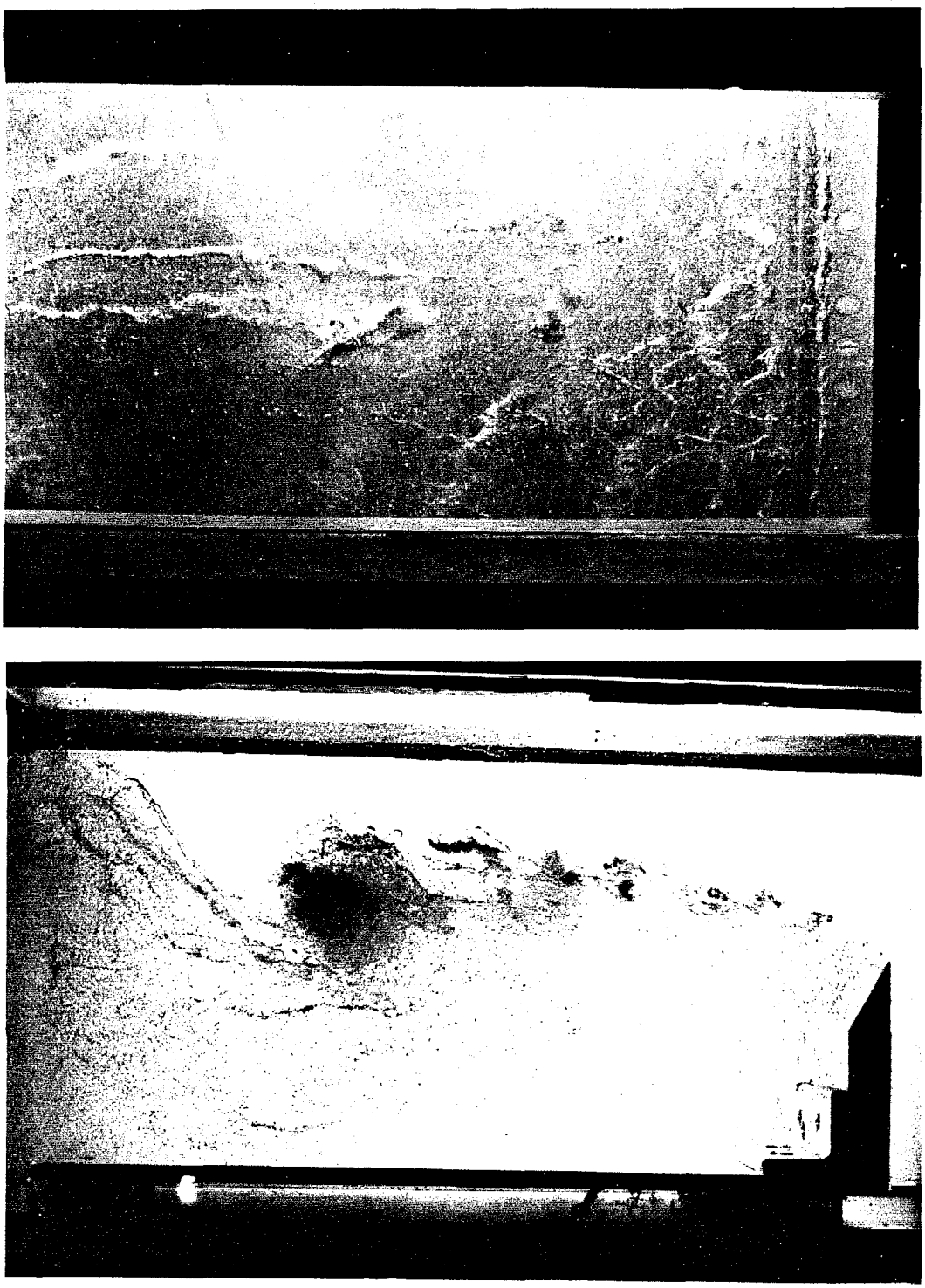

Figure II.4.10. Simultaneous top and side photographs of well-developed cavitation in the free shear layer. $U_L = 10.14\ m/s$, σ_L=0.39, $Re_L = 1.84 \times 10^6$, $\alpha = 10.1\ ppm$.

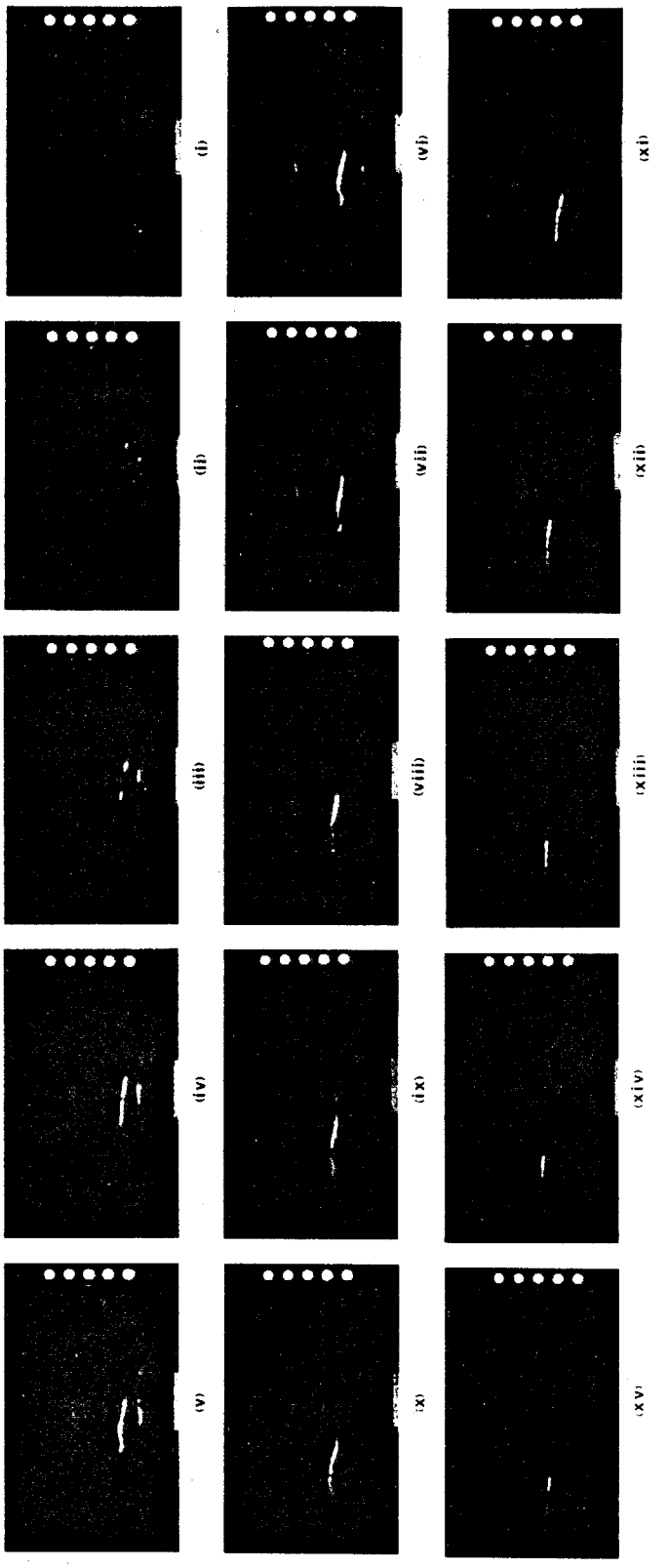

Figure II.4.11. High speed movie sequence showing top view of inception, growth and collapse of an axial cavity. Sequence runs from right to left as numbered. Flow direction is right to left. The steady streamwise line covering full length of each frame is a scratch on the lucite viewing window. Elapsed time between frames is 2 ms, exposure time is approximately 200 μs. $U_L = 9.5\ m/s$, $\sigma_L = 0.88$, $Re_L = 1.84 \times 10^6$, $\alpha = 4.70\ ppm$.

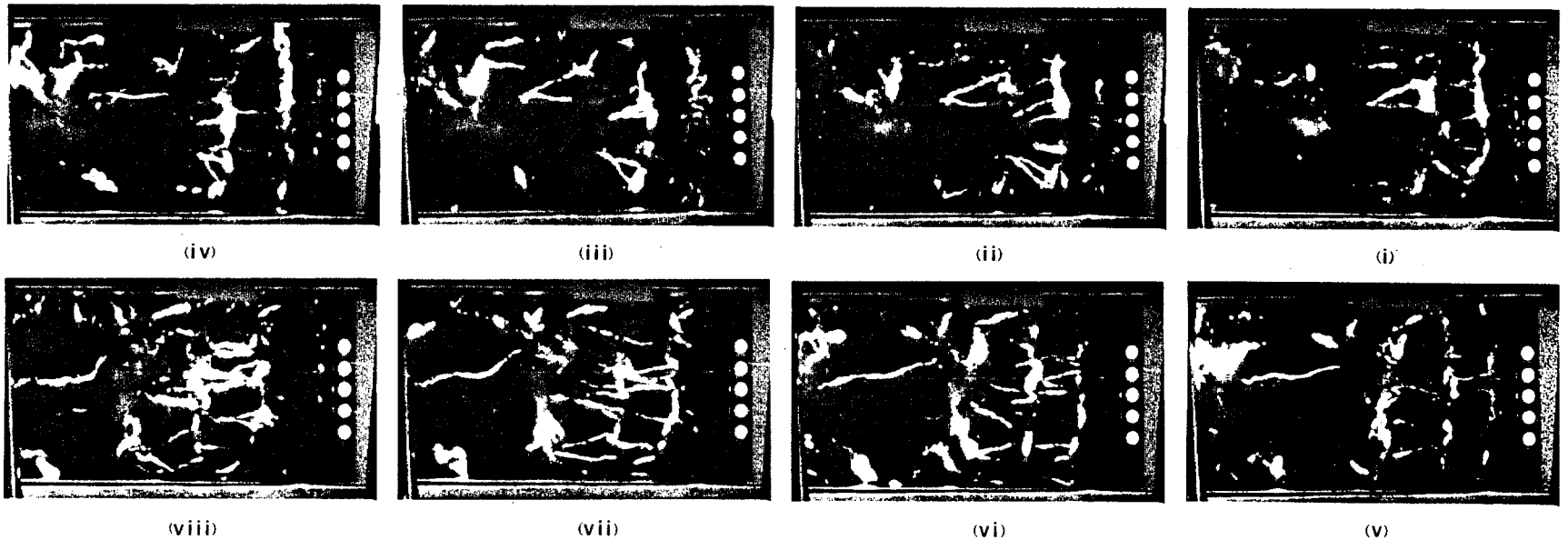

Figure II.4.12. High speed movie sequence showing top view of fairly heavy cavitation in the shear layer. Sequence runs from right to left as numbered. Flow direction is right to left. The steady streamwise line covering full length of each frame is a scratch on the lucite viewing window. Elapsed time between frames is 4.2 ms, exposure time is approximately 170 μs. $U_L = 11.60\ m/s$, $\sigma_L = 0.63$, Re_L=2.26×10^6, α= 2.72 ppm.

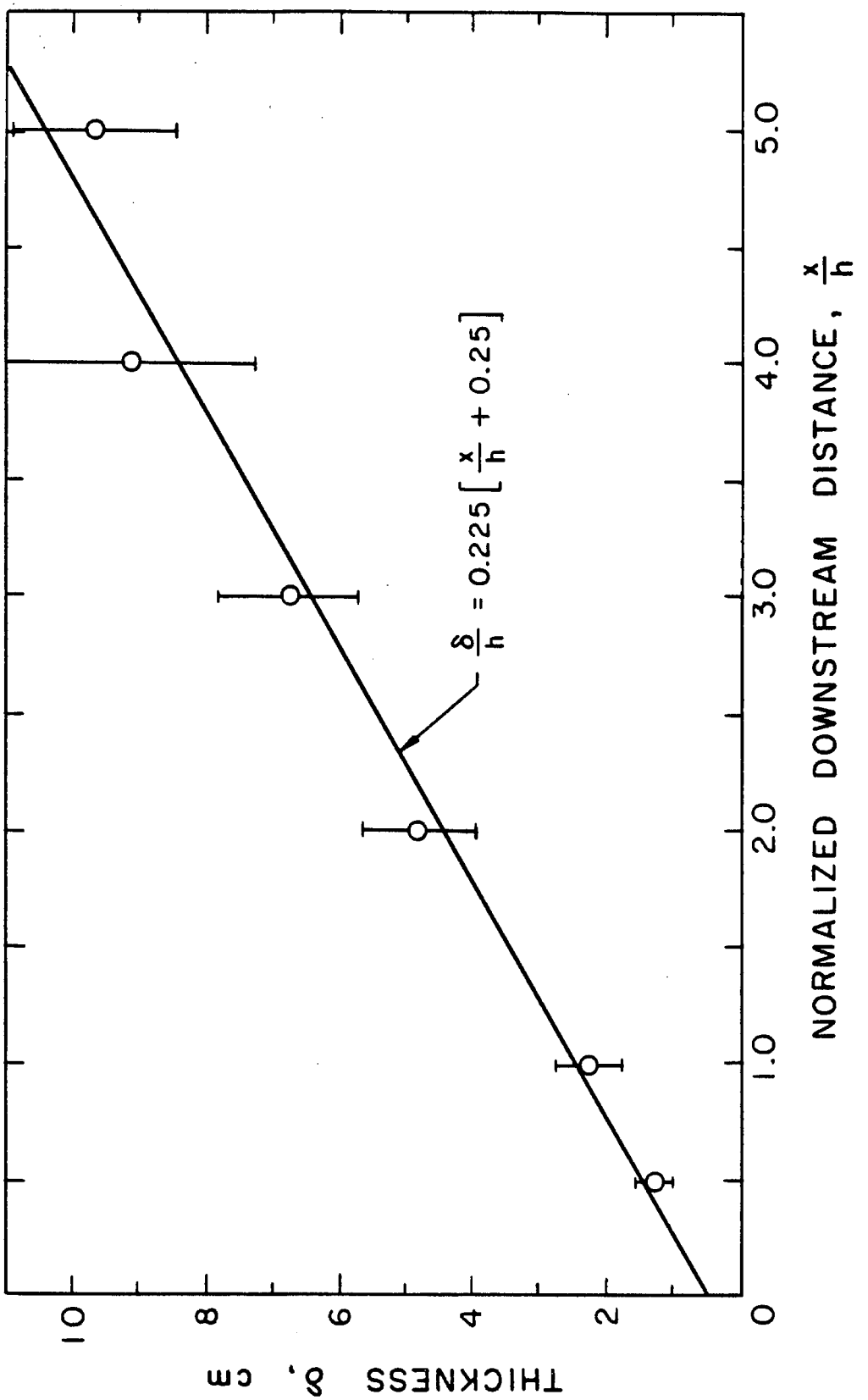

Figure II.4.13. Shear layer growth rate. "Visual" thickness of layer measured from high-speed motion pictures at fixed downstream stations.

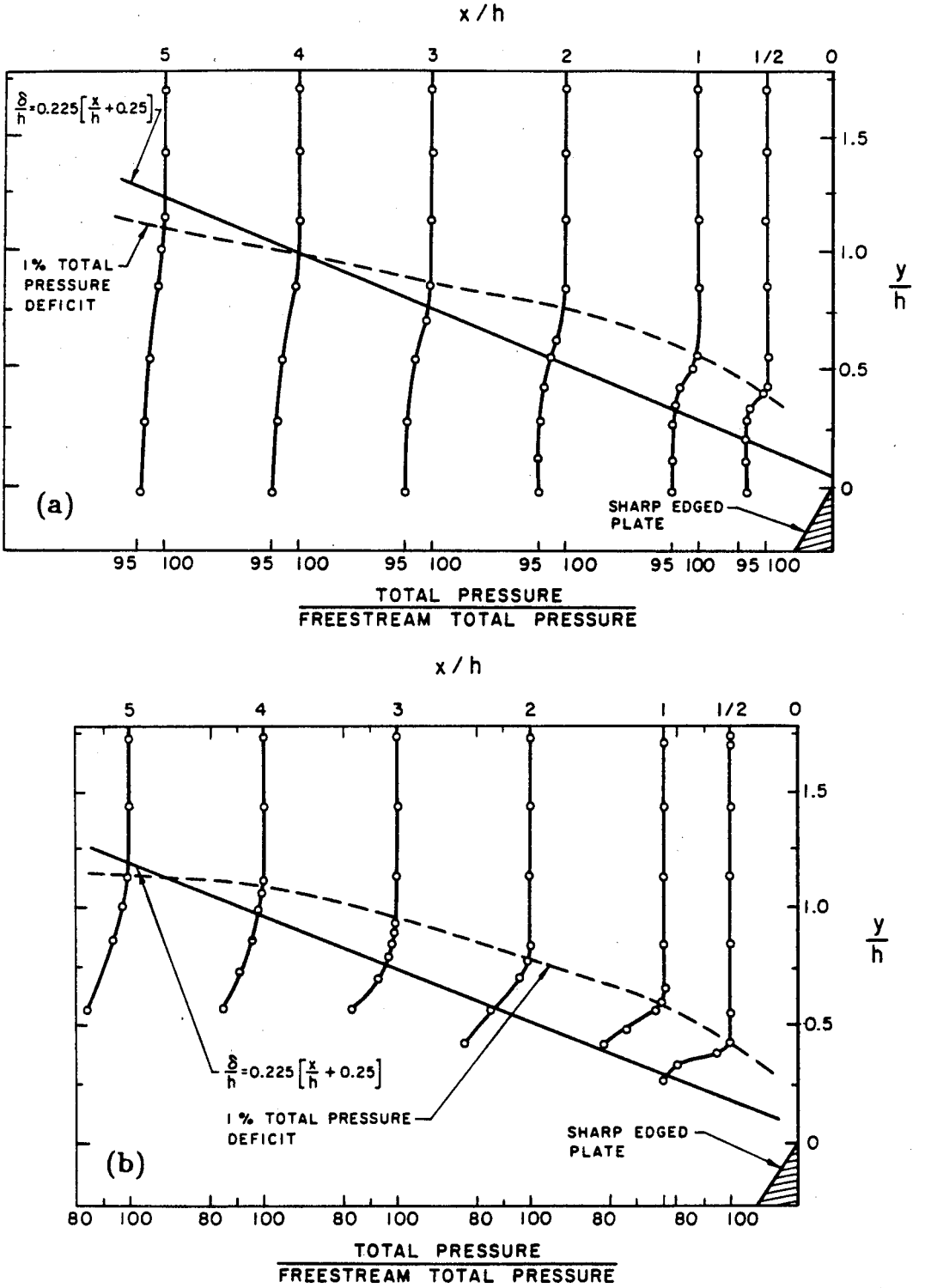

Figure II.4.14. Shear layer total pressure profiles.
(a) U_L= 3 m/s, Re_L=5.28 $\times 10^5$
(b) U_L= 7 m/s, Re_L=1.23 $\times 10^6$

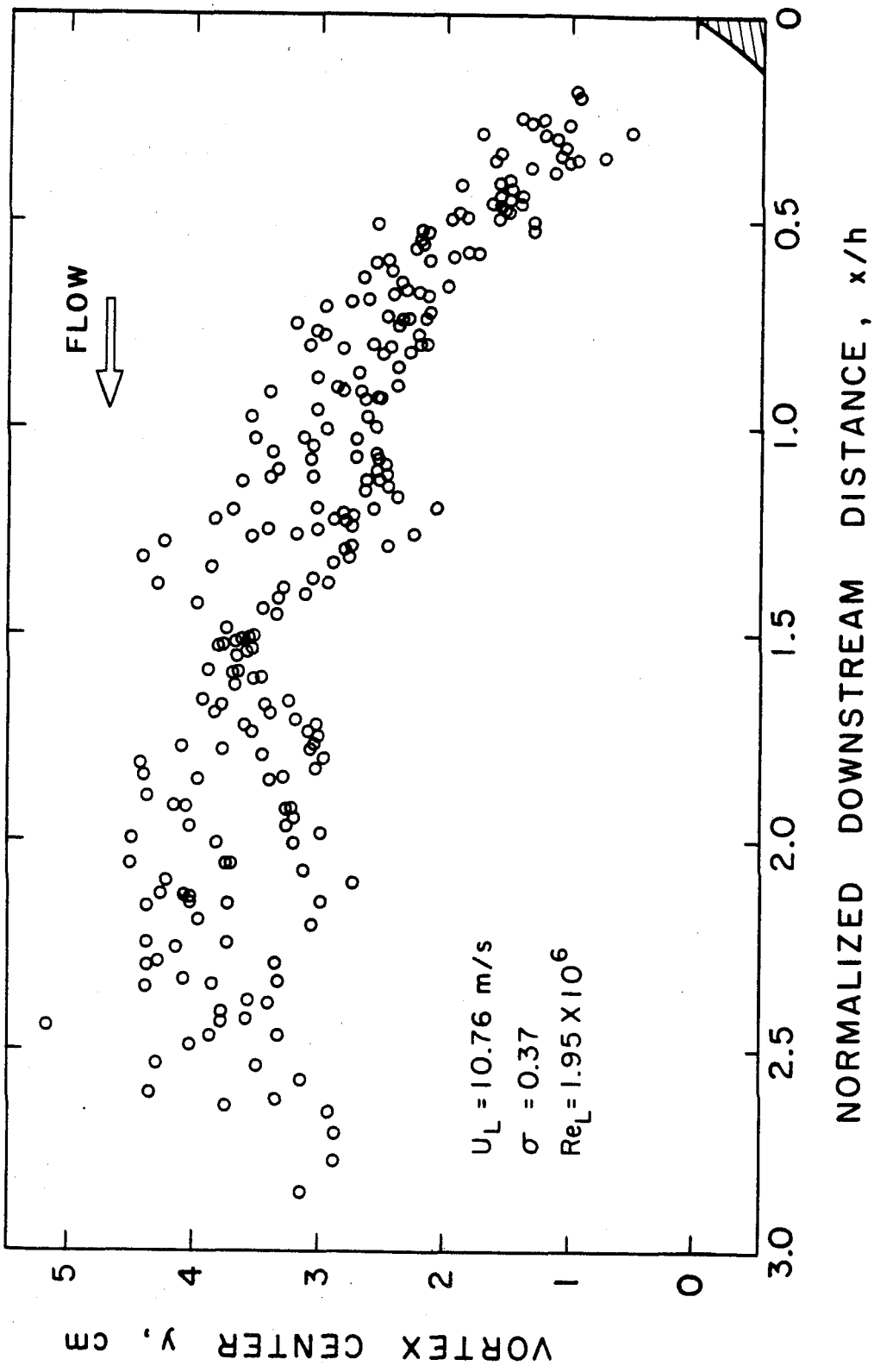

Figure II.4.15. Trajectory of spanwise vortices in shear layer behind sharp edged plate. $U_L = 10.76\ m/s$, $\sigma_L = 0.37$, $Re_L = 1.95 \times 10^6$.

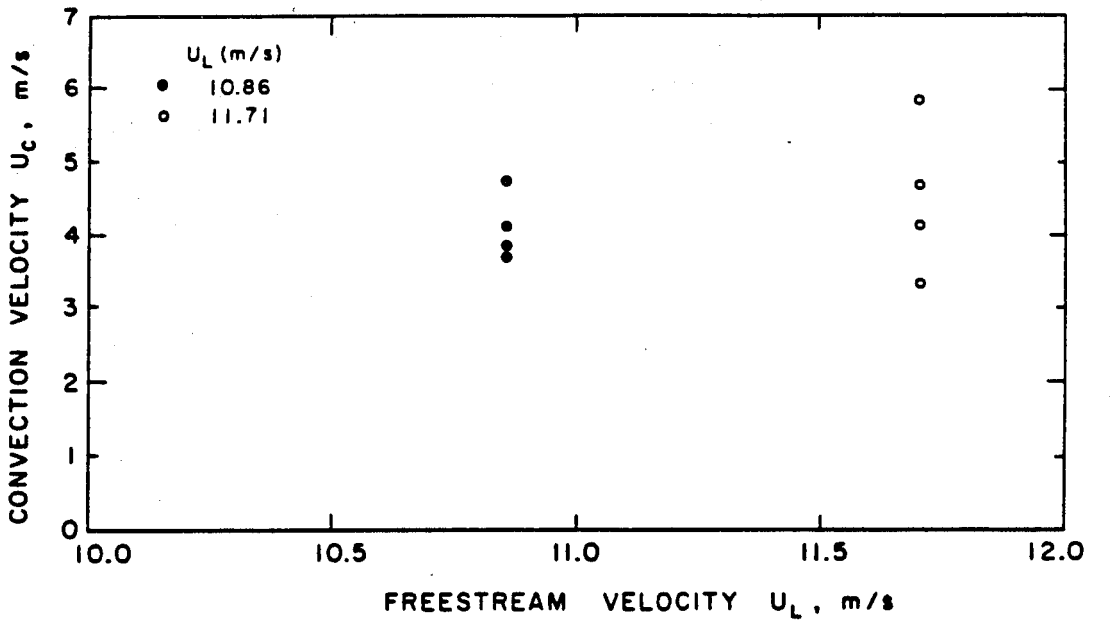

Figure II.4.16. Average convection velocity of spanwise vortices as a function of freestream velocity above the shear layer (from 8 motion picture sequences).

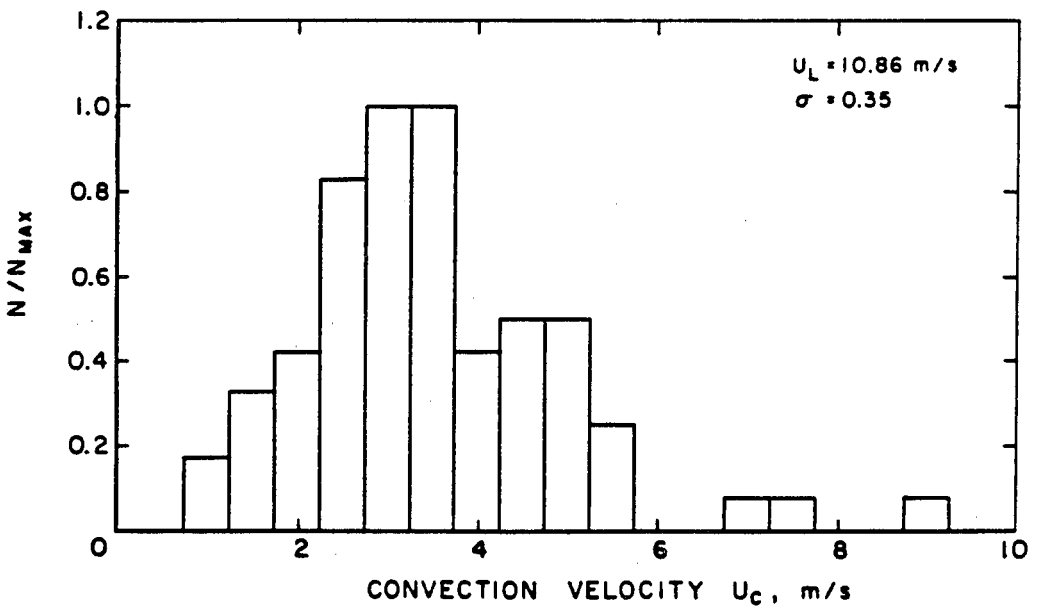

Figure II.4.17. Convection velocity frequency distribution. Spread of convection velocity values measured during tracking of a single spanwise core. Average $U_c = 0.33\ U_L$ for this case.

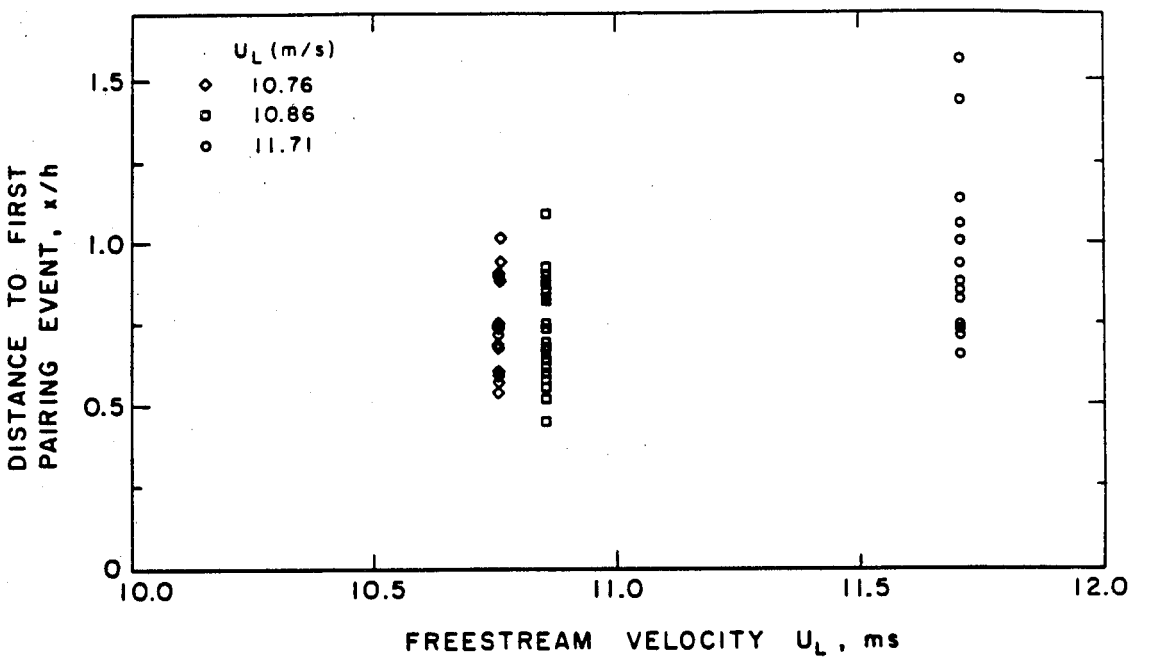

Figure II.4.18. Measured downstream distances to first pairing event for three freestream velocities.

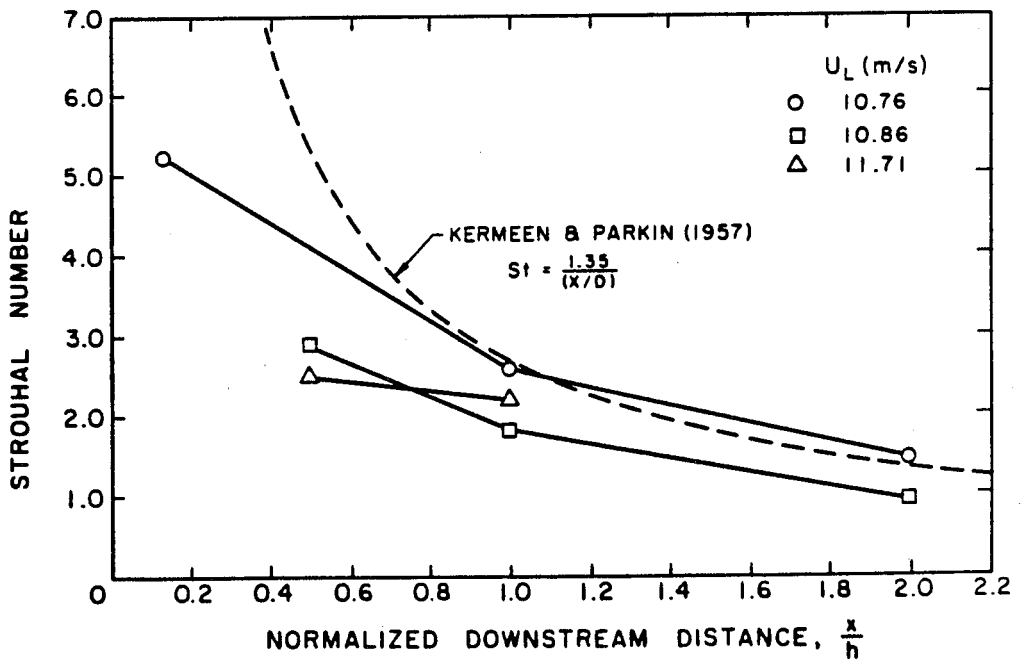

Figure II.4.19. Strouhal number as a function of downstream distance. Dashed line indicates the measured results of Kermeen & Parkin (1957) for the wake of a sharp edged disk assuming $D = 2h$.

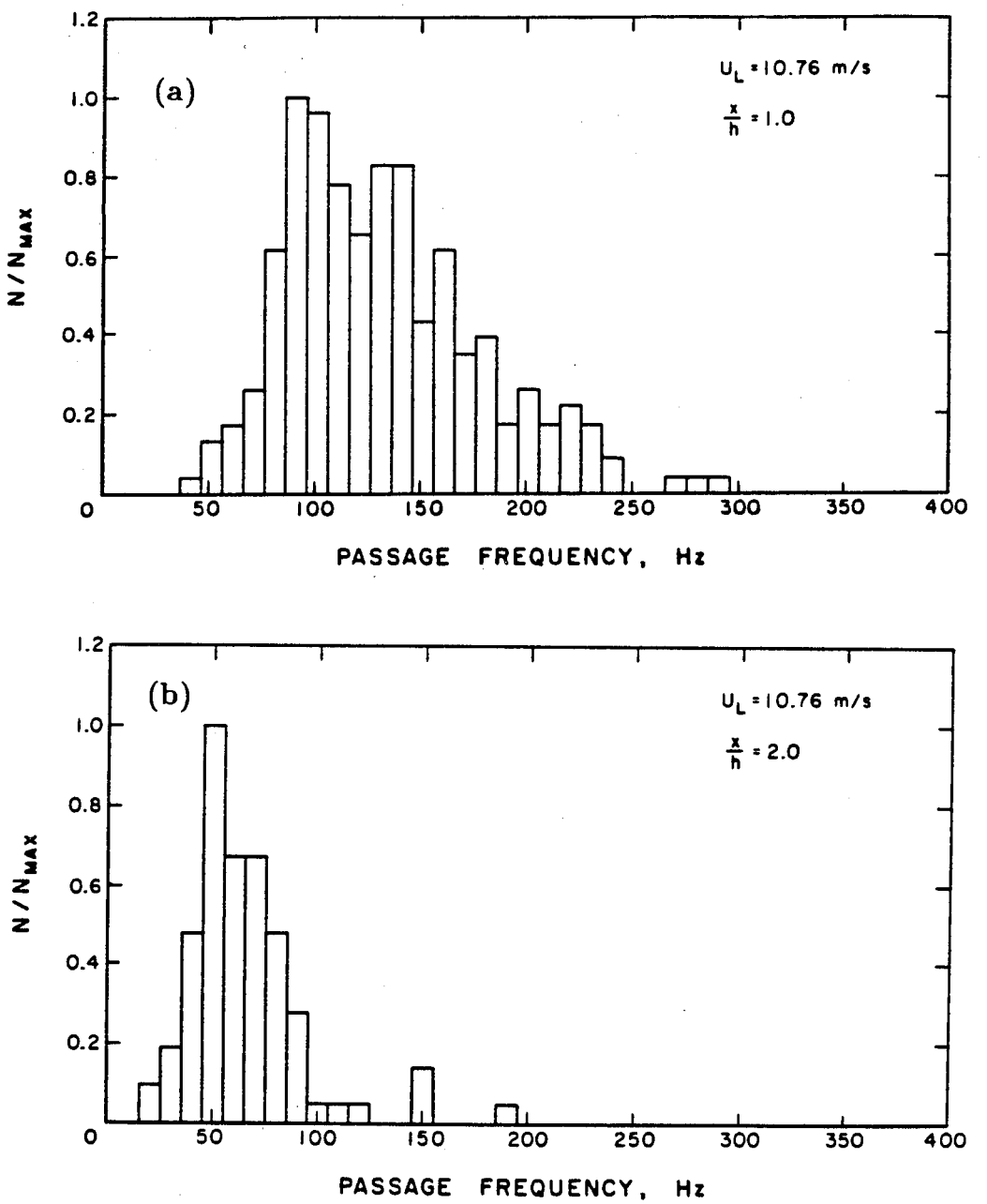

Figure II.4.20. Distribution of vortex passage frequencies measured at fixed downstream stations.
(a) x/h= 1.0, U_L=10.76 m/s, $\overline{St}$ = 2.57.
(b) x/h= 2.0, U_L=10.76 m/s, $\overline{St}$ = 1.43.

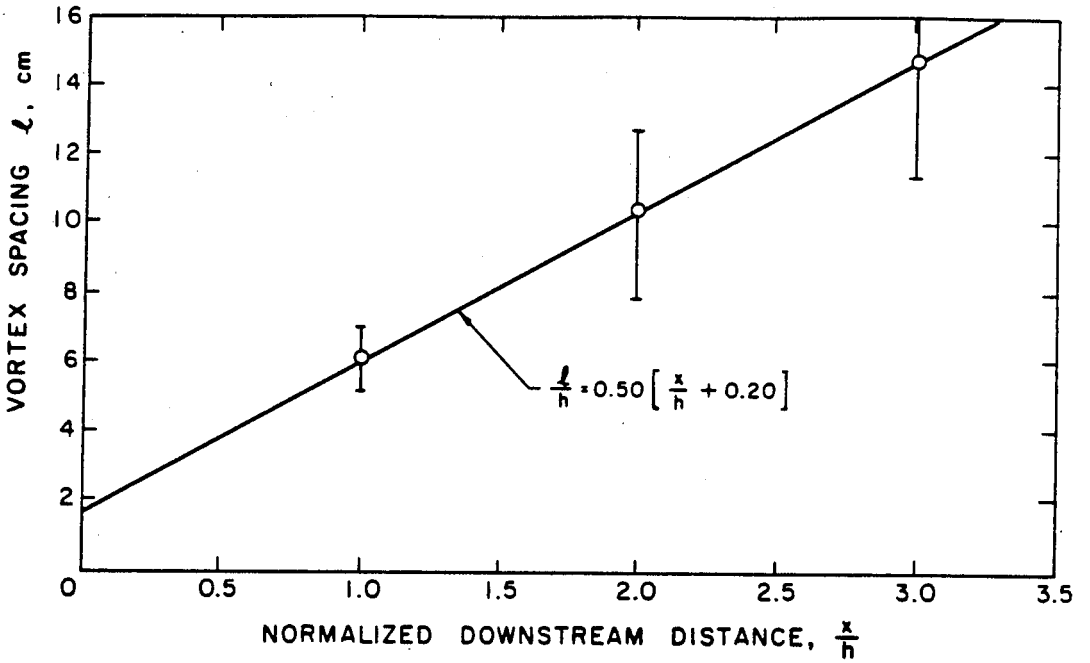

Figure II.4.21. Spacing l of spanwise vortices as a function of downstream distance. Error bars indicate $\pm$ one standard deviation from the mean.

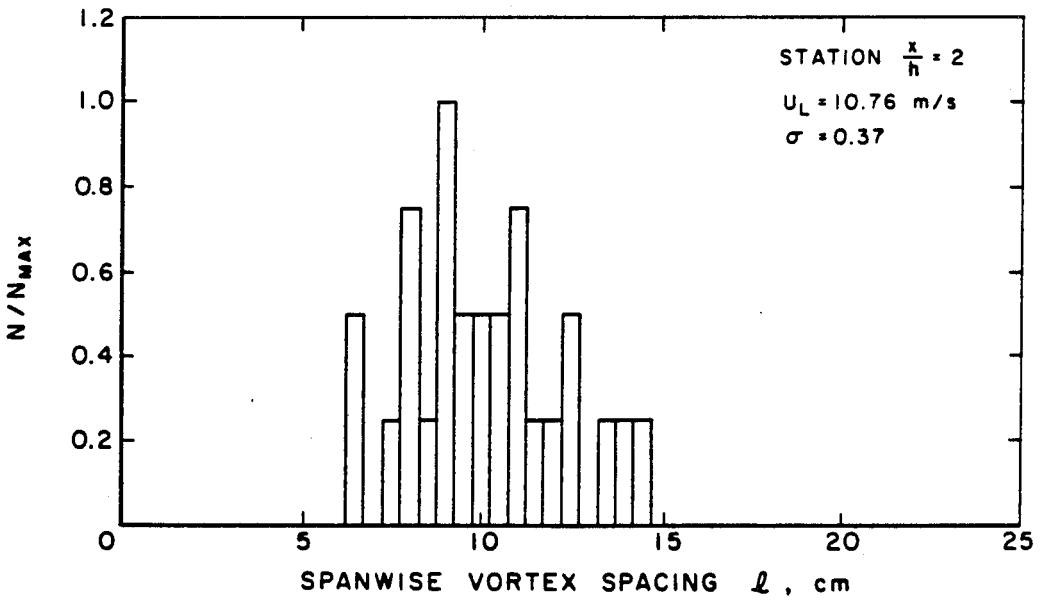

Figure II.4.22. Distribution of spanwise vortex wavelengths measured at fixed downstream station x/h=2.0. Mean value $\bar{l} = 10.2\ cm$.

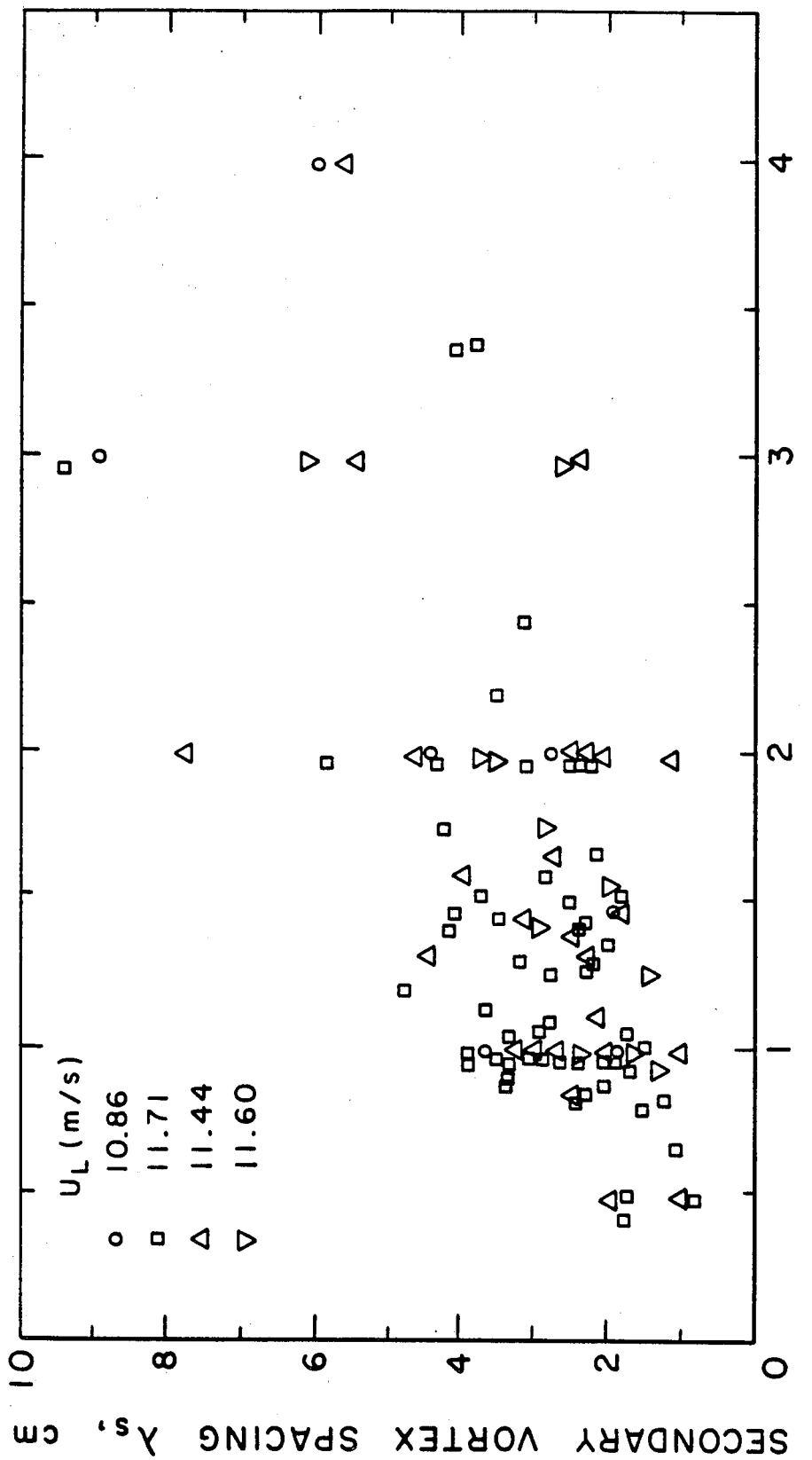

Figure II.4.23. Average spanwise spacing of longitudinal vortices as a function of downstream distance.

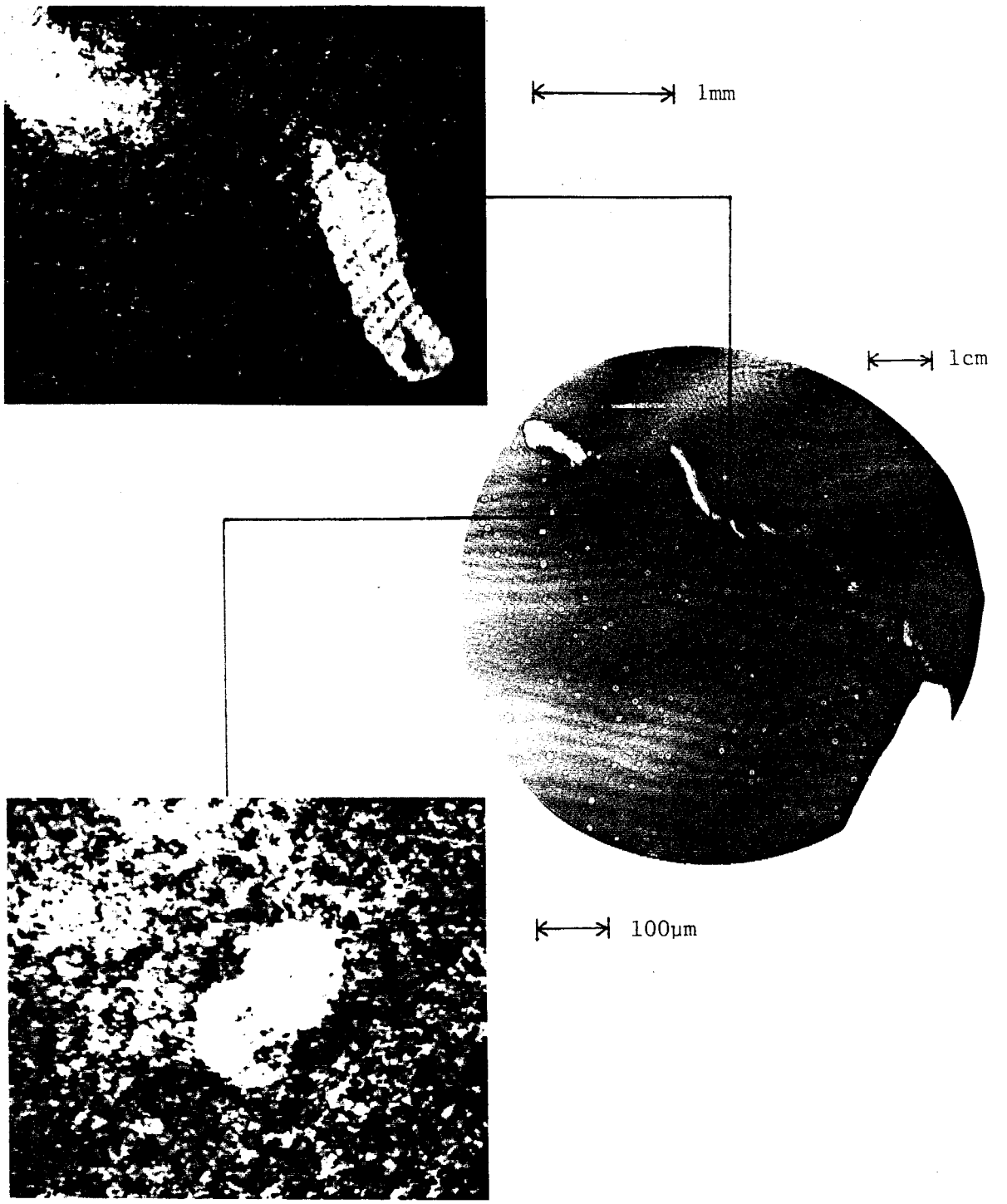

Figure II.4.24. Determination of three-dimensional velocity components from double-pulsed holographic images. Center photograph is of hologram (including tip of sharp edged plate), upper shows reconstructed image demonstrating translation of 1.7 *mm* long streamwise vortex core, and lower shows translation of 100 μm diameter bubble. Separation period between laser pulses is 200 μs. U_L=7 m/s, $\sigma_L = 0.50$, α=3.3 *ppm*.

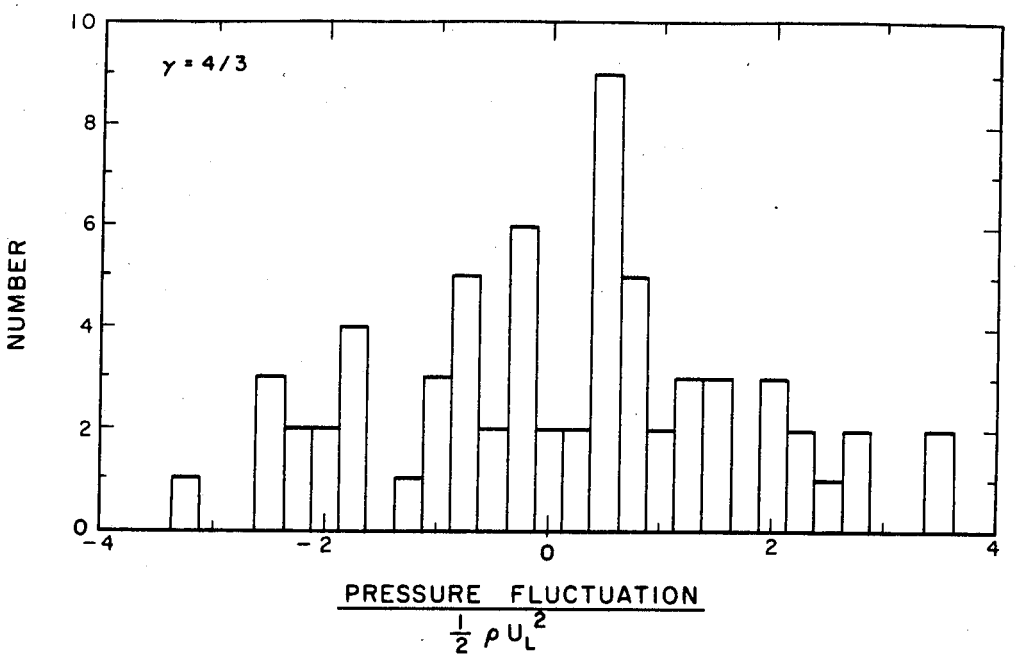

Figure II.4.25. Normalized pressure fluctuation distribution. Polytropic constant $\gamma = 4/3$.

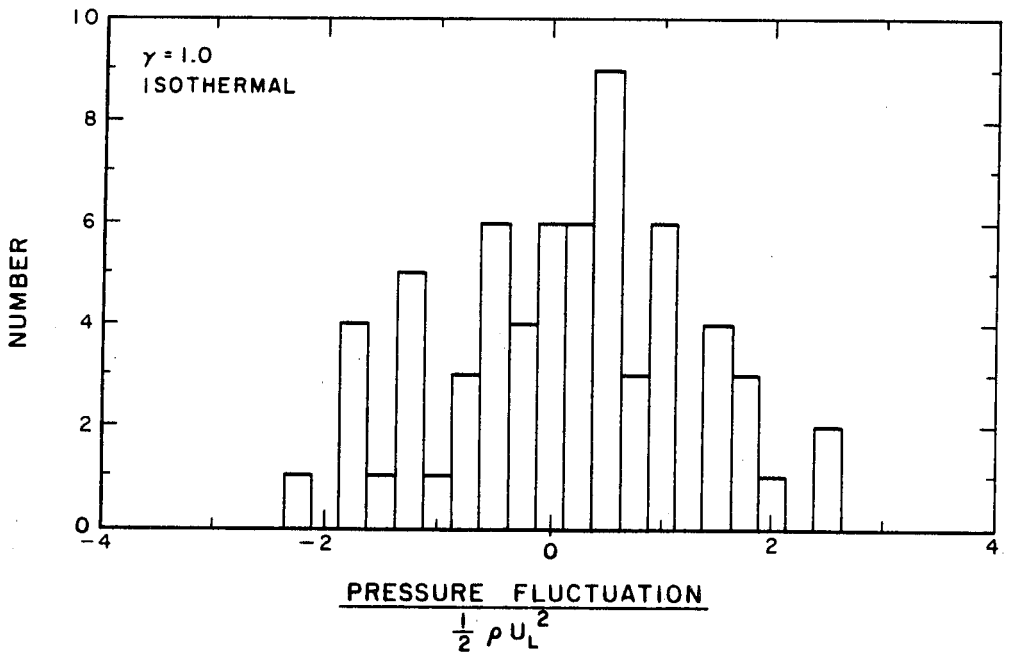

Figure II.4.26. Normalized pressure fluctuation distribution. Polytropic constant $\gamma = 1.0$.

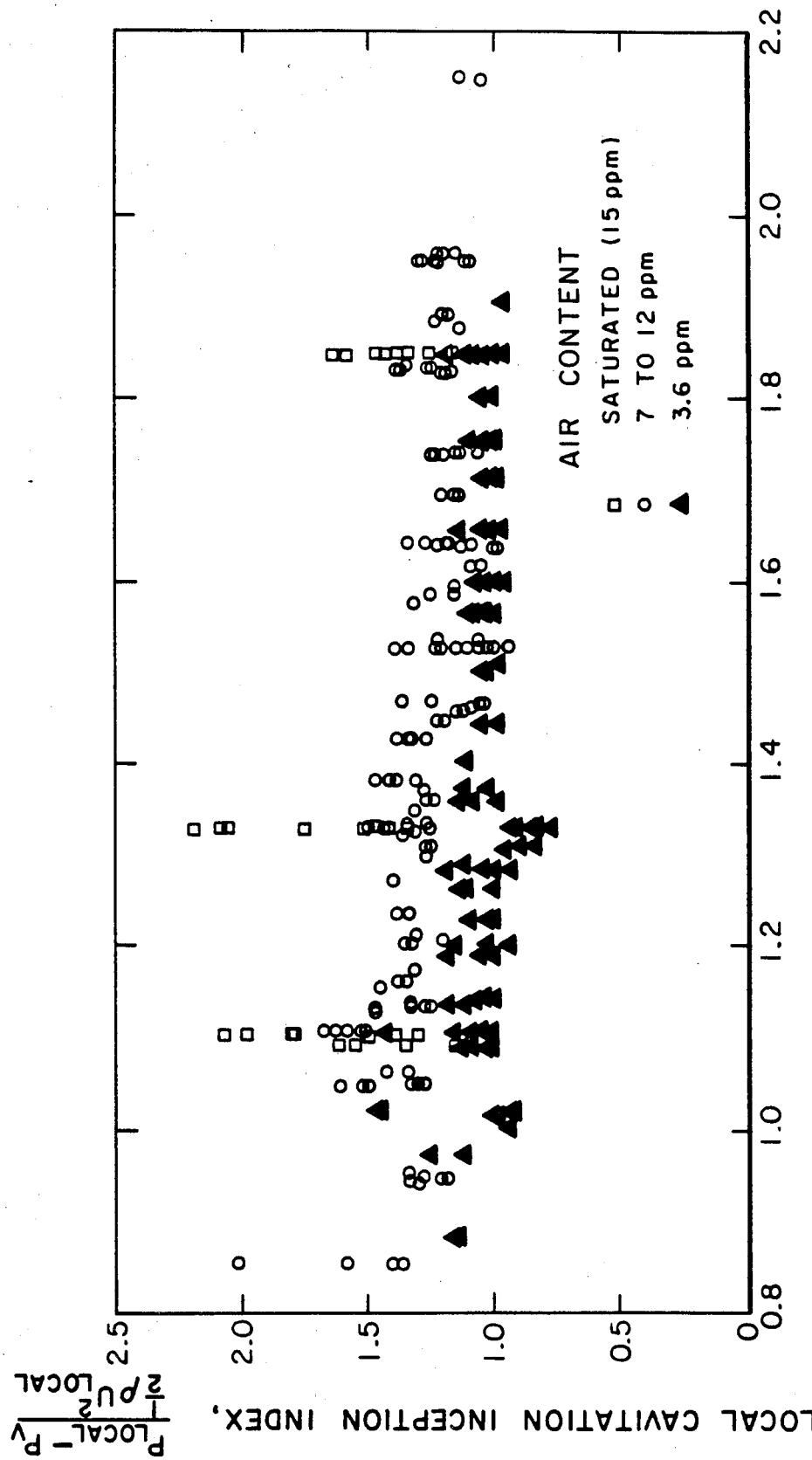

Figure II.4.27. Cavitation inception indices in the free shear layer. Note sharp dependence of inception index on dissolved air content.

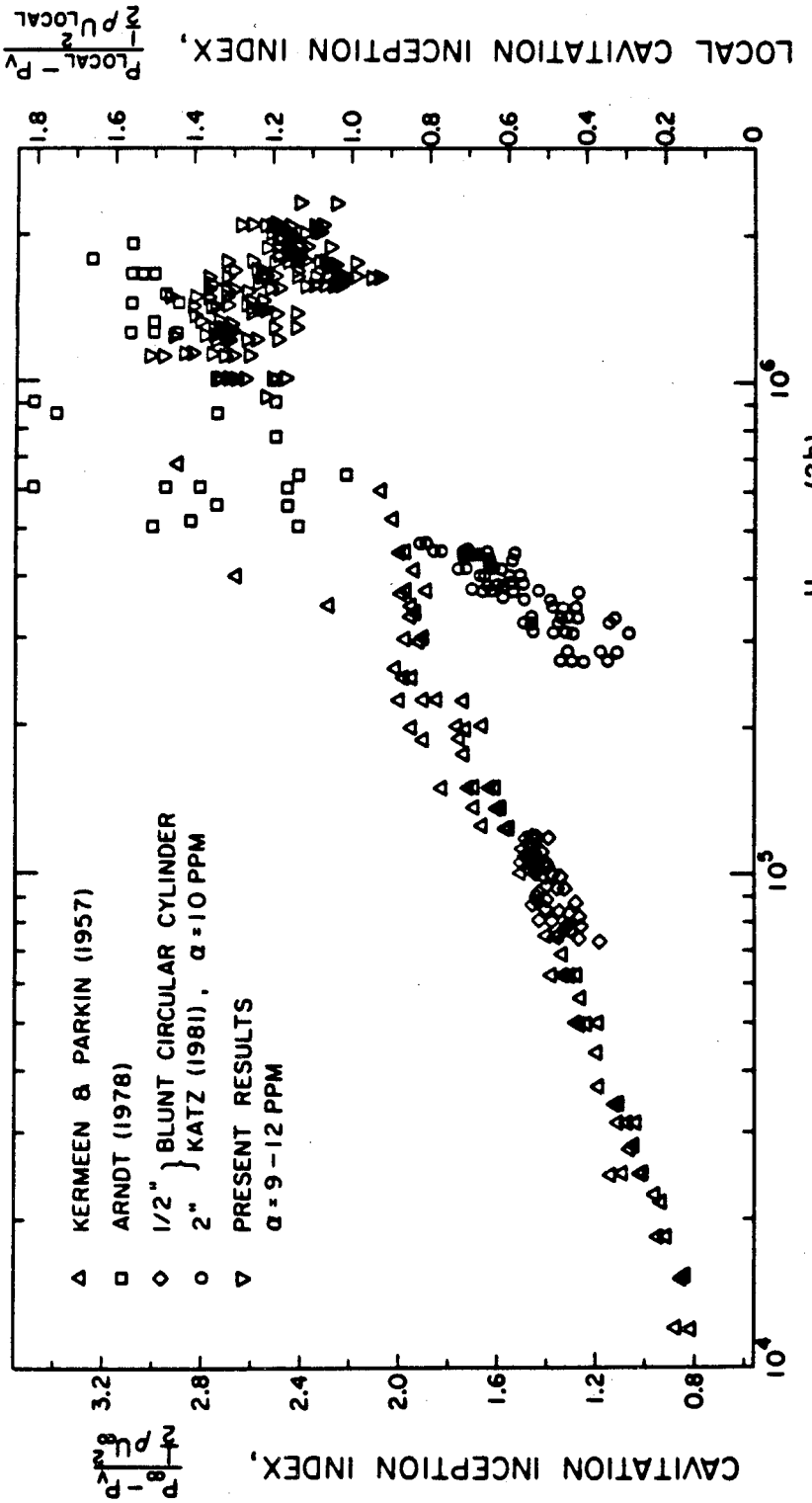

Figure II.4.28. Comparison of the data of Figure II.4.27 with inception measurements on sharp edged disks by Kermeen & Parkin (1957) and Arndt (1978), and on blunt circular cylinders by Katz (1981).

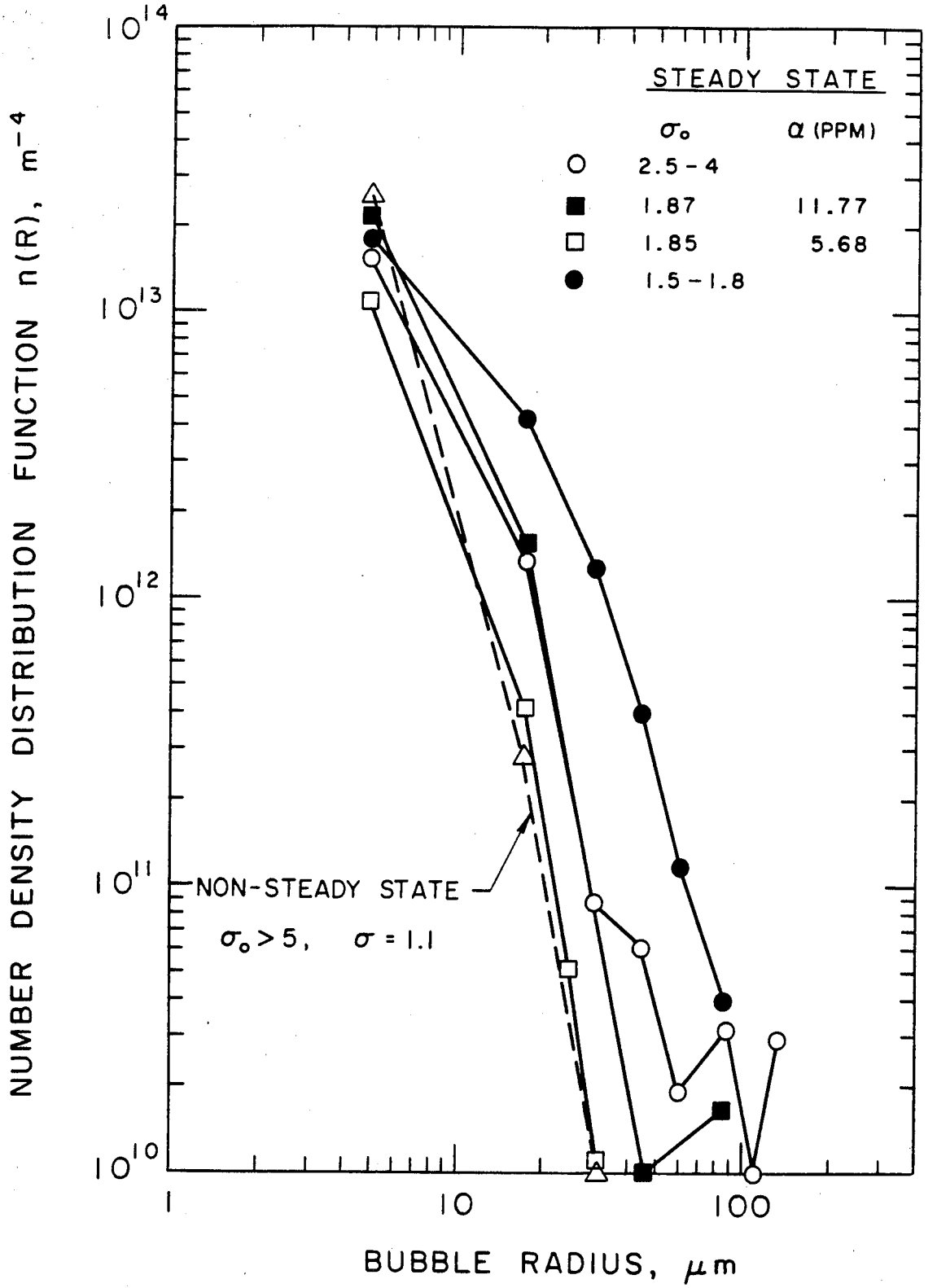

Figure II.4.29. Bubble number density distribution function $n(R)$ in LTWT under steady and instantaneous conditions (from Katz & O'Hern 1983).

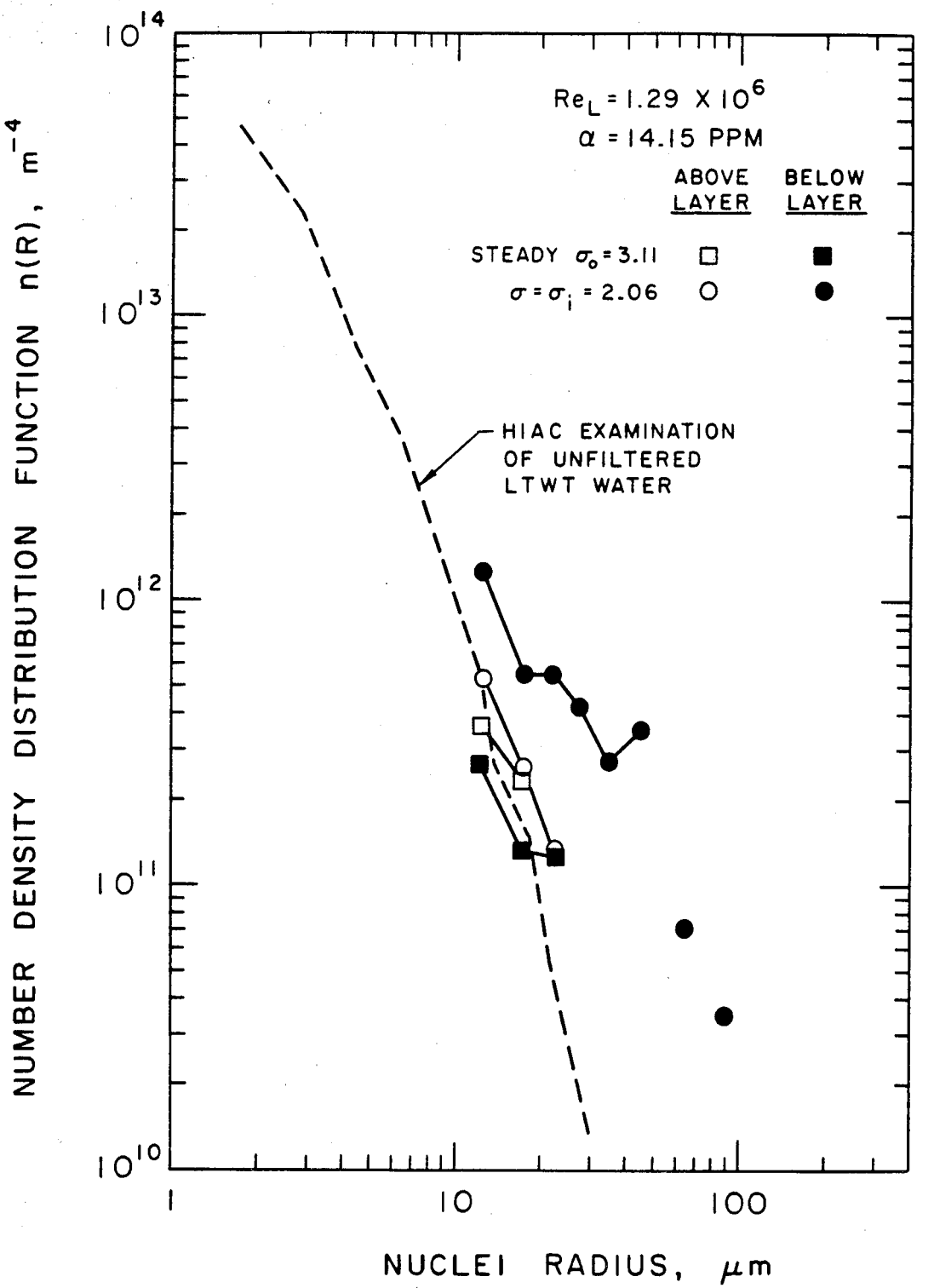

Figure II.4.30. Bubble number density distribution function $n(R)$ in LTWT in flow regions above and below the shear layer behind the sharp edged plate. Particulate concentration measured with HIAC optical counter also included.

Relative Vortex Strengths								
U_L (m/s)	Re_L	σ_L	r_c (mm)	$\frac{x}{h}$	Γ_s (m^2/s)	Γ_p (m^2/s)	$\frac{\Gamma_s}{\Gamma_p}$	$\frac{\Gamma_s}{r_c U_L}$
7.8	1.39×10^6	1.52	0.48	2.7	0.02	1.06	0.02	5.48
7.8	1.39×10^6	1.52	0.79	3.7	0.03	1.40	0.02	5.48
7.8	1.39×10^6	1.52	0.79	4.6	0.03	1.69	0.02	5.48
7.8	1.39×10^6	1.52	0.79	3.6	0.03	1.34	0.02	5.48
7.8	1.39×10^6	1.52	2.70	3.4	0.12	1.06	0.09	5.48
8.9	1.59×10^6	0.92	0.48	2.2	0.02	1.02	0.02	4.28
8.9	1.59×10^6	0.92	0.48	2.2	0.02	1.02	0.02	4.28
8.9	1.59×10^6	0.92	0.51	2.2	0.02	1.02	0.02	4.28
8.9	1.59×10^6	0.92	0.52	3.4	0.02	1.47	0.01	4.28
8.9	1.59×10^6	0.92	0.63	2.4	0.02	1.09	0.02	4.28
8.9	1.59×10^6	0.92	0.71	3.9	0.03	1.66	0.02	4.28
8.9	1.59×10^6	0.92	0.87	5.0	0.03	2.08	0.02	4.28
8.9	1.59×10^6	0.92	1.07	4.3	0.04	1.83	0.02	4.28
8.9	1.59×10^6	0.92	1.11	1.8	0.04	0.86	0.05	4.28
8.9	1.59×10^6	0.92	2.50	4.7	0.10	1.97	0.05	4.28
8.9	1.59×10^6	0.92	4.28	5.0	0.16	2.07	0.08	4.28
9.5	1.68×10^6	1.47	0.48	3.2	0.02	1.49	0.02	5.40
9.5	1.68×10^6	1.47	0.56	4.2	0.03	1.87	0.02	5.40
9.5	1.68×10^6	1.47	0.60	4.4	0.03	1.96	0.02	5.40
9.5	1.68×10^6	1.47	0.92	2.9	0.05	1.36	0.03	5.40
9.5	1.68×10^6	1.47	1.04	3.1	0.05	1.45	0.04	5.40
9.5	1.68×10^6	1.47	1.44	2.9	0.07	1.35	0.06	5.40
10.4	1.85×10^6	1.02	0.48	3.2	0.02	1.62	0.01	4.48
10.4	1.85×10^6	1.02	0.48	3.2	0.02	1.64	0.01	4.48
10.4	1.85×10^6	1.02	0.93	4.3	0.04	2.10	0.02	4.48

Table II.4.1. Relative strength of streamwise and spanwise vortices in the shear layer. The streamwise vortex strength was determined using the Rankine vortex model and measurements from photographs recorded near inception.

3-D Velocity Components			
Object	U_x (m/s)	U_y (m/s)	U_z (m/s)
150 μm bubble	3.46	-1.71	-0.86
110 μm bubble	-0.82	-0.54	-1.98
140 μm bubble	1.10	-0.21	0.81
85 μm bubble	1.68	-0.13	-0.04
125 μm bubble	-0.44	0.44	-2.55
90 μm bubble	-0.28	0.14	-0.86
80 μm bubble	1.08	-0.36	0.55
160 μm bubble	0	0.54	1.35
90 μm bubble	-0.40	-0.49	0.72
165 $\times$ 145 μm sheared bubble	2.70	-2.54	-2.70
230 μm long vortex core	1.33	0.83	0.60

Table II.4.2. Measured velocity components near one of the streamwise cores. The freestream speed is nominally 7 m/s. U_x is the measured velocity in the mean flow direction, U_y is normal (up) and U_z is in the spanwise direction. The cavitation index $\sigma_L = 0.5$.

CHAPTER II.5
DISCUSSION

This chapter will include a discussion of the meaning and applicability of results presented in the previous chapter, and interpretation of their significance in terms of cavitation inception behavior. An extensive literature is available on shear flows of various types, and some comparison and discussion will also be made of appropriate elements of that literature with respect to the present findings.

II.5.1 Flow Field

II.5.1.1 Primary Vortex Structure

Cavitation was successfully applied as a means of visualizing the low pressure cores of large primary vortices, allowing measurement of such flow characteristics as growth rates, convection velocities, pairing location, vortex spacing, and shedding and passage frequencies. Although the underlying flow fields are significantly different, the overall appearance of the cavitating flows observed by Young & Holl (1966) and Franc & Michel (1983) in the wakes of various wedges was quite similar to the present observations in that the spanwise vortices remain visible far downstream, but begin to lose their sharp appearance at some distance as bubbles become more dispersed within their cores. Nevertheless, in both the present investigation and in the wedge wake studies, the vortex cores maintained their clarity for sufficient time to make detailed observations and measurements of them. In most of the present cases the spanwise cavities could be tracked from their first appearance near the sharp edge to the end of the splitter plate. In fact, the degree of organization was remarkable, and the "survival" times of coherent structures seem to be significantly higher in both the present investigation and the work of Franc & Michel than those seen in such studies as Hussain & Clark

(1981), who claim that the mixing layer of their investigation is "organized into large-scale vortical motions only infrequently."

Shear layer growth rates determined by the various means described in the previous chapter were all essentially equal. The analysis made by high speed motion picture examination was felt to be the most reliable, and the growth rate determined in this manner was given in Equation II.4.1 as

$$\frac{\delta}{h} = 0.225 \left[\frac{x}{h} + 0.25\right]$$

This growth rate agrees fairly well with that determined by Kermeen & Parkin (1957) for the shear layer in wake of a sharp edged disk, given by

$$\frac{\delta}{d} = 0.26 \left[\frac{x}{d}\right]$$

where d is the disk diameter. The results of Kermeen & Parkin show no clear growth rate dependence on velocity or disk diameter over the range of test velocities (1.5 to 18 m/s) covered in their experiments. Tollmein reported a growth rate $\delta/x = 0.255$ determined by total and static pressure surveys in a two-dimensional half jet (Goldstein, ed. 1965), and Batt (1977) reports the results of Sunyach & Mathieu of a growth constant ($\delta/(x - x_o)$, where x_o is the virtual origin) of 0.21 for the same type flow, basing the growth rate on the shear layer points of 10% velocity deviation from freestream values. The agreement between these various growth rates is quite good, especially considering the different means of generation of the shear layers. Most of the specific studies of turbulent structure (e.g., Brown & Roshko 1974; Winant & Browand 1974; Bernal 1981) have been made in plane two-stream mixing layers behind splitter plates, so a comparison of the growth rate in this situation will be useful. Batt (1977) tabulates the results of numerous investigations into the characteristics of several types of shear flows, including mixing layers with various values of the velocity ratio r, defined as $r = U_2/U_1$, where U_1 and U_2 are the velocities of the high

and low speed streams, respectively. For a growth rate based on the mixing layer 10% velocity deviation points, Table I of Batt gives growth constants for mixing layers with $r < 0.1$ ranging from 0.17 to 0.23, while for $r > 0.1$, the growth rate is lower, with growth constants in the range 0.04 to 0.13, lower growth rates corresponding to higher values of r. The growth rate of the present shear layer is fairly close to that of low velocity ratio mixing layers. The low growth rates for higher velocity ratio cases may be partially a matter of definition, however, since Bernal & Roshko (1986) found a growth rate based on 1% concentration deviation to have a growth constant of 0.22 for $r = 0.38$.

The spacing of spanwise vortices, l, in the present study was given by Equation II.4.2, which can be rewritten as $l = 0.50(x - x_o)$, with $x_o = -0.88\ cm.$ Brown & Roshko (1974) found a mean spacing $l = 0.31(x - x_o)$ from examination of high speed shadowgraph motion pictures of a mixing layer with $r = 0.38$ and a density ratio of 7 across the layer. Dimotakis & Brown (1976) found that the spacing constant $l/(\alpha(x - x_o))$, where α is the velocity parameter $(U_1 - U_2)/(U_1 + U_2)$, fell in the range 0.4 to 0.5 for a plane two-stream mixing layer in water. Jimenez et al. (1985) reexamined the flow visualization motion pictures recorded by Bernal (1981) and found a spacing constant of 0.694 for a limited number of counts. Hernan & Jimenez (1982) found a value of 0.578 ± 0.193 in analysis of another portion of the Bernal film. In half-jets ($U_2 = 0$) Fiedler & Mensing (1985) found a value of 0.56 in an excited case, and Jimenez (1983) found 0.561 in an unexcited case. Except for the Brown & Roshko result, which may be a special case because of the large density difference across the layer, and the value given by Jimenez et al., which they state seems large since it was not measured in a self-similar region of the layer, these spanwise spacing values are all in good agreement with the present measured value. The agreement between the various vortex spacing values is better than between the growth rate values discussed above, possibly because unlike the growth rate, there is no ambiguity in defining the mean vortex spacing.

The expected convection velocity of spanwise vortices, U_c, is the average of the stream velocities on either side of the layer, so a value of $U_c = 0.5\ U_1$ is expected for cases with $U_2 = 0$. Convection velocities were measured in both side- and top-view motion pictures, with the results shown in Figure II.4.16. There was a considerable jitter in the data, as demonstrated by the frequency distribution of Figure II.4.17, but the mean convection velocity was found to be about 40% of the freestream velocity U_L above the shear layer. Kermeen & Parkin (1957) found $U_c/U_\infty \simeq 0.6$ from their high speed movie analysis of vortices in a disk wake. Clark & Kit (1980) measured $U_c/U_\infty = 0.54 \pm 0.06$ for the vortices in a jet emitted through a sharp edged orifice. In the two-stream plane mixing layer behind a splitter plate, Brown & Roshko (1974) found convection velocities in the range $0.4\ U_1$ to $0.60\ U_1$, with an average of $0.53\ U_1$, considerably lower than the average of the two stream speeds given by $0.69\ U_1$. One possible reason put forth for the lower convection velocity was an effect the high density difference across the layer. Reexamination of the motion pictures of Bernal (1981) by Jimenez et al. (1985) led to convection velocities of $0.35\ U_1$. All of these measured values for the convection velocity of large spanwise vortices in various shear flows are in rough agreement, although there are considerable variations. Part of this discrepancy may be due to differences in experimental technique. Hussain & Clark (1981) used smoke to visualize the vortices of a round air jet, and measured convection velocities of 44% and 62% of the freestream velocity at the vortex leading and trailing edges, respectively, due to asymmetric vortex growth. This effect can lead to significantly different convection velocity values, depending on which portion of a vortex is tracked. In the present results the vortex mean centers were tracked. Overall, the mean measured convection velocities in the present tests are lower than expected, however; as shown by Figures II.4.16 and II.4.17, the spread of the data is very large.

The shedding and passage frequencies of spanwise vortices expressed in terms of the Strouhal number were presented in Figure II.4.19. Also shown in that

figure was the experimental curve determined by Kermeen & Parkin (1957), indicating fairly good agreement between these two cases. The decrease in passage frequencies with downstream distance is due to vortex coalescence. The wide range of frequencies with which vortex cores were observed to pass a given station was interpreted by Kermeen & Parkin as evidence of the turbulent nature of the shear layer, and similar behavior and interpretation hold for the present motion picture analysis, as shown in Figures II.4.20 (a) and (b). Kermeen & Parkin found no Reynolds number dependence of the Strouhal number over the Reynolds number range 2×10^4 to 3.4×10^5. It is not clear why the measured vortex shedding and passage frequencies in the present investigation and that of Kermeen & Parkin are so much higher that those typically measured for bluff body flows. For example, Roshko (1954) shows that the Strouhal number based on the shedding (not passage) frequency for a normal plate at high Reynolds numbers is about 0.14. The high values of St in the present flow may be due to the high blockage. Foss (in discussion of Clark & Kit 1980) demonstrates a possible aspect ratio dependence of St in the jet shear layer generated by a sharp-edged orifice, with higher aspect ratio leading to higher St. This argument cannot explain the high St values measured by Kermeen & Parkin, however. In the case of plane two-stream mixing layers, Winant & Browand (1974) measured a passage frequency of 0.6 Hz 15 cm downstream of the virtual origin in a very low Reynolds number flow ($U_1 = 4.06\ cm/s$, $r = 0.35$). Hernan & Jimenez (1982) estimated a midspan passage frequency of 300 Hz for the spanwise vortices observed in the film of Bernal (1981), at $U_1 = 10\ m/s$ and $r = 0.38$. The present average passage frequencies range from 173 to 86 Hz as the downstream distance is increased from $x/h = 1$ to 3. Franc & Michel (1983) studied the dependence of the shedding frequency on the cavitation index σ, and found that at high σ values the Strouhal number remained essentially constant at its single phase value, but as the cavitation index was lowered, St increased and reached a peak of about 1.1, exceeding its non-cavitating value by about 20%. The peak

value of St was seen to increase slightly with Re_D. Similar dependence of St on σ was measured by Young & Holl (1966), although the peak magnitude of St was of the order 0.2, considerably less than that measured by Franc & Michel. Both studies were made for body Reynolds numbers of the order 10^5, and the reason for the large difference in St values is not clear. The present vortex shedding and passage frequency data had to be recorded at low values of σ in order to fully visualize the vortices, and the σ dependence of St could thus not be examined. The passage frequencies for the present flow are in reasonable agreement with those estimated by Hernan & Jimenez (1982) for the high velocity plane mixing layer examination of Bernal.

Clearly, the flow examined in the present study has some fundamental differences from the more traditional two-stream plane mixing layer, the major difference being the high initial streamline curvature just downstream of the sharp edge in the present case. Inception was never observed in this high curvature region, indicating that the lowest pressures occurred farther downstream where the layer was more similar to a plane mixing layer. The growth rates, spanwise vortex spacing and shedding and passage frequencies were in fairly good agreement with those measured in plane mixing layers, although the convection velocity of spanwise vortices was lower. Ho & Huerre (1984) discuss "facility forcing," pointing out that discrepancies of up to 100% are common between measurements of such shear flow characteristics as growth rate and Strouhal number for examinations made in different test facilities. These large differences are attributed to variations in freestream turbulence level and to details of the facility construction, which may lead to acoustic resonances at or near shear layer instability frequency ranges. The differences between the measured characteristics of the present flow and those of plane mixing layers reported in the literature were relatively small, especially in consideration of these large expected variations. There is no reason to doubt that the basic turbulent vortex structure of the present wake shear layer is the same as that in the plane cases. High strain

rates in the curved portion of the flow may provide additional amplification to the streamwise vortices, but the presence of these vortices is surely due to the same basic instability mechanism as in the plane mixing layer. Most previous examinations of turbulent structure have been made in single phase flows, while all but the inception observations of the present examination were made for well-developed stages of cavitation (needed for motion picture clarity). As shown by Young & Holl (1966) and Franc & Michel (1983) cavitation is not a passive flow visualization technique, and some of the observed differences may be attributed to the effect of heavy cavitation.

The measured flow characteristics agree quite well with those measured in the wake of a sharp edged disk by Kermeen & Parkin (1957) in one of the only previous fully documented investigations into cavitation inception in a large separated shear flow. Comparison of the cavitation behavior observed in these two examinations will be made below.

II.5.1.2 Secondary Vortex Structure

The existence of a secondary, longitudinal vortex structure superimposed on the primary structure had been speculated, based on flow visualization observations (Brown & Roshko 1974; Konrad 1976) for some time before the study of Bernal (1981) demonstrated conclusively the true vortex nature of the "streaks" observed in prior studies. The mechanism of formation of secondary vortices has not been clarified, although numerous proposals have been put forth (Ho & Huerre 1984). The properties and significance of these vortices in the overall turbulent flow have also not yet been firmly established. Roshko (1980) speculates that the secondary vortices act to modify the Reynolds stress (controlled by the primary vortices) and to increase internal mixing. Konrad (1976), Briedenthal (1979, 1981) and Bernal (1981) all report the mixing transition in plane mixing layers, beyond which the degree of mixing between the two streams increases markedly. The increased interface between the streams when the secondary vor-

tices begin to "corrugate" the primary structure may explain this transition. Lasheras et al. (1986) claim that the streamwise vortices may be as important as the spanwise in the entrainment process, based on the fact that the dimensions of the two structures were of the same order of magnitude in their low Reynolds number study. However, the present results as well as those of several previous investigators (e.g., Konrad 1976; Briedenthal 1981) in high Reynolds number flows indicate that the longitudinal vortices are significantly smaller than the spanwise vortices. Numerical shear flow models that do not include the streamwise vortices may not be able to predict properly the Reynolds stress or growth rate of primary vortices (Hernan & Jimenez 1982, Bernal & Roshko 1986) and certainly cannot predict the cavitation inception behavior observed in the present study.

Secondary longitudinal vortex structures are not unique to plane mixing layers behind splitter plates. Velocity measurements made by Jimenez (1983) led to his recognition of the existence of "longitudinal streamers" in a rectangular air half-jet. Ruderich & Fernholz (1986) observed longitudinal structures in the braid between large spanwise vortices in the separated shear layer behind a sharp edged plate, "as observed in plane mixing layers." Clark & Kit (1980) noted an "umbilical cord of vorticity" connecting the primary vortices in the wake of a sharp edged orifice. Longitudinal vortices have also been detected in several cavitation studies, the details of which will follow in Section II.5.3. It is clear that these structures are present in the separated shear layer of the present study, as can be seen in Figures II.4.3 through II.4.12. In fact, curvature at the ends of otherwise linear streamwise cores seen in some of the photographs and motion pictures may indicate the curved spanwise core/braid junction shown in the flow schematic of Figure II.1.1. Frame (vii) of Figure II.4.12 is an example demonstrating such a case.

All previous investigations into the secondary structure have noted an increased spanwise spacing of the streamwise vortices with downstream distance

(Briedenthal 1979; Bernal 1981; Jimenez 1983; Jimenez et al. 1985; Bernal & Roshko 1986; Lasheras et al. 1986). Measurements of the average distance between longitudinal vortices in the high speed motion pictures, shown in Figure II.4.23, demonstrated very wide scatter, and thus cannot be reliably used to determine a quantitative spacing rate change, but overall did seem to support the observation of increased spacing with downstream distance.

Examination of the critical Reynolds number of mixing transition, or transition to full three-dimensionality, indicates necessary conditions for the occurrence of secondary vortices. Roshko (1980) presents results of Jimenez et al. (1979), showing that the frequency dependence of the power spectrum of velocity fluctuations in the inertial subrange in a plane mixing layer with velocity ratio $r = 0.5$ changed from the -3 to the $-5/3$ power for a change in Reynolds number $(= U_1 x/\nu)$ from 3×10^4 to 6×10^4, suggesting a change from two-dimensional to three-dimensional turbulent structure of the small scales. For liquids, the transition Re_x is much lower, in the range of 750 to 1700 (Briedenthal 1981; Ho & Huerre 1984). For typical freestream velocity values on the order of 10 m/s, and for $\nu = 1 \times 10^{-6}$ m^2/s, the present flow would be past critical, or susceptible to a three-dimensional instability, for almost all downstream positions (beyond several mm). This may be one reason why no dependence of the downstream location of streamwise vortex visibility on U_L was observed; the full flow field is equally likely to contain three-dimensional structure over all freestream velocities.

Estimates of the strength (circulation) of the longitudinal vortices seen at inception were made using a Rankine vortex model, with the results presented in Table II.4.1. The results show that the strength of secondary vortices is always less than 10% of the spanwise strength ($\Gamma_s/\Gamma_p \leq 0.1$). These relative strengths seem reasonable, since a strong streamwise vorticity would tend to destroy the spanwise coherence, which is never observed in any of the investigations. Nevertheless, cavitation inception is always seen to occur in the streamwise rather

than in the larger and stronger spanwise structure. Jimenez et al. (1985) estimated the relative strengths of spanwise and streamwise vorticity by examining the equations of motion for a fluid particle on the braid, at equilibrium between the motions induced by the spanwise and streamwise vorticity fields. Use of this model and measurements from the flow visualization movies of Bernal led to an estimate of the relative strength as $\Gamma_s/\Gamma_p = 0.61 \pm 0.79$. The scatter is very large, but the mean value indicates much stronger secondary vortices than were determined using the Rankine vortex model and the photographs at inception. Measurement of the thickness of the braid region, used in calculating this relative strength expression, could not be made in the present study, so direct comparison was not possible.

Jimenez (1983) used hot-wire velocity measurements in a rectangular half-jet in air to determine that the strength of the secondary vortices is approximately equal to Γ_{po}, the initial circulation of each wave of the Kelvin-Helmholtz instability. Jimenez et al. (1985) found a higher ratio, $\Gamma_s/\Gamma_{po} = 1.59 \pm 2.08$, for the Bernal mixing layer experiment, although the uncertainty is very large. Estimates of Γ_{po} in the present flow were made by applying Equations II.4.2 and II.4.6. The nearest downstream location of visibility of spanwise cores in heavily cavitating flows was on the order of 1 cm, and Equation II.4.2 gives a vortex spacing l of 1.4 cm at this location. Therefore, by Equation II.4.6, the circulation of the initial wave of the Kelvin-Helmholtz instability is expected to be of the order 0.1 m^2/s. This value agrees fairly well with the estimated strengths of longitudinal vortices made by the Rankine vortex model and listed in Table II.4.1, thus supporting the finding of Jimenez (1983) that $\Gamma_s \simeq \Gamma_{po}$. Jimenez et al. (1985) claim that the longitudinal vortices have "more or less constant circulation," so the ratio Γ_s/Γ_p should decrease downstream as the spanwise circulation increases. For the Rankine vortex model, vortex strength is determined by core radius, freestream velocity and inception index. Therefore, the ratio Γ_s/Γ_p would decrease with downstream distance in this model as well, since ob-

servations indicate that the longitudinal vortex core thickness (measured cavity thickness) increases only very slightly with downstream distance. The assumptions used in developing the Rankine vortex model used for determination of the vortex strengths were discussed in the previous chapter. Overall, the assumptions are valid for order of magnitude estimates.

Holographic measurements of the local near-core tangential velocity U_θ were attempted as an alternate means of determination of the strength of the longitudinal vortices. This measurement is difficult, since the vortices occur at random throughout a fairly large volume. The concept of forcing the structure to try to maintain spatially well-defined vortex cores was considered but not implemented because of questions as to the effect of forcing on the overall flow. Ho & Huerre (1984) state that low level forcing can "alter significantly the downstream development of the flow." As discussed in the previous chapter, the measured velocity components clearly demonstrate the three-dimensional nature of the flow, but the velocities do not seem high enough to explain the fact that inception occurs in these cores rather than the stronger, larger primary cores. This may be due to the lack of tracers very close to the cavitating cores, preventing measurement of the *peak* velocities.

II.5.2 Turbulent Pressure Fluctuations

The existence of large fluctuating pressure peaks in free turbulent flows is well known and is expected to play a critical role in cavitation inception in these flows (Arndt & George 1979; Ooi 1981; Ooi & Acosta 1983). Ooi (1981) developed the air bubble injection technique as a means of determination of localized instantaneous pressures at discrete sites throughout a turbulent flow field, and was the first to use this method to measure pressure fluctuations in a Lagrangian frame.

Since the pressure fluctuation results of Ooi are the only comparable ones reported to date, the present results will be compared with those found in his

survey of a turbulent jet shear layer. The measured pressure peaks in his investigation were as high as +160% and −120% of the jet dynamic pressure, the fluctuations fitting a Gaussian distribution slightly skewed toward positive pressures. The r. m. s. pressure fluctuations were 64% of the jet dynamic pressure, 4 to 8 times higher than any previously reported, possibly because previous measurements had been made with transducers that were larger than the bubble "pressure sensors" and so tended to spatially average the pressure signal (Ooi 1981). Ooi pointed out that peak pressures as high as 10 times the r. m. s. values had been predicted based on aeroacoustic measurements, whereas his measured peaks were considerably closer to the r. m. s. levels. The present results ($U_L = 4.9\ m/s$) also demonstrate very large pressure fluctuations, with r. m. s. values up to 150% of the local dynamic pressure and peaks on the order of $\pm$ 3 times the local dynamic pressure. The uncertainty in the present measurements is considerably higher than in the investigation made by Ooi however, especially in consideration of the somewhat arbitrary (though reasonable) means of determination of which bubbles to count. Overall the pressure excursions in the present flow are of the same order of magnitude of those determined by Ooi in a turbulent jet flow, and are in better agreement with his findings than with aeroacoustic estimates.

Arndt & George (1979) made a theoretical investigation into the turbulent pressure spectrum in homogeneous, isotropic turbulent flows, with and without shear, which led to the conclusion that the peak pressure fluctuations will increase with Reynolds number, which could be a very important point in terms of shear flow cavitation scaling. The present results are for only one velocity, since the distribution corresponding to the injected bubbles could not be recovered for the high velocity case. Therefore no experimental verification of the dependence of pressure peaks on Reynolds number can be made with the present results. The jet flow measurements of Ooi were also made at a fixed Reynolds number, and so cannot be used to confirm this predicted scaling either.

The uncertainty in the present results is high since the presence of a large recirculating wake region limits the applicability of the air bubble injection technique. The primary difficulty in determination of the fluctuating pressures by analysis of bubble sizes is in establishing whether the bubbles measured and counted in the water sample were actually the ones that had just been injected. Determination of which bubbles to include in the distribution had to be made by the process described in the previous chapter, discarding bubble counts in order to center the distribution about its mean diameter while simultaneously bringing the mean diameter closer to the mode and bringing the mean indicated static pressure closer to the base pressure. The choice of which bubbles to use as valid pressure indicators changes the value of the mean indicated static pressure and therefore the magnitude of the pressure fluctuation peaks. The approximations inherent in determination of the pressure fluctuations and the small number of measurements in the present experiments leads to a large experimental uncertainty in the exact magnitude of the positive and negative peaks, as well as the exact shape of the normalized pressure fluctuation distribution (see Figures II.4.25 and II.4.26). However, even with these caveats, the calculated peak pressure values are very large and significant in terms of cavitation inception. The minimum pressure in the flow is given by the maximum negative pressure deviation from the mean, i.e., $p_{min} = p_B - p'$, where p_B is the base pressure and p' is the maximum fluctuation. The local cavitation inception index σ_L is based on the mean local flow velocity and pressure values, so the minimum pressure coefficient in the flow at the moment of inception can be given by:

$$\frac{p_{min} - p_v}{\frac{1}{2}\rho {U_L}^2} = C_{pb} + \sigma_L - \frac{p'}{\frac{1}{2}\rho {U_L}^2} \qquad \text{(II.5.1)}$$

where C_{pb} is the base pressure coefficient based on the local pressure and velocity, which is on the order of -0.01 over all flow velocities for the present tests (see Section II.4.1). The measured negative pressure peaks on the order of 3 times the local dynamic pressure are easily intense enough to explain cavitation inception

at relatively large values of σ_L.

Even if it were possible to isolate and measure only injected bubbles at the downstream measurement location, several potential sources of error exist in this pressure measurement technique. First, it is not clear what value to use for the polytropic index γ, although both the present results and those of Ooi show that this choice has only a minor effect on the calculated pressure fluctuation values. Use of γ values of 4/3 and 1.0 made very little difference in the pressure calculations, with the isothermal case ($\gamma = 1.0$) having only slightly lower peak and r. m. s. pressure fluctuations, as shown in Figures II.4.25 and II.4.26. Second, the bubbles are strongly sheared when they enter the turbulent shear region, so their reconstructed images typically project an ellipsoidal cross-sectional area when recorded downstream. Ooi has shown that ellipsoidal bubbles remain valid pressure indicators, the difficulty being in determination of what bubble diameter to use, since only a major and minor diameter can be measured from the reconstructed image. The geometric mean is assumed to correctly characterize the bubble, which should lead to insignificant error except for the case of highly sheared bubbles, which were not encountered in the measurements. Again, it should be stressed that although the injected bubbles were strongly sheared as they entered the shear flow, no evidence of bubble breakup was ever observed.

Instantaneous pressure measurements cannot provide the spectrum of pressure fluctuations, so the duration of the pressure peaks is unknown. In particular, the question arises as to whether bubbles and other nuclei are exposed to the low pressures for a sufficient time period to allow cavitation to occur. Further investigations must be made in order to determine the duration of the peak pressures. However, since the low pressure peaks are assumed to correspond to streamwise vortex cores, they are expected to persist for a significant time relative to the bubble response time. The high speed motion pictures showed longitudinal vortex core lifetimes on the order of 0.1 *sec*, very long relative to typical bub-

ble response times given by Equation II.3.7. For example, the equation gives a response time of about 100 μs for a 100 μm radius bubble.

II.5.3 Effect of Flow Field on Cavitation Inception

The dependence of inception on the secondary vortex structure is not unique to the present flow configuration. van der Muelen (1980) noted the "irregular threadlike appearance of cavitation" in the separated flow past NACA 16-012 hydrofoils at a 16° angle of incidence. Cavitation in the separated shear layer around flat-faced circular cylinders studied by Katz (1981, 1984) clearly shows inception occurring in thin, axially oriented vortices, which remain visible even when heavier cavitation fills in the primary circumferential vortices, and very similar behavior is evident in the photographs of Keller (1979). Although not mentioned in their paper, close examination of photographs of shear layer cavitation in Kermeen & Parkin (1957) provides evidence that early stages of cavitation in the wake of a sharp edged disk are present as similar thin, streamwise oriented structures. The study of vortex shedding in the wake of wedges by Franc & Michel (1983) showed cavitation in both the large shed vortices as well as thin "three-dimensional rotational filaments" connecting the large vortices, as noted by the authors and clearly visible in several of their figures. They did not state whether inception takes place in the longitudinal structure, although their photographs taken at conditions near inception indicate that this is the case. Ooi (1981) made flow visualization studies of the turbulent submerged water jet and observed "cellular structures" just downstream of the laminar portion of the jet, similar to the hairpin vortices seen by Konrad (1976) in a water mixing layer. Inception in the jet did not occur in the cores of primary ring vortices, indicating that the secondary instability of the axisymmetric jet shear layer may be important in the cavitation inception process of this flow as well. This survey is by no means comprehensive, but clearly shows that the turbulent shear layer of the present examination is not the only flow situation in which cavitation behavior,

particularly inception, is dominated by the streamwise vorticity.

The occurrence of inception in the cores of longitudinal vortices may provide an explanation for the commonly observed dependence of the inception index in shear flows on the Reynolds number. Although the strength of streamwise vortices and their dependence on flow conditions have not yet been firmly established, several overall concepts concerning their behavior are becoming generally accepted. The secondary vortices are created by an instability of the primary structure. The layer is unstable to three-dimensional disturbances, with flow perturbations upstream acting to trigger the instability. However, as Bernal (1981) has pointed out, the streamwise vortices respond differently to different downstream flow conditions, indicating that they are formed by a true instability mechanism and are not "anchored" to the initial disturbances. Bernal has demonstrated a velocity dependence of the three-dimensional instability amplification process, in that the downstream location of the "streak" visibility threshold can be shifted by changing the velocity or the velocity ratio. The number of axial vortices and their spanwise pattern also changes with velocity. This velocity-dependent behavior indicates that the vortex strength increases with velocity, so cavitation occurring in these vortex cores would be expected to occur more readily at higher velocities, possibly explaining the observations of increasing cavitation index with increasing Reynolds number. The vortex strengths calculated with the Rankine model (shown in Table II.4.1) do not indicate any clear velocity dependence. The random appearance of cavitation in the present investigation, particularly near inception, limits its usefulness as a visualization technique, so that such factors as the spacing and pattern of streamwise vortices measured by Bernal could not be corroborated with any certainty by the present results.

II.5.4 Nuclei Availability Effects

All inception testing was performed with a steady-state population of nuclei. The pressure was lowered for only a few seconds during each test; then the tunnel

was returned to steady conditions and maintained there for at least 10 minutes prior to the next test. The importance of operation at steady conditions is demonstrated in Figure II.4.29, which shows that the bubble population density is much more dependent on the steady tunnel operating pressure than on the instantaneous pressure at the time each hologram is recorded. For example, the "non-steady" case in the figure is one in which a steady-state cavitation index $\sigma_o > 5$ was maintained between tests, and the instantaneous σ at the time of hologram recording was 1.1. The bubble distribution in this case is much closer to the steady results for a high σ_o than to those for a low σ_o (nearer to the instantaneous σ at the time of hologram recording).

The cavitation indices plotted in Figure II.4.27 demonstrate a clear dependence of the inception index on the dissolved air content. The concentration of freestream bubbles in the LTWT test facility has been shown to be dependent on the dissolved air content in several previous investigations; see Katz (1984) and Ooi (1985). For example, Ooi found that a decrease of dissolved air content from 14.3 to 4.2 *ppm* lowers the bubble concentration by a factor of about 35 in the size range $5 < R < 20\ \mu m$. This air content effect can be seen in Figure II.4.29, which shows that an increase in air content from 5.68 to 11.77 *ppm* leads to a substantial increase of the bubble number density distribution function for otherwise similar conditions. The present inception results are significantly different than those of Arndt & George (1979), who measured the desinent cavitation index σ_d (cavitation index needed to stop existing cavitation) in the confined jet flows generated by nozzles and orifice plates, finding that the desinent index was independent of air content for undersaturated conditions, while for supersaturated conditions the desinent index increased linearly with dissolved air content. The present results are all for tests made with air contents in the undersaturated-to-saturated range, and exhibit the strong air content dependence mentioned above. The discrepancy between these results may be due to the difference between inception and desinence; i.e., the effect of air content may be less significant for desinence

since sufficient nuclei are always available in this case because of existing cavities and the bubbles formed when they collapse. The overabundance of nucleation sites in supersaturated conditions may be sufficient to change the desinent index. Desinent cavitation indices were not measured during the present tests.

Discussion of the effect of nuclei availability as measured in the non-cavitating free stream is valid only for the behavior at inception. Beyond inception (lower σ values), the full shear layer is no longer exposed to a constant bubble nuclei concentration, since the collapse of large cavities produces clouds of small bubbles, as several of the high speed movies have clearly shown. This is a particularly important problem in the present flow, since these small bubbles can be entrained in the recirculating wake region and thus expose the low pressure points of the shear layer to additional nuclei. However, even below inception the air content has a strong effect on the state of cavitation, in general, the higher air content cases exhibiting a more fully developed state of cavitation. This can be demonstrated by comparing the two sets of figures, II.4.5 and II.4.6 with II.4.7 and II.4.8. Both sets were recorded at similar velocity and pressure conditions, the only difference being the dissolved air content. The high air content cases (II.4.5 and II.4.6) clearly exhibit a more fully developed state of cavitation, and more freestream bubbles are visible as well.

Katz (1981) performed detailed holographic nuclei measurements above and below the separating streamline in the flows around various blunt axisymmetric bodies and determined that the population of microscopic bubbles (less than several hundred μm in diameter) in the cavitation region below the separating streamline increased just prior to onset of visible macrocavitation, while the bubble concentration in the rest of the flow remained unchanged. The concentration difference between the two regions increased as σ was lowered, leading Katz to speculate that the flow was already cavitating on a limited scale prior to the onset of visible "macrocavitation." The bubble population below the separating streamline increased by an order of magnitude at macroscopic cavitation incep-

tion, and the growth of microbubbles to a visible state at inception was confined to the flow region below the separating streamline. As mentioned in the previous chapter, similar results were obtained in the present testing. Figure II.4.30 shows that bubble populations above and below the shear layer are essentially equal at steady non-cavitating conditions (high σ_o). When σ is lowered to the point of visible cavitation ($\sigma_i = 2.06$), the bubble population below the layer increases by up to an order of magnitude over all size ranges, with the larger bubble size ranges especially affected. The freestream bubble population above the shear layer remains constant at the steady value. Vertical traverses through several reconstructed images recorded at incipient conditions show that the highest bubble concentrations occur at or near the estimated location of the separating streamline, thus supporting the idea put forth by Katz (1981), that "microcavitation" occurs in the shear layer prior to the appearance of the first visible vortex cavitation. When the cavitation number is lowered to below incipient conditions, a large increase in bubble population in the recirculating wake region becomes evident, as can be clearly seen in the photographs of Figures II.4.2, II.4.3, II.4.9 and I.4.10. The data of Figure II.4.30 and the discussion above are for a high dissolved air content. For lower dissolved air contents, similar behavior is seen, although the magnitude of the difference in bubble concentration between the flow regions above and below the shear layer is much lower, on the order of a factor of two.

The holograms examined to give the data of Figure II.4.30 and for the discussion above were all recorded close to the plate tip in order to simultaneously sample the flow regions above and below the shear layer. Streamwise vortices were never observed so close to the plate under near-incipient flow conditions, so the pressure fluctuations here are expected to be lower than those measured farther downstream. This may explain why the magnitude of the difference between bubble concentrations measured above and below the shear layer was not as high as that measured by Katz.

II.5.5 Scaling Laws for Shear Flows

The key parameters controlling cavitation inception in any flow are the susceptibility of the liquid, that is, the concentration, size distribution, and type of nuclei available, and the characteristics of the pressure field to which the nuclei are exposed. In turbulent flows, the magnitude and spectra of the minimum pressure peaks are needed, along with the nuclei distributions, in order to define the conditions at inception.

Nuclei populations play an important role in cavitation scaling, and the dissolved air content has been shown numerous times to characterize the bubble nuclei concentrations fairly well. The present inception index results shown in Figure II.4.27 demonstrate that at a fixed velocity (fixed Reynolds number), the water containing the highest dissolved air content will tend to cavitate most readily. Therefore, the detailed nuclei content, or at least the dissolved air content, must be included in cavitation scaling laws.

The cavitation index σ is the standard parameter used to characterize cavitation behavior. However, difficulties arise when applying σ to characterize the inception conditions of shear flows since a strong Reynolds number dependence has commonly been observed. The results of Kermeen & Parkin (1957) provide inception indices for disks of various diameters and freestream velocities, and clearly show that the Reynolds number is a valid parameter to collapse the experimental data to a single curve (as included in Figure II.4.28). Close examination of experimental data of Kermeen & Parkin indicates a possible leveling off of the inception index at the high Reynolds number limit ($\simeq 10^6$), leaving only a size dependence. The narrow range of Reynolds numbers covered during inception tests, and the scatter of the data, prevent determination of any particular trend in the present data, although the leveling trend seems to best fit the present data. Size dependence could not be investigated with the present test apparatus. Section II.5.3 included discussion as to the possible effect of streamwise vortices on Reynolds number dependence of the inception index for those flows in which secondary vorticity plays a dominant role in the inception process. Further work remains in determining the characteristics and scaling of

secondary vortices in shear flows, but the early investigation of Bernal (1981) indicated that the secondary vortex strength may be velocity-dependent, possibly explaining the Reynolds number effect on the inception index (although not its leveling off).

A practical difficulty in using the inception index σ_i is that in high air content cases the nature of inception changes, possibly because of a change from vaporous to gaseous cavitation, making determination of the exact moment of inception difficult. This was discussed in Sections II.4.2.1 (in relation to the scatter of Figure II.4.27) and II.5.4.

One of the limitations of the cavitation index as commonly measured, based on mean freestream velocity and pressure, is that it does not include the fluctuating pressure components needed to explain cavitation behavior in turbulent flows. Equation II.5.1 shows that fluctuations can cause a minimum flow pressure significantly lower than the mean freestream value used in determining σ.

II.5.6 Suggestions for Future Work

As a major portion of this chapter was spent establishing areas of similarity between the shear flow in the wake of a sharp edged plate and the plane two-stream mixing layer, it should be clear that a useful examination would be of the cavitation characteristics of the traditional mixing layer and other types of shear flows that have been more specifically characterized in terms of their coherent structure. Such investigations may clarify the relation between streamwise vortices and cavitation, particularly their Reynolds number scaling. It would be useful to combine a flow visualization technique that did not require maintaining low values of the cavitation index, since this restricts the range of flow conditions to be tested, and may also affect the underlying flow to some extent.

The effect of upstream conditions on the secondary vortices seems clear from the results of Bernal (1981) and Lasheras et al. (1986), although the present results could not be used to support their observations. A specific examination of this effect through controlled upstream disturbances would be helpful. Along these same lines, it would be useful to repeat the present tests in a towing tank or other quiescent test facility, to see whether the longitudinal vortices remain

the cavitation inception sites when upstream disturbances that may trigger the three-dimensional instability are eliminated.

The primary difficulty in all of the observations and measurements was the randomness of cavitation inception (both spatially and temporally) at fixed flow conditions. Temporal fluctuations are an inherent part of the cavitation process, but the spatial distribution of low pressure vortex cores could conceivably be controlled by low-level forcing of the layer. Detailed examination of the pressure and velocity fields in the near-core region could be performed if the flow was excited in such a way as to fix the locations of the longitudinal vortices. For example, laser doppler velocimetry could be then applied to determine the tangential velocity U_θ near the longitudinal cores.

Even without forcing, some of this velocity information can be obtained using the same double-pulsed holographic technique applied in the present investigation. Carefully controlled tracer injection must be used, however, to increase the data rate in order to obtain a useful number of velocity measurements in the region of interest. The concept of forcing again becomes attractive as a guide to the proper injection site.

The air bubble injection technique of measuring pressure fluctuations was moderately successful in the present study, although it is not well suited to this flow where the existence of a large recirculating wake leads to bubble entrainment. Accurate use of this technique would require a more definite means of certifying which bubbles could be counted as valid pressure sensors. In addition to peak pressure values, measurement of the spectrum of fluctuating pressures is needed to define the duration of exposure of nuclei to low pressure. These measurements must be made from a Lagrangian viewpoint in order to define the pressure field a bubble will be exposed to, as it traverses the flow.

CHAPTER II.6
SUMMARY AND CONCLUSIONS

Cavitation phenomena were studied in the turbulent shear flow behind a sharp edged plate at Reynolds numbers up to 2×10^6. Two distinct types of vortex motion were evident in the shear layer, the primary spanwise and secondary streamwise vortices. While both theoretical and experimental investigations of turbulent shear flows point out the dominant role of the primary vortex structure in the overall flow field, the present results show that the secondary vortices control cavitation inception, indicating that the lowest flow pressures occur in the cores of these vortices. Inception occurred at random locations throughout the shear layer, although not in the high curvature region just downstream of the sharp edged plate. No clear downstream or spanwise location of most probable occurrence of inception could be defined. More fully developed cavitation was visible in both vortex structures, with the streamwise cavities primarily confined to the braid regions between the spanwise cores.

Estimates using a Rankine vortex model showed that the strength of the secondary vortices was always less than 10% of that of the primary vortices, and thus could not explain the occurrence of inception in the streamwise vortex cores. Holographic velocity measurements near the streamwise vortices demonstrated the strong three-dimensionality of the shear flow but were unable to measure the high expected near core velocities needed to explain inception in the secondary vortex cores.

The overall flow characteristics including growth rate and vortex spacing displayed a high scatter characteristic of turbulent flows but overall showed that the present shear layer is similar to other free turbulent shear flows, including the plane two-stream mixing layer.

Air bubble injection was used to measure fluctuating pressure peaks in the shear layer and indicated very large pressure fluctuations, with positive and negative peaks as high as 3 times the local dynamic pressure. The observed magnitude of the negative pressure peaks is sufficient to explain cavitation inception occurring at large values of the inception index. However, there is a large experimental uncertainty due to the limited number of measurements and to the fact that the present flow, with its large recirculating region, is not well suited to the air bubble injection technique.

Cavitation inception indices display a strong dependence on the air content and thus on the availability of freestream bubbles as cavitation nuclei. The dissolved air content also regulates the appearance of more fully developed cavitation. The concentration of microscopic bubble nuclei in the recirculating flow region below the shear layer increased markedly at the moment of inception, with peak concentrations occurring close to the high shear region. Differences between the bubble concentrations above and below the shear layer were as large as an order of magnitude for 25 to 50 μm radius bubbles when the water was saturated with air, and were approximately a factor of two for undersaturated conditions.

The Reynolds number scaling effect on the inception indices was examined at higher values of the Reynolds number than previously reported. The narrow range of Reynolds numbers covered during inception tests, and the scatter of the data, prevented determination of a clear relation between the inception indices and the velocity (or Reynolds number), although the present data are generally consistent with the commonly observed trend of increasing inception index with increasing Reynolds number. Bernal (1981) demonstrated that the strength of the streamwise vortices may be velocity-dependent. This observation along with the present results indicating the importance of these vortices in the cavitation inception process may be the key to explaining the commonly observed Reynolds number dependence of the inception index.

REFERENCES

Acosta, A.J., Katz, J., O'Hern, T.J. (1983), "Microbubbles and Cavitation," Final Report on Contract N00014-75-C-0064, Caltech Report No. E261.2.

Acosta, A.J. and Parkin, B.R. (1975), "Cavitation Inception – A Selective Review," *J. Ship Research, 19*, 4, 193–205.

Acosta, A.J. and Parkin, B.R. (1974), "Cavitation Inception," 17th American Towing Tank Conference, Pasadena, CA.

Akulichev, V.A. and Ilyichev, V.I. (1986), "Acoustic Cavitation in Sea Water," Proceedings of the International Symposium on Propellers and Cavitation, Wuxi, China.

Alldredge, A. (1986), Department of Biological Sciences and Marine Science Institute, University of California at Santa Barbara, private communication.

Arakeri, V.H. and Acosta, A.J. (1973), "Viscous Effects in the Inception of Cavitation on Axisymmetric Bodies," *ASME J. Fluids Engineering, 95*, 4, 519–528.

Arakeri, V.H. and Acosta, A.J. (1979), "Viscous Effects in the Inception of Cavitation," ASME International Symposium on Cavitation Inception, New York.

Arie, M. and Rouse, H. (1956), "Experiments on Two-Dimensional Flow Over a Normal Wall," *J. Fluid Mechanics, 1*, 129–141.

Arndt, R.E.A. (1981), "Cavitation in Fluid Machinery and Hydraulic Structures," *Annual Review of Fluid Mechanics, 13*, 273–328.

Arndt, R.E.A. (1978), "Investigation of the Effects of Dissolved Gas and Free Nuclei on Cavitation and Noise in the Wake of a Sharp-Edged Disk," Joint IAHR/ASME/ASCE Symposium on Fluid Machinery, Fort Collins, Colorado.

Arndt, R.E.A. (1976), "Semiempirical Analysis of Cavitation in the Wake of a Sharp-Edged Disk," *ASME J. Fluids Engineering, 98*, 560–562.

Arndt, R.E.A. and George, W.K. (1979), "Pressure Fields and Cavitation in Turbulent Shear Flows," 12th Symposium on Naval Hydrodynamics, Washington, D.C.

Bader, H. (1970), "The Hyperbolic Distribution of Particle Sizes," *J. Geophysical Research, 75*, 15, 2822–2830.

Batt, R.G. (1977), "Turbulent Mixing of Passive and Chemically Reactive Species in a Low-Speed Shear Layer," *J. Fluid Mechanics, 82*, 53–95.

Bernal, L.P. (1981), "The Coherent Structure of Turbulent Mixing Layers, I. Similarity of the Primary Vortex Structure, II. Secondary Streamwise Vortex Structure," Ph.D. Thesis, Graduate Aeronautical Laboratories, California Institute of Technology.

Bernal, L.P. and Roshko, A. (1986), "Streamwise Vortex Structure in Plane Mixing Layers," *J. Fluid Mechanics, 170*, 499–525.

Billet, M.L. (1985), "Cavitation Nuclei Measurements - A Review," ASME Cavitation and Multiphase Flow Forum, Albuquerque, N.M.

Billet, M.L. (1984), "Cavitation Nuclei Measurements," ASME International Symposium on Cavitation Inception – 1984, New Orleans, LA.

Billet, M.L. (1981), "The Effect of Secondary Vorticity on the Inception of Vortex Cavitation," *ASME J. Fluids Engineering, 103*, 19–27.

Billet, M.L. and Gates, E.M. (1979), "A Comparison of Two Optical Techniques for Measuring Cavitation Nuclei," ASME International Symposium on Cavitation Inception, New York.

Billet, M.L. and Holl, J.W. (1979), "Scale Effects on Various Types of Limited Cavitation," ASME International Symposium on Cavitation Inception, New York.

Bradbury, L.J.S. (1976), "Measurements with a Pulsed-Wire and a Hot-Wire Anemometer in the Highly Turbulent Wake of a Normal Flat Plate," *J. Fluid Mechanics, 77*, 473–497.

Briedenthal, R.E. (1981), "Structure in Turbulent Mixing Layers and Wakes Using a Chemical Reaction," *J. Fluid Mechanics, 109*, 1–24.

Briedenthal, R.E. (1979), "Chemically Reacting Turbulent Shear Layer," *AIAA Journal, 17*, 310–311.

Brown, G.L. and Roshko, A. (1974), "On Density Effects and Large Structure in Turbulent Mixing Layers," *J. Fluid Mechanics, 64*, 775–816.

Bunville, L.G. (1984), "Commercial Instrumentation for Particle Size Analysis," Chapter One of *Modern Methods of Particle Size Analysis*, H.G. Barth. editor, John Wiley & Sons, New York, pp. 1–42.

Burrill, L.C. (1951), "Sir Charles Parsons and Cavitation," 1950 Parsons Memorial Lecture, *Trans. Inst. Marine Engineers, 63*, 149–167.

Cantwell, B.J. (1981), "Organized Motion in Turbulent Flow," *Annual Review of Fluid Mechanics, 13*, 457–515.

Carder, K.L., Beardsley, G.F., Jr. and Pak, H. (1971), "Particle Size Distributions in the Eastern Equatorial Pacific," *J. Geophysical Research, 76*, 21, 5070–5077.

Carder, K.L., Steward, R.G., and Betzer, R.P. (1982), "*In Situ* Holographic Measurement of the Sizes and Settling Rates of Oceanic Particulates," *J. Geophysical Research, 87*, C8, 5681–5685.

Carmody, T. (1964), "Establishment of the Wake Behind a Disk," *ASME J. Basic Engineering*, 869–882.

Cha, Y.S. (1981), "On the Equilibrium of Cavitation Nuclei in Liquid-Gas Solutions," *ASME J. Fluids Engineering, 103*, 425–431.

Chandrsuda, C., Mehta, R.D., Weir, A.D. and Bradshaw, P. (1978), "Effect of Free-Stream Turbulence on Large Structure in Turbulent Mixing Layers," *J. Fluid Mechanics, 85*, 693–704.

Clark, J.A. and Kit, L. (1980), "Shear Layer Transition and the Sharp-Edged Orifice," *ASME J. Fluids Engineering, 102*, 219–225.

Collier, R.J., Burkhardt, C.B. and Lin, L.H. (1971), *Optical Holography*, Academic Press, Inc., New York.

Corcos, G.M. (1979), "The Mixing Layer: Deterministic Models of a Turbulent Flow," U.C. Berkeley College of Engineering Report No. FM-79-2-a.

Crane, J., Dunn, P., Malyak, P.H. and Thompson, B.J. (1982), "Particulate Velocity and Size Measurements Using Holographic and Optical Processing Methods," Proceedings of 15th International Congress on High Speed Photography and Photonics, SPIE Vol. 348, 634–642.

d'Agostino, L. (1986), Department of Mechanical Engineering, California Institute of Technology, private communication.

d'Agostino, L. and Acosta, A.J. (1983), "On the Design of Cavitation Susceptibility Meters," 20th American Towing Tank Conference, Stevens Institute of Technology, New Jersey.

De Velis, J.B., Parrent, G.B. Jr. and Thompson, B.J. (1966), "Image Reconstruction with Fraunhofer Holograms," *J. Optical Society of America, 56*, 4, 423–427.

Dimotakis, P.E. and Brown, G.L. (1976), "The Mixing Layer at High Reynolds Number: Large-Structure Dynamics and Entrainment," *J. Fluid Mechanics, 78*, 3, 535–560.

Dunn, P. and Walls, J.M. (1979a), "Improved Micro-images from In-Line Absorption Holograms," *Applied Optics, 18*, 3, 263–264.

Dunn, P. and Walls, J.M. (1979b), "Absorption and Phase In-Line Holograms: A Comparison," *Applied Optics, 18*, 13, 2171–2174.

Epstein, P.S. and Plesset, M.S. (1950), "On the Stability of Gas Bubbles in Liquid-Gas Solutions," *J. Chemical Physics, 18*, 11, 1505–1509.

Farmer, D.M. and Lemon, D.D. (1984), "The Influence of Bubbles on Ambient Noise in the Ocean at High Wind Speeds," *J. Geophysical Research, 14*, 1762–1778.

Feldberg, L.A. and Shlemenson, K.T. (1973), "The Holographic Study of Cavitation Nuclei," Discussion to Proceedings of the IUTAM Symposium on Non-Steady Flow of Water at High Speeds, Leningrad, USSR.

Fiedler, H.E. and Mensing, P. (1985), "The Plane Turbulent Shear Layer with Periodic Excitation," *J. Fluid Mechanics, 150*, 281–309.

Fox, F.E. and Herzfeld, K.F. (1954), "Gas Bubbles with Organic Skin as Cavitation Nuclei," *J. Acoustical Society of America, 26*, 6, 984–989.

Franc, J.P. and Michel, J.M. (1983), "Two- and Three-Dimensional Rotational Structures in the Cavitating Turbulent Wake of a Wedge," submitted to the Fourth Symposium on Turbulent Shear Flows, Karlsruhe, Germany.

Frenkel, J. (1946), *Kinetic Theory of Liquids*, Clarendon Press, Oxford.

Garretson, G.A. (1973), "Bubble Transport Theory with Application to the Upper Ocean," *J. Fluid Mechanics, 59*, 187–206.

Gates, E.M. (1977), "The Influence of Freestream Turbulence, Freestream Nuclei Populations and a Drag-Reducing Polymer on Cavitation Inception on Two Axisymmetric Bodies," Ph.D. Thesis, California Institute of Technology, Report No. 183-2.

Godefroy, H.W.H.E., Jansen, R.H.J., Keller, A.P., Lecoffre, Y., Oldenziel, D.M. and van Renesse, R.L. (1981), "Comparison of Measuring and Control Methods of the Water Quality With Respect to Cavitation Behaviour," Delft Hydraulic Laboratory Report.

Goldish, J. (1984), undergraduate student, Division of Engineering and Applied Science, California Institute of Technology, private communication.

Goldstein, S., ed. (1965), *Modern Developments in Fluid Dynamics*, Volume II, Dover Publications, Inc., New York, p. 599.

Gowing, S. and Ling, S.C. (1980), "Measurements of Microbubbles on a Water Tunnel," 19th American Towing Tank Conference, Ann Arbor, MI.

Harigel, G. et al. (1986), "Pulse Stretching in a Q-Switched Ruby Laser for Bubble Chamber Holography," *Applied Optics, 25*, 22, 4102–4110.

Harvey, E.N., McElroy, W.D. and Whiteley, A.H. (1947), "On Cavity Formation in Water," *J. Applied Physics, 18*, 162–172.

Hausmann, G. and Lauterborn, W. (1980), "Determination of the Size and Position of Fast Moving Gas Bubbles in Liquids by Digital 3-D Image Processing of Hologram Reconstructions," *Applied Optics, 19*, 3529–3535.

Herdan, G. (1960), *Small Particle Statistics*, Academic Press, New York, p. 47.

Hernan, M.A. and Jimenez, J. (1982), "Computer Analysis of a High-Speed Film of the Plane Turbulent Mixing Layer," *J. Fluid Mechanics, 119*, 323–345.

Ho, C.M. and Huerre, P. (1984), "Perturbed Free Shear Layers," *Annual Review of Fluid Mechanics, 16*, 365–424.

Hoerner, S.F. (1958), *Fluid Dynamic Drag*, published by the author.

Holl, J.W. (1970), "Nuclei and Cavitation," *ASME J. Basic Engineering*, 681–688.

Holl, J.W. and Wislicenus, G.F. (1961), "Scale Effects on Cavitation," *ASME J. Basic Engineering*, 385–398.

Holliday, D.V. and Pieper, R.E. (1980), "Volume Scattering Strengths and Zooplankton Distributions and Acoustic Frequencies Between 0.5 and 3 MHz," *J. Acoustical Society of America, 67*, 135–146.

Holman, J. P. (1966), *Experimental Methods for Engineers*, McGraw-Hill Book Co., New York.

Huang, T.T. (1981), "Cavitation Inception Observations on Six Axisymmetric Headforms," *ASME J. Fluids Engineering, 103*, 273–279.

Huang, T.T. and Peterson, F.B. (1976), "Influence of Viscous Effects on Model/Full-Scale Cavitation Scaling," *J. Ship Research, 20*, 4, 215–223.

Hussain, A.K.M.F. and Clark, A.R. (1981), "On the Coherent Structure of the Axisymmetric Mixing Layer: A Flow Visualization Study," *J. Fluid Mechanics, 104*, 263–294.

Jimenez, J. (1983), "A Spanwise Structure in the Plane Shear Layer," *J. Fluid Mechanics, 132*, 319–336.

Jimenez, J., Cogollos, M. and Bernal, L. (1985), "A Perspective View of the Plane Mixing Layer," *J. Fluid Mechanics, 152*, 125–143.

Johnson, B.D. and Cooke, R.C. (1979), "Bubble Populations and Spectra in Coastal Waters: A Photographic Approach," *J. Geophysical Research, 84*, C7, 3761–3766.

Johnson, B.D. and Cooke, R.C. (1981), "Generation of Stabilized Microbubbles in Seawater," *Science, 213*, 209–211.

Johnsson, C.A. (1969), "Cavitation Inception on Head Forms, Further Tests," 12th International Towing Tank Conference, Rome.

Katz, J. (1984), "Cavitation Phenomena Within Regions of Flow Separation," *J. Fluid Mechanics, 140*, 397–436.

Katz, J. (1981), "Cavitation Inception In Separated Flows," Ph.D. Thesis, California Institute of Technology, Report No. 183-5.

Katz, J. (1979), "Construction and Calibration of a Holographic Camera Designed for Microbubble Observation in Cavitation Research," California Institute of Technology, Engineering Report No. 183-4.

Katz, J. and O'Hern, T.J. (1986), "Cavitation in Large Scale Shear Flows," *ASME J. Fluids Engineering, 108*, 373–376.

Katz, J. and O'Hern, T.J. (1983), "Holographic Observations of Cavitating Flows within Regions of Flow Separation," Eighth Symposium on Turbulence, University of Missouri-Rolla.

Katz, J., Gowing, S., O'Hern, T. and Acosta, A.J. (1983), "A Comparative Study Between Holographic and Light-Scattering Techniques of Microbubble Detection," Proceedings of IUTAM Symposium on Measuring Techniques in Gas-Liquid Two-Phase Flows, Nancy, France, July, 1983.

Keller, A.P. (1979), "Cavitation Inception Measurement and Flow Visualization on Axisymmetric Bodies at Two Different Freestream Turbulence Levels and Test Procedures," ASME International Symposium on Cavitation Inception, New York.

Keller, A.P. (1972), "The Influence of the Cavitation Nucleus Spectrum on Cavitation Inception, Investigated with a Scattered Light Counting Method," *ASME J. Basic Engineering*, 917–925.

Keller, A.P. and Weitendorf, E.A. (1979), "A Determination of the Free Air Content and Velocity in Front of the *Sydney Express* Propeller in Connection with Pressure Fluctuation Measurements," 12th Symposium on Naval Hydrodynamics, Washington, D.C.

Kermeen, R.W. and Parkin, B.R. (1957), "Incipient Cavitation and Wake Flow Behind Sharp-Edged Disks," California Institute of Technology, Hydrodynamics Lab Report No. 85-4.

Knapp, R.T. and Hollander, A. (1948), "Laboratory Investigations of the Mechanism of Cavitation," *Transactions of the ASME, 70*, 419–435.

Knapp, R.T., Daily, J.W. and Hammitt, F.G. (1970), *Cavitation*, McGraw Hill Inc., New York, 1979; unabridged edition from Iowa Institute of Hydraulic Research, University of Iowa, Iowa City.

Knox, C. (1966), "Holographic Microscopy as a Technique for Recording Dynamic Microscopic Subjects," *Science, 153*, 989–990.

Koechner, W. (1976), *Solid State Laser Engineering*, Springer-Verlag, New York.

Konrad, J.H. (1976), "An Experimental Investigation of Mixing in Two- Dimensional Turbulent Shear Flows with Application to Diffusion Limited Chemical Reactions," Project SQUID, Technical Report CIT-8-PU, GALCIT, California Institute of Technology.

Kuiper, G. (1985), "Reflections on Cavitation Inception," ASME Cavitation and Multiphase Flow Forum, Albuquerque, N.M.

Kuiper, G. (1981), "Cavitation Inception on Ship Propeller Models," Ph.D. Thesis, Netherlands Ship Model Basin, Wageningen, the Netherlands.

Langley, D.S. (1984), "Light Scattering from Bubbles in Liquids," Ph.D. Thesis, Washington State University.

Lasheras, J.C., Cho, J.S. and Maxworthy, T. (1986), "On the Origin and Evolution of Streamwise Vortical Structures in a Plane, Free Shear Layer," *J. Fluid Mechanics, 172*, 231–258.

Lecoffre, Y. and Bonnin, J. (1979), "Cavitation Tests and Nucleation Control," ASME International Symposium on Cavitation Inception, New York.

LeGoff, J.P. and Lecoffre, Y. (1983), "Nuclei and Cavitation," 14th Symposium on Naval Hydrodynamics, Ann Arbor, Michigan.

Levi, B.G. (1986), "Soviets Assess Cause of Chernobyl Accident," *Physics Today, 39*, 12, 17–20.

Liebermann, L. (1957), "Air Bubbles in Water," *J. Applied Physics, 28*, 2, 205–211.

Liepmann, H.W. (1979), "The Rise and Fall of Ideas in Turbulence," *American Scientist, 67*, 221–228.

Medwin, H. (1977), "*In Situ* Acoustic Measurements of Microbubbles at Sea," *J. Geophysical Research, 82*, 6, 971–976.

Medwin, H. (1970), "*In Situ* Acoustic Measurements of Bubble Populations in Coastal Ocean Waters," *J. Geophysical Research, 75*, 3, 599–611.

Messino, C.D., Sette, D. and Wanderlingh, F. (1967), "Effects of Solid Impurities on Cavitation Nuclei in Water," *J. Acoustical Society of America, 41*, 3, 573–583.

Modi, V.J. and El-Sherbiny, S.E. (1977), "A Free-Streamline Model for Bluff Bodies in Confined Flow," *ASME J. Fluids Engineering, 99*, 585–592.

Moore, D.W. and Saffman, P.G. (1975), "The Density of Organized Vortices in a Turbulent Mixing Layer," *J. Fluid Mechanics, 69*, 465–473.

Morgan, W.B. (1972), "Air Content and Nuclei Measurement," Report of the Cavitation Committee, Appendix I, 13th International Towing Tank Conference.

Mulhearn, P.J. (1981), "Distribution of Microbubbles in Coastal Waters," *J. Geophysical Research, 86*, C7, 6429–6434.

Newell, G.E. and Newell, R.C. (1977), *Marine Plankton*, Fifth Edition, Hutchinson & Co., Ltd., London.

Oba, R., Kim, K.T., Niitsuma, H., Ikohagi, T., and Sato, R. (1981), "Cavitation Nuclei Measurements by a Newly Made Coulter Counter without Adding Salt in Water," *Report of the Institute of High Speed Mechanics, 43*, 163–176.

Oldenziel, D.M. (1982), "A New Instrument in Cavitation Research: the Cavitation Susceptibility Meter," *ASME J. Fluids Engineering, 104*, 136-142.

Oldenziel, D.M. (1979), "Bubble Cavitation in Relation to Liquid Quality," Ph.D. Thesis, Technical University Twente, Delft Hydraulic Laboratory Publication Number 211.

Ooi, K.K. (1985), "Scale Effects of Cavitation Inception in Submerged Water Jets: A New Look," *J. Fluid Mechanics, 151*, 367–390.

Ooi, K.K. (1981), "Scale Effects on Cavitation Inception in Submerged Jets," Ph.D. Thesis, California Institute of Technology, Report No. 183-6.

Ooi, K.K. and Acosta, A.J. (1983), "The Utilization of Specially Tailored Air Bubbles as Static Pressure Sensors in a Jet," ASME Paper No. 83-FE-34.

Parkin, B.R. and Holl, J.W. (1953), "Incipient Cavitation Scaling Experiments for Hemispherical and 1.5 Caliber Ogive-Nosed Bodies," Joint CIT/Penn State Ordnance Laboratory Report NORD 7958-264.

Parrent, G.B. and Thompson, B.J. (1964), "On the Fraunhofer (Far Field) Diffraction Pattern of Opaque and Transparent Objects with Coherent Background," *Optica Acta, 11*, 183–193.

Peterson, F.B. (1972), "Hydrodynamic Cavitation and Some Considerations of the Influence of Free Gas Content," 9th Symposium on Naval Hydrodynamics, Paris.

Peterson, F.B., Daniel, F., Keller, A.P. and Lecoffre, Y. (1975), "Determination of Bubbles and Particulate Spectra and Number Density in a Water Tunnel with Three Optical Techniques," 14th International Towing Tank Conference, Vol. 2, Ottawa.

Peterson, L.L. (1974), "The Propagation of Sunlight and the Size Distribution of Suspended Particles in a Municipally Polluted Ocean Water," Ph.D. Thesis, California Institute of Technology.

Pieper, R.E. (1986), Institute for Marine and Coastal Studies, University of Southern California, private communication.

Pieper, R.E. and Holliday, D.V. (1984), "Acoustic Measurements of Zooplankton Distributions in the Sea," *J. Cons. int. Explor. Mer, 41*, 226–238.

Pierrehumbert, R.T. and Widnall, S.E. (1982), "The Two- and Three- Dimensional Instabilities of a Spatially Periodic Shear Layer," *J. Fluid Mechanics, 114*, 59–82.

Plesset, M.S. (1986), Professor of Engineering Science, Emeritus, California Institute of Technology, private communication.

Plesset, M.S. (1949), "The Dynamics of Cavitation Bubbles," *J. Applied Mechanics*, 277–288.

Plesset, M.S. (1969), "The Tensile Strength of Liquids," Proceedings of ASME Symposium on Cavitation State of Knowledge, 15–25.

Plesset, M.S. and Prosperetti, A. (1977), "Bubble Dynamics and Cavitation," *Annual Review of Fluid Mechanics, 9*, 145–185.

Prikryl, I. and Vest, C.M. (1982), "Holographic Imaging of Semitransparent Droplets or Particles," *Applied Optics, 21*, 14, 2541–2547.

Riley, G.A. (1963), "Organic Aggregates in Sea Water and the Dynamics of Their Formation and Utilization," *Limnology and Oceanography, 8*, 4, 372–381.

Roshko, A. (1954), "On the Drag and Shedding Frequency of Two-Dimensional Bluff Bodies," NACA Technical Note 3169.

Roshko, A. (1980), "The Plane Mixing Layer, Flow Visualization Results and Three Dimensional Effects," in *The Role of Coherent Structures in Modelling Turbulence and Mixing, Lecture Notes in Physics, Vol. 136*, Springer-Verlag, New York, pp. 208–217.

Ruderich, R. and Fernholz, H.H. (1986), "An Experimental Investigation of a Turbulent Shear Flow with Separation, Reverse Flow, and Reattachment," *J. Fluid Mechanics, 163*, 283–322.

Sheldon, R.W., Prakash, A. and Sutcliffe, W.H., Jr. (1972), "The Size Distribution of Particles in the Ocean," *Limnology and Oceanography, XVII*, 3, 327–340.

Shen, Y.T. and Peterson, F.B. (1983), "Cavitation Inception: A Review - Progress Since 19th ATTC," 20th American Towing Tank Conference, New Jersey.

Shen, Y.T., Gowing, S. and Eckstein, B. (1986), "Cavitation Susceptibility Measurements of Ocean, Lake and Laboratory Waters," David Taylor Naval Ship Research and Development Center Report Number 86/019.

Shen, Y.T., Gowing, S. and Pierce, R. (1984), "Cavitation Susceptibility Measurements by a Venturi," ASME International Symposium on Cavitation Inception-1984, New Orleans.

Smith, D.L. (1977), *A Guide to Marine Coastal Plankton and Marine Invertebrate Larvae,* Kendall/Hunt Publishing Co., Dubuque.

Stewart, G.L., Beers, J.R. and Knox, C. (1973), "Application of Holographic Techniques to the Study of Marine Plankton in the Field and in the Laboratory," Proceedings of Developments in Laser Technology II, SPIE Volume 14, San Diego.

Strasberg, M. (1957), "The Influence of Air-Filled Nuclei on Cavitation Inception," David Taylor Model Basin Hydromechanics Laboratory Research and Development Report 1078.

Sutcliffe, W.H., Jr., Baylor, E.R. and Menzel, D.W. (1963), "Sea Surface Chemistry and Langmuir Circulation," *Deep-Sea Research, 10,* 3, 233–243.

Taneda, S. (1983), "The Main Structure of Turbulent Boundary Layers," *J. Physical Society of Japan, 52,* 12, 4138–4144.

Taylor, J.R. (1982), *An Introduction to Error Analysis,* University Science Books, Oxford University Press, Mill Valley, CA, p. 211.

Thompson, B.J. (1974), "Holographic Particle Sizing Techniques," *J. Physics E: Scientific Instruments, 7,* 781–788.

Thompson, B.J. and Ward, J.H. (1966), "Particle Sizing - The First Direct Use of Holography," *Scientific Research, 1,* 10, 37–40.

Thorpe, S.A. (1982), "On the Clouds of Bubbles Formed by Breaking Wind-Waves in Deep Water, and Their Role in Air-Sea Gas Transfer," *Phil. Trans. R. Soc. Lond. A, 304,* 155–210.

Trevena, D.H. (1984), "Cavitation and the Generation of Tension in Liquids," *J. Physics D: Appl. Phys., 17,* 2139–2164.

Trolinger, J.D. (1980), "Analysis of Holographic Diagnostic Systems," *Optical Engineering, 19,* 5, 722–726.

Trolinger, J.D. (1975), "Particle Field Holography," *Optical Engineering, 14,* 5, 383–392.

Trolinger, J.D. and Heap, M.P. (1979), "Coal Particle Combustion Studied by Holography," *Applied Optics, 18,* 11, 1757–1762.

Turner, W.R. (1961), "Microbubble Persistence in Fresh Water," *J. Acoustical Society of America, 33,* 9, 1223–1233.

Tyler, G.A. and Thompson, B.J. (1976), "Fraunhofer Holography Applied to Particle Size Analysis–A Reassessment," *Optica Acta, 23,* 9, 685–700.

van de Hulst, H.C. (1981), *Light Scattering by Small Particles,* Dover Publications, Inc., New York, p. 221.

van der Muelen, J.H.J. (1980), "Boundary Layer and Cavitation Studies of NACA 16-012 and NACA 4412 Hydrofoils," 13th Symposium on Naval Hydrodynamics, Sasakawa Hall, Tokyo.

van Slyke, D.D. and Neill, J.M. (1924), "The Determination of Gases in Blood and other Solutions by Vacuum Extraction and Manometric Measurements," *J. Biological Chemistry, 61*, 2, 523–573.

Vikram, C.S. and Billet, M.L. (1984), "In-Line Fraunhofer Holography at a Few Far Fields," *Applied Optics, 23*, 18, 3091–3094.

Walsby, A.E. (1977), "The Gas Vacuoles of Blue-Green Algae," *Scientific American, 237*, 2, 90–97.

Winant, C.D. and Browand, F.K. (1974), "Vortex-Pairing: The Mechanism of Turbulent Mixing Layer Growth at Moderate Reynolds Number," *J. Fluid Mechanics, 63*, 237–255.

Wislicenus, G.F. (1969), "Remarks on the History of Cavitation as an Engineering Problem," ASME Cavitation State of Knowledge, 10–14.

Witherow, W.K. (1979), "A High Resolution Holographic Particle Sizing System," *Optical Engineering, 18*, 3, 249–255.

Young, J.O. and Holl, J.W. (1966), "Effects of Cavitation on Periodic Wakes Behind Symmetric Wedges," *ASME J. Basic Engineering, 88D*, 163–176.

Yount, D.E., Gillary, E.W. and Hoffman, D.C. (1984), "A Microscopic Investigation on Bubble Formation Nuclei," *J. Acoustical Society of America, 75*, 5, 1511–1521.

APPENDIX I

RUBY LASER HOLOCAMERA ELECTRICAL SCHEMATICS

This appendix contains the electrical schematics for the holocamera control systems and circuits. Special acknowledgments to Haskell Shapiro and staff of Shapiro Scientific Instruments for their design and assembly work on these circuits, and to Leonard Montenegro for his assistance during system modifications and trouble-shooting. These schematics are modified versions of those contained in Appendix II of Acosta et al. (1983).

LIST OF FIGURES

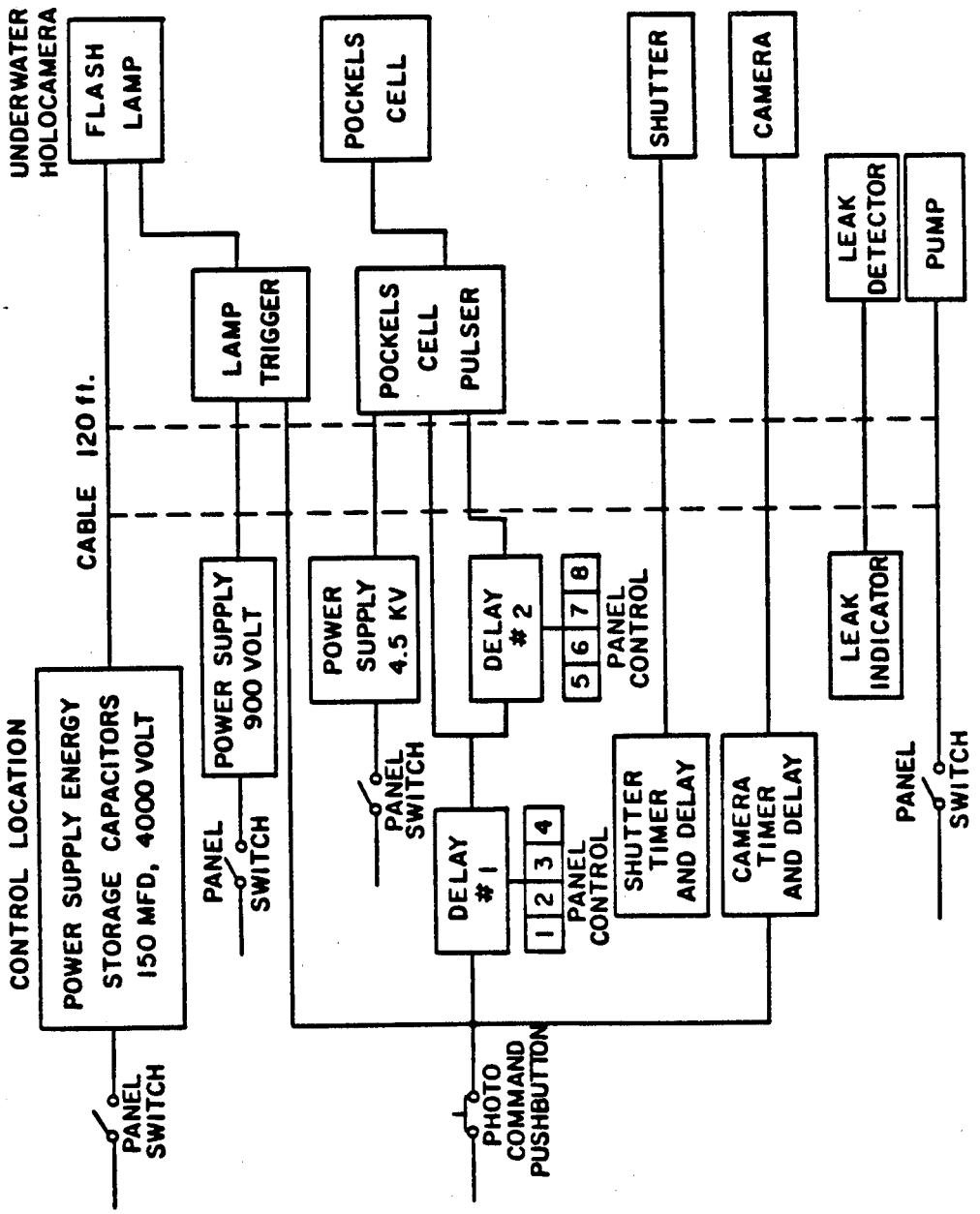

Figure I-1. Block diagram of electronic control functions.

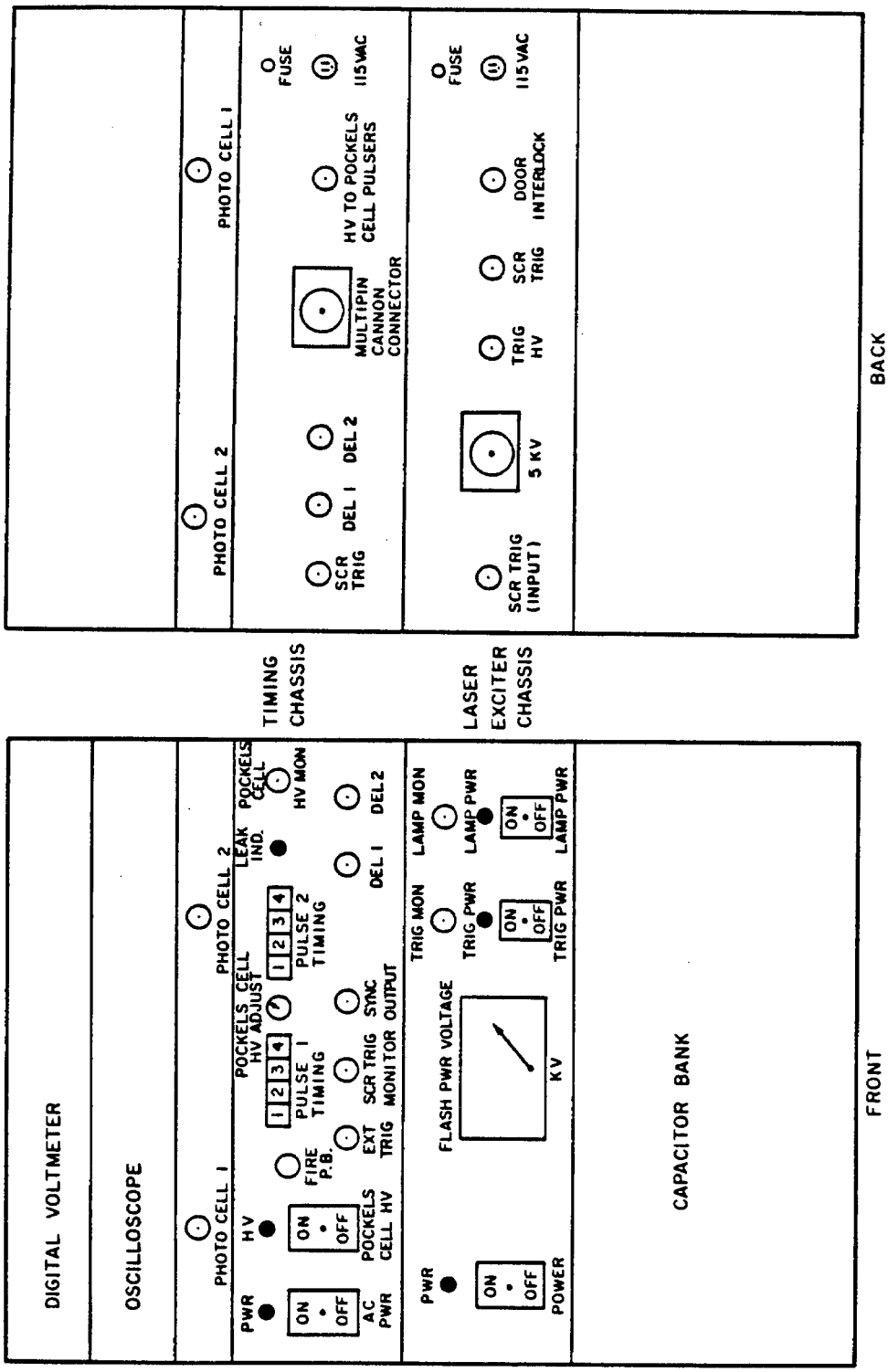

Figure I-2. Control rack panel layout.

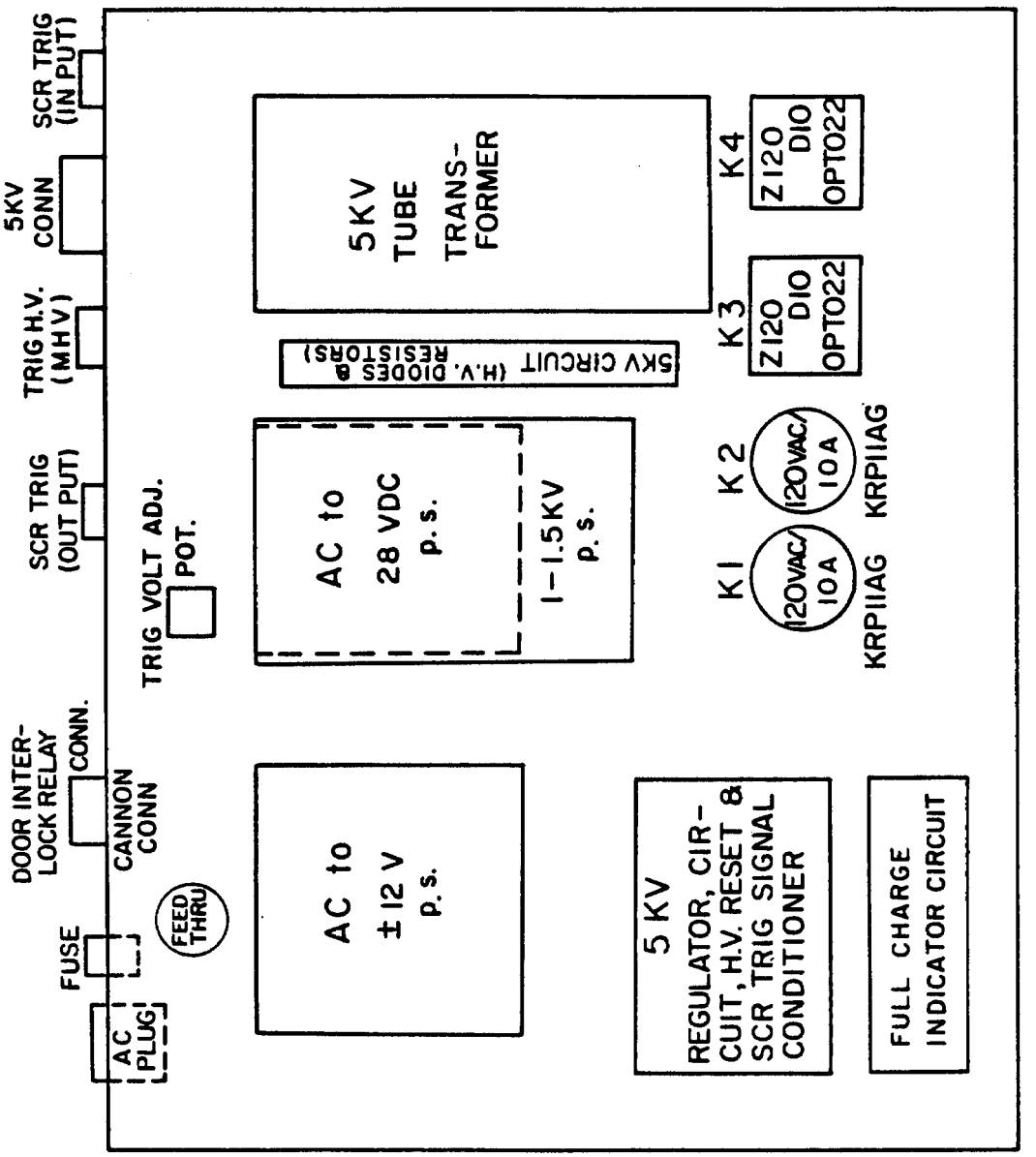

Figure I-3. Laser exciter chassis layout.

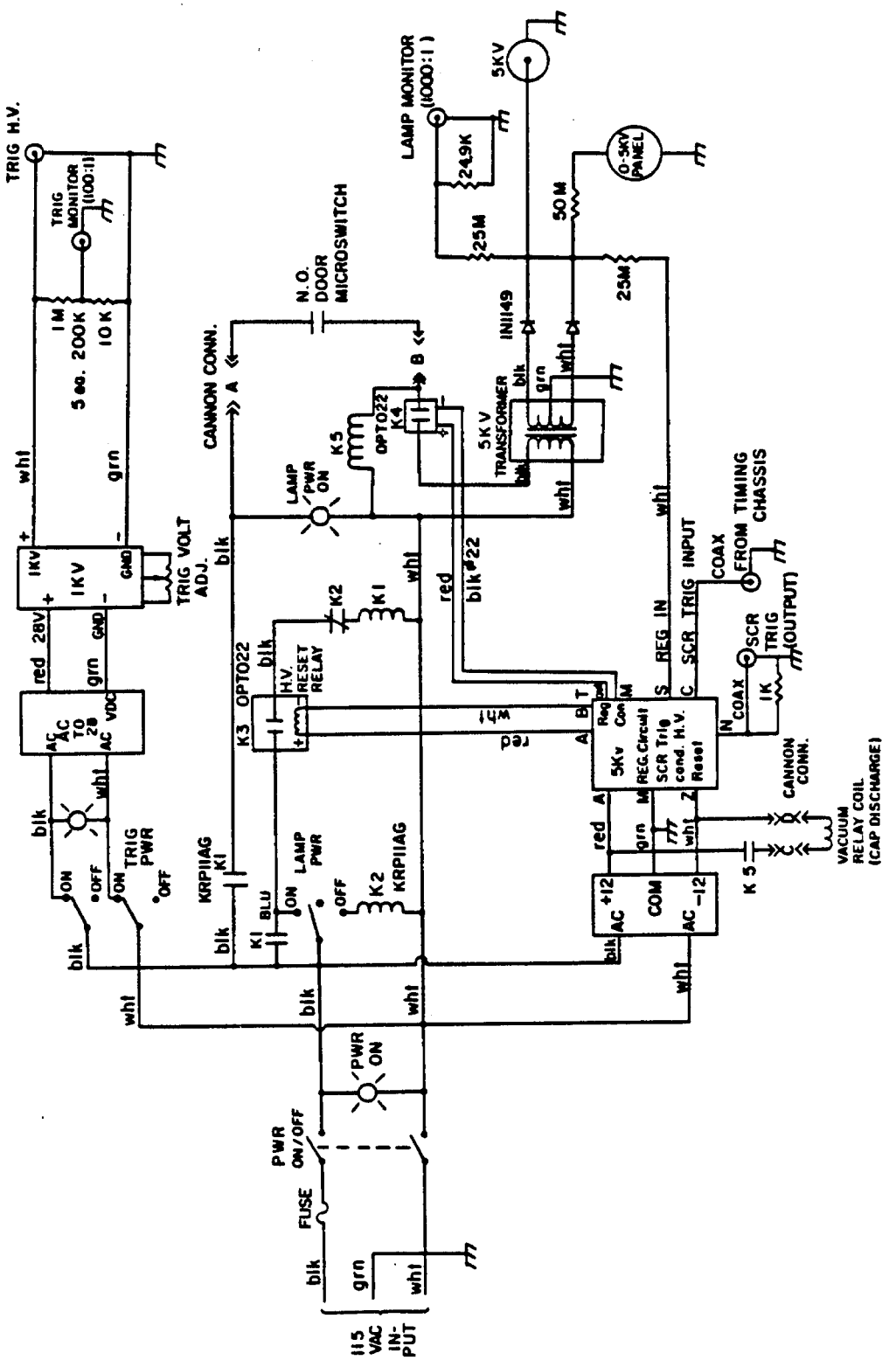

Figure I-4. Laser exciter chassis wiring diagram.

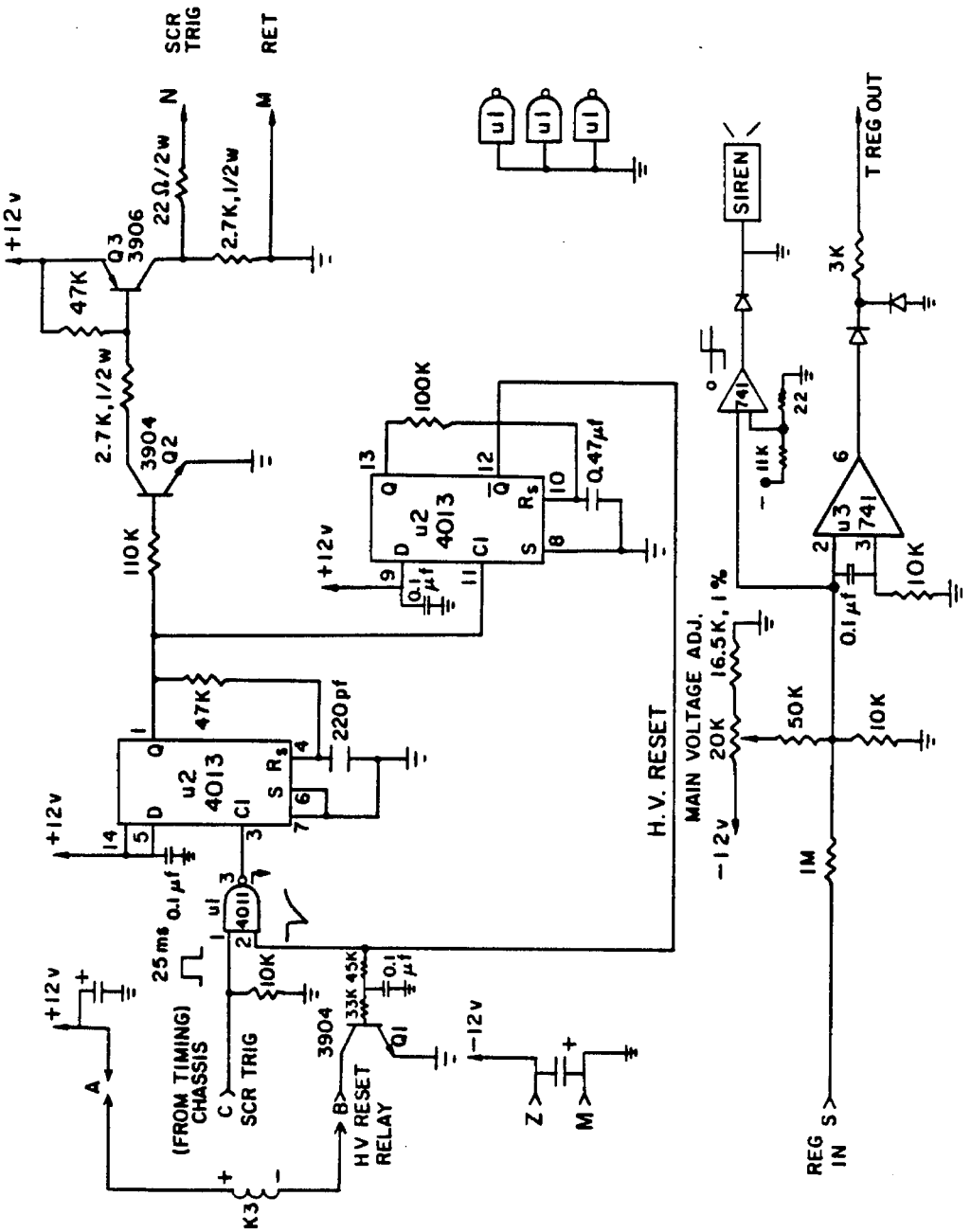

Figure I-5. Laser exciter chassis circuit board.

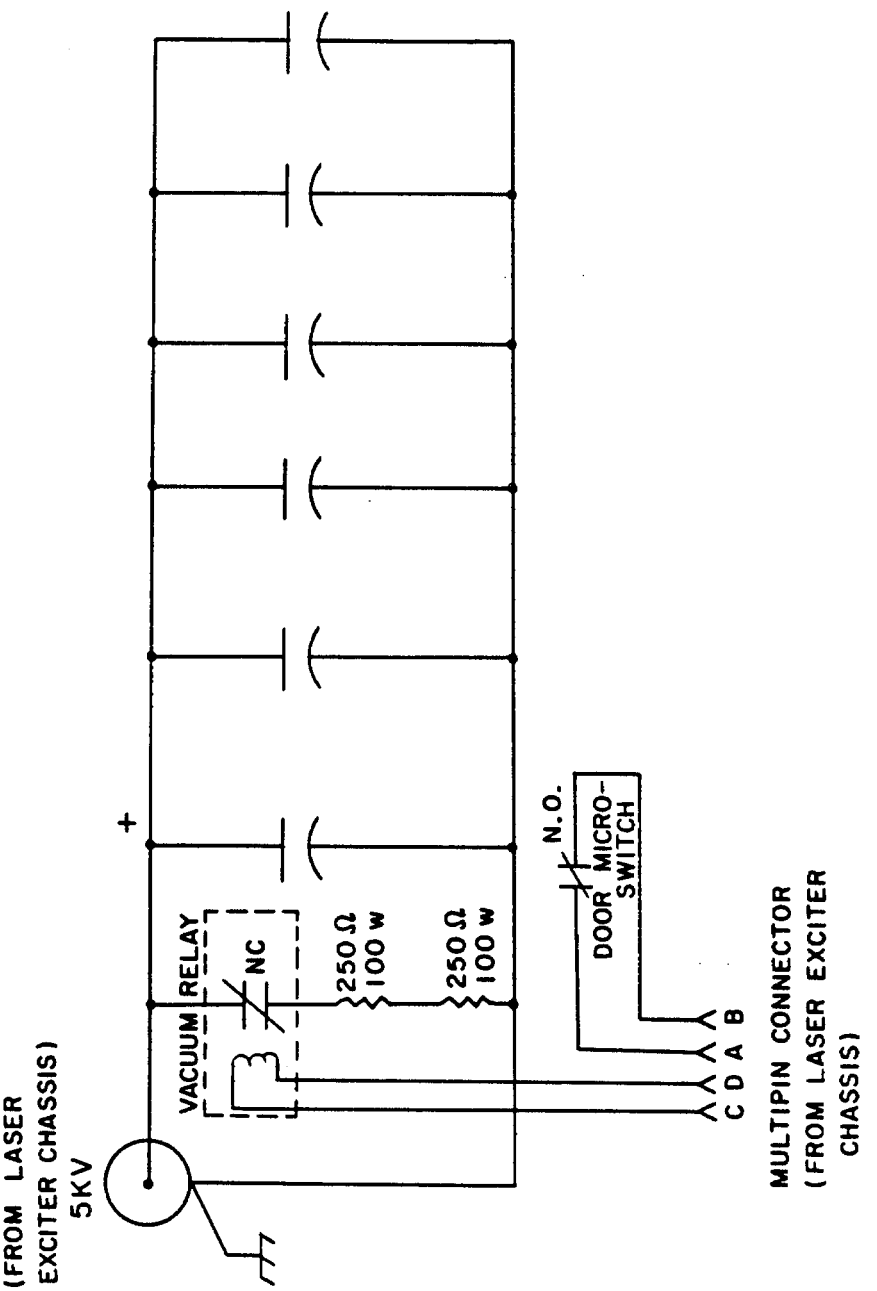

Figure I-6. Wiring diagram for main power capacitors and capacitor discharge circuits.

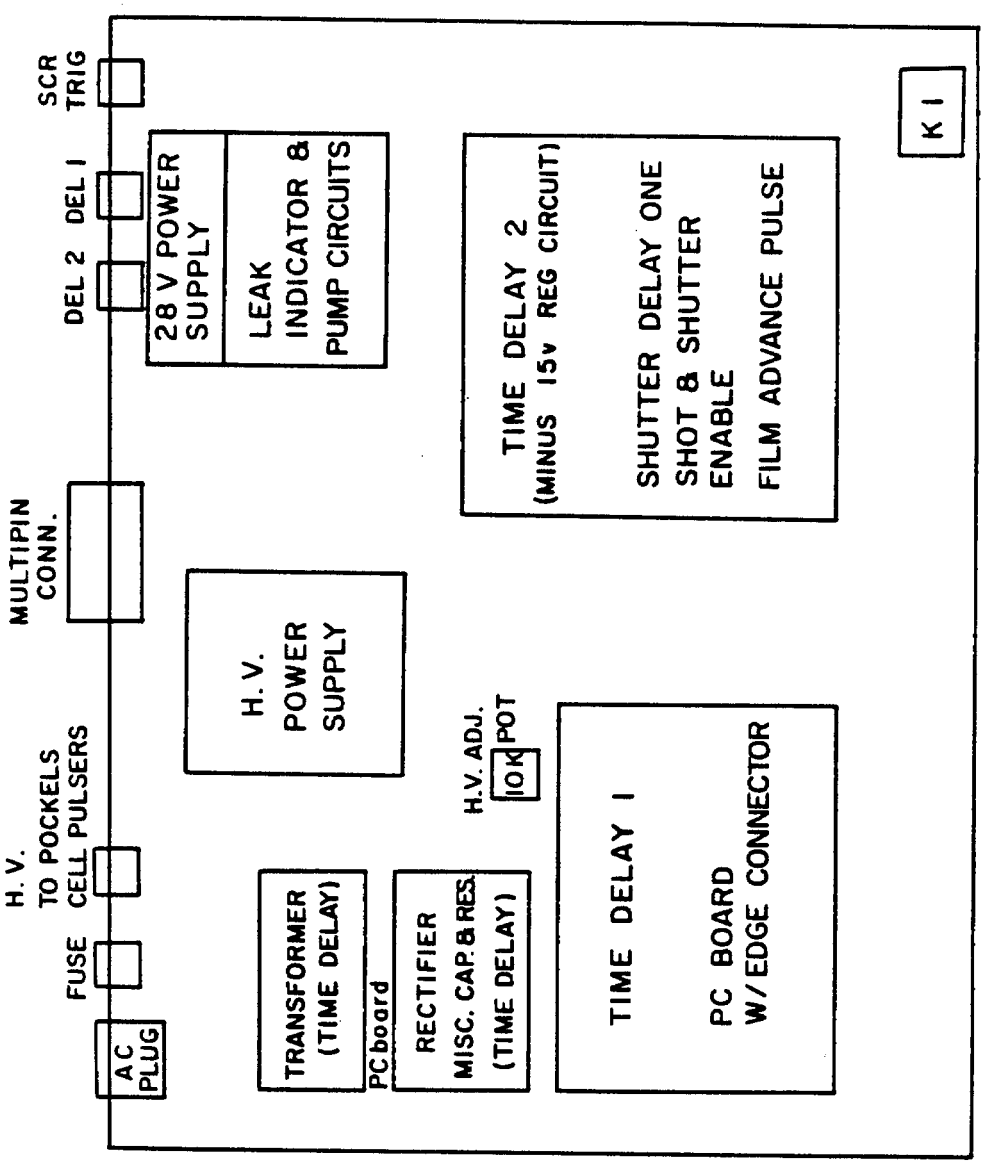

Figure I-7. Timing chassis layout.

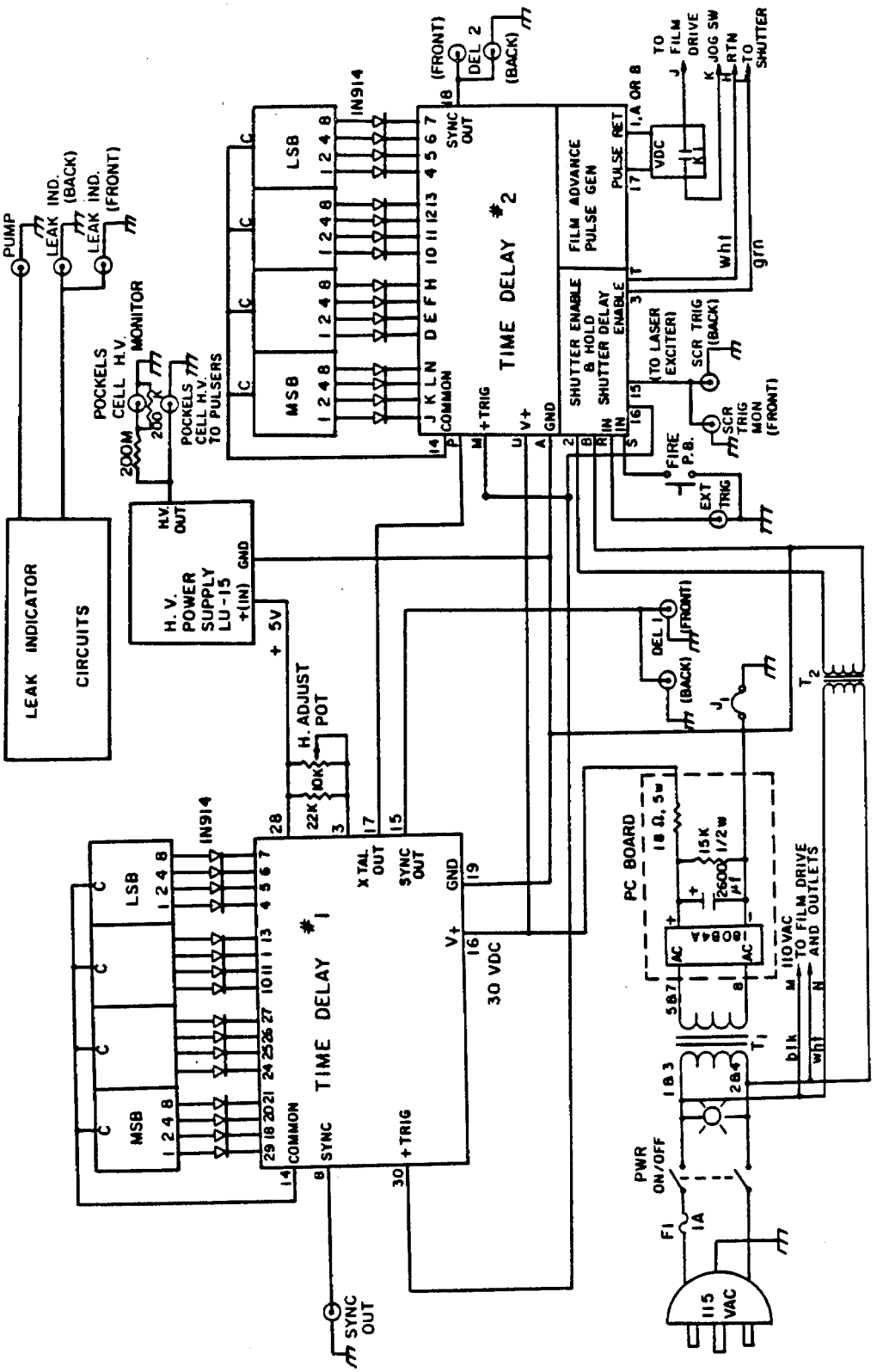

Figure I-8. Timing chassis wiring diagram.

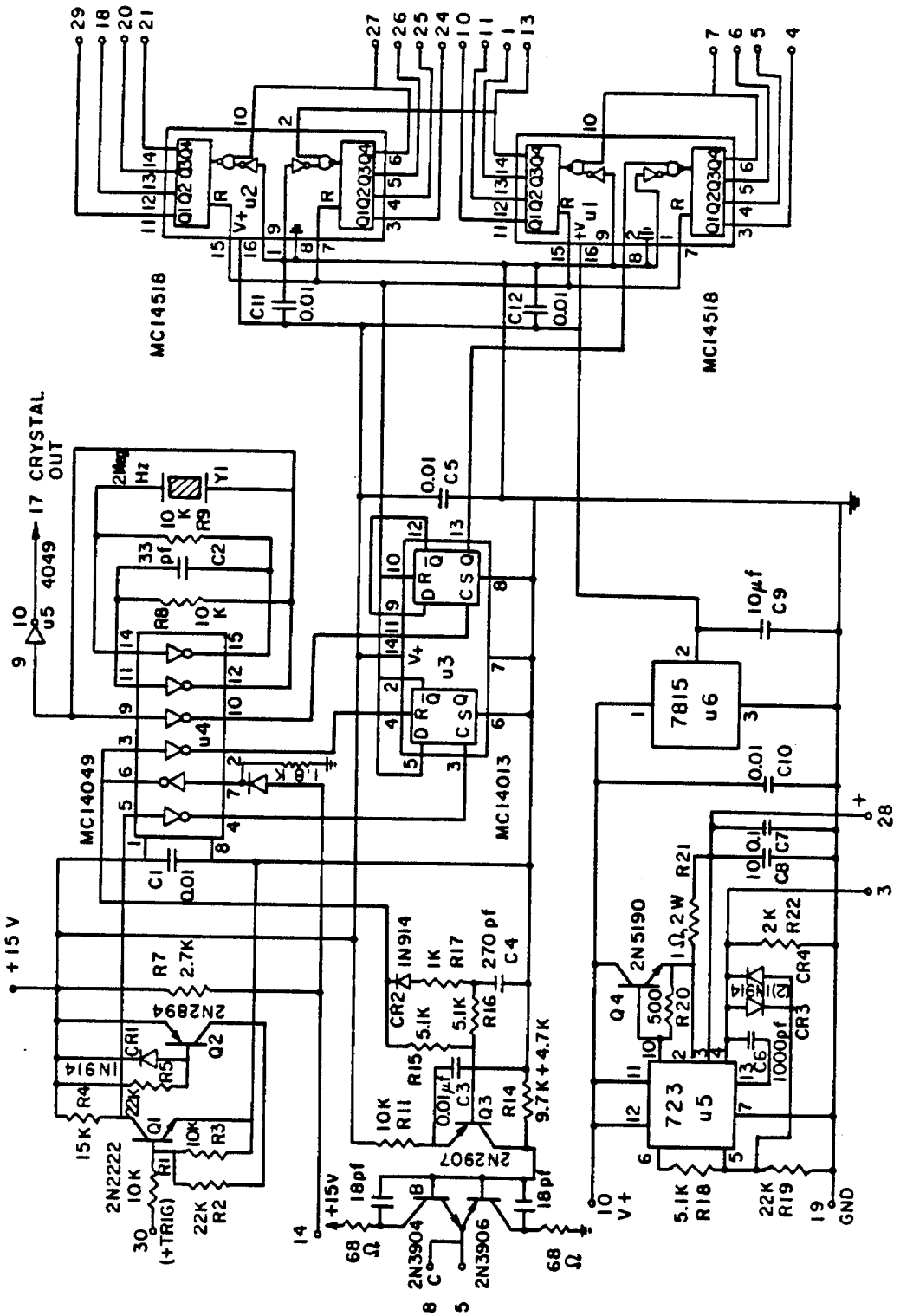

Figure I-9. Time delay 1 circuit board.

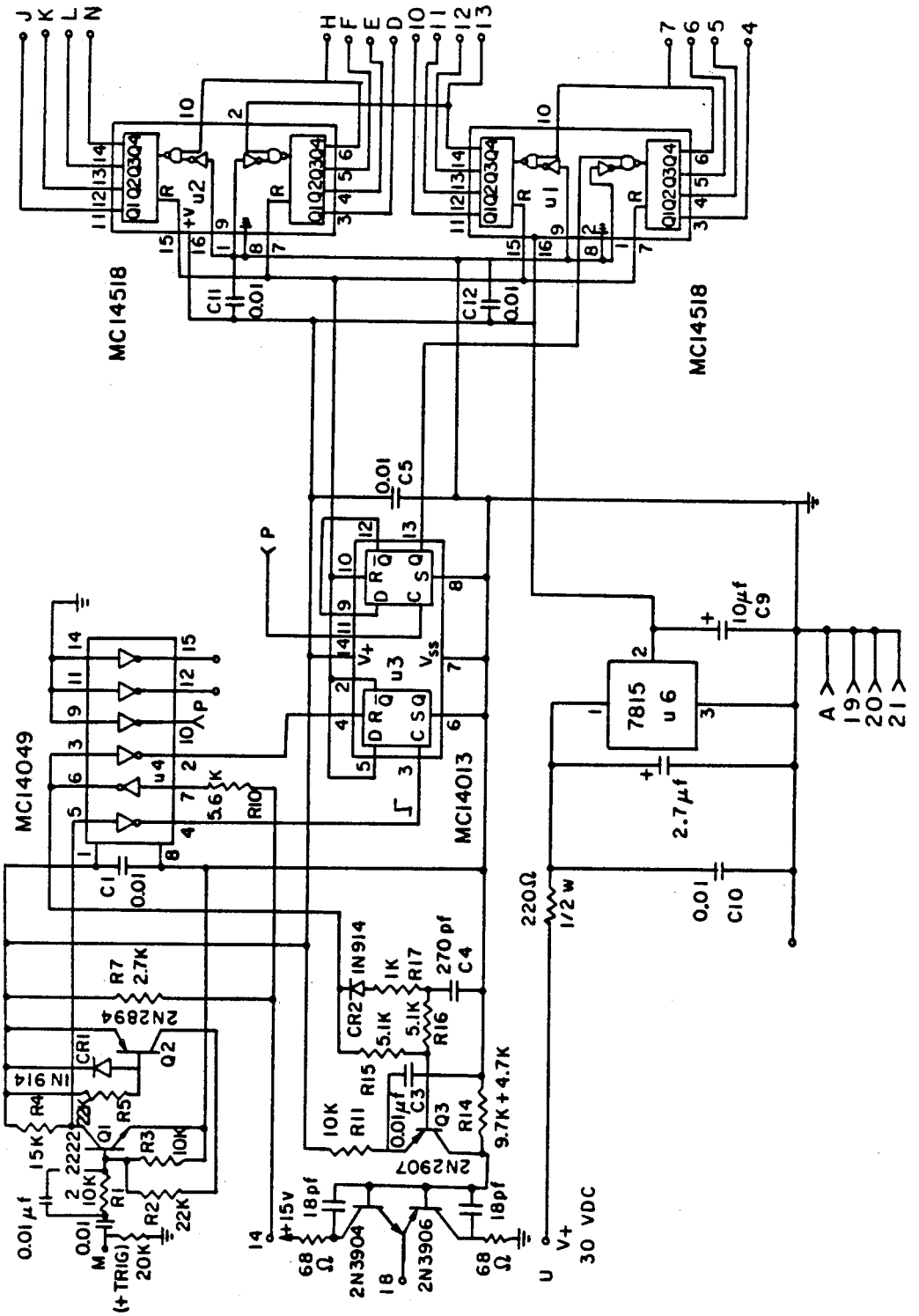

Figure I-10. Time delay 2 circuit board.

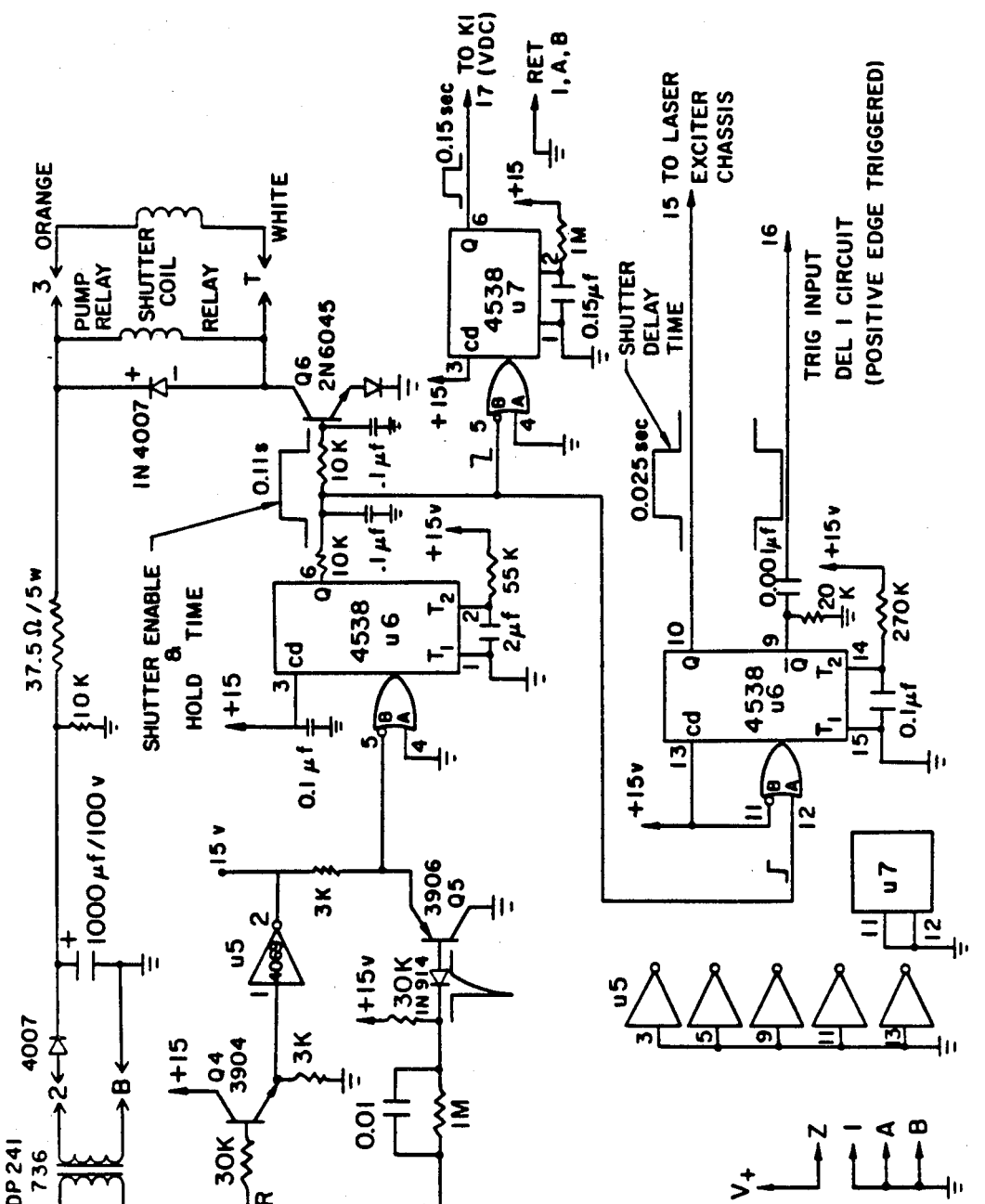

Figure I-11. Shutter control circuit board.

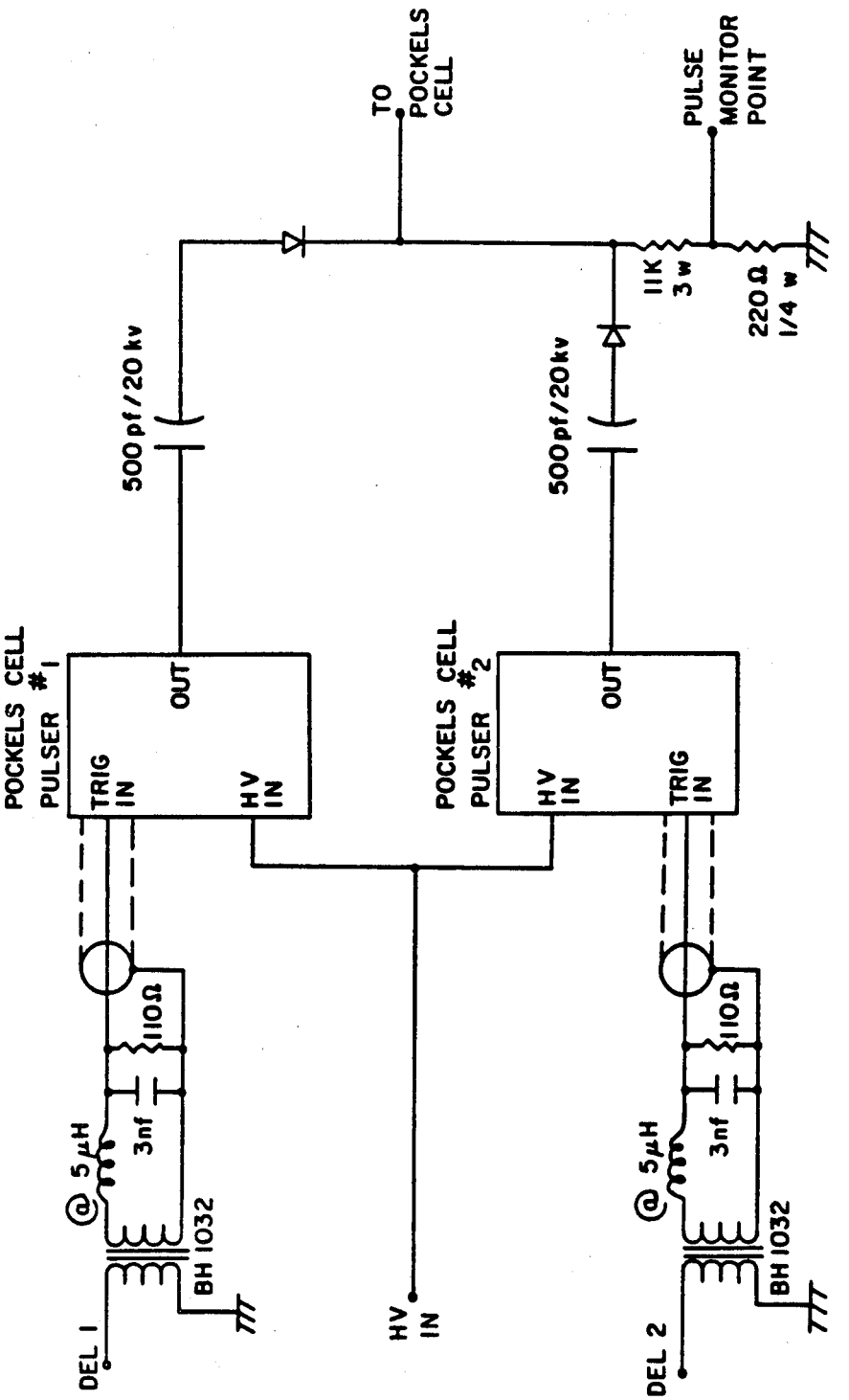

Figure I-12. Pockels cell pulser chassis.

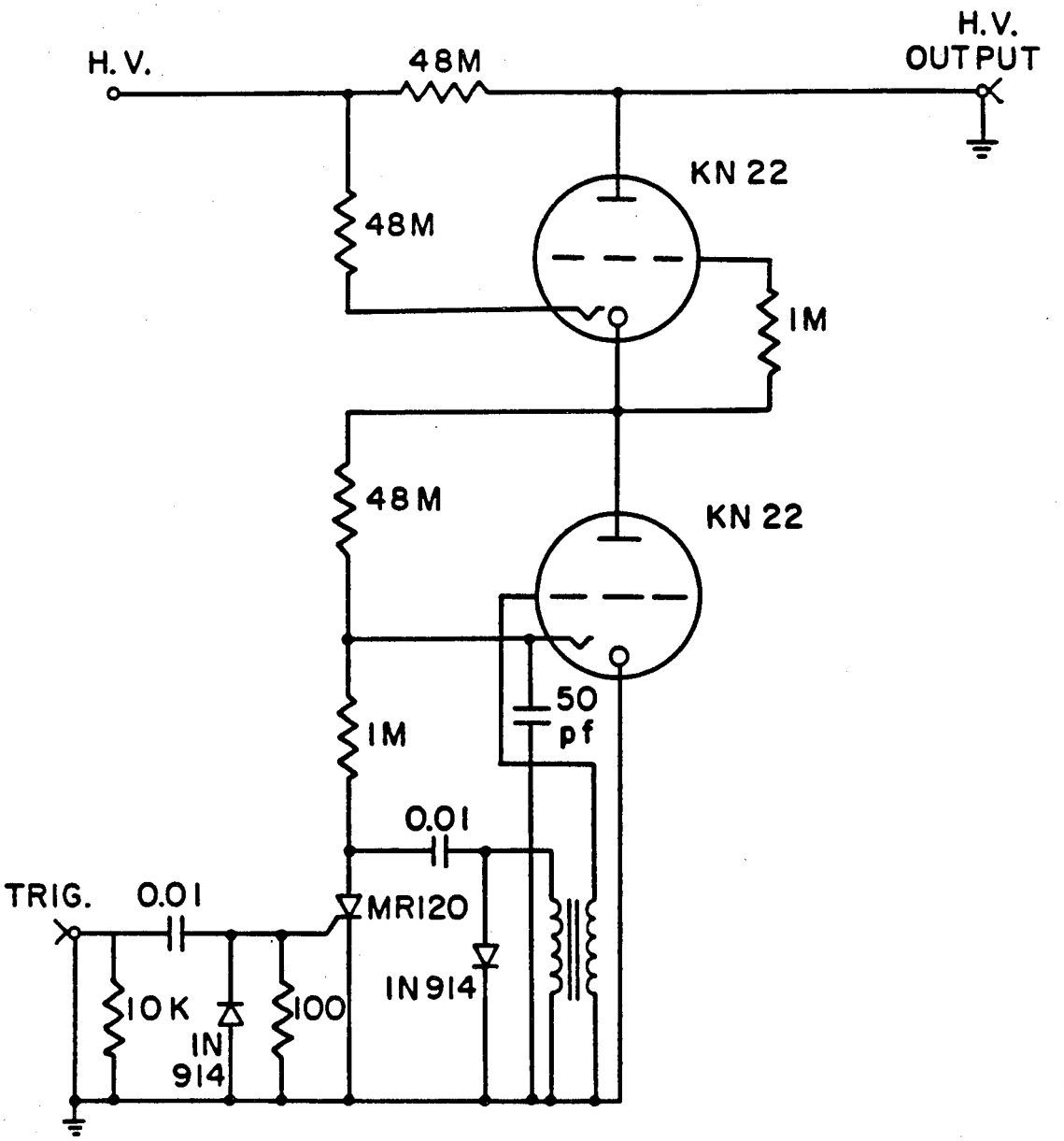

Figure I-13. Delay 1 Pockels cell pulser.

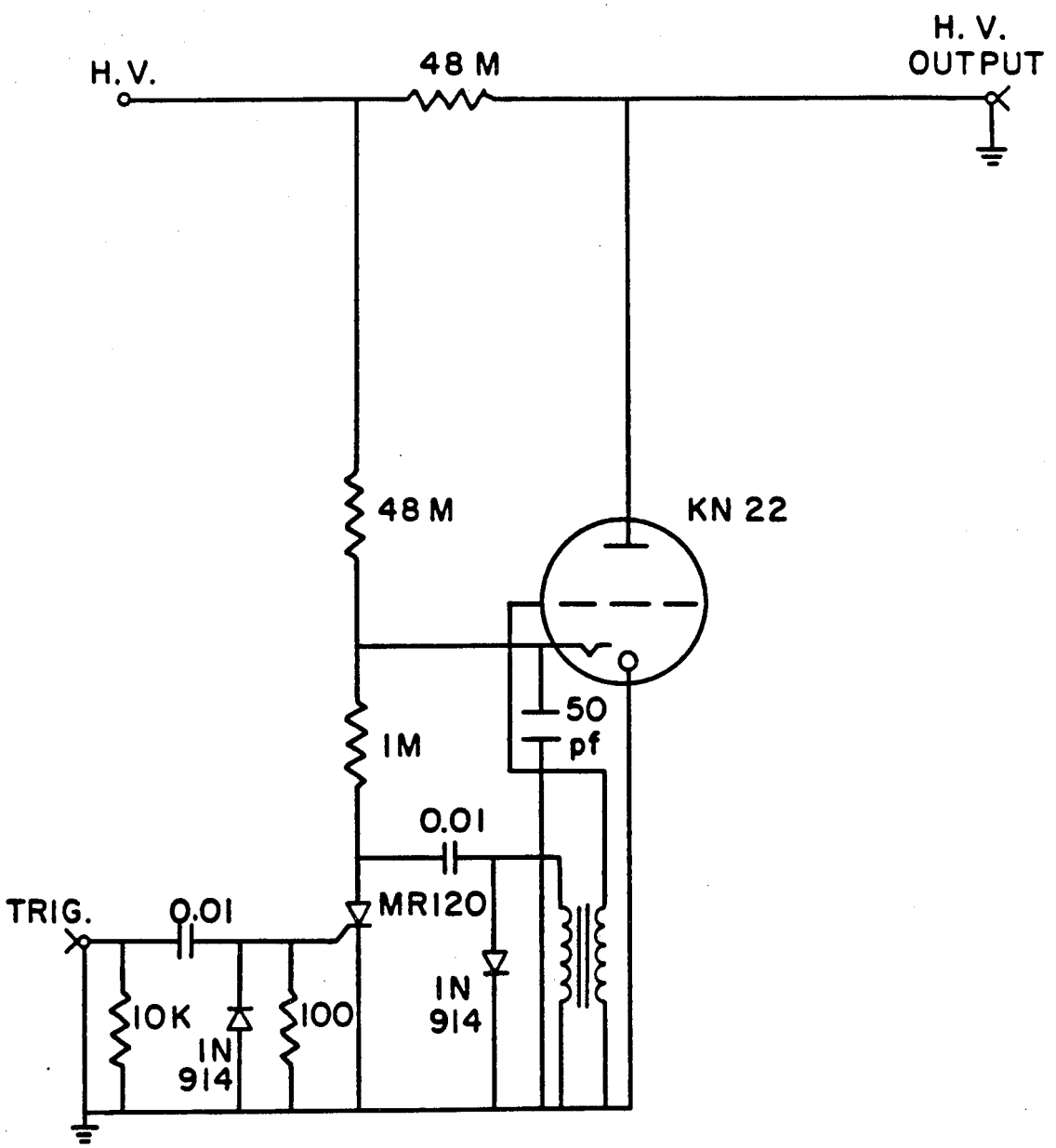

Figure I-14. Delay 2 Pockels cell pulser.

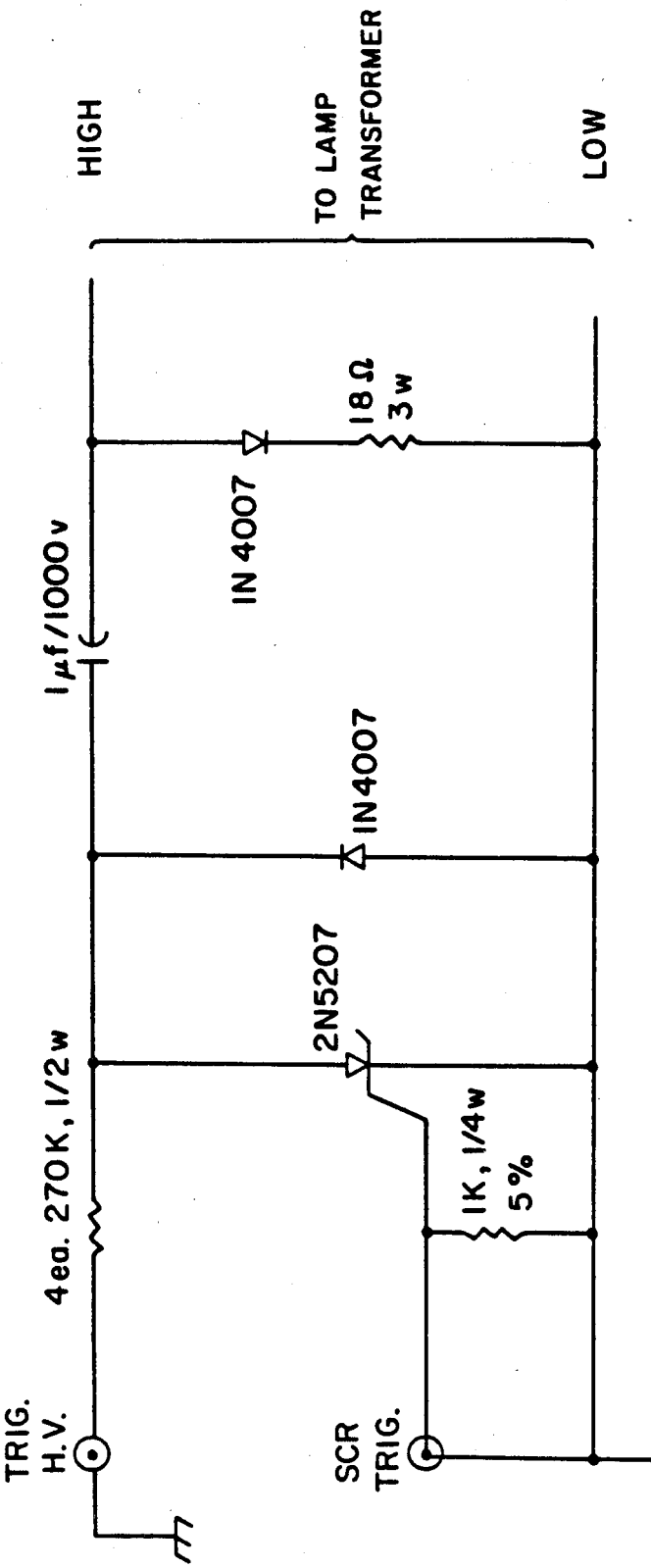

Figure I-15. Flashlamp transformer trigger circuit.

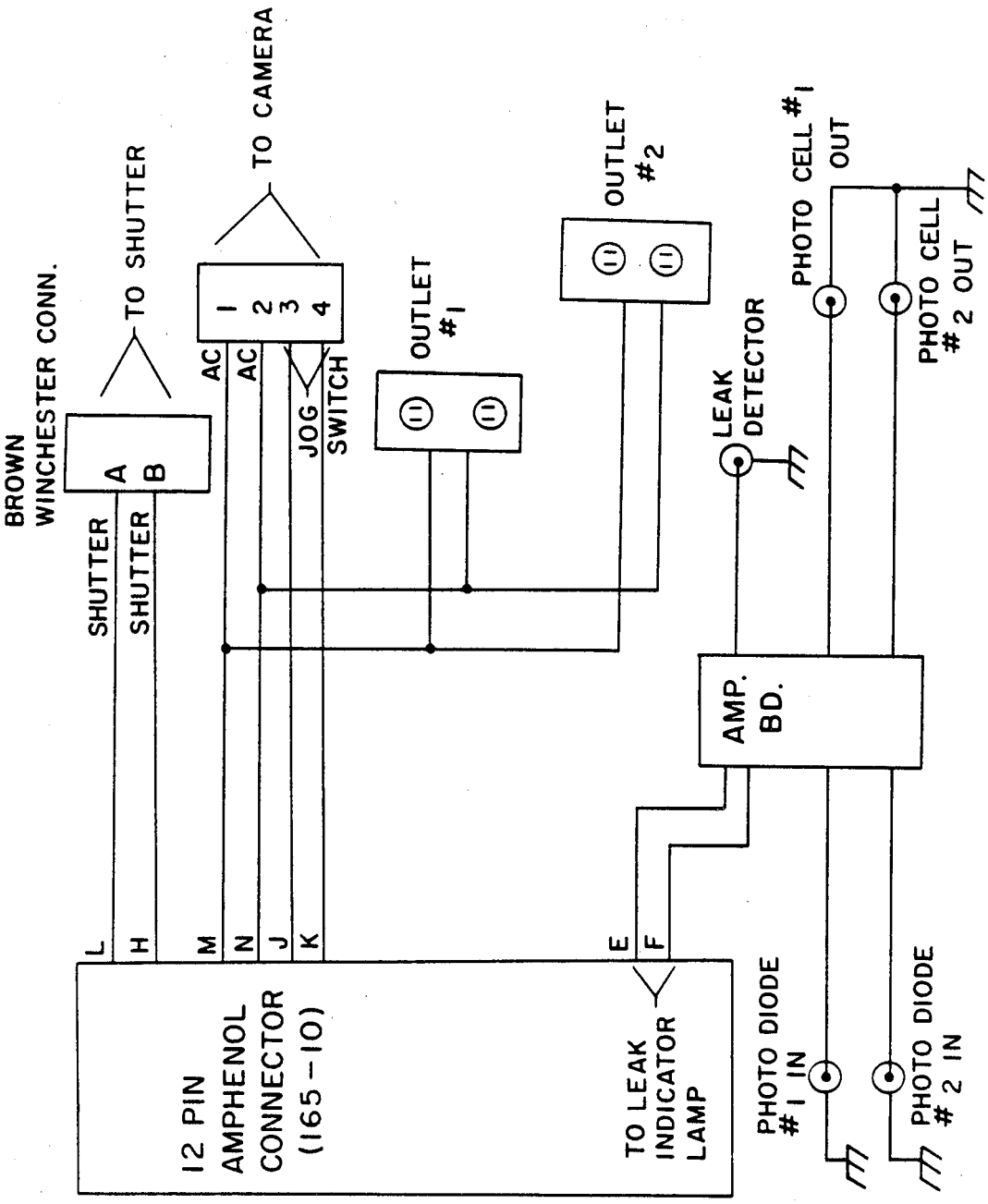

Figure I-16. Wiring diagram for shutter, film drive, photodiode and leak detector chassis.

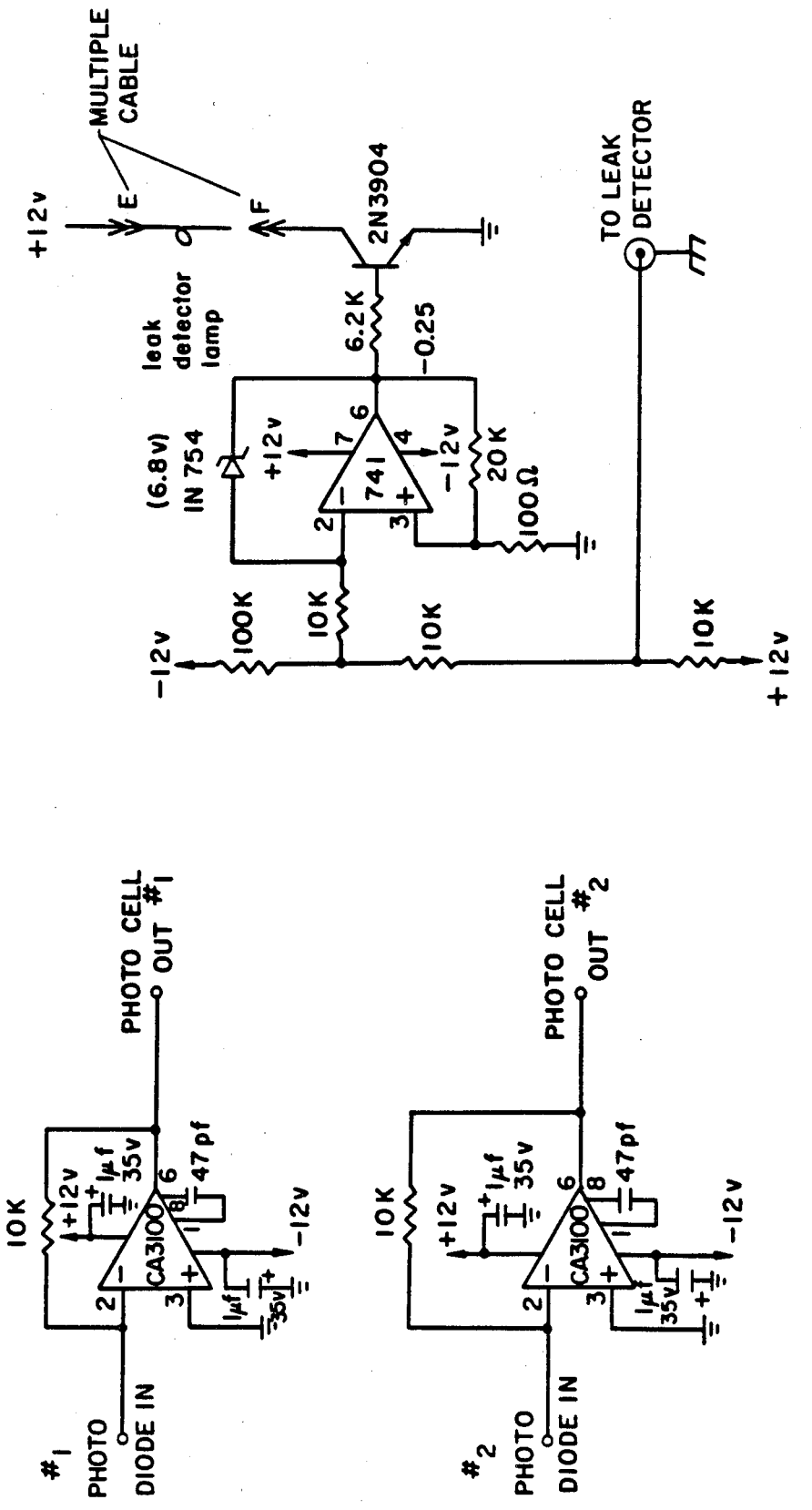

Figure I-17. Photodiode and leak detector amplifiers.

APPENDIX II

Comparison of Holographic and Coulter Counter Measurements of Cavitation Nuclei in the Ocean

T.J. O'Hern, L. d'Agostino and A.J. Acosta

submitted to *ASME J. Fluids Engineering*, 1987

COMPARISON OF HOLOGRAPHIC AND COULTER COUNTER MEASUREMENTS OF CAVITATION NUCLEI IN THE OCEAN

by Tim J. O'Hern, Luca d'Agostino and Allan J. Acosta
Division of Engineering and Applied Sciences
California Institute of Technology
Pasadena, California, 91125

ABSTRACT

Holographic and Coulter Counter detection techniques were jointly used to measure the concentration density distribution of cavitation nuclei in the ocean. Comparison of the two techniques indicates that Coulter Counter analysis underestimates the particulate content by up to an order of magnitude and may produce a distorted number concentration distribution. Several possible explanations of the observed discrepancies are proposed and discussed, including fundamental differences between the *in situ* holographic samples and the collected samples examined with the Coulter Counter, differences between the unknown electrical conductivity of the measured particles in the sea water samples and the non-conductive particles used to calibrate the Coulter Counter, the rupture of aggregate particles in the flow through the Coulter Counter orifice, the effect of electronic noise on the Coulter Counter signal, and the effect of statistical sampling error. The particle number concentration distributions decrease approximately with the fourth power of the particle radius in the observed size range of 10 to 50 μm radius. Both sets of data indicate an increase in particle concentration near the bottom of the thermocline, and the holographic bubble concentrations also indicate a similar behavior. Much higher concentrations of particles were detected in the ocean, according to the holographic analysis, than in typical cavitation test facilities. Consideration of the static equilibrium of individual bubbles indicates that the average tensile strength of the ocean waters examined in this study is on the order of a few thousand Pascals, with a minimum expected value of about one hundred Pascals.

NOMENCLATURE

a	particle cross-sectional area
A	Coulter Counter orifice cross-sectional area
c	MCA channel index corresponding to calibration radius R_c
i, j	MCA channel index
l	particle length
L	Coulter Counter orifice length
$n(R)$	nuclei number concentration density distribution function
$N(R)$	concentration of nuclei with radius smaller than R
N_g	number of nuclei counts in each radius group
N_{tot}	total particle concentration in the measured radius range
ΔN	nuclei concentration in the radius range ΔR
p_o	bubble equilibrium external pressure
p_v	liquid vapor pressure
$(p_v - p)_{cr}$	bubble critical tension
R	particle radius
$\overline{R}$	nominal radius of each data group
R_c	radius of Coulter Counter calibration particles
R_i, R_j	particle radius corresponding to channel i, j of MCA
R_o	bubble equilibrium radius
ΔR	nuclei radius range about R
ΔR_{or}	change of Coulter Counter orifice electrical resistance
S	bubble surface tension
T	liquid temperature
V_p	particle volume
V_s	liquid sample volume
α, β	PSA calibration constants
σ	liquid electrical conductivity
σ'	particle electrical conductivity

1. INTRODUCTION

The maximum tensile stress of liquids is considerably reduced by the presence of weak spots, generically called nuclei, which act as preferential sites for the occurrence of liquid rupture. These nuclei have been the subject of considerable research effort, yet their exact nature and origin have not been firmly established. However, it has been recognized that bubbles, some kinds of solid particles and gas pockets inside crevices and cracks on the surface of particulates suspended in the liquid can act as cavitation nuclei and that their effect usually dominates that of the nuclei located at the liquid boundaries.

The presence of nuclei is particularly important in technical applications because they control the onset and the development of cavitation, which is a generally undesirable phenomenon because of the severe limitations it imposes on the overall performance of hydraulic operating machinery. The liquid characteristics that affect the occurrence of cavitation through their influence on the nuclei population are collectively called liquid quality. For the purpose of cavitation research the concentration of nuclei in the liquid and their dynamic behavior when exposed to a change of pressure are thought to be of special importance in trying to predict cavitation inception and to deduce scaling laws capable of correlating the results from model test to full-scale operation. Not all the nuclei respond in the same way to a change of the surrounding pressure. The dynamic properties of gas bubbles in mechanical equilibrium can be directly related to their size, so in this case the liquid quality is adequately described by the nuclei number concentration distribution as a function of bubble size. Traditionally, the nuclei number concentration distribution has also been used in the literature to characterize the liquid quality even when the main source of nuclei is represented by particles, whose dynamic behavior cannot be directly related to their geometry. In this case the size measurements of particulates contained in liquids still provide an upper limit for the concentration of potentially active cavitation nuclei. Significant efforts have been made to develop suitable methods of nuclei detection in liquids, based on various physical principles. In general, the results

obtained using these methods are in substantial qualitative agreement, but they often differ significantly under the quantitative point of view.

Ocean waters are known to contain the above nucleation agents as well as many others of organic origin. These waters represent a very interesting environment for cavitation research because of their great technical importance in various fields of applied sciences such as, for example, naval hydrodynamics, ship propulsion, underwater acoustics and optics. Detailed knowledge of the sea water liquid quality is essential for the simulation of marine conditions in the laboratory and for the scaling of model tests to prototype operation. However, relatively little is known about nuclei in marine environments because, due to the inherent experimental difficulties, there are not many reported studies in the literature on this subject. The various types of nuclei found in the ocean are of interdisciplinary interest far beyond cavitation, leading previous researchers to separately explore bubbles [see, for example: Medwin 1977; Thorpe 1982], particles [Carder et al. 1982] and organisms [Pieper and Holliday 1984]. A review of the work on nuclei detection in ocean waters pertaining to cavitation is included in Billet 1985. In this paper we report the application and compare the results of two of these methods, namely, holographic and Coulter Counter detection, to the monitoring and sizing of cavitation nuclei in the ocean.

2. HOLOGRAPHIC EXPERIMENTAL APPARATUS

The holographic investigation involves *in situ* optical recording of ocean water samples for later analysis and derivation of the size and concentration of both microbubbles and particulate matter. A sketch of the system used for recording Fraunhofer holograms of ocean water samples is depicted in Fig. 1, which shows a modified version of the system first described by Katz et al. 1984. Detailed descriptions of the Fraunhofer holographic process are available in several texts and articles (see, for example, Collier et al. 1971 and DeVelis et al. 1966), so only an elementary description will be given here. A pulsed ruby laser is used as the coherent light source for hologram recording. The laser is mounted inside a

submersible hull with windows through which the expanded laser beam passes to illuminate an external water sample. Particles in the illuminated sample scatter a portion of the laser beam, while the remaining portion passes through the sample undiffracted. The hologram is a record of the pattern formed by interference of the diffracted and undiffracted laser light on a high resolution roll film (Agfa 10E75). Maximum submersion is presently limited to 33.5 m by the electrical cables controlling and monitoring the laser and associated equipment.

Holographic reconstruction is accomplished by illuminating the developed hologram with a collimated continuous wave He-Ne laser beam. The hologram acts as a diffraction grating to produce three-dimensional real and virtual images of the original volume. Measurements are made by using a closed circuit vidicon system to examine a highly magnified portion of the real image. The resolution is approximately 5 μm. Discrimination of bubbles from solid particulates is important in monitoring cavitation nuclei and is made by visually examining the focused bubble image for roundness, brightness, and presence of a dark central spot due to the focusing effect of the bubble geometry. No attempt is made to establish the nature of nuclei with radii smaller than 10 μm.

Holographic determination of nuclei size is made by focusing a 220X magnified image of each nucleus on the reconstruction system monitor. At the focused plane, a major and minor diameter can be directly measured for non-circular objects. For purposes of comparison with the Coulter Counter results, the volume of the holographically detected particles is computed by assuming an ellipsoidal shape with the length of the third axis taken as the geometric mean of the two measured values, or, in cases of long thin objects, by assuming a cylindrical shape. The radius of a sphere of equal volume is then calculated.

3. COULTER COUNTER EXPERIMENTAL APPARATUS

The measurement of particulate matter in the sea water was carried out using the particle sizing and counting instrumentation of the Department of Environmental Engineering of the California Institute of Technology. This system includes a Model B Coulter Counter in conjunction with a Hewlett Packard 1208B oscilloscope, a Nuclear Data Particle Sizing Amplifier (PSA), a Multi-Channel Analyzer (MCA) for sorting of the signal amplitudes and a Teletype for output of the data. The apparatus is described in detail by Hunt 1980. Here the principles of operation of the system and the procedure used for computing the particle size distributions are briefly reviewed to the extent needed for the interpretation of the results presented in this paper.

In the Coulter Counter a known volume of the sampled liquid is forced through a small orifice of known diameter in an electrically insulating medium. When an electric field is established in the conducting liquid across the orifice, inhomogeneities (here generally called particles regardless of their true nature) whose electrical resistivity is different from that of the surrounding liquid can be detected, counted and sized by the perturbation they induce in the electrical resistance across the orifice. The amplitude of the electrical signal is approximately proportional to the volume of the particle as long as its dimensions are less than about 40% of the orifice diameter. The signal amplitude also depends on the orifice diameter, electrical excitation, signal amplification and on the conductivities of the liquid and of the particle. Because of finite lower resolution, different electronic settings and orifice diameters are needed to measure relatively wide size distributions.

In the present apparatus the Coulter Counter pulse signal is amplified by the PSA, whose output is proportional to the logarithm of the volume of the sampled particle through two adjustable gain constants. The MCA then sizes the incoming pulses according to their amplitude and stores the corresponding counts in 128 separate channels. At the same time the MCA data are also displayed on the oscilloscope. During each run a preset volume of liquid is

sampled. Data from multiple consecutive runs can be summed in the MCA in order to reach the required number of counts for a statistically significant measurement of the particle population. Because of the logarithmic response of the PSA, particles of radius R are counted in the channel of index $i = \alpha + \log_\beta R^3$. The calibration constants α and β depend in general on the instrument settings (excitation, amplification, orifice size and electrical conductivities of the liquid and of the particle) and are determined by sampling two or more suspensions of monodisperse particles of known size and electrical conductivity. Ideally in this case all the counts should be concentrated in just one channel, but in practice the distribution is broader and the channel corresponding to the mode of the distribution is used for calibration purposes. In this process care must be taken to correctly isolate the mode, since aggregation of two or more particles is possible and can cause misleading results. Then, if R_c is the radius of the calibration particles and c the corresponding channel index, the radius corresponding to any channel i is:

$$R_i = R_c \beta^{(i-c)/3} \tag{1}$$

At high amplification levels electronic noise determines the maximum useful sensitivity and, together with the characteristics of the MCA, limits the measurement range to a maximum to minimum radius ratio of about 4.

The system was initially calibrated with monodisperse suspensions of electrically non-conductive polystyrene latex spheres (Duke Scientific Corporation) in filtered sea water at room temperature for given electronic settings (current excitation and signal amplification) and orifice diameter. The size distribution of the calibration particles was very nearly Gaussian, with modal diameters of 19.1 μm, 49.4 μm and 99.1 μm and standard deviations 1.4 μm, 2.5 μm and 4.8 μm, respectively. Only one orifice of 140 μm diameter was used with two different electronic settings to cover the particle radius range from about 10 μm to about 50 μm. The calculated logarithmic bases of the PSA agreed within the achievable experimental accuracy with the values obtained with the same apparatus by previous investigators.

4. DATA REDUCTION

In cavitation research literature the liquid quality is usually expressed in terms of the nuclei number concentration density distribution function:

$$n(R) = \frac{dN}{dR} \simeq \frac{\Delta N}{\Delta R} \tag{2}$$

where $N(R)$ is the concentration of nuclei with radius smaller than R and ΔN is the observed concentration of particles with radius in the range ΔR containing the nominal radius R. From this definition it follows that the total concentration of particles in the liquid is:

$$N_{tot} = \int_0^{+\infty} n(R)\, dR \tag{3}$$

The nuclei number concentration density distribution $n(\overline{R})$ is measured by grouping together adjacent radii counts until a predetermined number of counts N_g is reached. This value is then divided by the corresponding radius range and sampled volume, V_s. Thus, if the nuclei radii are ordered by decreasing size and R_j is the maximum radius of the group:

$$n(\overline{R}) \simeq \frac{N_g}{V_s(R_j - R_{j+N_g})} \tag{4}$$

The statistical error associated with this procedure is uniform and depends only on the size of the groups, N_g. Assuming that the occurrence of nuclei in the liquid sample volume is a Poisson process, as it should be if the nuclei were spatially uncorrelated, the best estimate of the relative r. m. s. error in the computation of the number concentration density distribution is equal to the reciprocal of the square root of the group size, $1/\sqrt{N_g}$. The nominal radius $\overline{R}$ of each group is defined as the geometric mean of the minimum and maximum values of the radii of the group. This choice usually minimizes the difference between the observed total concentration of particles and the value calculated by integrating the measured nuclei number distribution.

The above reduction procedure differs slightly from the more common way of computing the number concentration distribution density based on the number of counts observed in each prefixed interval subdividing the size range. First,

it assures that the statistical error due to the finite number of counts of the sampled population is uniform for all the computed data points. Furthermore, by adjusting the size interval to the occurrence of the observed data, it avoids the upward bias that occurs when sparse data are assigned to fixed size intervals and zero counts are neglected, instead of being averaged with the neighboring ones over a wider size range. Finally, it preserves the information on the relative density of the distribution of the available data as a function of size, which would otherwise be lost.

5. OCEAN TESTS

Field tests were performed in late August 1985 at two locations near Santa Catalina Island, southwest of Los Angeles (see Fig. 2), using the 65 foot R/V Seawatch operated by the Institute for Marine and Coastal Studies of the University of Southern California. At each site holograms were recorded at various depths and sea water samples were collected with Nansen bottles for later Coulter Counter analysis. At approximately the same time, standard oceanographic measurements were made including Secchi disk casts together with transmissometer and salinity-temperature-depth (STD) profiles. Holographic data were collected only while anchored or drifting to avoid recording of artifact boat-generated bubbles. The water samples for Coulter Counter analysis were transferred to opaque polyethylene bottles, kept refrigerated while on board in order to reduce alteration as much as possible, stored overnight at ambient conditions to reach room temperature and processed within 24 hours. Just before the analysis each water sample was stirred with a magnetic agitator to resuspend those particles that settled to the bottom of the container, taking care not to entrain new bubbles in the process.

The first test location was off Long Point, Santa Catalina Island. The boat drifted in waters ranging from 132 to 228 m depth during the two hours while holograms were being recorded. The water was quite clear, with the Secchi disk visible to 17 m depth. Sea state was 0 to 1, with less than 0.3 m swells, and no

wind. Temperature and transmissivity profiles are presented in Fig. 3. Thirty holograms were recorded, sampling the water column from the surface to 32 m. The second test location was off the eastern point of Santa Catalina Island and was not as well protected from winds as the first station. The sea floor depth was 92.7 m, Secchi disk visibility was 19 m, with sea state and wave activity the same as at the first test location. Temperature and transmissivity profiles are presented in Fig. 4. Fourteen holograms were recorded at this station, all at either 27.4 or 32 m.

6. EXPERIMENTAL RESULTS AND DISCUSSION

For the purpose of cavitation research, the most important nuclei are the largest ones, which usually have smaller critical tensions and whose effects in cavitating flows therefore tend to dominate those of the smaller, generally less susceptible nuclei. For this reason the present paper focuses on nuclei of relatively large radius (more than 10 μm), unlike most previous investigations of particulate content of the ocean that used similar optical or electrical detection techniques.

Some results of particulate concentrations in the ocean obtained by holographic and Coulter Counter analysis of sea water from the same locations and at comparable depths and time are shown in Figs. 5 through 8. Data are expressed in terms of the number concentration density distribution, $n(R)$, as a function of the particle radius, R, obtained as explained in Sec. 4. Here the number of radius counts per group is chosen as $N_g = 4$, and the corresponding estimate of the relative r. m. s. error of the data is 50%. The Coulter Counter analysis was carried out on 20 ml water samples, using two electronic settings of different sensitivity in order to extend as much as possible the radius range of the measurement. In the computation of the number concentration density distribution from holographic records, the sample volumes examined were on the order of 1 ml for nuclei from 10 to 25 μm radius and 100 ml for larger sizes. Since the sea water samples rested for about 24 hours before being processed with the

Coulter Counter, no bubbles with radii larger than 10 μm were expected nor observed at the time of examination. Therefore, for better comparison of the data obtained with the two methods, the bubble population determined holographically has not been included in the data of Figs. 5 through 8, but will be discussed separately below.

The holographic results are consistently higher than the ones deduced using the Coulter Counter by as much as one order of magnitude. Since the holographic number concentration density distributions were determined by visual inspection of a magnified image recorded *in situ*, there is little reason to doubt their validity. The fact that the Coulter Counter consistently indicated fewer nuclei is not surprising in view of the following considerations. First, some of the particles may have permanently settled during the relatively long time (about 24 hours) from water sample collection to the actual processing of the sample, despite the efforts to resuspend them by agitation prior to the analysis. Second, the sampling of the Nansen bottles for Coulter Counter analysis differs from the recording of holographic data in both depth (within one meter), horizontal location (within five meters, neglecting drift) and time (less than one hour). Fluctuations of the particle population over relatively small distances are known to exist in ocean waters [Pieper and Holliday 1984]. These fluctuations do not introduce a systematic error, yet they may have contributed to some of the observed differences between the Coulter Counter and holographic data. However, in our opinion the most likely and important reason for the observed discrepancy in the results of the two detection techniques is the fundamental difference between the unknown electrical conductivity of the measured particles in the sea water samples and the non-conductive particles used to calibrate the Coulter Counter. In order to estimate the importance of this effect, let us consider a small cylindrical particle of cross-sectional area a, length l and electrical conductivity σ' suspended in a liquid of electrical conductivity σ at the center of a cylindrical orifice of cross-sectional area $A \gg a$ and length $L \gg l$. Then, from a simplified one-dimensional electrical model where the resistance of the

particle, $l/a\sigma'$, is in parallel with that of the surrounding liquid, $l/(A-a)\sigma$, the total change of the electrical resistance across the orifice due to the presence of the particle can be expressed by:

$$\Delta R_{or} = \frac{\frac{V_p}{A^2\sigma}\left(\frac{\sigma'}{\sigma}-1\right)}{1+\frac{a}{A}\left(\frac{\sigma'}{\sigma}-1\right)} \tag{5}$$

where $V_p = al$ is the particle volume. For small particles the denominator of Equation (5) can be approximated to unity, the above change in the electrical resistance of the orifice is small with respect to the unperturbed value, and the Coulter Counter signal is therefore proportional to $V_p(\sigma'/\sigma - 1)$. Then, for example, the size of particles whose electrical conductivity is equal to 90% of the conductivity of the suspending liquid would be underestimated by one order of magnitude. Indeed, relatively high values of the electrical conductivity are not unrealistic in our case, since most of the particles suspended in unpolluted oceans are of organic origin [Sheldon et al. 1972] and therefore their electrical conductivity is likely to be of the same order of magnitude as that of the surrounding waters.

The number concentration density distributions determined using the Coulter Counter are steeper than those determined holographically, as indicated by Figs. 5 through 8. A possible reason for this difference is the rupture of the aggregate particles because of the shearing and elongational strains in the flow of the sampled liquid through the Coulter Counter orifice. The rupture of aggregate particles would increase the number of counts at smaller size ranges and therefore steepen the number concentration density distribution. Aggregate particles were indeed observed in the holographic images of the sample. Since recognition could be made only for relatively large aggregate particles, we cannot estimate their total concentration and therefore the importance of their potential contribution to this effect.

The Coulter Counter also displays the general tendency to produce slightly concave number concentration density distribution curves, unlike the holographic data. We believe that this is the result of the change of relative impor-

tance of the electronic noise with particle size, which was found to be significant only for the higher radius range, where the number of spurious, noise-induced counts becomes comparable to the original particle signal. However, no correction could be made due to the extreme sparsity of the data in this region of the size spectrum.

The particle number concentration density distributions deduced from holographic data decrease approximately with the fourth power of the particle radius in the observed size range. Similar dependence has been reported in the literature for the population of particles in many natural environments, including sea waters [Bader 1970], as well as for the population of bubbles of comparable size in the ocean [Mulhearn 1981; Medwin 1977].

The holographic and Coulter Counter determinations of total concentration of particles for various depths at the two test sites are presented in Figs. 9 and 10. Only particles in the 10 to 50 μm radius range are used in the calculation of the total concentration, as the holographic and Coulter Counter data directly overlap only over this radius range. Results are based on the analysis of eight holograms (six from the Long Point site and two from off east Santa Catalina Island) and eight Coulter Counter water samples (four from each site). The holographic data in Figs. 9 and 10 indicate higher total particulate concentrations in the 10 to 50 μm radius range than those reported in the literature for either ocean or laboratory waters. They also clearly reflect the previously noted discrepancy between the concentrations measured using the two methods. Both sets of data in Fig. 9 from the Long Point test site seem to indicate an increase in particle concentration near the bottom of the thermocline and to correlate well with the transmissometer trace of Fig. 3, which shows a drop in transmissivity near the thermocline depth. Similar behavior at the test site off east Santa Catalina Island is displayed by the Coulter Counter data of Fig. 10, as well as by the transmissometer trace of Fig. 4. The holographic results at this site are too sparse to indicate any trend with depth.

The observation of particle concentration increase near the bottom of the

thermocline is supported by the data of Pieper and Holliday 1984, who present zooplankton concentrations determined by microscopic examination of organisms deposited on filters as sea water samples were pumped through from various depths. This testing was done in May, 1978, at a location and at depths very similar to the Long Point test site examined in this study. The thermoclines were similar in each test, with the top at about 18 m and the bottom at about 30 m, although that in Pieper and Holliday 1984, was stronger ($5°C$) and the surface temperature was lower ($17°C$). Their results show peak zooplankton concentrations near the bottom of the thermocline. The present holographic results support this finding, clearly showing that a large percentage of the "particles" observed, especially below the thermocline, are living organisms. The finding of high zooplankton counts in deeper waters should be of interest in cavitation studies since zooplankton, with their metabolic gases, can presumably act as cavitation nuclei.

Although the Coulter Counter can be used, with some limitations, for detection of bubbles [Oba et al. 1981 for example] such an investigation was not undertaken in the present study since, as mentioned earlier, the sea water samples used for Coulter Counter analysis were handled in such a way that no bubbles were expected nor observed at the time of analysis. However, since bubbles are known to be primary cavitation nuclei, results of the holographic study of bubbles will be included and briefly discussed here. Table 1 presents bubble concentrations, and total number of bubbles counted, in various radius ranges for several depths at the two test sites. No bubbles larger than 50 μm radius were seen in any of the holographic samples. Recall that no attempt was made to distinguish bubbles from particulates in the smallest size range, about 2.5 to 10 μm radius, so these data are not presented here.

Several observations can be made based on the small number of bubbles seen in the holographic images. The concentration of small bubbles (10 to 25 μm radius) at the test site off Long Point seems to be very high near the surface, then to decrease with depth until the thermocline is reached, at which

point the concentration increases. Larger bubbles (25 to 50 μm radius) are found only below the thermocline. The bubble data for the test site off east Santa Catalina Island are sparse and represent water below the thermocline only, indicating a fairly high concentration of larger bubbles at the 32 m depth. The relative r. m. s. error for each bubble size interval is expected to be equal to $1/\sqrt{N_g}$, where N_g is the corresponding number of counts, shown in brackets in Table 1. This error is often large, especially for those size ranges with sparse bubble observations. The overall high bubble concentrations, particularly near the surface at the Long Point site, are surprising in view of the calm windless conditions at the time these holograms were recorded, as well as for several days earlier. Strong dependence of ocean bubble concentrations on wind speed have been reported by Medwin 1977 and Thorpe 1982. The existence of microbubbles down to 32 m and the apparent population inversion below the thermocline are also surprising. Shen et al. 1984 detected microbubbles to 25 m depth at both stations reported, with decreasing bubble concentration as a function of depth, although sampling below the deep thermocline at their subtropical test sites was not reported [Zsolnay et al. 1986]. Medwin 1977 observed bubbles as deep as 36 m, and under a windrow observed peak bubble concentrations at that depth. He speculates that the Langmuir cells under the windrow acted to deplete the upper waters without affecting the deep water bubbles, which are postulated to be of biological origin. Windrows were not present at the stations holographically examined in the present study but, as discussed above, there seemed to be a peak in biological activity below the thermocline, so bubbles of organic origin may play a role here. Several hypotheses have been formulated to explain the presence of bubbles at depth [Johnson and Cooke 1981; Medwin 1977; Mulhearn 1981].

The relationship between the nuclei number concentration density distribution and the tensile strength of the suspending liquid is still an elusive problem in cavitation research because of the many complexities and uncertainties involved. Little can be said about the role of particulates as cavitation nuclei from their

holographic observation or from the Coulter Counter sizing, apart from the obvious consideration that larger concentrations of particulates are likely to lead to higher active cavitation nuclei populations. This difficulty can be overcome only by direct observation of cavitation induced by the liquid particulates under controlled circumstances, for example, by means of cavitation susceptibility meters [Oldenziel 1982]. On the other hand, the dynamic properties of gas bubbles are indirectly related to their size by the Rayleigh-Plesset equation [Knapp et al. 1970]. However, even in this case cavitation results from the combination of the dynamic and interference effects among developing cavities with the statistical occurrence of bubble nuclei and depends significantly on the specific flow conditions. Therefore, a constant relation between the tensile strength of liquids and their bubble population can be established only in the idealized situation where dynamic and interference effects are neglected, i.e., by considering the static equilibrium of individual bubbles. Then a lower bound for the tension required to cause cavitation is given by the critical tension of a spherical gas bubble which, in the absence of viscosity, mass diffusion and thermal effects, is expressed by [Knapp et al. 1970]:

$$(p_v - p)_{cr} = \frac{4S}{3R_o}\left[3\left(1 + \frac{p_o - p_v}{2S/R_o}\right)\right]^{-1/2} \tag{6}$$

where R_o and p_o are the equilibrium radius and external pressure of the bubble and S is the surface tension. This relation is plotted in Fig. 11 for the case of an air bubble in water at a temperature of 20 $°C$ and for several equilibrium pressures. The sparse bubble measurements are insufficient to determine a statistically significant value of the tensile strength for each water sample examined, but several important points can still be made. A single bubble with 50 μm radius was seen at 23 m submergence at the site off Long Point (see Table 1), so Fig. 11 indicates that this water would be expected to cavitate at least occasionally under an applied tension of about 100 Pa. In general, Table 1 shows that all samples contained some bubbles larger than 10 μm radius, so Fig. 11 can be used to show that each of these would be expected to cavitate

under an applied tension of about 2000 Pa.

7. CONCLUSIONS

Holographic detection clearly is the more reliable of the two methods considered in this paper for measuring the nuclei number concentration density distributions. The unique capability of holography to provide discrimination between bubbles, particles and organisms is also of great value for *in situ* sea water analysis. However, the reconstruction and detailed visual analysis of holographic images are extremely time-consuming.

The comparison of representative data obtained using the two techniques indicates that Coulter Counter analysis tends to underestimate the particulate content by up to an order of magnitude as a probable consequence of the combined effects of particle settling and of the assumption of electrically non-conducting particles implicit in the calibration procedure. It is conceivably possible to introduce empirical corrections to compensate for the latter phenomenon when the general nature of the major portion of the particulate population in the sampled water is known. The apparent distortions of the number concentration density distributions obtained from the Coulter Counter also suggest that rupture of particle aggregates might take place during the analysis of the sample because of the strain produced by the flow of the liquid through the orifice, and that electronic noise is likely to be important only in the upper radius range where particle counts tend to become very sparse. These problems can be limited by using large aperture orifices and increasing the signal-to-noise ratio of the Coulter Counter electronics.

The observation that the Coulter Counter may consistently underestimate the size of organic particles could be an important one, as this device is commonly used for sea water analysis (see, for example, Carder et al. 1971, and Sheldon et al. 1972). Despite these limitations, in our opinion the Coulter Counter is still a practical, time-effective device for monitoring the particulate content of liquid samples in cavitation research when great accuracy is not required, and

the electrical conductivity of the major portion of the particulate population in the sample can be estimated.

The population of particulates obtained with the two techniques examined here are in agreement with previous comparable data from the literature within the expected experimental and statistical errors. They also confirm that the number concentration density distribution of particulates in the range covered by our investigation decreases approximately with the fourth power of the particle size, as often reported in the literature. Both the holographic and Coulter Counter results indicate an increase in particle concentration near the bottom of the thermocline, in agreement with the zooplankton population measurements made by Pieper and Holliday 1984. The holographic data also indicate similar behavior for the bubble concentration, although the relatively large statistical indetermination of these data makes them less conclusive.

Further study is necessary to clarify exactly the dependence of the tensile strength of liquids on their nuclei content and therefore to deduce scaling laws for cavitation phenomena. This is especially true in the case of particles, whose effect on the liquid susceptibility is not yet fully understood. However, the concentration of particles and bubbles in a liquid still provides an upper bound for the number of potentially active cavitation nuclei. Much higher concentrations of particles were detetected in the ocean, according to the holographic analysis, than in typical cavitation test facilities [Billet 1985]. These differences should be taken into consideration in trying to relate laboratory results to prototype operation. Finally, the bubble concentration density distributions indicate that the average tensile strength of the ocean waters examined in this study should be on the order of a few thousand Pascals, with a minimum expected value of about one hundred Pascals.

8. ACKNOWLEDGEMENTS

A field experiment must necessarily rely on the assistance and cooperation of many parties. Special thanks to to Professor J. Katz of Purdue University, to Elton Daly and staff of Caltech's W.M. Keck Laboratory of Hydraulics and Water Resources, and to the Captain and crew of the R/V Seawatch. Raymond Moberly together with Doug Gray resuscitated Caltech's Coulter Counter and later cooperated in the analysis of the samples and the reduction of the data. Sheldon Green assisted in the ocean tests and carried out a large portion of the holographic reconstruction. Esther (Cindy) Morss and Richard Arrieta provided valuable help during experimentation. This work has been supported by the Office of Naval Research under Contract No. N00014-83-K-0506 and by a Fellowship for Technological Research administered by the North Atlantic Treaty Organization - Consiglio Nazionale delle Ricerche, Italy, Competition No. 215.18/11 of 9.24.1984. Their support is gratefully acknowledged.

9. REFERENCES

Bader, H. 1970, "The Hyperbolic Distribution of Particle Sizes," *J. Geophysical Research, 75*, 15, 2822–2830.

Billet, M.L. 1985, "Cavitation Nuclei Measurements - A Review," ASME Cavitation and Multiphase Flow Forum, Albuquerque, N.M.

Carder, K.L., Beardsley, G.F.,Jr. and Pak, H. 1971, "Particle Size Distributions in the Eastern Equatorial Pacific," *J. Geophysical Research, 76*, 21, 5070–5077.

Carder, K.L., Steward, R.G. and Betzer, R.P. 1982, "In Situ Holographic Measurement of the Sizes and Settling Rates of Oceanic Particulates," *J. Geophysical Research, 87*, C8, 5681–5685.

Collier, R.J., Burckhardt, C.B. and Lin, L.H. 1971, *Optical Holography*, Academic Press Inc., New York.

De Velis, J.B., Parrent, G.B., Jr. and Thompson, B.J. (1966), "Image Reconstruction with Fraunhofer Holograms," *J. Optical Society of America, 56*, 4, 423–427.

Hunt, J.R. 1980, "Coagulation in Continuous Particle Size Distributions: Theory and Experimental Verification," Ph. D. Thesis, California Institute of Technology.

Johnson, B.D. and Cooke, R.C. 1981, "Generation of Stabilized Microbubbles in Seawater," *Science, 213*, 209–211.

Katz, J., O'Hern, T.J. and Acosta, A.J. 1984, "An Underwater Holographic Camera System for Detection of Microparticulates," ASME Cavitation and Multiphase Flow Forum, New Orleans, LA.

Knapp, R.T., Daly, J.W. and Hammitt, F.G. 1970, *Cavitation*, McGraw Hill.

Medwin, H. 1977, "*In Situ* Acoustic Measurements of Microbubbles at Sea," *J. Geophysical Research, 82*, 6, 971–976.

Mulhearn, P.J. 1981, "Distribution of Microbubbles in Coastal Waters," *J. Geophysical Research, 86*, C7, 6429–6434.

Oba, R., Kim, K.T., Niitsuma, H., Ikohagi, T., and Sato, R. 1981, "Cavitation Nuclei Measurements by a Newly Made Coulter Counter without Adding Salt in Water," *Report of the Institute of High Speed Mechanics, 43*, 340, 163–176.

Oldenziel, D.M. 1982, "A New Instrument in Cavitation Research: the Cavitation Susceptibility Meter," *ASME J. Fluids Engineering, 104*, 136–142.

Pieper, R.E. and Holliday, D.V. 1984, "Acoustic Measurements of Zooplankton Distributions in the Sea," *J. Cons. int. Explor. Mer, 41*, 226–238.

Sheldon, R.W., Prakash, A. and Sutcliffe, W.H., Jr. 1972, "The Size Distribution of Particles in the Ocean," *Limnology and Oceanography, XVII*, 3, 327–340.

Shen, Y.T., Gowing, S. and Pierce, R. 1984, "Cavitation Susceptibility Measurements by a Venturi," ASME International Symposium on Cavitation Inception-1984, New Orleans, LA.

Thorpe, S.A. 1982, "On the Clouds of Bubbles Formed by Breaking Wind-Waves in Deep Water, and Their Role in Air-Sea Gas Transfer," *Phil. Trans. R. Soc. Lond. A, 304*, 155–210.

Zsolnay, A., Lavoie, D.M., Wiesenburg, D.A. and Reid, D. 1986, "Environmental Parameters in Exuma Sound and the Straits of Florida," Naval Ocean Research and Development Activity Technical Note 252.

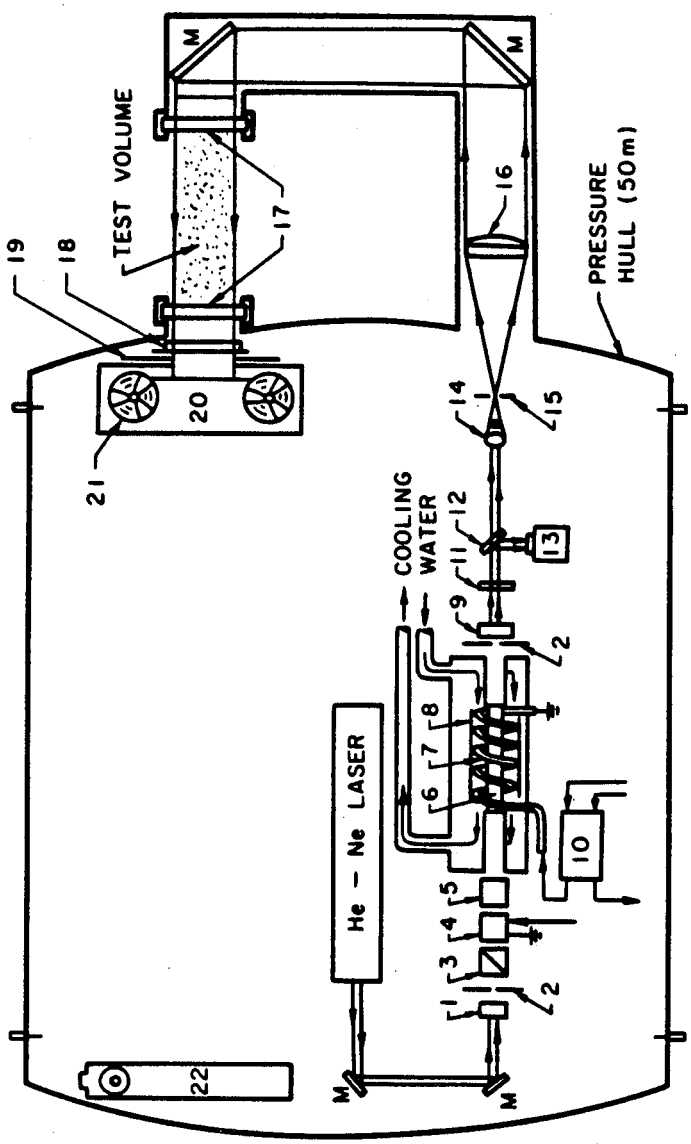

1. BACK MIRROR
2. IRIS APERTURE
3. POLARIZER
4. POCKELS CELL
5. POLARIZER (OPTIONAL)
6. RUBY ROD
7. XENON FLASH LAMP
8. REFLECTOR
9. FRONT MIRROR-SAPPHIRE ETALON
10. TRIGGER TRANSFORMER
11. NEUTRAL DENSITY FILTER
12. BEAM SPLITTER (4% REFLECTIVITY)
13. PIN DIODE
14. MICROSCOPE OBJECTIVE
15. SPATIAL FILTER - 10μ PINHOLE
16. COLLIMATING LENS
17. GLASS WINDOWS
18. INTERFERENCE FILTER
19. SHUTTER
20. AUTOMATIC FILM DRIVE
21. HOLOGRAPHIC FILM SPOOLS
22. AUTO COLLIMATOR
M. MIRROR

Figure 1. Line drawing of the holographic camera system mounted inside the submersible hull.

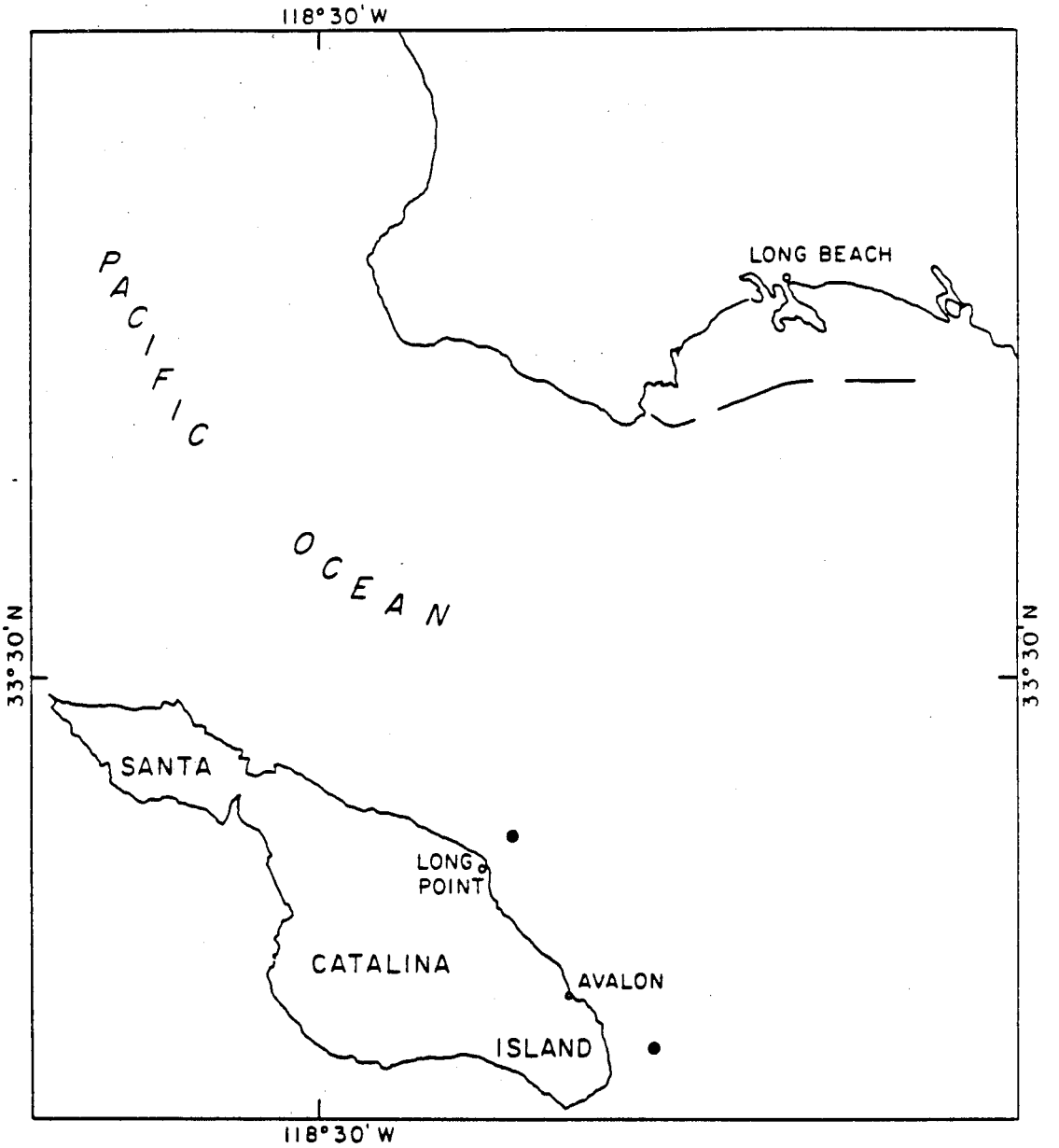

Figure 2. Map of the Los Angeles coastal area indicating the two test sites, off Long Point at 33°24′47″ N, 118°21′45″ W and east of Santa Catalina Island at 33°18′30″ N, 118°17′12″ W.

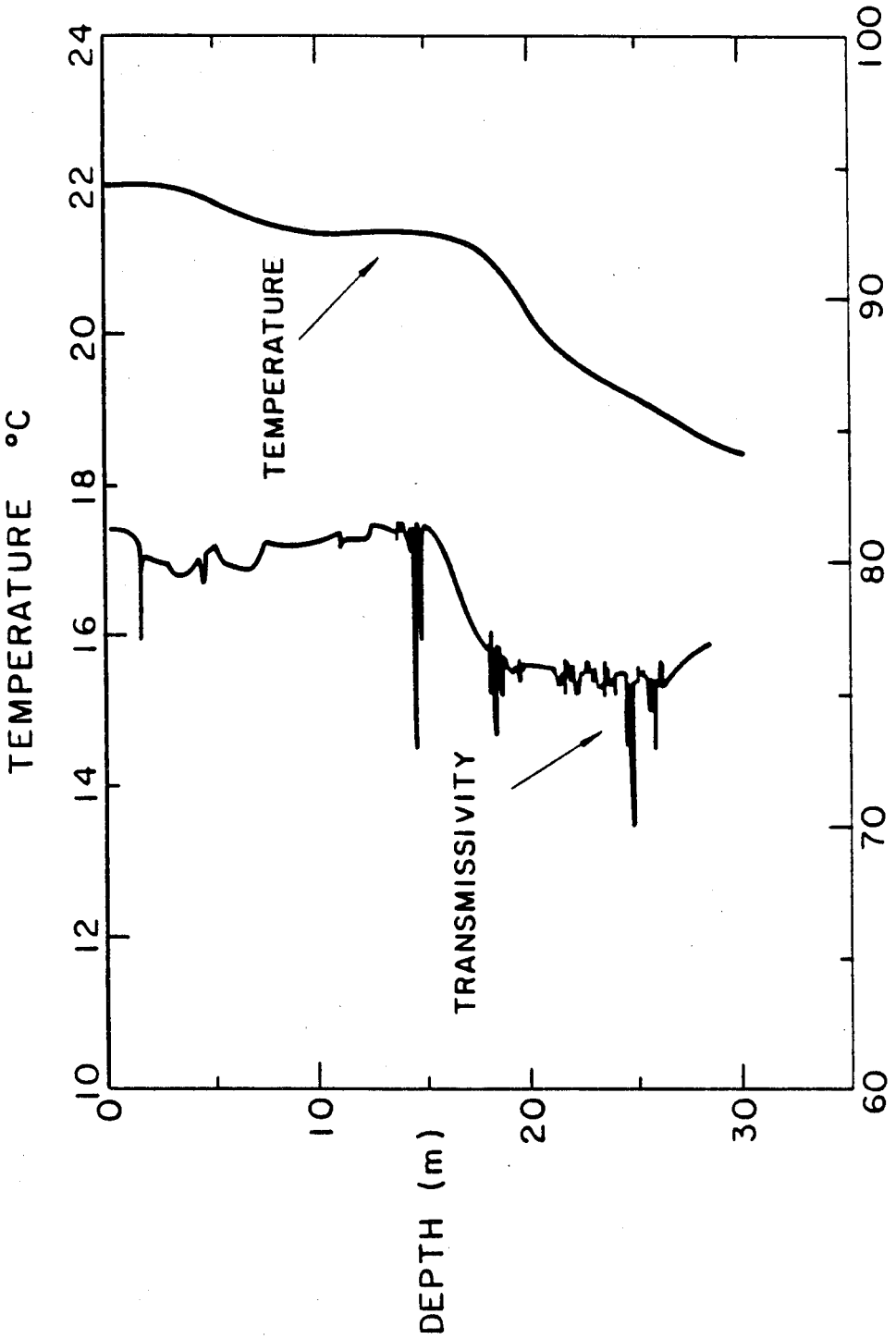

Figure 3. Temperature and transmissivity profiles for the test site off Long Point, Santa Catalina Island.

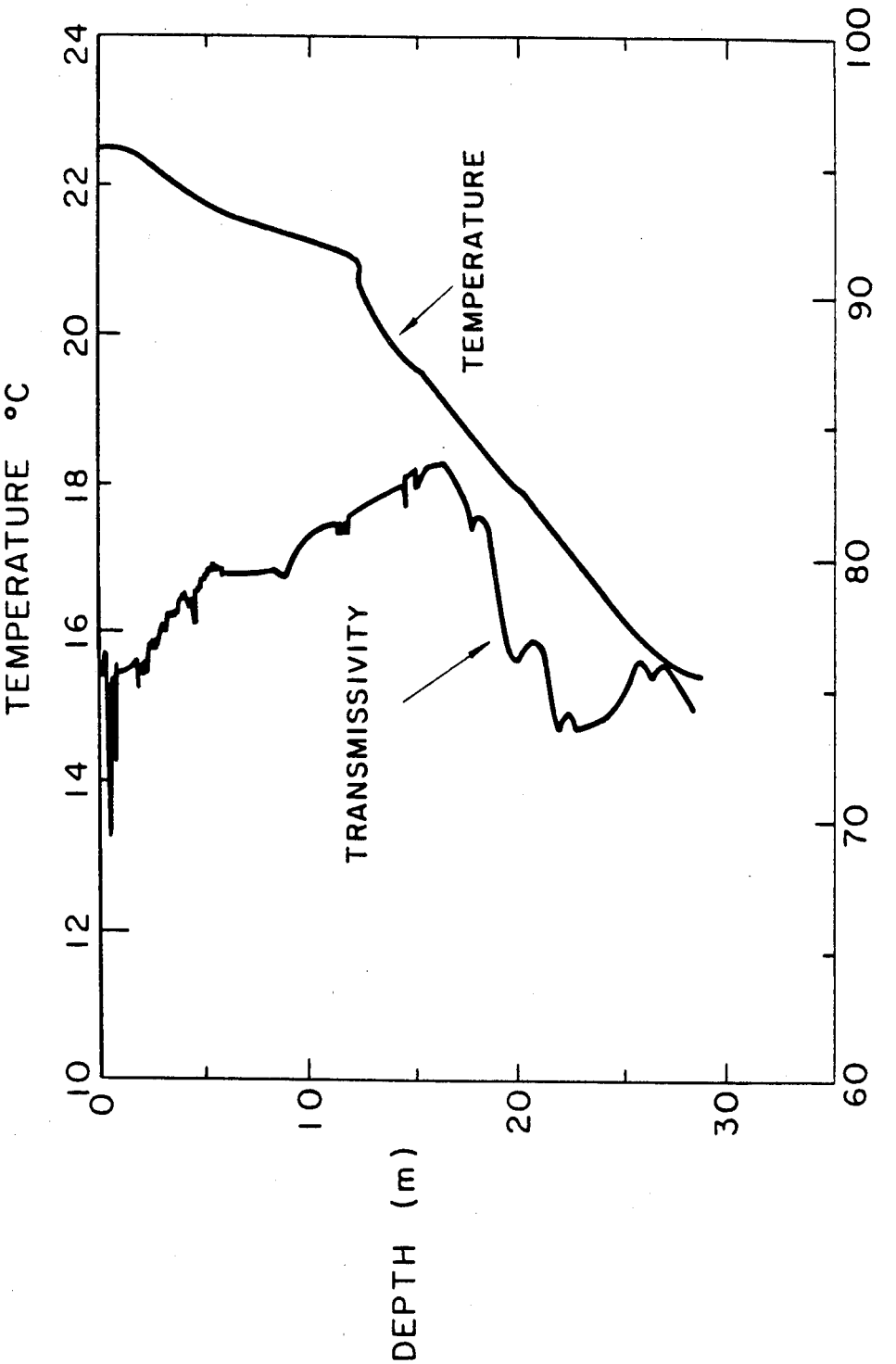

Figure 4. Temperature and transmissivity profiles for the test site off east Santa Catalina Island.

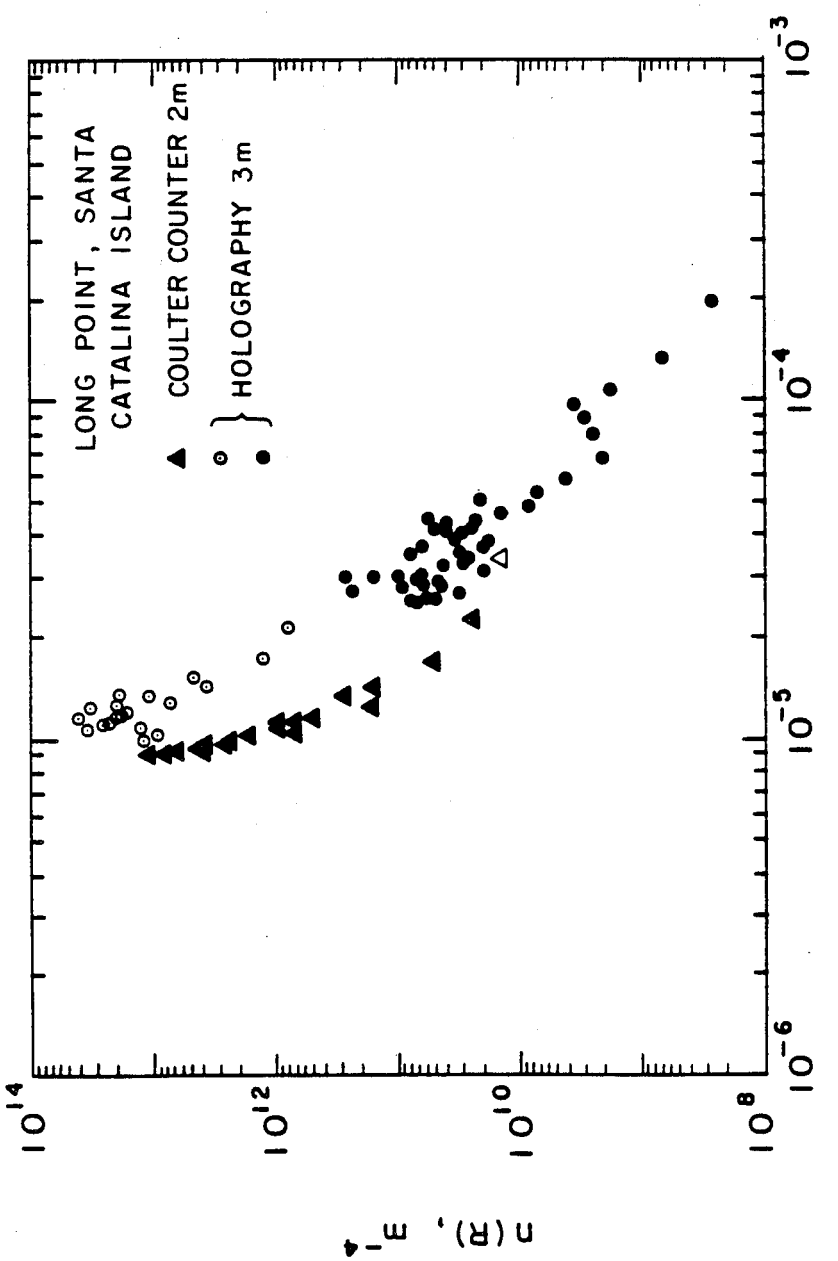

Figure 5. Number concentration density distributions of particulates, $n(R)$, in the waters off Long Point, Santa Catalina Island, as a function of the particle radius, R. The number of radius counts per group is $N_g = 4$ and the expected r.m.s. error is 50%. Holographic data (circles) were recorded at 3 m depth with sampling volumes: 1 (open symbols) and 150 ml (solid symbols). Coulter Counter data (triangles) were obtained analyzing 20 ml water samples from 2 m depth with different sensitivity: high (solid symbols) and low (open symbols).

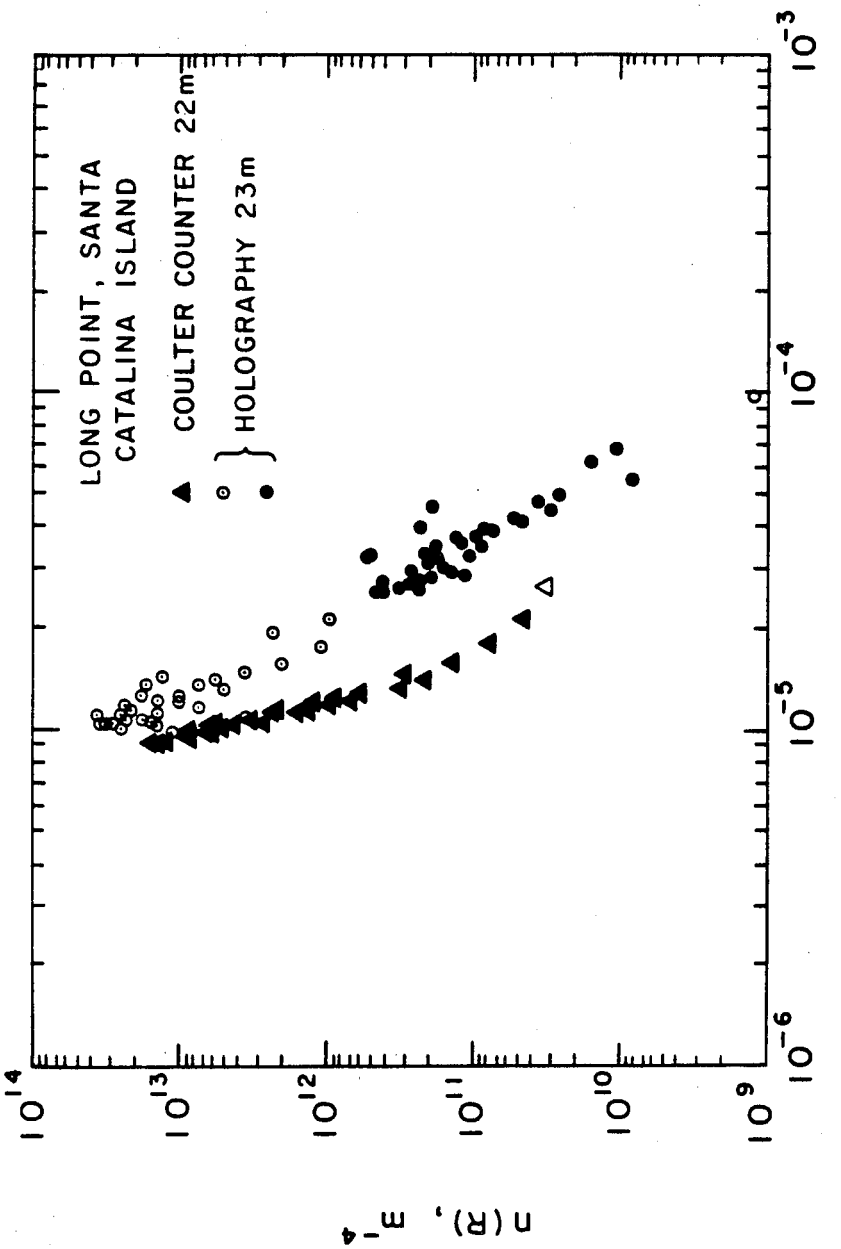

Figure 6. Number concentration density distributions of particulates, $n(R)$, in the waters off Long Point, Santa Catalina Island, as a function of the particle radius, R. The number of radius counts per group is $N_g = 4$ and the expected r.m.s. error is 50%. Holographic data (circles) were recorded at 23 m depth with sampling volumes: 1.6 (solid symbols) and 54 ml (open symbols). Coulter Counter data (triangles) were obtained analyzing 20 ml water samples from 22 m depth with different sensitivity: high (solid symbols) and low (open symbols).

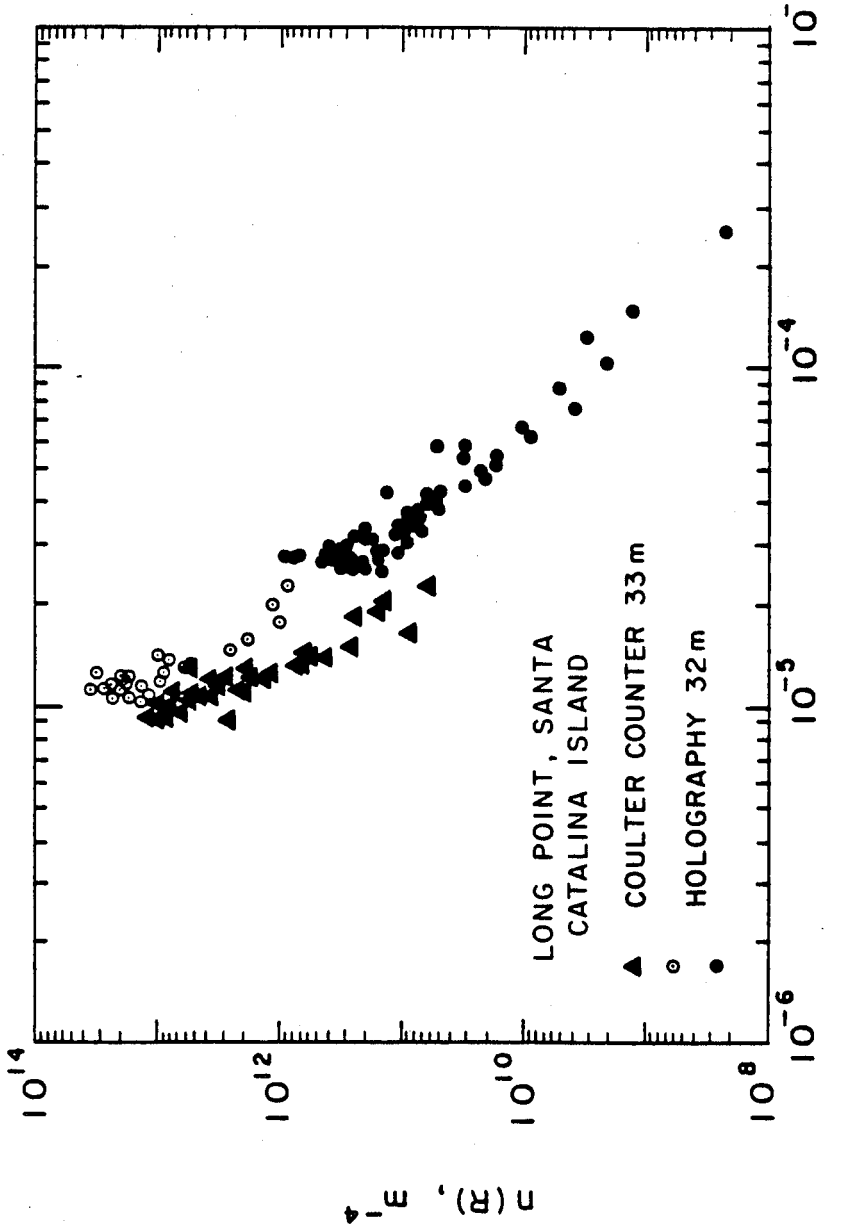

Figure 7. Number concentration density distributions of particulates, $n(R)$, in the waters off Long Point, Santa Catalina Island, as a function of the particle radius, R. The number of radius counts per group is $N_g = 4$ and the expected r.m.s. error is 50%. Holographic data (circles) were recorded at 32 m depth with sampling volumes: 1.6 (open symbols) and 79 ml (solid symbols). Coulter Counter data (triangles) were obtained analyzing 20 ml water samples from 33 m depth with different sensitivity: high (solid symbols) and low (open symbols).

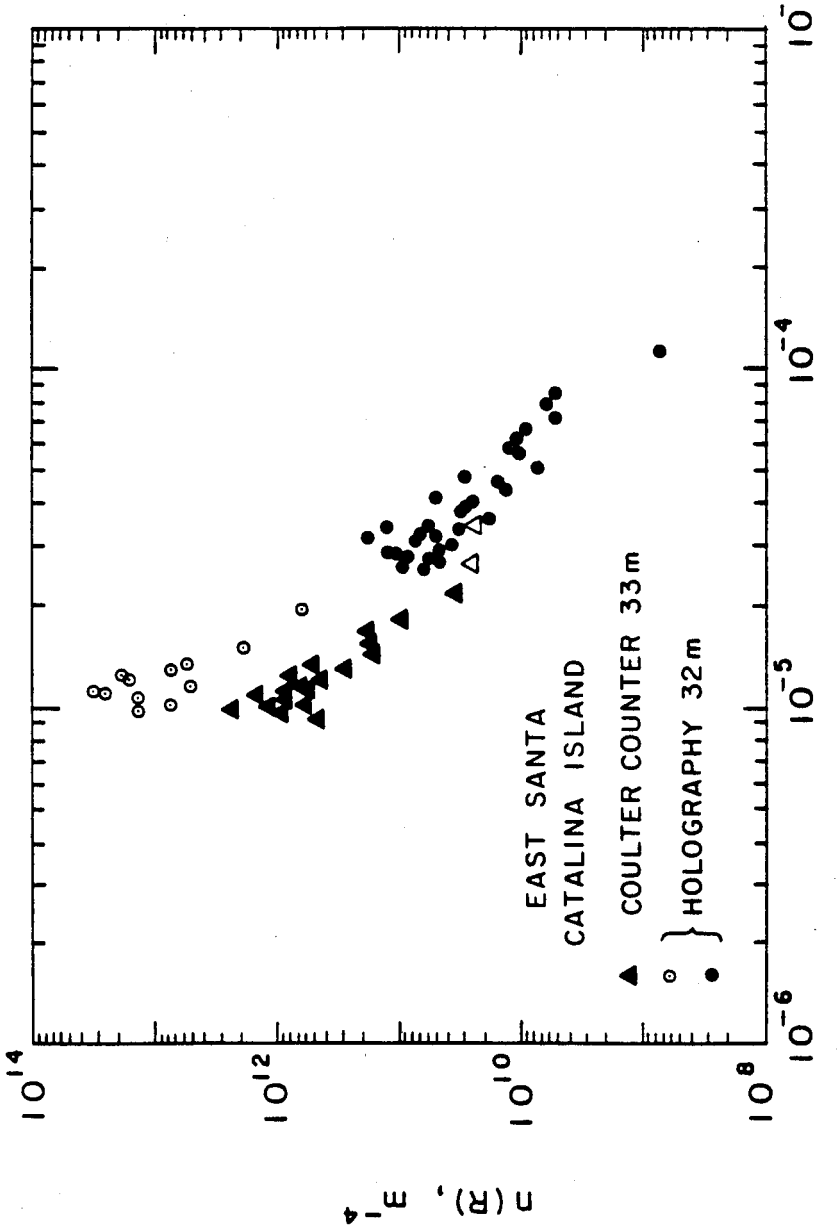

Figure 8. Number concentration density distributions of particulates, $n(R)$, in the waters off east Santa Catalina Island as a function of the particle radius, R. The number of radius counts per group is $N_g = 4$ and the expected r.m.s. error is 50%. Holographic data (circles) were recorded at 32 m depth with sampling volumes: 0.9 (open symbols) and 100 ml (solid symbols). Coulter Counter data (triangles) were obtained analyzing 20 ml water samples from 33 m depth with different sensitivity: high (solid symbols) and low (open symbols).

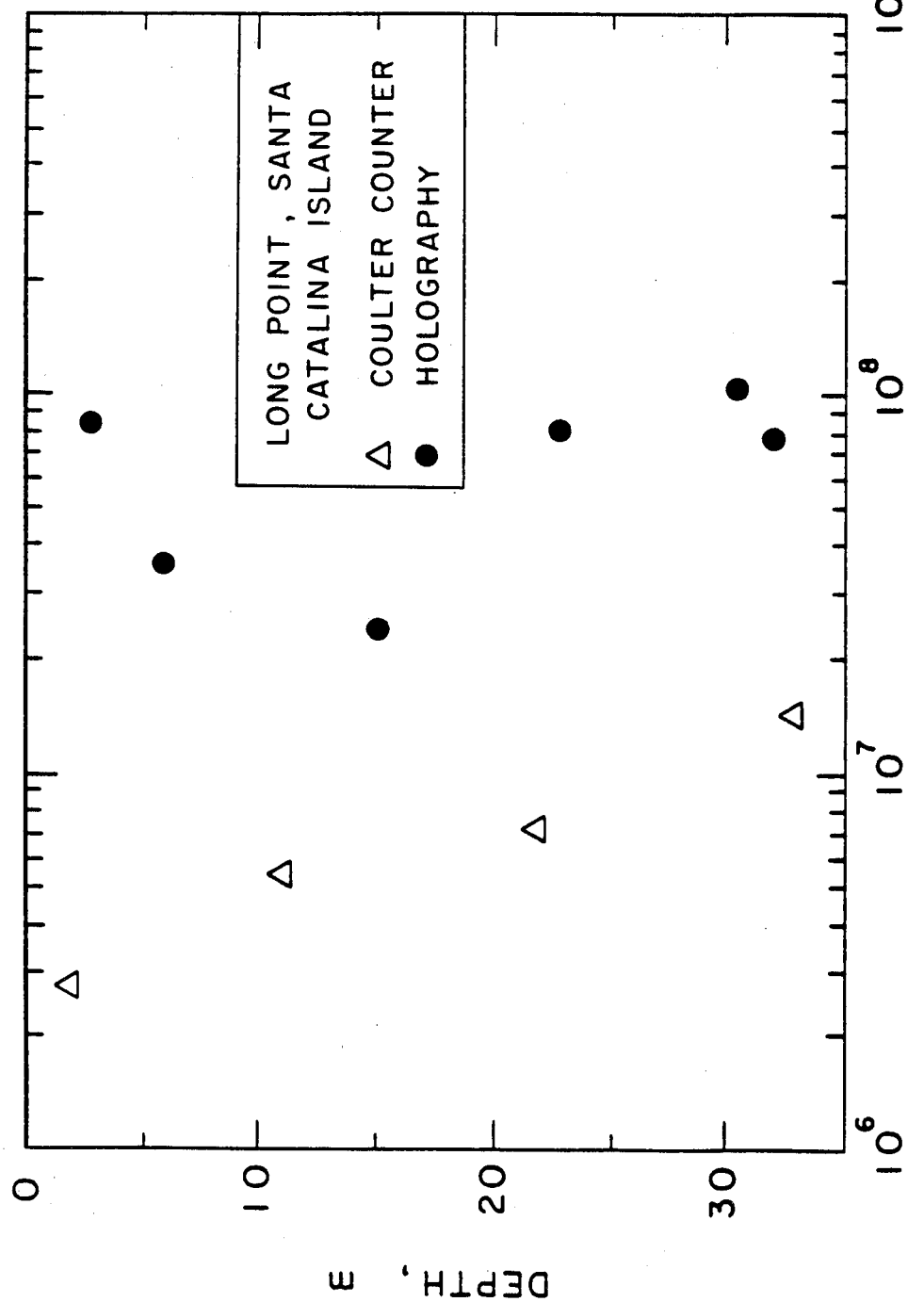

Figure 9. Particle number concentration depth profiles off Long Point, Santa Catalina Island from holographic (circles) and Coulter Counter data (triangles) in the radius range from 10 to 50 μm.

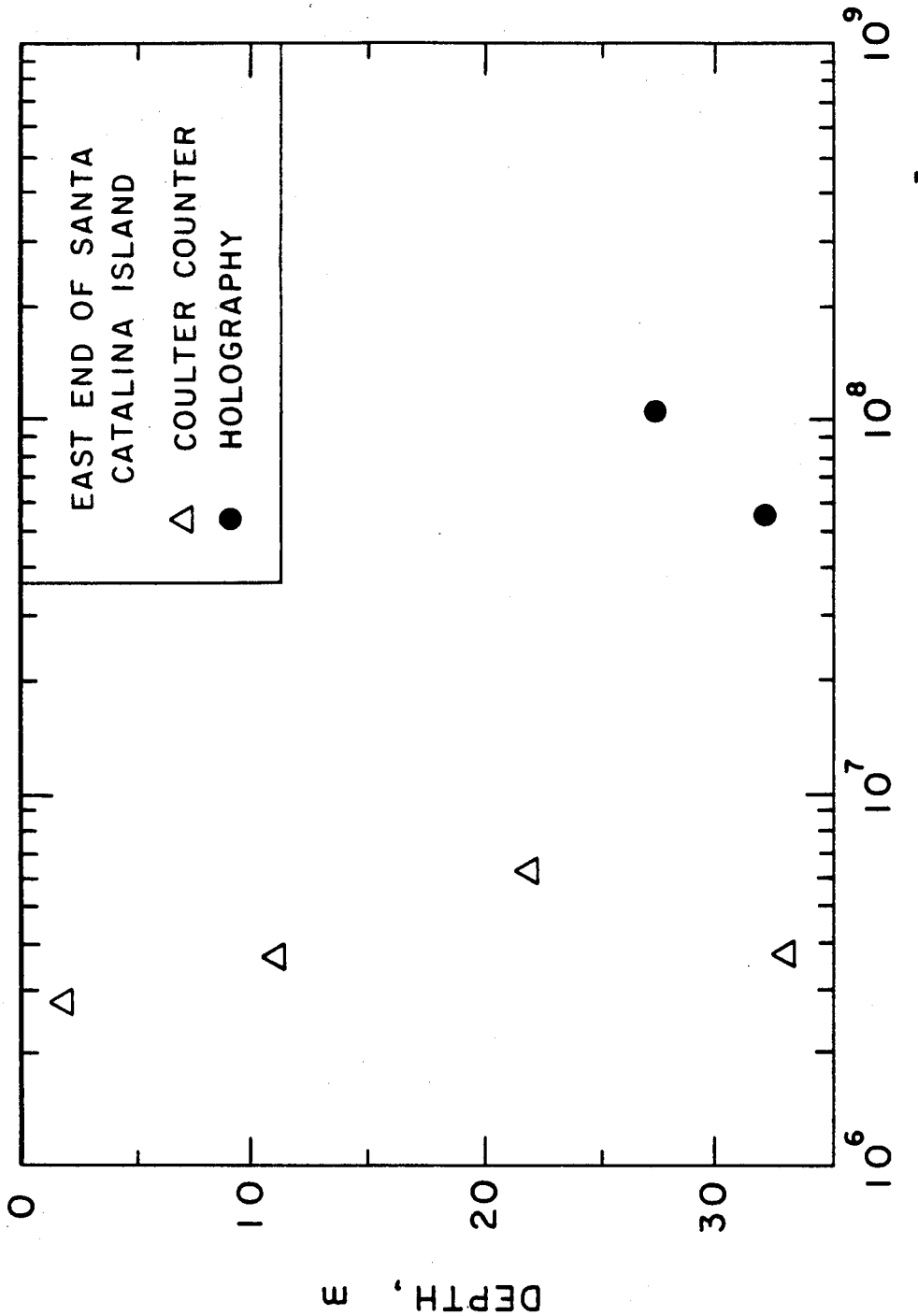

Figure 10. Particle number concentration depth profiles off east Santa Catalina Island from holographic (circles) and Coulter Counter data (triangles) in the radius range from 10 to 50 μm.

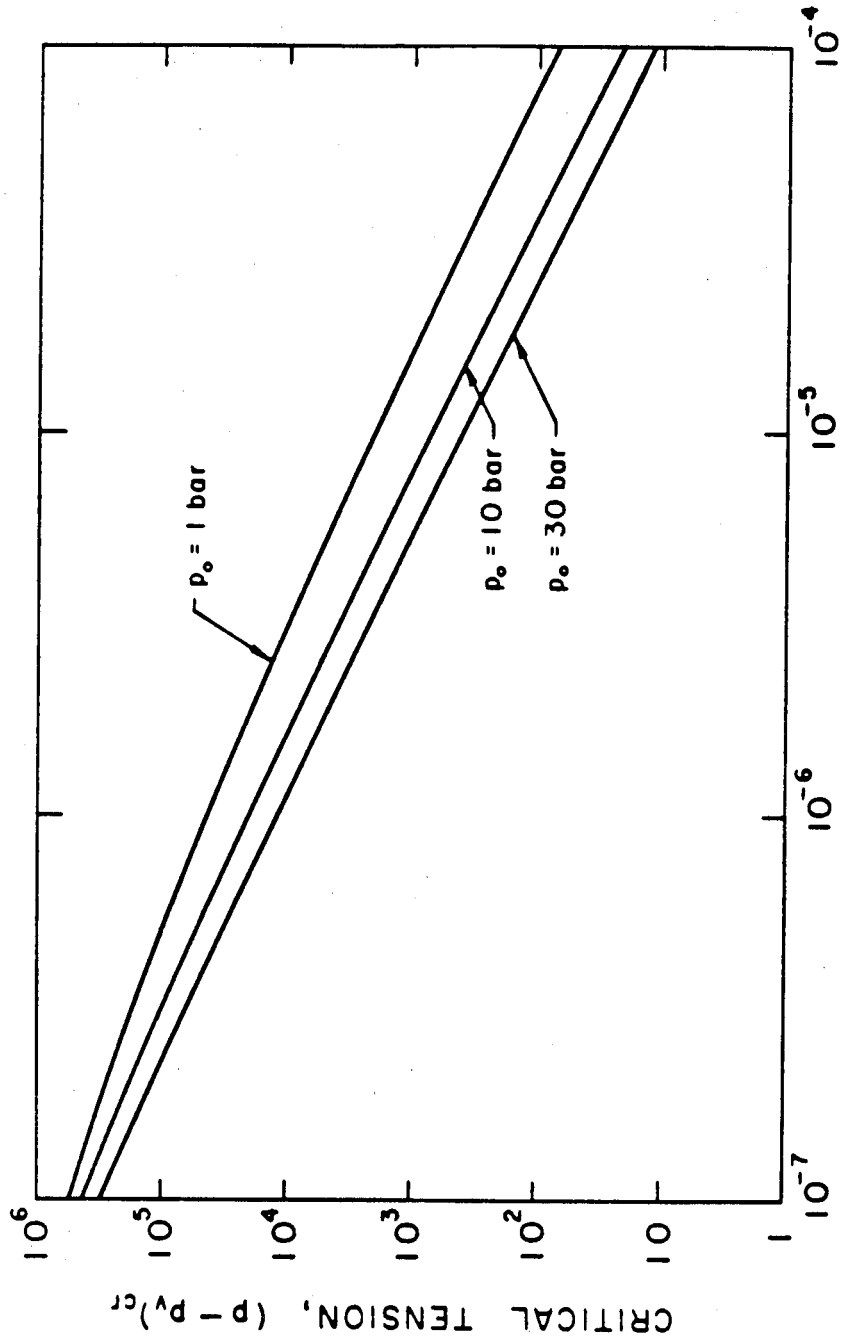

Figure 11. Critical tension, $(p_v - p)_{cr}$, of an isolated air bubble in unbounded water as a function of its static equilibrium radius, R_o, at various external pressures: $p_o = 1$ bar (upper curve), $p_o = 10$ bar (intermediate curve) and $p_o = 30$ bar (lower curve) with $T = 20\,^{\circ}\mathrm{C}$ (surface tension $S = 0.073\,\mathrm{N/m}$ and vapor pressure $p_v = 1919\,\mathrm{Pa}$).

TABLE 1

NUMBER CONCENTRATION (Number per ml) [TOTAL NUMBER COUNTED]							
Test Location	**Depth (m)**	**Radius Range (μm)**					
		10–15	15–20	20–25	25–30	30–40	40–50
off Long Point	3	15 [15]	–	–	–	–	–
off Long Point	6	3.3 [7]	–	–	–	–	–
off Long Point	15	1.6 [5]	–	–	–	–	–
off Long Point	23	0.6 [1]	–	0.6 [1]	–	–	–
off Long Point	30	8.3 [10]	–	–	–	–	–
off Long Point	32	2.5 [4]	0.6 [1]	0.6 [1]	–	–	–
off East Catalina	27	1.1 [1]	–	1.1 [1]	–	–	–
off East Catalina	32	2.2 [2]	–	–	0.03 [3]	–	0.01 [1]

Table 1. Holographic results of bubble concentrations in number per *ml*. The total number of bubbles counted in each radius range, N_g, is indicated in brackets. The estimated relative r.m.s. error of the bubble number concentration is $1/\sqrt{N_g}$.

APPENDIX III

CATALOG OF ORGANISMS IN OCEAN HOLOGRAMS

Several photographs of typical reconstructed holographic images of various objects seen in the ocean were included as figures in the main text; see, for example, Figures I.2.10, I.4.1 and I.4.11. This appendix is intended to provide additional examples of such objects, particularly organisms, which may be of interest to ocean investigators in other fields. Preliminary attempts have been made to identify each of the organisms by comparing the holographic images to sketches of organisms in standard plankton handbooks (e.g., Smith 1977; Newell & Newell 1977). In cases where no obvious identification could be made, the objects have been labeled as "unidentified." The location, recording depth and scale of each image are included in the captions. Details of the location and conditions at each of the test stations are included in Chapter I.3 of the main text.

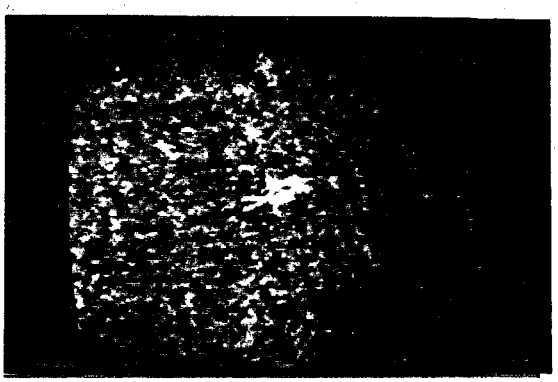

(a) Copepod nauplius.
Scale: $1/2\ in = 150\ \mu m$

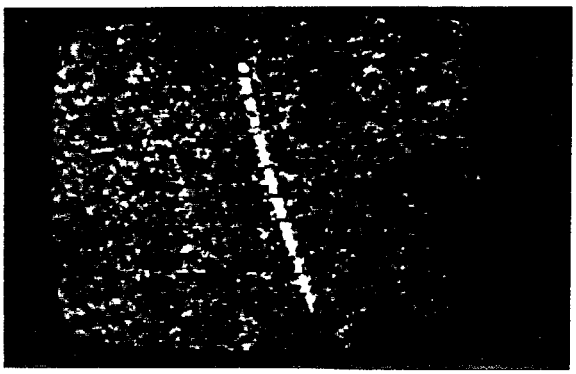

(b) Diatom.
Scale: $1/2\ in = 150\ \mu m$

(c) Unidentified.
Scale: $1/2\ in = 150\ \mu m$

(d) Unidentified.
Scale: $1/2\ in = 150\ \mu m$

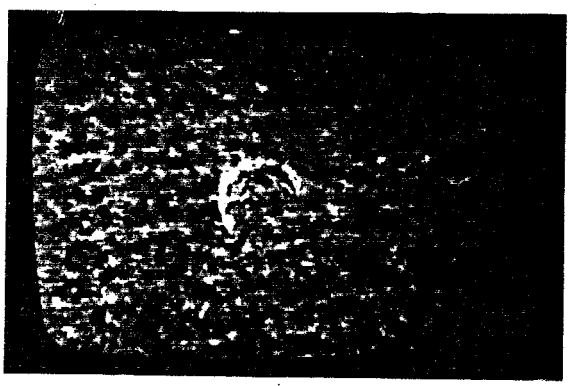

(e) Generic particle.
Scale: $1/2\ in = 150\ \mu m$

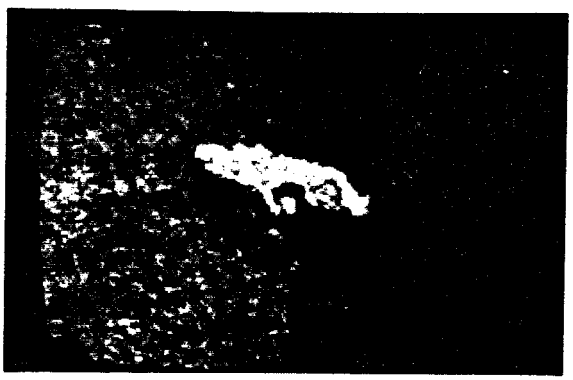

(f) Diatom.
Scale: $1/2\ in = 150\ \mu m$

Figure III-1. Station 2, all recorded at 3 m.

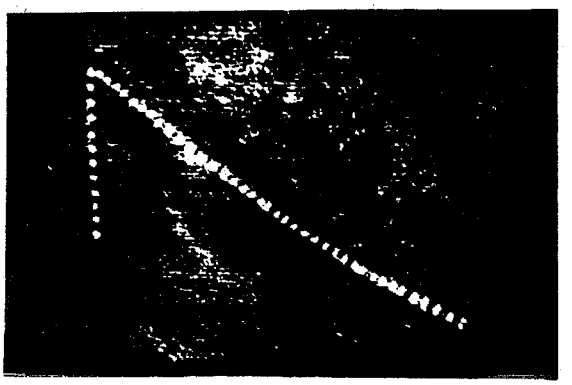

(a) Diatom.
Scale: $1/2\ in = 400\ \mu m$

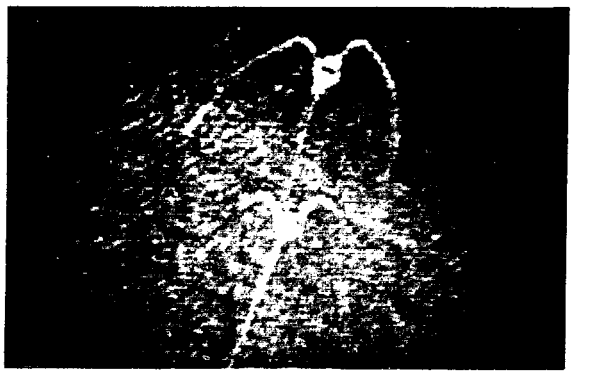

(b) Dinoflagellate *Ceratium.*
Scale: $1/2\ in = 150\ \mu m$

(c) Dinoflagellate *Ceratium.*
Scale: $1/2\ in = 150\ \mu m$

(d) Cladocera *Daphnia*
Scale: $1/2\ in = 400\ \mu m$

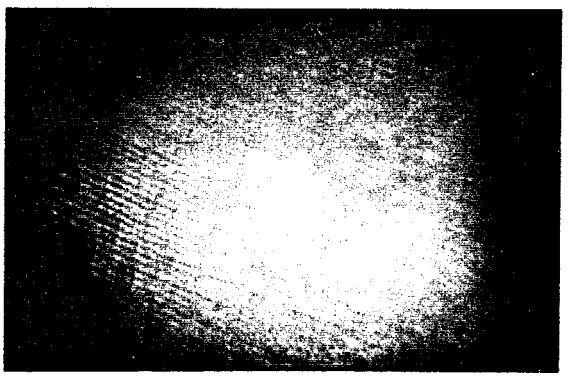

(e) Unidentified.
Scale: $1/2\ in = 400\ \mu m$

(f) Unidentified.
Scale: $1/2\ in = 150\ \mu m$

Figure III-2. Station 3. Various depths: (a) 2 m, (b) and (c) 3 m, (d) 15 m, (e) 30 m, (f) 32 m.

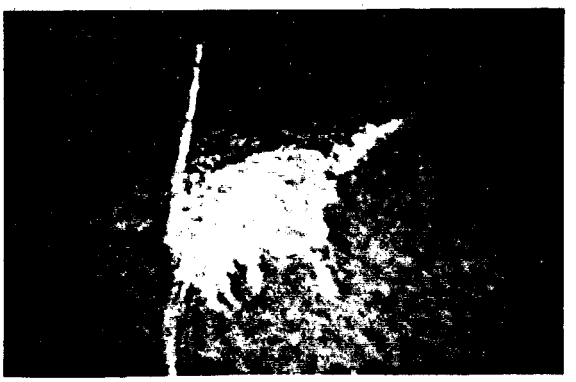

(a) Copepod.
Scale: $1/2\ in = 150\ \mu m$

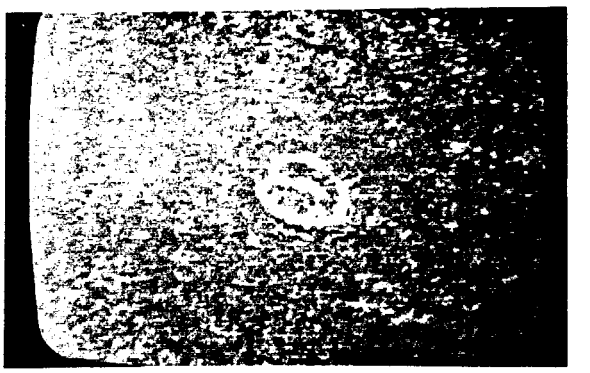

(b) Unidentified.
Scale: $1/2\ in = 150\ \mu m$

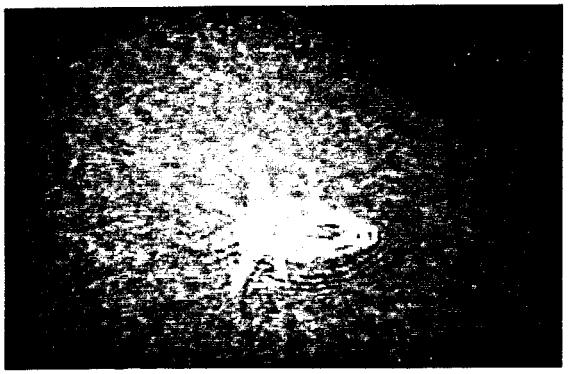

(c) Copepod nauplius.
Scale: $1/2\ in = 150\ \mu m$

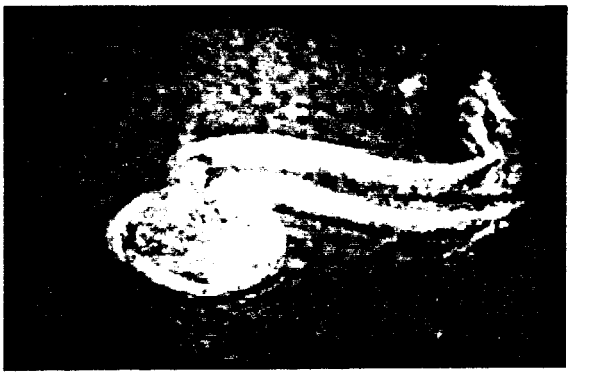

(d) Tunicata. Ascidian tadpole stage.
Scale: $1/2\ in = 150\ \mu m$

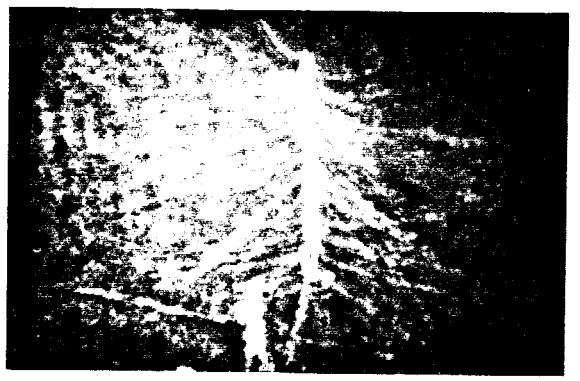

(e) Diatom.
Scale: $1/2\ in = 150\ \mu m$

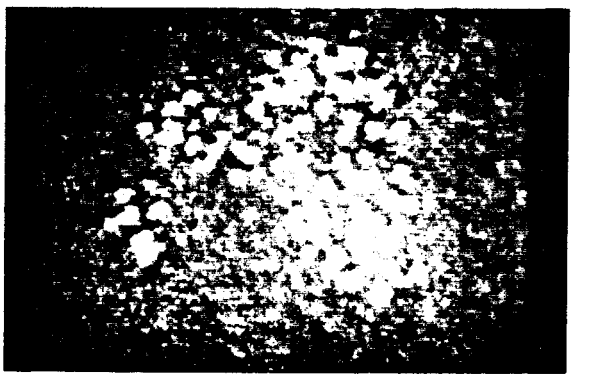

(f) Aggregate particle, "Marine snow."
Scale: $1/2\ in = 250\ \mu m$

Figure III-3. Station 3, all recorded at 30 m.

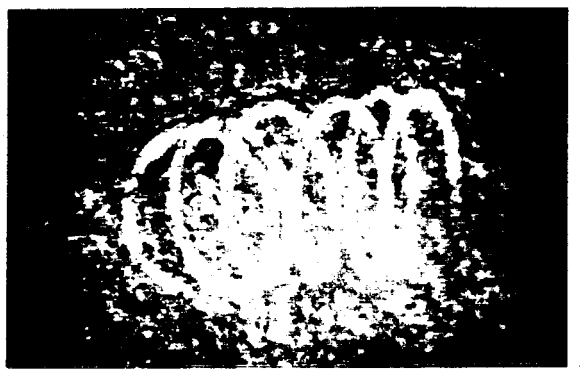

(a) *Chaetoceros* diatom.
Scale: $1/2\ in = 115\ \mu m$

(b) *Chaetoceros* diatom.
Scale: $1/2\ in = 400\ \mu m$

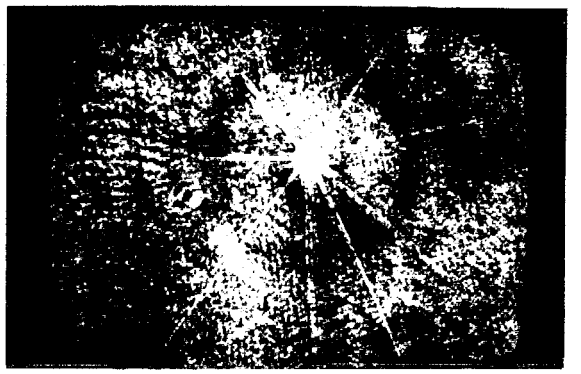

(c) Radiolarian.
Scale: $1/2\ in = 500\ \mu m$

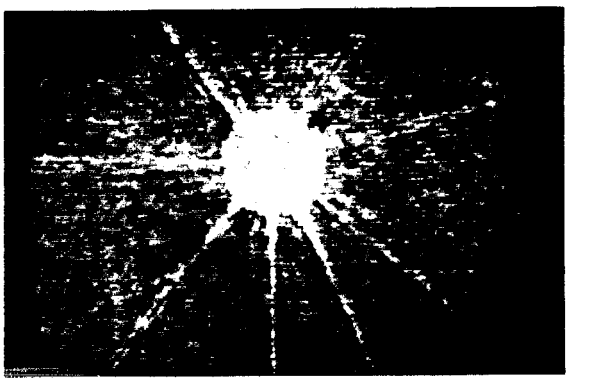

(d) Higher magnification view of (c).
Scale: $1/2\ in = 150\ \mu m$

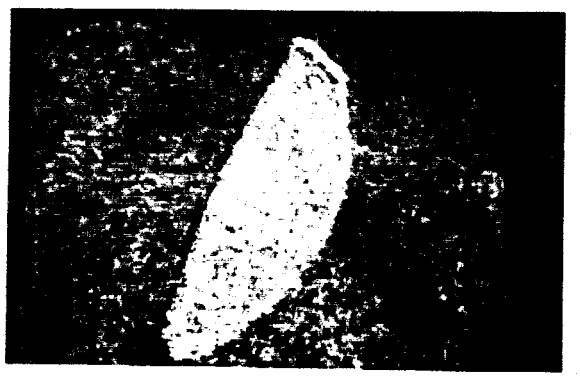

(e) Unidentified.
Scale: $1/2\ in = 150\ \mu m$

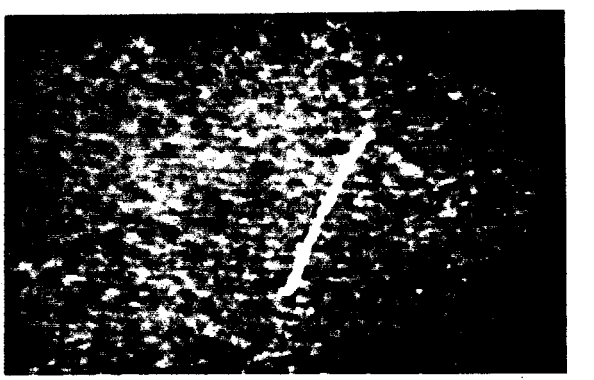

(f) Diatom.
Scale: $1/2\ in = 150\ \mu m$

Figure III-4. Station 3, all recorded at 32 m.

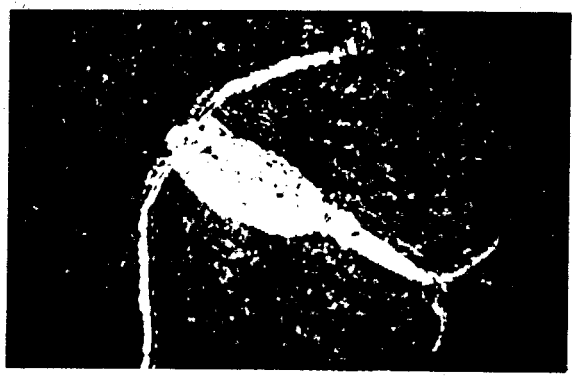

(a) Copepod.
Scale: $1/2\ in = 250\ \mu m$

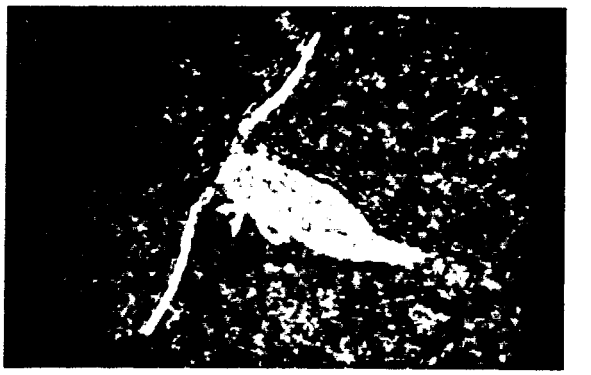

(b) Copepod.
Scale: $1/2\ in = 150\ \mu m$

(c) Copepod.
Scale: $1/2\ in = 400\ \mu m$

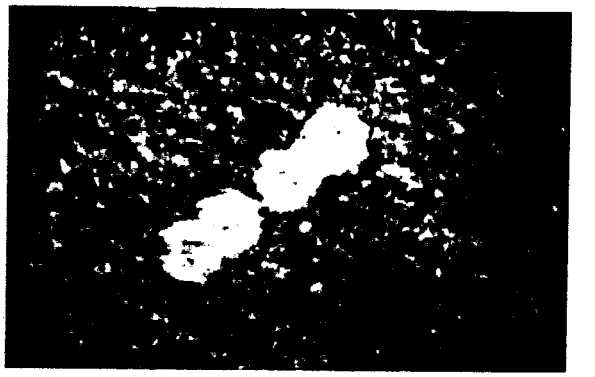

(d) Fecal pellets.
Scale: $1/2\ in = 150\ \mu m$

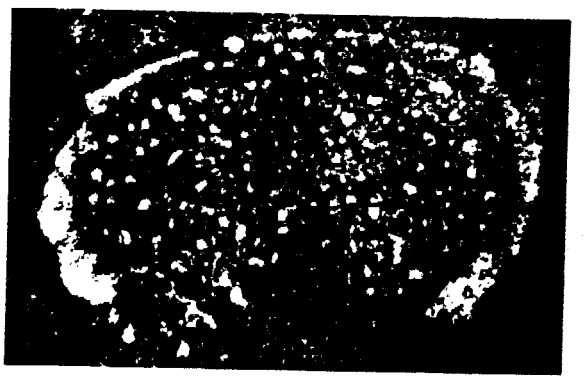

(e) Aggregate particle, "Marine snow."
Scale: $1/2\ in = 250\ \mu m$

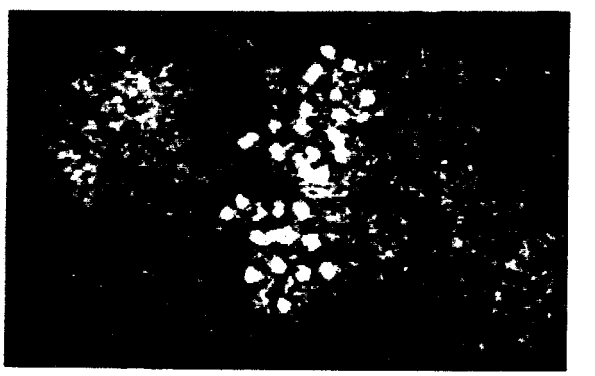

(f) Aggregate particle, "Marine snow."
Scale: $1/2\ in = 150\ \mu m$

Figure III-5. Station 4, all recorded at 32 m.

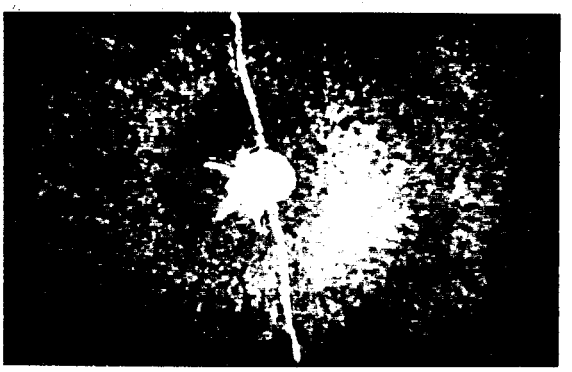

(a) Copepod. (End view).
Scale: $1/2\ in = 400\ \mu m$

(b) Dinoflagellate *Ceratium.*
Scale: $1/2\ in = 150\ \mu m$

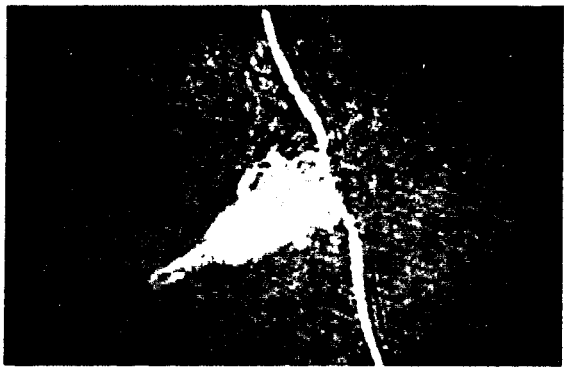

(c) Copepod.
Scale: $1/2\ in = 300\ \mu m$

(d) Copepod nauplius.
Scale: $1/2\ in = 150\ \mu m$

(e) Copepod. (End view).
Scale: $1/2\ in = 250\ \mu m$

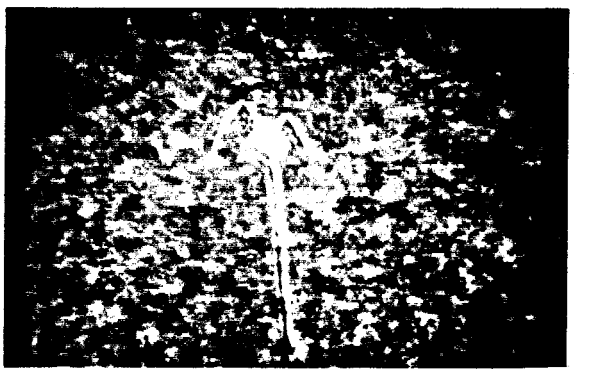

(f) Dinoflagellate *Ceratium.*
Scale: $1/2\ in = 150\ \mu m$

Figure III-6. Station 5. Various depths: (a) - (d) 3 m, (e) and (f) 6 m.

(a) Unidentified.
Scale: $1/2\ in = 150\ \mu m$

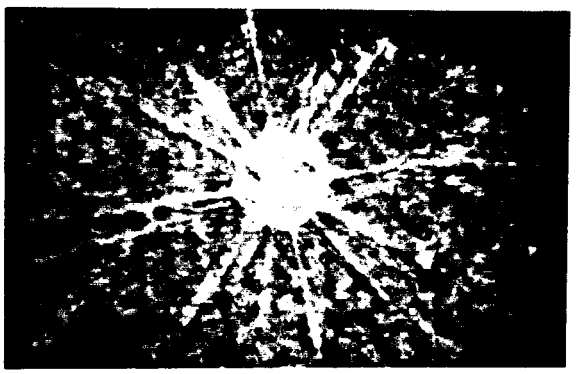

(b) Radiolarian.
Scale: $1/2\ in = 150\ \mu m$

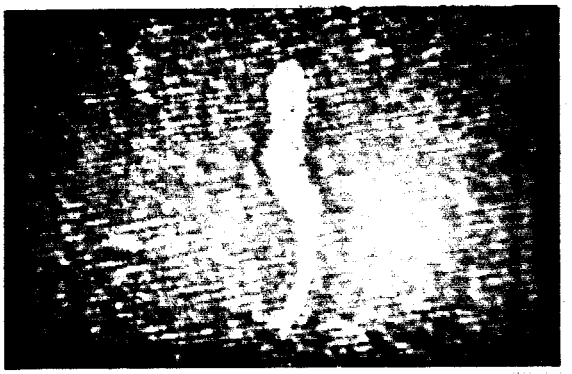

(c) Larvacean *Oikopleura.*
Scale: $1/2\ in = 150\ \mu m$

(d) Unidentified.
Scale: $1/2\ in = 150\ \mu m$

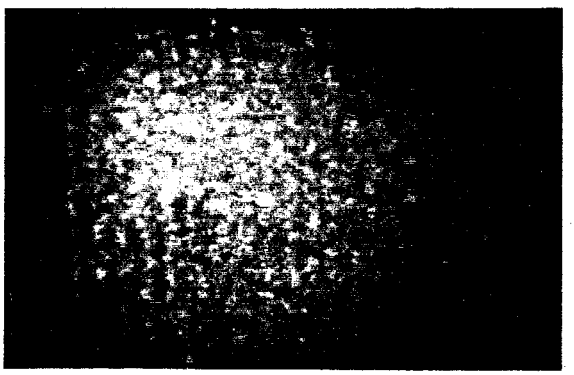

(e) Tiny unidentified object.
Scale: $1/2\ in = 150\ \mu m$

(f) Fecal pellets.
Scale: $1/2\ in = 150\ \mu m$

Figure III-7. Station 5. Various depths: (a) 6 m, (b) 12 m, (c) - (e) 21 m, (f) 34 m.